Énergie, Matériaux et Télécommunications

Toward Accurate Photoluminescence Nanothermometry Using Rare-Earth Doped Nanoparticles for Biomedical Applications

Par

Miao Liu

Thèse présenté(e) pour l'obtention
du grade de Philosophiae Doctor (Ph.D.)
en sciences de l'énergie et des matériaux

Jury d'évaluation

Président du jury et examinateur interne	Prof. Dongling Ma INRS-ÉMT
Examinateur externe	Prof. Niko Hildebrandt Department of Engineering Physics McMaster University
Examinateur externe	Prof. Gabriella Tessitore Faculté de sciences et de génie Université Laval
Directeur de recherche	Prof. Jinyang Liang INRS-ÉMT
Codirecteur de recherche	Prof. Fiorenzo Vetrone INRS-ÉMT

ACKNOWLEDGMENTS

It is my honor to express my deepest and sincere gratitude to my supervisor: Prof. Jinyang Liang, and my co-supervisor Prof. Fiorenzo Vetrone, for offering me this wonderful opportunity to do my doctoral research under their supervision. “Get down to the bottom” was the most impressive lesson among many others that I learned from Prof. Jinyang Liang. This mantra of sorts guided me throughout my whole PhD to explore deeply and will continue to inspire me in the future life. “Go ahead” was always the phrase from Prof. Fiorenzo Vetrone together with his unwavering support and encouragement − giving me lots of freedom to strive for greater accomplishments and enjoy the academic journey. I cannot put in words all my gratitude toward them, as there is nothing less than being lucky for having them as my PhD supervisors. They are always there to teach me basics from zero with great patience, provide me advice with crucial insights, and clear my doubts in invaluable discussions meanwhile leaving me the freedom to work independently. I am also fortunate to know them outside of academia during the deep conversations, some of which took place in Prof. Vetrone’s office with his freshly ground espresso, and some happened in different restaurants with Prof. Liang after enjoying the group dinner. I am forever grateful for having them as supervisors.

During my PhD, I had the pleasure to talk with many exceptional scientists whom I would like to thank for their collaborative efforts and insightful comments: Prof. Luís D. Carlos, Prof. Carlos D. S. Brites, Prof. Fernando Aparecido Sigoli, Prof. Louis Cuccia. My extended appreciation to Prof. Dongling Ma, Prof. Gabriella Tessitore, and Prof. Niko Hildebrandt as members of my dissertation committee.

I would like to also thank my colleagues in the two labs: Arohan Dutta, Dr. Xianglei Liu, Yingming Lai, Dr. Miguel Marquez, Dr. Jingdan Liu, Dr. Patrick Kilcullen, Dr. Cheng Jiang, Beniwal Madhu, Siqi Wang, Hanzi Liu, Dr. Lina Zhou, Mingrui Guo, Vivienne Tam. Prof. Artiom Skripka deserves special mention as the “survival guide” he left did help me a lot when I was alone in the lab during COVID. I am grateful to become scientific and personal friends with them.

Many friends enriched my experience on this journey, and I appreciate the chance to meet with them: Prof. Junliang Dong, Paulina Rajchel-Mieldzioć, Feng Zhu, Dr. Xin Liu, Joao Antonio, Bakshi Avik, Fang Dong, Dr. Wanting He, Almohammed Bahaa, Sixiang Liu, Dr. Xiaohua Yang, Dr. Pan Wang, Dr. Hao Yu, Dr. Yang Liu, Xiaofeng Pan, Ruiqi Yang.

Lastly, my deepest appreciation to my family for their emotional support throughout the journey every day. I am indebted to my parents over and beyond. They deserve to have their name mentioned here: Zhongyi Liu and Yaqin Wang, rather than just being simply referred to as my parents. Also, thanks to my brother and his two lovely kids with whom I enjoyed a wonderful time.

RÉSUMÉ

La température influence tous les aspects de notre vie, en particulier à notre époque. La mesure de la température locale est d'une importance cruciale dans les sciences de la vie, où elle constitue un paramètre essentiel. Depuis la génération précédente de thermomètres de contact, invasifs et à l'échelle microscopique, jusqu'aux nouveaux thermomètres télécommandés, mini-invasifs et à l'échelle submicrométrique, la nanothermométrie par photoluminescence a révolutionné notre façon de mesurer la température, avec un accent particulier sur les applications biomédicales. Parmi les différents nanothermomètres photoluminescents, les nanoparticules dopées aux terres rares (RENPs) sont privilégiées en raison de leur grande photostabilité, de leur faible toxicité et de la facilité relative de modification de leur surface. Leurs propriétés optiques polyvalentes comprennent des émissions multicolores couvrant les régions ultraviolette, visible et proche infrarouge (NIR), ainsi que la capacité de conversion ascendante sous une excitation unique en NIR, compatible avec les milieux biologiques. Par ailleurs, le processus de conversion descendante transforme l'excitation en NIR en une émission à des longueurs d'onde encore plus longues. Cette double capacité d'excitation et d'émission dans le NIR rend les RENPs particulièrement adaptées à l'imagerie des tissus en profondeur et à la nanothermométrie. En effet, les RENPs ont déjà suscité un grand intérêt et ont été appliquées avec succès dans des expériences *in vitro* et *in vivo*.

La détermination de la température repose sur deux éléments essentiels : des instruments optiques et des nanothermomètres. Cette thèse explore ces deux aspects afin de développer une nanothermométrie précise à base de RENPs pour des applications biomédicales. Une attention particulière est portée aux émissions en NIR situées dans la fenêtre biologique. Notamment, une microscopie de luminescence résolue en temps en NIR, utilisant une caméra streak entièrement optique, est développée pour la première fois du côté instrumental. La cartographie bidimensionnelle des durées de vie en NIR est ainsi exploitée pour la mesure de la température, ouvrant la voie à la nanothermométrie basée sur la durée de vie des RENPs dans les applications biologiques en profondeur. Par ailleurs, une nouvelle architecture, cœur inerte-coquille active-coquille inerte, est conçue afin d'améliorer l'intensité d'émission de l'Er^{3+} au-delà de 1500 nm en dopant davantage d'activateurs. Le phénomène de quenching par concentration est atténué grâce à l'extension de la couche active aux interfaces cœur-coquille. Cette intensité NIR considérablement renforcée permet d'obtenir un rapport signal/bruit élevé lors de la

détection, conférant aux RENPs un fort potentiel pour la mesure de la température en profondeur dans les tissus biologiques. Enfin, les aspects fondamentaux régissant la réponse optique des RENPs aux variations de température en milieu aqueux sont examinés. L'impact de l'eau sur le spectre de photoluminescence et sur les mesures de température met en lumière à la fois le potentiel et les limites de la nanothermométrie basée sur les RENPs.

Mots-clés: Nanoparticules dopées aux terres rares, nanothermométrie, conversion descendante, proche infrarouge, durée de vie de la photoluminescence, intensité de la photoluminescence, cœur-coquille, effet de l'eau.

ABSTRACT

Temperature touches all aspects of our lives, particularly in this day and age. Measurement of local temperature is especially pertinent in the life sciences where it is a critical parameter. From the previous generation of contact, invasive, microscale level thermometers to new remote control, minimally invasive, sub-micrometer scale thermometers, photoluminescence nanothermometry has revolutionized the way we read temperature with specific emphasis on applications in biomedicine. Among various photoluminescent nanothermometers, preference is given to rare-earth doped nanoparticles (RENPs) that showcase high photostability, low toxicity, and the relative ease of surface modifications. The versatile optical properties of RENPs include their multicolour emissions spanning the ultraviolet, visible, and near-infrared (NIR) regions--the ability to undergo upconversion with a single biologically friendly NIR excitation wavelength. At the same time, the downshifting process converts NIR excitation to the emission of even longer wavelengths. In particular, this ability to be excited but also emit in the NIR region makes RENPs especially suitable for deep tissue imaging and nanothermometry. In fact, RENPs have already gained significant traction and have been successfully applied in both *in vitro* and *in vivo* experiments.

Determination of temperature necessitates two essential components: optical instruments and nanothermometers. This thesis pushes from both the instrument and materials side to develop accurate RENP nanothermometry for biomedical applications. NIR emissions falling within the biological window are of special interest. Particularly, first-of-its-kind NIR photoluminescence lifetime imaging microscopy using an all-optical streak camera is developed on the instrumental side. Two-dimensional NIR lifetime can be efficiently mapped for temperature sensing, paving the way for RENP lifetime-based nanothermometry in deep tissue biological applications. Furthermore, a new architecture, inert core-active shell-inert shell, is designed to enhance the emission intensity of Er^{3+} beyond 1500 nm via doping more activators. Concentration quenching is suppressed by extending the active layer at the core-shell interfaces. The highly boosted NIR intensity provides high signal-to-noise during signal detection, offering RENPs great potential for deep tissue temperature sensing. Finally, fundamental aspects governing the optical response of RENPs to temperature change in aqueous environments are scrutinized. Reported water effect on the photoluminescence spectrum as well as the temperature readouts paint a realistic outlook on the potential and pitfalls of RENP nanothermometry.

Keywords: Rare-earth doped nanoparticles, nanothermometry, downshifting, near-infrared, photoluminescence lifetime, photoluminescence intensity, core-shell, water effect

TABLE OF CONTENTS

LIST OF FIGURES

LIST OF TABLES

LIST OF ABBREVIATIONS

RENPs	Rare-earth doped nanoparticles
UV	Ultraviolet
NIR	Near-infrared
UC	Upconversion
DS	Downshifting
SNR	Signal-to-noise ratio
ESA	Excited state absorption
ETU	Energy transfer upconversion
CR	Cross relaxation
PA	Photon avalanche
LSPR	Localized surface plasmon resonance
PLIR	Photoluminescence intensity ratio
CF_3COONa	Sodium trifluoroacetate
CF_3COOLi	Lithium trifluoroacetate
RE_2O_3	Rare-earth oxides
$(CF_3COO)_3RE$	Rare-earth trifluoroacetate
H_2O	water
D_2O	Heavy water
OA	Oleic acid
ODE	Oleylamine
ODE	1-octadecene
$NOBF_4$	Nitrosonium tetrafluoroborate
RE^{3+}	Rare-earth ions
TCSPC	Time-correlated single photon counting
SPAD	Single-photon avalanche diode
SWIR	Short-wave infrared
1D	One-dimensional

2D	Two-dimensional
CCD	Charge-coupled device
CMOS	Complementary metal-oxide-semiconductor
PLIMASC	Photoluminescence lifetime imaging microscopy using an all-optical streak camera
mm	Millimeter
μm	Micrometer
nm	Nanometer
Hz	Hertz
kHz	Kilohertz
fps	Frames per second
XRD	X-ray diffraction
TEM	Transmission electron microscopy
HAADF-STEM	High-angle annular dark-field scanning transmission electron microscopy
EDS	Energy-dispersive X-ray spectrometry
C	Core
S	Shell
AC	Active core
IC	Inert core
IS	Inert shell
FN	First nuclei

LIST OF PUBLICATIONS

Journal publications:

[1] **M. Liu**, Y. Lai, M Marquez, F. Vetrone, J. Liang, “Short-wave Infrared Photoluminescence Lifetime Mapping of Rare-Earth Doped Nanoparticles Using All-Optical Streak Imaging”, Adv. Sci., 11, 11, 2305284–2305292 (2024)

[2] **M. Liu**, J. Liang, F. Vetrone, “Toward Accurate Photoluminescence Nanothermometry Using Rare-Earth Doped Nanoparticles for Biomedical Applications”, Acc. Chem. Res., 57, 18, 2653–2664 (2024)

[3] **M. Liu**, J. Liang, F. Vetrone, Adv. Mater., “Increasing Downshifting Luminescence Intensity Through an Extended Active Layer” Adv. Mater., under review (2025)

[4] **M. Liu**, Paulina Rajchel-Mieldzioć, Piotr Fita J. Liang, F. Vetrone, “Effect of H_2O on the Upconversion and Downshifting Luminescence Nanothermometry”, Nanoscale, submitted (2025)

Patent:

J. Liang, F. Vetrone, X. Liu, A. Skripka, Y. Lai, **M. Liu,** Method and system for real-time wide-field dynamic temperature sensing. US12130186B2, 2024.

Conference proceedings:

[1] **M. Liu**, J. Liang, F. Vetrone. “Manipulating and mapping the short-wave infrared photoluminescence lifetime of rare-earth doped nanoparticles”, UPCON, 2024, Nanoscale and Nanoscale Advances Poster Prize

[2] **M. Liu**, Y. Lai, M Marquez, F. Vetrone, J. Liang. “Short-wave infrared streak camera for photoluminescence lifetime mapping of rare-earth doped nanoparticles", UltrafastX, 2023, Best Student Oral Award

[3] **M. Liu**, J. Liang, F. Vetrone. “Near-infrared lifetime mapping of rare-earth doped nanoparticles using ultrahigh-speed line-scanning microscopy", QCAM/CQMF, 2023, Prize for Best Talk – Biomedical

1 INTRODUCTION

1.1 Nanothermometry

As one of the most important biomarkers in biology, temperature directly affects innumerable processes in the body including metabolic rate, gene expression, immune reaction, cell cycle, and apoptosis.(Campbell-Staton *et al.*, 2021; Daniel *et al.*, 2008; Evans *et al.*, 2015) Monitoring temperature could thus be a feasible and effective way to study basic biological functions (e.g., brain activity and enzyme activity) where the temperature variations are minute (ca. 1 °C).(Daniel *et al.*, 2008; Rodriguez-Sevilla *et al.*, 2022) Furthermore, the first sign of most illnesses (e.g., cancer, infection, inflammation, and cardiovascular conditions) is the presence of a thermal gradient(Shen *et al.*, 2022a; Tan *et al.*, 2020a; Ximendes *et al.*, 2016a), and hence temperature sensing can potentially be of great value in disease detection.

From the invention of the thermoscope by Galileo (Anonyme, 2001) until our days, temperature sensing probes have been developed from the previous generation of contact, invasive, microscale level thermometers (e.g., thermocouple) to new remote control, minimally invasive, sub-micrometer scale thermometers (e.g., photoluminescent nanothermometers). Photoluminescence nanothermometry is based on the optical performance of the probe, which will be influenced by its surrounding temperature, establishing a correlation between its photoluminescence properties and temperature. Such thermal sensing at a well-defined local area with high spatial resolution has been recognized as a promising technique for accurate temperature measurement with specific emphasis on applications in biomedicine.(Jaque *et al.*, 2012; Wang *et al.*, 2013b) A variety of nanoscale optical probes have been studied for photoluminescence nanothermometry, for example, organic fluorophores, quantum dots, and diverse carbon nanostructures.(Jaque *et al.*, 2012; Wolfbeis, 2015; Zhou *et al.*, 2020d) Among these studied photoluminescent probes, rare-earth doped complexes and nanoparticles have shown great promise for nanothermometry. In particular, rare-earth doped nanoparticles (RENPs) are at the forefront as they have high photostability, low toxicity, and the relative ease of biofunctionalization such that their surfaces could be altered by specific biological moieties.(Gai *et al.*, 2014; Matulionyte *et al.*, 2023) Most importantly, RENPs present unique optical properties, such as narrow 4*f*-4*f* transition bandwidths, long lifetimes, and high resistance to interference from the surrounding environment.(Dong *et al.*, 2015; Gai *et al.*, 2014; Matulionyte *et al.*, 2023) When excited with NIR wavelengths, RENPs possess multiple emissions in the ultraviolet (UV), visible, and NIR ranges. Specifically, their ability to be excited

but also emit in the NIR region makes them especially suitable for deep tissue imaging and nanothermometry. These distinguishing properties showcase their versatility and allow RENPs to stand out from their counterparts.

1.2 Rare-earth doped nanoparticles

1.2.1 Structure

RENPs are generally comprised of an inorganic host doped with rare-earth ions as sensitizers and activators. Typically, the sensitizer absorbs excitation energy and then transfers it to the luminescence center which is called the activator.

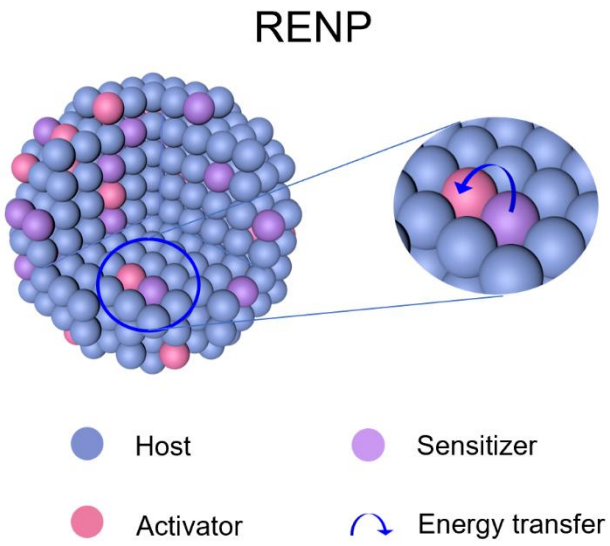

Figure 1.1 Typical structure of RENPs.

Host: An appropriate host matrix is essential for high-efficiency photoluminescence emissions. Ideal host materials should be chemically and thermally stable, transparent in the spectral range of interest, and have a high optical damage threshold. Most importantly, the phonon energy of the host lattice closely relates to the non-radiative relaxations. To get a high photoluminescence intensity, hosts with low phonon energy are preferred. Typical hosts are fluorides, oxides (Y_2O_3, phonon energy: ~550 cm^{-1})(Martínez *et al.*, 2010), vanadates (YVO_4,(Mialon *et al.*, 2010) phonon energy: ~890 cm^{-1}), oxysulfides (Y_2O_2S phonon energy: ~520 cm^{-1}), and oxy-fluorides or -chlorides (Y_2O_2S phonon energy: ~500 cm^{-1}).(Kumar *et al.*, 2012) Fluorides are usually chosen for their high chemical stability and low phonon energies (~350 cm^{-1}) which can be synthesized

with uniform morphology for efficient photoluminescence processes. The normally used fluorides host include: LaF_3, $Na(RE)F_4$, $Li(RE)F_4$, CaF_2, et al.

Sensitizer: the sensitizer plays an important role in photoluminescent RENPs, as it efficiently absorbs the excitation energy and then transfers it to adjacent luminescent ions. To enable a high photoluminescence efficiency, the incorporated sensitizer normally has a high absorption cross-section at the excitation wavelength, and a simple energy diagram to avoid self-emission. Certainly, it is required that efficient energy transfer between the sensitizer and activator can occur. Yb^{3+} is the classical sentisizer with only one excited state $^2F_{5/2}$ as well as a high absorption cross-section ($1.77x10^{-20}$ cm^2 at 976 nm).(Wiesholler *et al.*, 2019) Nd^{3+} ($1.25x10^{-19}$ cm^2 at 794 nm) has also been used as a sensitizer which switches the excitation wavelength from 980 nm to ~800 nm. Besides, the distance between the sensitizer and the luminescence centers also largely determines the efficiency of the energy transfer process. The distance from sensitizers to activators relies on the concentration of sensitizer, usually optimized at a concentration of 20% for Yb^{3+}.

Activator: most rare-earth ions have abundant energy levels which can be used to produce different color emissions while some are more emissive than others.(Carnall, 1979; Carnall *et al.*, 1968; Werts *et al.*, 2002) The emission corresponds to the radiative transitions from the excited states to lower-level excited states or ground state of rare-earth ions. Benefiting from the ladder-like arrangement of their energy states, some rare-earth ions are capable of absorbing more than two photons sequentially to pump to high energy levels. Emission with high energy normally takes more photons to participate during the pumping process. For example, the main emission of Er^{3+} in the visible range is at ~520 nm and ~540 nm, originating from the $^2H_{11/2}$ and $^4S_{3/2}$ state respectively, which are pumped by two photons absorption process. UV emission at 290 nm and 350 nm due to the $^1I_6 \rightarrow {}^3H_6$ and $^1I_6 \rightarrow {}^3F_4$ transitions of Tm^{3+} via five-photon upconversion luminescence process.(Chen *et al.*, 2020; Wen *et al.*, 2018)

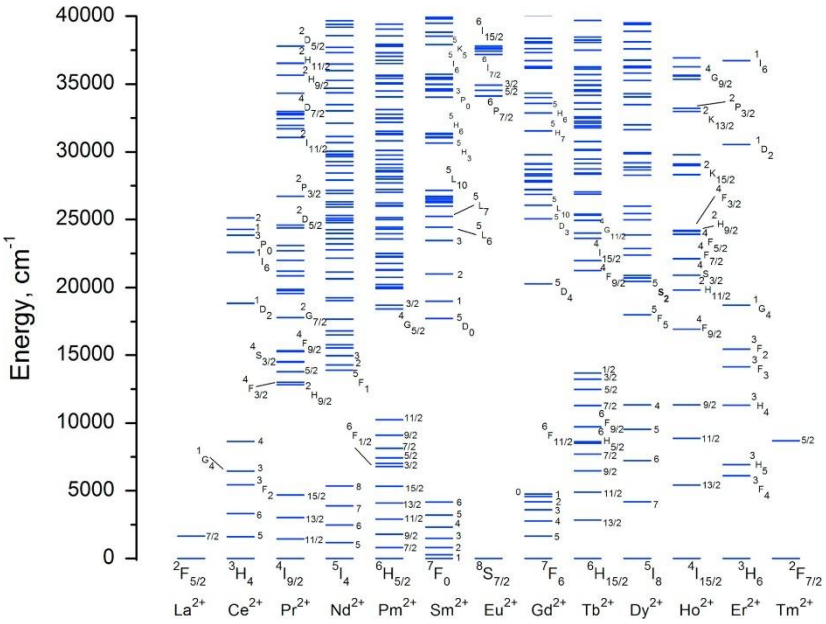

Figure 1.2 Energy diagrams for the lanthanide ions. (Ma *et al.*, 2016)

1.2.2 Basics of rare-earth ions

Lanthanides refer to the elements with atomic numbers from 57 to 71 in the sixth period of periodic table, ranging from lanthanum to lutetium. These 15 lanthanide elements, together with scandium and yttrium which are chemically similar, are the so-called rare-earth elements. From the first discovery in 1787 till now, these elements have been studied which led to many technological progresses and wide applications mainly including chemistry, biomedicine, optoelectronics, and aerospace. (Cheng *et al.*, 2013; Jung *et al.*, 2018; Zhou *et al.*, 2015)

Electronic configuration: the electronic configuration of lanthanide atoms is [Xe] $4f^n$ $5d^{0-1}$ $6s^2$ (n = 0−14) where n denotes the number of electrons in the unfilled 4*f* shell. When these rare-earth elements are introduced into the host, they easily lose two or three electrons to acquire the stable electronic configuration. Although RE elements are found in +2, +3 and even +4 oxidation states, +3 oxidation state is considered as the most stable one.(Sun *et al.*, 2015) The 4*f* shell is shielded by the outer $5s^2$ and $5p^6$ shells and thus the optical properties of 4*f* electrons of lanthanides are slightly impacted by the surrounding environment. Therefore, the emission properties of RENPs include their narrow emission bandwidth and long photoluminescence lifetime. Electronic transitions between 4*f* levels are parity forbidden by Laporte's selection rules. However, when incorporated into a host matrix, the electronic structure of rare-earth ions is perturbed. By intermixing $4f^n$ and $4f^{n-1}5d$ orbitals, the parity of levels is changed, and the optical transitions become allowed which are known as electronic dipole-allowed transitions. Crystal

field theory has been used to describe the interaction between doped elements and the host matrix. The energy levels of rare-earth elements can be represented by the total orbital angular momentum *L* (sum of total quantum number l), total spin angular momentum *S* (sum of total quantum number s), and the total angular momentum *J*. The interaction energy of free rare-earth ions in the crystal field can be described from three aspects: 1. from valence electrons and nucleus, 2. from valence electrons themselves and 3. spin-orbit interaction of electrons. Coulomb interaction among 4*f* valence electrons is the strongest one on the energy scale of ~10^4 cm^{-1}. Due to the Coulomb interaction, the energy levels of any rare-earth ions are divided into $^{(2S+1)}L$ folds. For rare-earth ions doped in the host material, the most significant interaction between them is spin-orbit interaction on the order of ~10^3 cm^{-1}. The value of total angular momentum *J* is affected by the filling of orbitals. Specifically, $J = L-S$ is for less than half-filled while $J = L+S$ for more than half-filled shells. In this case, the split levels are represented as $^{(2S+1)}L_J$. Sometimes the crystal field strength in low symmetry hosts increases and hence the energy levels can be further split into Stark sublevels. For even value of electrons in the outer orbitals, the degeneracy of $^{(2S+1)}L_{Jm}$ level is (2*J*+1) fold while it becomes (*J*+1/2) for odd values of valence electrons. The energy scale of this change is ~10^2 cm^{-1}. Because of the weak crystal field effect, the spin-orbit interaction normally dominates in RENPs and the Stark sublevels only occurs in special cases where the crystal field strength is high e.g., $LiYF_4$ and $LiLuF_4$ host.

Generally, the multiple energy levels of rare-earth ions endow RENPs with various emissions from UV, visible to NIR range. Due to the forbidden *f*→*f* transitions, host martials with low symmetry are preferred to relax the selection rules to improve the electric dipole transition probabilities. The shielded *f*→*f* transition with long-lived time at the excited states also make it easy to multi-photon absorption process and thus for UC emission.

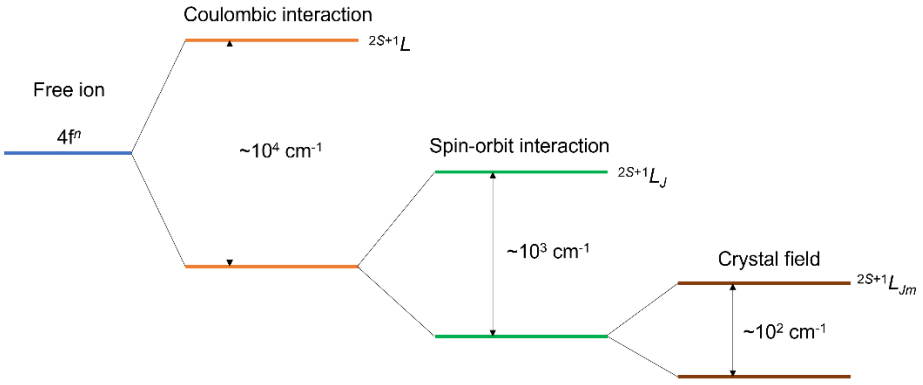

Figure 1.3 Energy level splitting of rare-earth ions.

1.2.3 Photoluminescence mechanism

Conferring to the diverse positions of the excitation and emission bands, the photoluminescent materials can be categorized into Stokes- and Anti-stokes-type materials. In most cases, excitation energy is higher than emitted photon energy, which is called Stokes emission, and the corresponding energy loss is known as Stokes shift. In certain circumstances, emitted energy is higher than absorbed energy; this is known as Anti-stokes emission.

1.2.3.1 Upconversion

UC is a typical Anti-stokes emission that converts the two or more lower energy photons into one high-energy photons. The upconversion process was first proposed by N. Bloembergen in a conceptual device named “infrared quantum counter” in 1959.(Bloembergen, 1959) Compared with two-photon absorption which needs high excitation intensity (10^6−10^9 W cm^{-2}), (Li *et al.*, 2019) UC process can be induced by a low-power (1−10^3 W cm^{-2}) continuous wave laser. A metastable intermediate state is necessary in UC emission process. The mechanism of upconversion processes explored in upconversion nanoparticles (UCNPs) up to now, is mainly divided into four basic classes: excited state absorption (ESA), energy transfer upconversion (ETU), cross-relaxation (CR), and photon avalanche (PA). They are briefly highlighted below.

Excited state absorption (ESA): in the case of ESA, sequential absorption of two photons within the energy levels of one ion is responsible for UC emission. Owing to the ladder-like energy level of most lanthanide ions and the relatively long-lived lifetime at the intermediate state (ranging from tens of microseconds to several milliseconds), ESA is the simplest mechanism that happens in many RENPs (e.g., Er^{3+}, Tm^{3+}, Ho^{3+}, Pr^{3+}, Dy^{3+} doped RENPs).

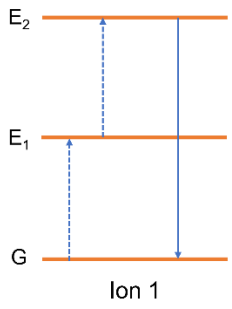

Figure 1.4 Schematic illustration of ESA.

Energy transfer upconversion (ETU): In the case of ETU (Figure 1.5), UC emission is induced by the energy transfer between two Ln^{3+} ions, normally happens in the co-doped activator and sensitizer. The two ions can actually be the same kind or different lanthanide ions. The distance

between two ions is critical to enable an efficient ETU process. It is obvious that the ETU is more likely to occur between the neighboring ions. Compared with ESA, ETU owns a much robust UC intensity due to the large absorption cross section of the introduced sensitizer ions. So far, ETU is the most adopted mechanism for UC emissions.

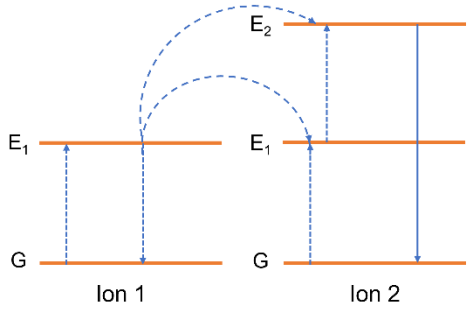

Figure 1.5 Schematic illustration of ETU process.

Cross-relaxation (CR): CR is an energy transfer process resulting from ion-ion interaction in which part of the excited state energy of ion 1 is transferred to the neighboring ion 2. CR is the main reason for the undesired "concentration quenching" effect when activators are highly doped into the host with a close distance among them. The dopant concentration of different activators thus needed to be optimized e.g., 2 mol% is ideal for Er^{3+} dopant while 0.5 mol% is the normal concentration for Tm^{3+}-doped RENPs. Although self-quenching is mostly not helpful for efficient photoluminescence intensity, CR can be positively harnessed in Er^{3+} enriched host materials to tune the red-to-green emission color and is one of the cornerstones for photon avalanche UC emission.

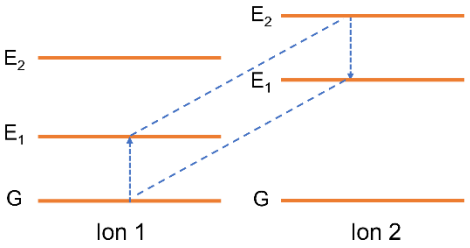

Figure 1.6 Schematic illustration of CR process.

Photon avalanche (PA): The phenomenon of PA was first discovered by Chivian et al in Pr^{3+}-based infrared quantum counters.(Joubert *et al.*, 1994) PA is a distinctive UC process with steep optical nonlinear dynamics in RENPs. In PA, the ground state absorption is extremely inefficient (for ion 2 from ground state to excited state 1 as shown in Figure 1. 7). In contrast, ESA from the metastable excited state to the higher one, E_2 sate, is highly efficient. Moreover,

the population of the metastable excited sate can be significantly promoted through CR. The triggered positive feedback loop efficiently populates the E_2 excited state in ion 2, leading to a photoluminescence enhancement by orders of magnitude. A remarkable optical feature of PA is the prolonged rise time attributed to the sequential accumulation of the positive feedback cycles.

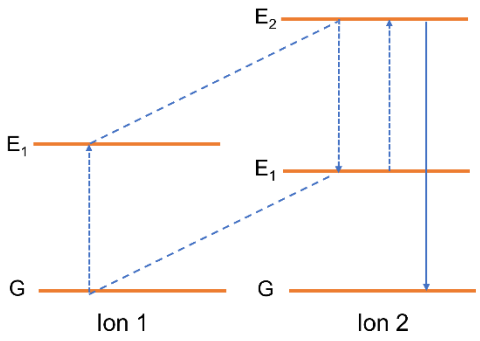

Figure 1.7 Schematic illustration of PA process.

1.2.3.1 Downshifting

DS: the Stokes emission possess two types of processes: downconversion and downshifting. In downconversion, two or more photons with lower energy are emitted after absorption of one high energy photon. Whereas only one photon with lower energy is emitted in downshifting process when excited by high energy photon. The energy is lost by non-radiative transition in DS. Following the 980 nm or 800 nm excitation, DS process makes it possible for RENPs to be both excited and emit in the NIR range. NIR light enables RENPs to exhibit high resistance to photo-bleaching and photochemical degradation under photoexcitation conditions. Advances of NIR light in biomedicine have demonstrated that longer wavelengths can greatly suppress photon scattering and reduce tissue autofluorescence thereby greatly enhancing the penetration depth in biological samples.

1.2.4 Photoluminescence of RENPs

The radiative transitions originated from the oscillating electric dipole, oscillating magnetic dipole, oscillating electric quadrupole, and so on. The electric dipole and the magnetic dipole radiation contribute more among these transitions. According to the transition rule, electronic dipole transition happens when the initial and final states are of opposite parity. However, magnetic dipole transition takes place when the two states have the same parity. In RENPs, $4f-4f$ transitions are parity forbidden. By intermixing $4f^n$ and $4f^{n-1}5d$ orbitals, the optical transitions become allowed. After exciting the rare-earth ions into a higher excited state, they

can radiatively or non-radiatively relax to the low-lying energy levels or directly transit to the ground state. When an electron relaxes from higher energy state to lower energy state without emitting a photon, the relaxation process is called non-radiative transition. Because of the lost energy without emission in this process, non-radiative transitions should be minimized. Phonons normally take part in this non-radiative transition process. The number of phonons involved in the multi-phonon relaxation depends on the energy gap between the two states and the maximum phonon energy. Therefore, the phonon energy of the host should be low as mentioned in 1.2.1 to reduce the likelihood of multi-phonon emission and increase the radiative transitions.

Radiative transitions of RENPs take place from an excited state that may be directly populated by absorption of the excitation light, or through energy transfer from the closely neighboring energy state in the same ions or from other ions. Through different luminescence mechanisms, UC and DS emissions of RENPs can be observed. In a typical Yb^{3+}/Er^{3+} co-doped system, Yb^{3+} acts as the sensitizer and Er^{3+} is the activator. The energy difference between $^2F_{5/2}$ and $^2F_{7/2}$ of Yb^{3+} is ~10300 cm^{-1},(Falin *et al.*, 2004) corresponding to ~980 nm radiation. Similar energy separation can be found in Er^{3+} such as the following energy state pairs: $^4I_{11/2}$ and $^4I_{15/2}$, $^4I_{11/2}$ and $^4F_{7/2}$, $^4I_{13/2}$ and $^4F_{9/2}$, $^4F_{9/2}$ and $^2H_{9/2}$. Under 980 nm laser excitation, Yb^{3+} absorbs the energy to populate at the $^2F_{5/2}$ energy level. The absorbed energy can be transferred to adjacent Er^{3+} due to the matched energy gap. Thus, the $^4I_{11/2}$ state of Er^{3+} is populated, followed by the population at the higher $^4F_{7/2}$ state via the ESA or ETU process. The same process also happens to the population of $^4F_{7/2}$, $^4F_{9/2}$, and $^2H_{9/2}$ states. The radiative transitions from $^4F_{9/2}\rightarrow{}^4I_{15/2}$ and $^2H_{9/2}\rightarrow{}^4I_{15/2}$ correspond to the UC red and blue emissions, respectively. Non-radiative transition occurs from $^4F_{7/2}$ to the lower $^2H_{11/2}$, and $^4S_{3/2}$ state, eventually producing the UC green emission. It should be noted that this is not the only way to produce UC emission, and the detailed mechanism should be explored in different cases. The non-radiative transition from $^4I_{11/2}\rightarrow{}^4I_{13/2}$ causes the population at the $^4I_{13/2}$ state and the subsequent transition from $^4I_{13/2}\rightarrow{}^4I_{15/2}$ is assigned to the DS emission.

The photons that participated during the UC photoluminescence in various materials can be investigated in detail. Specifically, the UC emission intensity (*I*) is related to the excitation power density (P) as the following expression:

$$I \propto P^n \tag{1.1}$$

Where n is the number of photons participated during the UC emission process. By measuring the slope of log(*I*) *vs* log(*P*), n can be calculated to determine the number of photons. However,

the power density dependence of the UC emission described in this equation is only valid in weak excitation power densities. High excitation power density may cause deviations in the n value due to the complicated energy transfer processes and the possible saturated population at some excited states. Therefore, the slope of the power dependence curve is known to decrease when the excitation intensity is too high. It is suggested to combine the intensity vs power plot and the photoluminescence lifetime analysis to better understand the excitation dynamics.

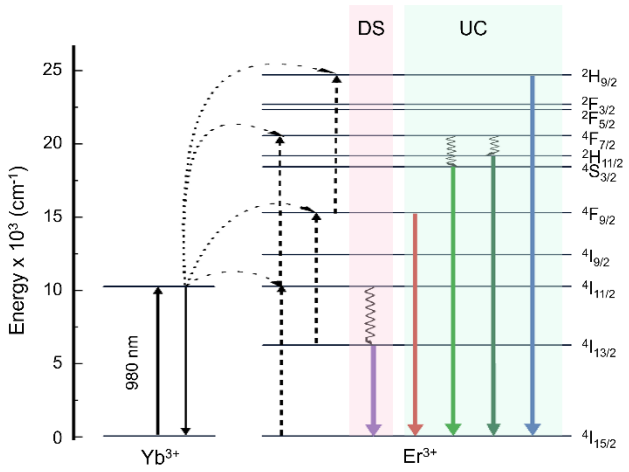

Figure 1.8 Photoluminescence process in Yb^{3+}/Er^{3+} co-doped system.

1.2.5 Routes to enhance photoluminescence intensity in RENPs

Suppression of surface quench

Smaller nanoparticles have a larger surface-to-volume ratio, which naturally leads to more defects. Moreover, ions at the surface area are easily exposed to the surface ligands and solvent vibrational modes, thereby causing more non-radiative energy loss. Synthesizing RENPs with large sizes is an effective way to improve the photoluminescence intensity. However, the maximum size of RENPs in some applications is limited. In biomedicine, smaller RENPs are appreciated, typically below 50 nm.

Constructing core-shell architecture is another way to protect the activators from surface quenchers. After deposition with a shell layer, the quenched activators in the core surface can be reactivated. Moreover, the distance between the activator in the core and the surface quenchers is lengthened and thus the nonradiative relaxation can be effectively minimized. Excellent matching in the phase structure and lattice parameter between the core and shell should be considered for the epitaxial shell growth process. Normally, the shell layer is inert with the same structure as the core and the thickness should be thick enough to ensure the total

protection of internal activators. Heterogeneous shells can also be used to enhance the photoluminescence intensity, and the requirement is to have a low lattice mismatch with that of the core nanoparticles. Versatile structures have been demonstrated to boost the photoluminescence intensity in both UC and DS emissions. For example, 450-fold enhancement in UC emission intensity has been realized by coating the $NaGdF_4$ shell on the $NaGdF_4$:Tm^{3+}/Er^{3+}core RENPs.(Kang *et al.*, 2019) The $NaYF_4$ shell with a thickness of 7 nm has also been demonstrated to improve the DS emission of Er^{3+} doped RENPs. (Zhong *et al.*, 2017b)

Removal of detrimental CR

CR is one of the deleterious processes which results in the reduction of photoluminescence intensity. Rare-earth ions with abundant energy levels are prone to have destructive CR processes with the closely located ions. When different rare-earth ions are co-doped in the same region, the small distance between the neighboring ions aids the detrimental non-radiative energy transfer processes. Increasing the spatial distance between rare-earth ions is thus a potential way.

It has been reported that spatially separated distribution of sensitizers and activators in neighboring layers can suppress their CR and enable highly efficient UC energy transfer at the interface. Specifically, a high quantum yield of 6.34% is reached in optimum $NaYF_4$:Er@$NaYbF_4$@$NaYF_4$ nanoparticles at a low excitation power density of 4.5 W cm^{-2}.(Zhou *et al.*, 2020a)

Tailoring the local symmetry of the photoluminescent center

It is the change of the local symmetry of rare-earth ions that makes the parity forbidden 4*f*−4*f* transitions partially allowed when they are embedded in the host matrix. Tailoring the local symmetry of the activators should facilitate the radiative transition and thus enhance the photoluminescence intensity. UC emission of Er^{3+} in the hexagonal crystalline phase $NaYF_4$ presents an order of magnitude higher intensity than it in the cubic phase due to the lower symmetry of the hexagonal phase of the host. Doping is one of the easiest ways to tailor the local symmetry in the crystal lattice. For the selection of dopant ions, optically inert ions with different ionic radii from the rare-earth ions are a good option. Li^+ ions, with a much smaller ionic radius than rare-earth ions, are thus expected to effectively tailor the local symmetry of the activators in RENPs. Zhang et al reported the first enhancement of UC emissions of Er^{3+} by incorporating Li^+ into Y_2O_3:Yb, Er nanoparticles.(Chen *et al.*, 2008) Besides, Bi^{3+}, Mo^{3+}, and Sr^{2+} ions have also been verified to tailor the local symmetry of rare-earth ions.(Jiang *et al.*, 2012; Yin *et al.*, 2014; Zhao *et al.*, 2013)

Other ways

Localized surface plasmon resonance (LSPR) is produced by the electromagnetic interaction of the metal with the incident light of a specific wavelength. LSPR enhanced photoluminescence intensity of RENPs has been reported in which the distance between the metallic structure and the RENPs is a critical influential factor.

Dye sensitization has been deployed to enhance the emission intensity by increasing the absorption cross-section efficiency of RENPs. For example, the molar extinction coefficient of IR-806 dye at 806 nm in $CHCl_3$ is ~5×10^6 times greater than that of β-NaYF4:Yb^{3+}, Er^{3+} RENPs under 975nm excitation.(Huang, 2017) By attaching the dye to the surface of RENPs, the excitation energy can be greatly absorbed and utilized in the photoluminescence process to improve the emission efficiency.

1.2.6 Surface modification of RENPs for biological applications

Initially synthesized RENPs are generally hydrophobic, as they are capped by oleic acid and other hydrophobic ligands. They can only be dispersed in nonpolar organic solvents which is not acceptable for biomedicine applications. Therefore, a crucial step in the use of these hydrophobic RENPs for biomedicine is surface engineering to make them biocompatible. Removing the ligands coordinating the surface of RENPs is a unique but simple way to disperse RENPs into aqueous phase. Ligand exchange, ligand oxidation, layer-by-layer assembly, surface silanization and amphiphilic polymer coating are some other common strategies to render RENPs water dispersible.

1.3 RENP nanothermometry

Temperature-dependent optical changes of nanothermometers can be observed with both steady-state and time-resolved photoluminescence measurements. Normally, the working principle for photoluminescence nanothermometry includes changes in the probes' polarization anisotropy, photoluminescence intensity, peak position, bandwidth, bandshape, and lifetime.(Brites *et al.*, 2018a) Polarization anisotropy is often observed in very specific cases while nanothermometry using photoluminescence peak position has been reported with relative success in semiconductor quantum dots.(Jaque *et al.*, 2012; Zhou *et al.*, 2020d) Photoluminescence intensity-based temperature sensing from a single peak is easy and simple but can be prone to measurement anomalies caused by intensity variations, which may lead to inaccurate temperature readouts.(Bednarkiewicz *et al.*, 2020) In the case of RENPs, the

photoluminescence peak position and bandwidth present only subtle differences at varying temperatures due to the shielding effect of the rare-earth ions (Brites *et al.*, 2018a; Dong *et al.*, 2015; Zhou *et al.*, 2020d). Consequently, the photoluminescence bandshape where the PLIR between two peaks or two transitions has gradually become the established method in photoluminescence nanothermometry. Following astonishing growth in RENP nanothermometry, the PLIR technique has become the most widely studied method and presents high temperature and spatial resolution for various applications with a specific emphasis on biomedicine. In contrast, RENP lifetime-based nanothermometry, while still in its infancy because of the expensive and complicated equipment, has been recognized as a potential technique for accurate temperature sensing with less biased error.(Liu *et al.*, 2021b; Tan *et al.*, 2020a) Taken together, concerted effort still needs to be made to enable RENP nanothermometry more user-friendly, potentially moving it closer to translational applications.

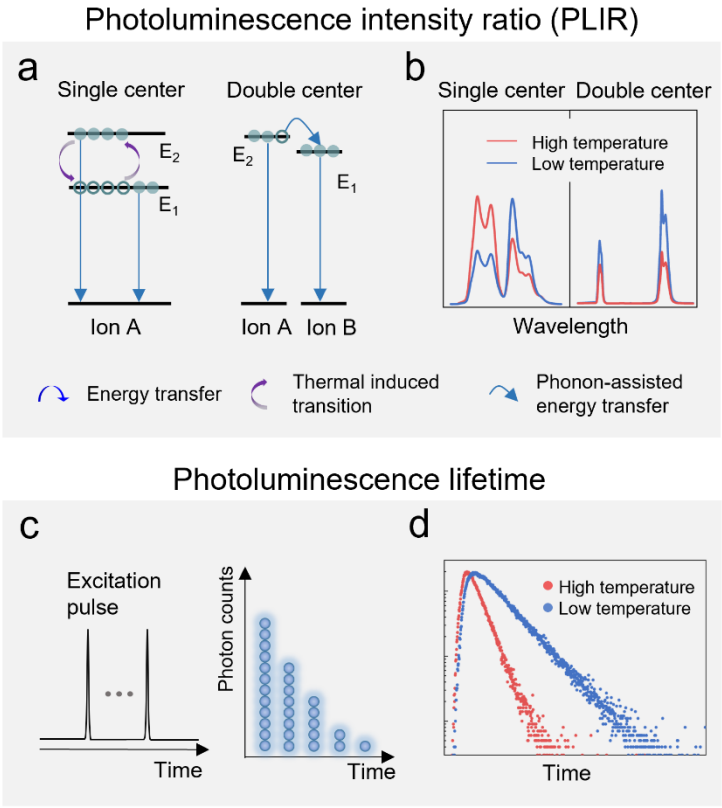

Figure 1.9 RENP photoluminescence nanothermometry.

(a, c) Basic working principles of PLIR (a) and lifetime-based (c) nanothermometry, respectively. (b, d) Schematic representations of the PLIR (d) and lifetime curves (e) at different temperatures, respectively.

Rare-earth ions have a plethora of 4*f* electronic energy states that lead to innumerable radiative and non-radiative processes after light excitation. In particular, the non-radiative pathways that

result from the absorption or emission of lattice phonons are especially temperature-dependent, and thus, the PLIR between the donor and acceptor states will subsequently be influenced by temperature.(Gai *et al.*, 2014; Wang *et al.*, 2013b). Depending on the different types of doped photoluminescent centers (activators), PLIR nanothermometry is divided into two categories: single center (singly doped) and double center (co-doped).(Brites *et al.*, 2018a)

1.3.1 Different types of RENP nanothermometry

1.3.1.1 Single-center PLIR nanothermometry

In a single-center nanothermometer, the PLIR is determined by the radiative transitions from two excited energy levels of the same activator to its ground state (as Figure 1.9a shows). The PLIR parameter, Δ, is presented by (Brites *et al.*, 2018a)

$$\Delta = \frac{I_2}{I_1} = \frac{A_2 h\nu_2 N_{2(\mathrm{T})}}{A_1 h\nu_1 N_{1(\mathrm{T})}}\ , \tag{1.2}$$

where I_1 and I_2, A_1 and A_2, ν_1 and ν_2 are the photoluminescence intensities, total spontaneous emission rates, and the frequency of transitions from excited states E_1 and E_2 to the ground state E_0 (excited state E_2 is of higher energy than E_1), respectively. h is Plank's constant. $N_{1(\mathrm{T})}$ and $N_{2(\mathrm{T})}$ are the populations of E_1 and E_2 levels, respectively, at a specific temperature *T*. Since E_1 and E_2 are thermally coupled, the energy difference between them cannot be too large, normally 200−2000 cm^{-1}.(Brites *et al.*, 2018a) This range ensures sufficient thermal energy to enable photons at the lower level to be populated to the upper level and each emission band can be resolved at room temperature. In a thermal equilibrium situation, N_1 and N_2 meet the following rules:

$$\frac{N_2}{N_1} = \frac{g_2}{g_1}\exp\left(-\frac{\delta E}{k_{\mathrm{B}} T}\right)\ . \tag{1.3}$$

Here, g_1 and g_2 are the degeneracies of the two levels, δE is the energy gap between the barycenters of the two emission bands, and k_{B} is the Boltzmann constant. Combining equation (1.2) and (1.3), equation (1.4) is written as:

$$\Delta = B\exp\left(-\frac{\delta E}{k_B T}\right)\ . \tag{1.4}$$

The linear correlation between $\ln(\Delta)$ and $1/T$ can be exploited to obtain a calibration curve for temperature reading. In this equation, the pre-exponential factor $B = A_2 h\nu_2 g_2 / A_1 h\nu_1 g_1$. It is noteworthy that although *B* is a constant here, it has been shown to be temperature-dependent

at sufficiently low temperatures as the reorganization of the populations among Stark sublevels occurs.(2020) Practically, the values of δE and B are obtained from a log-log fit from the graph of intensity ratio versus temperature.

The potential for single-center PLIR nanothermometry has been widely investigated (e.g. Er^{3+}, Eu^{3+}, Nd^{3+}, or Pr^{3+}-doped RENPs).(Brites *et al.*, 2018c; Cantarano *et al.*, 2020; Lucchini *et al.*, 2019) Perhaps the most studied are Er^{3+}, Yb^{3+} co-doped RENPs.(Vetrone *et al.*, 2010) In this classic system, the ion excited in the $^2H_{11/2}$ state of Er^{3+} will non-radiatively decay to the lower-lying $^4S_{3/2}$ state. These two states are in Boltzmann equilibrium and changes in surrounding temperature will cause a rearrangement of their populations (see Figure 1.9a: single center). The temperature is determined by the PLIR from these thermally coupled states once the calibration curve is obtained. These types of photoluminescent nanothermometers are called secondary nanothermometers since they necessitate an external thermal calibration.(Brites *et al.*, 2018a)

While many original photoluminescent nanothermometers exploited the temperature dependence of upconverted visible emissions, RENPs also show versatile NIR downshifting photoluminescence. In the context of NIR single-center nanothermometers, Nd^{3+} (1060 nm), Ho^{3+} (1150 nm), and Er^{3+} (1550 nm) activators have been reported as promising candidates as secondary NIR nanothermometers(Hazra *et al.*, 2020c; Jia *et al.*, 2020b). However, these activators do not typically possess thermally coupled energy states in the NIR region. Fortunately, the 4*f* states of the rare-earth ions have pronounced Stark splitting in host lattices that exert high crystal field strengths on the dopants. Since some of the Stark sublevels follow the Boltzmann distribution and these transitions can be easily optically resolved, they can be employed in NIR nanothermometry. An example was demonstrated by our group using $LiYF_4$:Yb^{3+}, Tm^{3+}@$LiYF_4$@$LiYF_4$:Nd^{3+} core-shell RENPs.(Skripka *et al.*, 2019a) The Nd^{3+} excited state, $^4F_{3/2}$, was further split into thermally coupled R_1 and R_2 Stark states, while the $^4I_{11/2}$ state was split into 6 levels with the Y_1 and Y_2 Stark states participating in the temperature sensing. Specifically, with temperature increase, the intensity of $R_2 \rightarrow Y_1$ (≈1046 nm) increases while $R_1 \rightarrow Y_2$ (≈1056 nm) decreases. The relative thermal sensitivity was circa 0.22% $°C^{-1}$ at room temperature, which was the highest among the fluoride-based hosts. The performance of this NIR nanothermometer was successfully evaluated *in vitro* using both 2D and 3D cell cultures and was a major step forward in ultimately demonstrating the feasibility of using Nd^{3+}-doped RENP nanothermometry in a biological setting with an eye on future *in vivo* translational applications.

1.3.1.2 Double-center PLIR nanothermometry

In the case of double-center nanothermometers, the PLIR is defined by two distinct emission bands from different activators. The temperature dependence of their PLIR is affected by phonon-based processes including non-radiative multiphonon relaxation and non-resonant phonon-assisted energy transfer. Examples of double-center nanothermometers in the visible range have been reported in Eu^{3+}/Tb^{3+}, Pr^{3+}/Tb^{3+}, and Ho^{3+}/Tm^{3+} co-doped systems.(Brites *et al.*, 2010; Gao *et al.*, 2016; Savchuk *et al.*, 2018) Akin to single-center nanothermometry, attention has lately shifted towards double-center nanothermometers operating in the NIR region.(Carrasco *et al.*, 2015; Ximendes *et al.*, 2016a) An excellent example was demonstrated by Marciniak et al. using $LiLa_{0.9-x}Nd_{0.1}Yb_xP_4O_{12}$ ($x = 0.05 - 0.5$) RENPs.(Marciniak *et al.*, 2015) The $Nd^{3+} \rightarrow Yb^{3+}$ energy transfer (ET), a phonon-assisted process, follows the Miyakawa-Dexter model, in which the probability of the interionic energy transfer is expressed as a function of the temperature.(Miyakawa *et al.*, 1970) Owing to the numerous ET processes, such as phonon-assisted $Nd^{3+} \rightarrow Yb^{3+}$ ET, $Yb^{3+} \rightarrow Nd^{3+}$ back ET, and $Yb^{3+} \rightarrow Yb^{3+}$ energy diffusion, the PLIR between Nd^{3+} ($^4F_{3/2} \rightarrow {}^4I_{9/2}$) and Yb^{3+} ($^2F_{5/2} \rightarrow {}^2F_{7/2}$) emission depend strongly on the temperature as well as concentration of Yb^{3+} ions due to the competition between $Yb^{3+} \rightarrow Nd^{3+}$ and $Yb^{3+} \rightarrow Yb^{3+}$ processes. The best thermometric performance occurs at a Yb^{3+} concentration of 50 mol% with relative sensitivity of 0.4%. In addition, various other NIR double-center nanothermometers that exploit ET mediated by the host/phonons, ions, or ligands have been reported, e.g. Tm^{3+}/Ho^{3+} (Savchuk *et al.*, 2018) and Er^{3+}/Ho^{3+} (Jia *et al.*, 2020b). Our group incorporated Ho^{3+}, Nd^{3+}, and Er^{3+} into $NaGdF_4$ RENPs for double-center PLIR nanothermometry.(Skripka *et al.*, 2017) Due to the phonon-assisted ET in Nd^{3+} ($^4F_{3/2}$) → Yb^{3+} ($^2F_{5/2}$), Yb^{3+} ($^2F_{5/2}$) → Ho^{3+} ($^5I_6$), and Er^{3+} ($^4I_{13/2}$) → Ho^{3+} ($^5I_7$), the PLIR of Ho^{3+}/Nd^{3+}, and Er^{3+}/Nd^{3+} emissions were determined to be temperature dependent. Interestingly, the Ho^{3+} and Er^{3+} temperature-dependent emissions were found to be closely linked to the dispersion solvents, which was ascribed to the O-H assisted non-radiative relaxation. Hence, it must be highlighted that any performance evaluation of nanothermometers intended for biomedical applications must be first and foremost assessed in the aqueous milieu. Otherwise, the same thermally driven optical processes of the nanothermometer dispersed in different solvents cannot be guaranteed and thus the reliability and sensitivity will be affected.

1.3.1.3 Lifetime-based nanothermometry

As discussed above, PLIR nanothermometry has been the mainstream method due to the representative thermally coupled states in RENPs. On the other hand, temperature-dependent non-radiative depopulation of the excited states enables photoluminescence lifetime as the contrast mechanism to infer the temperature.

Qiu et al fabricated a hybrid structure in which emission at around 810 nm could be obtained from both Tm^{3+}-doped RENPs and PbS quantum dots ($I_{total}= I_{Tm} + I_{PbS}$).(Qiu *et al.*, 2020) The overlapped emissions were then decoded via a time-resolved technique due to different photoluminescence lifetimes. This breakthrough work was the first to show the insensitivity of the nanothermometer to tissue thicknesses due to the same emission band used for PLIR which minimized the wavelength-induced attenuation coefficient difference of tissue. Although the real-time intensity (I_{total}) or the time-resolved intensity (I_{Tm}) decreased after passing through 2 mm pork tissue, the PLIR ($\frac{I_{\mathrm{total}}-I_{\mathrm{Tm}}}{I_{\mathrm{Tm}}}$) remained unchanged. Time-resolved nanothermometry could be considered as a transition between PLIR and lifetime-based nanothermometry since it introduced a time-resolved method but still essentially relied on the PLIR of two emission peaks.

True photoluminescence lifetime-based nanothermometry is an attractive alternative to the PLIR technique. The photoluminescence lifetime τ of an excited state can be expressed as:

$$\tau = \frac{1}{W_r + W_{nr}} . \tag{1.5}$$

Here, W_{r} and W_{nr} are the radiative and non-radiative decay rates, respectively. W_{r} is temperature independent since the radiative transition process is mostly determined by the electronic configuration of the ion while W_{nr} is strongly dependent on the existence of multiphonon relaxation, phonon-assisted non-resonant energy transfer, and other non-radiative processes.(Tan *et al.*, 2020a) Therefore, the total lifetime (τ) of the excited state is influenced by temperature and the relationship can be expressed by an Arrhenius-type equation as follows:

$$\frac{1}{\tau} = \frac{1}{\tau_0} + C \exp\left(-\frac{E_{\mathrm{A}}}{K_{\mathrm{B}}T}\right), \tag{1.6}$$

where $1/\tau_0$ is the temperature-independent decay rate, C is the pre-exponential constant and E_{A} is the activation energy.(Brites *et al.*, 2018a)

Notably, the photoluminescence lifetime is an intrinsic property that is less vulnerable to variations due to light penetration depth, the presence of other fluorophores/chromophores (for

example in a biological medium), the solvent in which the probe is dispersed, etc.(Shen *et al.*, 2022a; Tan *et al.*, 2020a) It has been confirmed that the photoluminescence lifetime signal maintains a high signal-to-noise ratio (SNR) after an 8 mm penetration depth of intralipid (1%) and was further applied in the biodistribution studies and diagnosis of tumor subtypes.(Fan *et al.*, 2018; Ortgies *et al.*, 2018) Lifetime-based nanothermometry is a robust technique that holds crucial potential to overcome the limitations associated with PLIR nanothermometry.(Fan *et al.*, 2018; Okabe *et al.*, 2012; Shen *et al.*, 2022a) A typical example in lifetime-based nanothermometry was reported by Tan et al using $NaYF_4$@$NaYF_4$:Yb^{3+}, Nd^{3+}@CaF_2 RENPs.(Tan *et al.*, 2020a) The lifetime-based nanothermometer was shown to be stable, reliable, and repeatable against different work conditions. In contrast to the thermal images using the photoluminescence intensity and thermal camera, photoluminescence lifetime images presented the precise temperature distribution profile in the area with accumulated RENPs. The evaluated average lifetime difference between inflamed and normal mice was 0.2 ms, and the corresponding temperature difference was 2.3 °C, indicating that the obvious lifetime/temperature difference could thus be an effective indicator for inflammation detection.

Despite the aforementioned advantages of photoluminescence lifetime-based nanothermometry, it is still not widely studied due to the high cost and complexity of the instrumentation, low measurement efficiency, and required expertise in data analysis. The most common technology is time-correlated single-photon counting (TCSPC). This technique features single photon detection but is time-consuming in both data acquisition and processing which impedes the further study of dynamic scenes or two-dimensional views.(Sen *et al.*, 2020) To accelerate data collection, our group developed single-shot photoluminescence lifetime imaging thermometry (SPLIT).(Liu *et al.*, 2021b) This optical system synergistically utilized an encoding mask for spatial information extraction and a galvanometer scanner which temporally shears dynamic scenes for photoluminescence lifetime measurement. Largely advancing current lifetime measurement techniques, SPLIT enables two-dimensional video-rate lifetime and temperature mapping of a moving biological sample, bridging the gap between instrument advancement and lifetime-based nanothermometry.

1.3.2 Characterization of nanothermometry

Absolute sensitivity: is defined as a quotient of the change in an indication and the change in the temperature value, and it is expressed in terms of the indication unit per kelvin.

$$S_{\mathrm{a}} = \left|\frac{\partial \Delta}{\partial T}\right| . \tag{1.7}$$

Relative sensitivity: To characterize the performance of all types of nanothermometers, the relative sensitivity S_r is defined as:

$$S_{\mathrm{r}} = \frac{1}{\Delta}\left|\frac{\partial \Delta}{\partial T}\right| . \tag{1.8}$$

Relative sensitivity is in fact the normalized value of sensitivity with respect to the indication value and is expressed in % K^{-1}. S_r be used to directly compare the performance of diverse nanothermometers despite different compositions or working mechanisms.(Brites *et al.*, 2018a)

Temperature uncertainty, δT, which represents the smallest resolved temperature for a given nanothermometer and is estimated as following(Brites *et al.*, 2018a):

$$\delta T = \frac{1}{S_{\mathrm{r}}}\frac{\delta \Delta}{\Delta} . \tag{1.9}$$

Temperature resolution is the smallest change in a temperature that causes a perceptible change in the indication.

1.3.3 Challenge of RENP nanothermometry

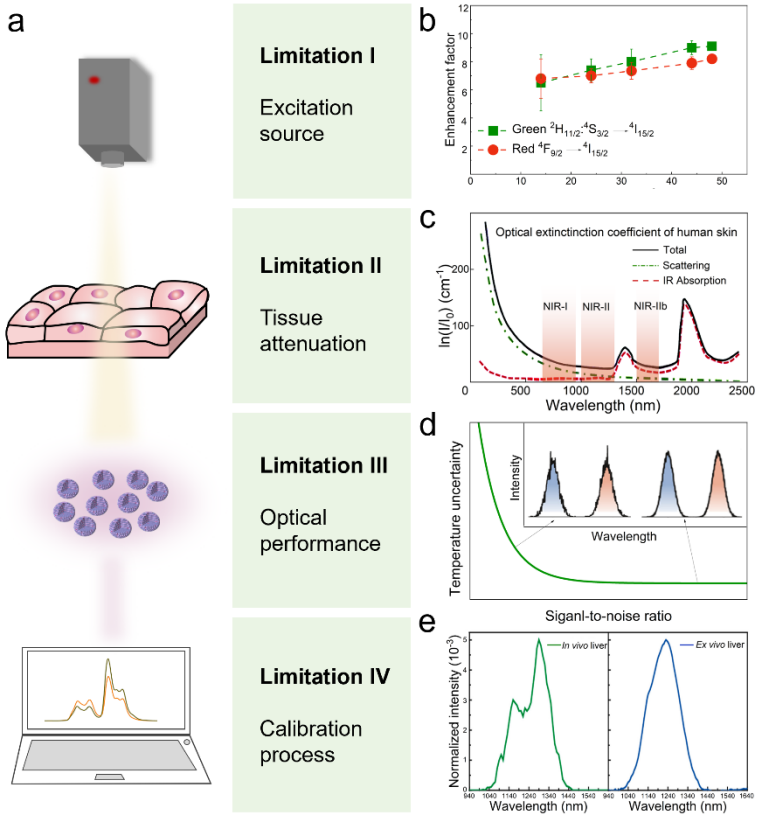

Figure 1.10 Possible limitations in RENP nanothermometry.

(a) Schematic representation of the complete process of temperature reading in biomedicine. (b) Enhancement factor of upconverted green and red emission bands versus excitation power density. (c) Extinction coefficient of human skin. (d) The temperature reading uncertainty of RENPs with varied signal-to-noise ratios. (e) Emission spectrum *in vivo* and *ex vivo* show the necessity of in situ calibration.

Although RENP nanothermometry using PLIR has undergone rapid development and has become a much-studied technique for temperature sensing(Brites *et al.*, 2018a), recent results point out that the accuracy of PLIR nanothermometry could be put into question. For instance, excitation intensity induced self-heating effects,(Pickel *et al.*, 2018a) the variation of photoluminescence intensity at different path lengths through the sample,(Pérez-Rodríguez *et al.*, 2014) and the altered sensitivity or disturbed Boltzmann equilibrium at high temperatures(Geitenbeek *et al.*, 2018) can lead to false temperature readout thereby compromising the reliability of the technique. Possible limitations in PLIR photoluminescence nanothermometry can originate from the excitation laser, biological tissues, the optical performance of the photoluminescent nanothermometers, and the calibration process (Figure 1.10).

1.3.3.1 Excitation source

An excitation source has two main characteristics: power density and wavelength. Optimizing the power density of the excitation source is a critical factor. For instance, in the case of $NaGdF_4:Yb^{3+}$, $Er^{3+}@SiO_2$ RENPs, our group showed that the PLIR of $^2H_{11/2}/^4S_{3/2} \rightarrow {}^4I_{15/2}$ transition strongly depended on the excitation power density of the 980 nm laser (Figure 1.10b).(Rohani *et al.*, 2015) Furthermore, Pickel et al discussed the same phenomenon in detail by modeling the PLIR of the $^2H_{11/2}/^4S_{3/2} \rightarrow {}^4I_{15/2}$ transition and showed experimentally that it increased by ~80% as the excitation power density was increased.(Pickel *et al.*, 2018a) To mitigate these artifacts, it is imperative to keep the excitation conditions identical during the temperature measurements and calibration process. Defining a standard excitation power to evaluate the S_r and other performance of each nanothermometer is also strongly recommended.

Continuous laser irradiation would inevitably cause a heating effect, particularly at 980 nm excitation, due to the strong absorption of water molecules. The heating effect does not only affect the accuracy of the temperature readout but may also irreversibly damage the biological samples under study.(Xie *et al.*, 2012) To avoid errors in temperature sensing caused by heating, minimizing the excitation time by chopping the continuous wave or using a pulsed laser is a feasible option. Another common strategy is to introduce Nd^{3+} as the sensitizer to tune the excitation wavelength to a more biocompatible range at about 808 nm, which is considered to be a heating-free wavelength compared with 980 nm.(Matulionyte *et al.*, 2023) However, it is noteworthy that the safety regulation (European EN60825 and American ANSI Z136.1) allows approximately double the irradiance for more than 10 s at 980 nm compared with 808 nm (circa 330 mW cm^{-2}).(Nsubuga *et al.*, 2024)

1.3.3.2 Tissue

Another potential source of error could be observed when working with biological tissues. As shown in Figure 1.10c, the extinction coefficient of tissue, which is mainly attributed to the absorption and scattering effect, is strongly wavelength-dependent. Nanothermometers, particularly RENPs, whose emissions lie in the biological windows (NIR-I: 700-900 nm, NIR-IIa:1300-1400 nm, NIR-IIb:1500-1700 nm) thus offer considerable advantages for accurate temperature reading.(Hazra *et al.*, 2020c) Our group synthesized a single-center nanothermometer, $LiLuF_4:Nd^{3+}@LiLuF_4$, covering the NIR-I and NIR-IIa windows at around 880

nm ($^4F_{3/2} \rightarrow {}^4I_{9/2}$), 1050 nm ($^4F_{3/2} \rightarrow {}^4I_{11/2}$), and 1320 nm ($^4F_{3/2} \rightarrow {}^4I_{13/2}$), respectively.(Skripka *et al.*, 2019b) However, even within the biological window, the acquired δT presented significant deviation changing from 0.19 to 1.23 °C with increased thickness of pork fat tissue from 1 to 5 mm, revealing its validity was highly compromised by tissue thickness.

Tissue components should also be considered in the actual temperature reading. While many different types of biological and phantom tissues have been studied as the *ex vivo* temperature sensing medium, it should be noted that the optical attenuation coefficient and the performance of nanothermometers are non-comparable in different tissues. A particular example was reported using AgS nanothermometer and the same phenomenon also occurred in RENPs.(Shen *et al.*, 2020) A comprehensive study of the thermally dependent optical properties of tissues could be an approach to solving this problem. Alternatively, employing lifetimes to estimate temperature is another approach to mitigate tissue-induced distortions (*vide infra*).

1.3.3.3 Optical performance of nanothermometers

Low SNR is also a severe problem hindering the further application of RENPs in nanothermometry, as shown in Figure 1.10d, where the temperature uncertainty of RENPs nanothermometers presents a strongly non-linear relationship with the SNR ratio.(van Swieten *et al.*, 2022) Design and synthesis of RENPs with high quantum yield is thus an urgent but still challenging topic. Many groups have proposed various methods to improve the photoluminescence quantum yield both in upconversion and downshifting (maximum reported 6.34%(Zhou *et al.*, 2020b) and 50%(Arteaga Cardona *et al.*, 2023a), respectively), such as tailoring the local crystal field of the doped activator, surface passivation with core-shell architectures, plasmonic enhancement using noble metals, and utilizing organic fluorophores as ligand antennae.(Bednarkiewicz *et al.*, 2020; Brites *et al.*, 2018a; Dong *et al.*, 2015; Matulionyte *et al.*, 2023) However, none of these strategies have become mainstream and the community needs to strive towards fostering the very bright RENPs. On the other hand, while RENPs have low quantum yields, the actual figure of merit is the SNR, which is comparatively high since they are excited in the NIR region and some of them also emit in the NIR region. Hence, even when the RENP signal is low, the SNR is high as the background autofluorescence is also very low.

In addition to the quantum yield, temperature itself will also affect the photoluminescence intensity of the RENPs. Most of the nanothermometers show decreased intensity under higher temperatures due to the stronger resonance of the host phonon and higher probability of non-

radiative relaxation processes. An intriguing positive thermal response also has been observed in $NaYF_4$:Yb^{3+}, Tm^{3+} RENPs.(Zhou *et al.*, 2018) This interesting effect should be further studied such that it can be broadly adopted by the community.

1.3.3.4 Calibration process

According to equation (1.4), knowing the value of δE and B is the key to resolving the temperature in the PLIR method. Based on whether the calibration is necessary to determine the δE and B, the nanothermometers can be classified as primary or secondary types. For secondary nanothermometers, δE and B result from a fit between the preset temperature and intensity ratio. Therefore, an additional temperature reference, e.g., thermocouple or thermal camera, is needed for in situ thermal calibration. However, our recent proof-of-concept work demonstrated that thermal cameras can only detect the surface temperature(Liu *et al.*, 2024b) and thus most applications necessitate using physical means of acquiring the reference temperature (e.g. thermocouple) which is especially challenging for *in vivo* studies. More recently, primary nanothermometers have been proposed where δE and B can be determined based on the knowledge of thermodynamic laws and thus do not require calibration.(Judd, 1962b; Martínez *et al.*, 2019) A seminal example of a primary nanothermometer was illustrated in SrF_2:Yb^{3+}, Er^{3+} RENPs where δE was calculated using the barycenters of the photoluminescence peaks and B was empirically calculated from the plot of δE versus laser power.(Balabhadra *et al.*, 2017) This work took a giant stride toward the demonstration that any photoluminescence nanothermometer that can be described using equation (1.4) has the potential to be a primary nanothermometer. However, it should be noted that to date, no primary nanothermometer in the NIR range has been reported.

1.4 Other applications of RENPs

Such unique optical properties of RENPs find specific interest in the temperature sensing field yet is by far not limited to nanothermometry, and its rising attraction has also been reported in other fields such as biomedicine and information security.

Benefiting from the high photostability, low toxicity, and relative ease of surface modification as mentioned before, RENPs have been widely applied in biomedical research. The typical applications include bioimaging, multi-modal sensing, photothermal therapy, photodynamic therapy, drug delivery, release, and chemotherapy. To combine all functions in one nanosystem, versatile strategies have been used to develop all-in-one diagnosis and therapeutic nanomedicines based on RENPs. This all-in-one nanomedicine can be able to image the aimed area, monitor the biological activities, and then target the cancer cells to do therapy. The development of this all-in-one theranostic nanoplatform is still underway.

Besides, RENPs are especially suitable for anti-counterfeiting due to their rich intermediate energy levels and distinguishable spectral characteristics. Multicolor emissions as well as multi-mode excitations can be realized simultaneously by designing the architectures. In addition to the emission colors, photoluminescence lifetime can also be deployed for encryption to further improve the security level.

1.5 Motivation, aims, and outline

Following the brief introduction of RENPs' structure and optical properties, the great potential of RENPs especially their application in photoluminescence nanothermometry has been demonstrated in detail including the temperature detection method, working principle, and the typical examples. Determination of thermodynamic temperature is a complicated procedure that involves precision instruments and nanothermometers. Multidisciplinary efforts of optical engineering and chemical materials have to be put together toward accurate temperature sensing.

Temperature-dependent optical changes of nanothermometers can be observed with both steady-state and time-resolved photoluminescence measurements. The PLIR between two peaks or two transitions has gradually become the most widely studied method owing to the readily available spectrometers for photoluminescence acquisition from the instrument perspective. Despite offering high-temperature sensitivity and spatial resolution, this technique is restricted by the optical performance of nanothermometers due to the relatively low intensity and undesirable fluctuation in photoluminescence intensity ascribed to factors such as excitation

power density and biochemical surroundings. The concerted effort remains to make PLIR nanothermometers with better optical performance suited for biomedicine. Meanwhile, the influence of surrounding factors on the accuracy of nanothermometry needs to be examined carefully since the main constituent of the body, water, has found its strong absorption on some of the emissions of RENPs. In contrast, the photoluminescence lifetime of RENPs is less susceptible than intensity to excitation intensity variation, inhomogeneous signal attenuation, and surrounding environment. Thereupon, RENP lifetime-based nanothermometry is recognized as a potential technique for accurate temperature sensing with less biased error.(Liu *et al.*, 2021b; Tan *et al.*, 2020a) However, lifetime-based nanothermometry is still in its infancy because of the relatively expensive and complex instrumentation. The most common technique, TCSPC, is not ideal for efficient lifetime measurement of RENPs because of its repetitive excitations, limited photon process capability at each excitation, and extended pixel dwelling time. The point scanning for wide-field lifetime mapping is also time-consuming and thus TCSPS will be limited in monitoring biological dynamic activities using lifetime as the indicator. Greater effort is required from the instrumentation side to make lifetime-based nanothermometry more user-friendly, potentially moving it closer to translational applications.

In biomedicine, NIR emission wavelengths that fall within the biological imaging windows hold the potential for deep penetration owing to their low scattering and low absorption by tissues. (Wang *et al.*, 2024a) Notably, NIR-IIb (1500-1700 nm) shows reduced scattering and near-zero autofluorescence, further enhancing spatial resolution and the signal-to-noise ratio in bioimaging. To push RENP nanothermometers to the end for biomedical applications, all the emissions of RENPs are simultaneously studied from UC and DS processes although the NIR emission properties are the focus of the thesis. Generally, a new optical system is developed (chapter 3) from the instrument side to efficiently extract NIR photoluminescence lifetime for temperature sensing. For the performance of the RENP nanothermometers, a new architecture is designed and synthesized with enhanced NIR intensity (chapter 4). Furthermore, RENPs are modified to be dispersed in aqueous solution and the effect of water on the DS and UC nanothermometry is explored (chapter 5).

From the instrumental perspective, a new optical system for NIR photoluminescence lifetime measurement with high efficiency will be developed. A streak camera that converts temporal information to space will be used to capture the whole intensity decay process in one image. According to the wide range of the lifetime of RENPs from microseconds to milliseconds, the imaging speed or the conversion speed of the system should be tunable. Using this new

system, we can efficiently characterize the NIR lifetime of RENPs within one shot. Different structures of RENPs with various lifetimes are prepared to showcase the capability of the system. Moreover, two-dimensional (2D) lifetime is mapped for wide-field temperature sensing, paving the way for lifetime-based nanothermometry in deep tissue biological applications.

On the nanothermometers side, we aim to improve the NIR intensity by doping more activators without severe internal CR. To do so, a new inert core-active shell-inert shell architecture is synthesized. The homogeneous double-layer core-shell interface is designed to allow the extension of the active layer so that the distance of highly dopant activators is enlarged and the concentration quenching effect is minimized. By controlling the crystallinity of the starting core, shell growth dynamics, and dopant concentrations, the optical performance of the new structure is further optimized. Improved NIR intensity presents a high signal-to-noise ratio in signal detection through the opaque medium, offering RENPs great potential for deep tissue temperature sensing.

To shed light on fundamental aspects governing the optical response of RENPs to temperature change in aqueous environments, water effects on the photoluminescence properties of RENPs are scrutinized. The resulting deviations in temperature readout are analyzed in mixed solutions with varying H_2O content, using D_2O as a standard. These findings paint a realistic outlook on the potential and pitfalls of RENP nanothermometry and highlight the necessity of further standardization to ensure reliable RENP nanothermometry in biomedical applications.

Anonyme (2001) Temperature Scales and Classification of Thermometers. *Temperature Measurement*. p 1-18.

Arteaga Cardona F, Jain N, Popescu R, Busko D, Madirov E, Arus BA, Gerthsen D, De Backer A, Bals S, Bruns OT, Chmyrov A, Van Aert S, Richards BS, Hudry D (2023a) Preventing cation intermixing enables 50% quantum yield in sub-15 nm short-wave infrared-emitting rare-earth based core-shell nanocrystals. *Nat Commun* 14(1):4462.

Balabhadra S, Debasu ML, Brites CDS, Ferreira RAS, Carlos LD (2017) Upconverting Nanoparticles Working As Primary Thermometers In Different Media. *J. Phys. Chem. C* 121(25):13962-13968.

Bednarkiewicz A, Marciniak L, Carlos LD, Jaque D (2020) Standardizing Luminescence Nanothermometry for Biomedical Applications. *Nanoscale* 12(27):14405-14421.

Bloembergen N (1959) Solid State Infrared Quantum Counters. *Physical Review Letters* 2(3):84-85.

Brites CD, Lima PP, Silva NJ, Millan A, Amaral VS, Palacio F, Carlos LD (2010) A Luminescent Molecular Thermometer for Long-Term Absolute Temperature Measurements at the Nanoscale. *Adv. Mater.* 22(40):4499-4504.

Brites CDS, Balabhadra S, Carlos LD (2018a) Lanthanide-Based Thermometers: At the Cutting-Edge of Luminescence Thermometry. *Adv. Optical Mater.* 7(5):1801239-1801268.

Brites CDS, Fiaczyk K, Ramalho JFCB, Sójka M, Carlos LD, Zych E (2018c) Widening the Temperature Range of Luminescent Thermometers Through the Intra-and Interconfigurational Transitions of Pr^{3+}. *Adv. Optical Mater.* 6(10):1701318-1701322.

Campbell-Staton SC, Velotta JP, Winchell KM (2021) Selection on Adaptive and Maladaptive Gene Expression Plasticity During Thermal Adaptation to Urban Heat Islands. *Nat. Commun.* 12(1):6195-6208.

Cantarano A, Yao J, Matulionyte M, Lifante J, Benayas A, Ortgies DH, Vetrone F, Ibanez A, Gerardin C, Jaque D, Dantelle G (2020) Autofluorescence-Free In Vivo Imaging Using Polymer-Stabilized Nd^{3+}-Doped YAG Nanocrystals. *ACS Appl. Mater. Interfaces* 12(46):51273-51284.

Carnall WT (1979) Chapter 24 The absorption and fluorescence spectra of rare earth ions in solution. *Handbook on the Physics and Chemistry of Rare Earths,* Elsevier, Vol 3. p 171-208.

Carnall WT, Fields PR, Rajnak K (1968) Electronic Energy Levels of the Trivalent Lanthanide Aquo Ions. IV. Eu3+. *The Journal of Chemical Physics* 49(10):4450-4455.

Carrasco E, del Rosal B, Sanz-Rodríguez F, de la Fuente ÁJ, Gonzalez PH, Rocha U, Kumar KU, Jacinto C, Solé JG, Jaque D (2015) Intratumoral Thermal Reading During Photo-Thermal Therapy by Multifunctional Fluorescent Nanoparticles. *Adv. Funct. Mater.* 25(4):615-626.

Chen B, Wang F (2020) Combating Concentration Quenching in Upconversion Nanoparticles. *Accounts of Chemical Research* 53(2):358-367.

Chen G, Liu H, Liang H, Somesfalean G, Zhang Z (2008) Upconversion Emission Enhancement in Yb3+/Er3+-Codoped Y2O3 Nanocrystals by Tridoping with Li+ Ions. *Journal of Physical Chemistry C* 112:12030-12036.

Cheng L, He W, Gong H, Wang C, Chen Q, Cheng Z, Liu Z (2013) PEGylated Micelle Nanoparticles Encapsulating a Non-Fluorescent Near-Infrared Organic Dye as a Safe and Highly-Effective Photothermal Agent for In Vivo Cancer Therapy. *Advanced Functional Materials* 23(47):5893-5902.

Daniel RM, Danson MJ, Eisenthal R, Lee CK, Peterson ME (2008) The Effect of Temperature on Enzyme Activity: New Insights and Their Implications. *Extremophiles* 12(1):51-59.

Dong H, Du SR, Zheng XY, Lyu GM, Sun LD, Li LD, Zhang PZ, Zhang C, Yan CH (2015) Lanthanide Nanoparticles: From Design toward Bioimaging and Therapy. *Chem. Rev.* 115(19):10725-10815.

Evans SS, Repasky EA, Fisher DT (2015) Fever and the Thermal Regulation of Immunity: the Immune System Feels the Heat. *Nat. Rev. Immunol.* 15(6):335-349.

Falin ML, Gerasimov KI, Latypov VA, Leushin AM (2004) EPR and optical spectroscopy of Yb3+ ions in CaF2: an analysis of the structure of tetragonal centers. *Applied Magnetic Resonance* 26(4):617-632.

Fan Y, Wang P, Lu Y, Wang R, Zhou L, Zheng X, Li X, Piper JA, Zhang F (2018) Lifetime-Engineered NIR-II Nanoparticles Unlock Multiplexed In Vivo Imaging. *Nat. Nanotechnol.* 13(10):941-946.

Gai S, Li C, Yang P, Lin J (2014) Recent Progress in Rare Earth Micro/Nanocrystals: Soft Chemical Synthesis, Luminescent Properties, and Biomedical Applications. *Chem. Rev.* 114(4):2343-2389.

Gao Y, Huang F, Lin H, Zhou J, Xu J, Wang Y (2016) A Novel Optical Thermometry Strategy Based on Diverse Thermal Response from Two Intervalence Charge Transfer States. *Adv. Funct. Mater.* 26(18):3139-3145.

Geitenbeek RG, de Wijn HW, Meijerink A (2018) Non-Boltzmann Luminescence in $NaYF_4:Eu^{3+}$: Implications for Luminescence Thermometry. *Phys. Rev. Applied* 10(6):064006-064015.

Hazra C, Skripka A, Ribeiro SJL, Vetrone F (2020c) Erbium Single-Band Nanothermometry in the Third Biological Imaging Window: Potential and Limitations. *Adv. Optical Mater.* 8(23):2001178-2001186.

Huang X (2017) Broadband dye-sensitized upconversion: A promising new platform for future solar upconverter design. *Journal of Alloys and Compounds* 690:356-359.

Jaque D, Vetrone F (2012) Luminescence nanothermometry. *Nanoscale* 4(15):4301-4326.

Jia M, Fu Z, Liu G, Sun Z, Li P, Zhang A, Lin F, Hou B, Chen G (2020b) NIR-II/III Luminescence Ratiometric Nanothermometry with Phonon-Tuned Sensitivity. *Adv. Optical Mater.* 8(6):1901173-1901179.

Jiang L, Xiao S, Yang X, Ding J, Dong K (2012) Enhancement of up-conversion luminescence in Zn2SiO4:Yb3+, Er3+ by co-doping with Li+ or Bi3+. *Applied Physics B* 107(2):477-481.

Joubert MF, Guy S, Jacquier B, Linarés C (1994) The photon-avalanche effect: review, model and application. *Optical Materials* 4(1):43-49.

Judd BR (1962b) Optical Absorption Intensities of Rare-Earth Ions. *Phys. Rev.* 127(3):750-761.

Jung HS, Verwilst P, Sharma A, Shin J, Sessler JL, Kim JS (2018) Organic molecule-based photothermal agents: an expanding photothermal therapy universe. *Chemical Society Reviews* 47(7):2280-2297.

Kang N, Zhao J, Zhou Y, Ai C, Wang X, Ren L (2019) Enhanced upconversion luminescence intensity of core–shell NaYF4 nanocrystals guided by morphological control. *Nanotechnology* 30(10):105701.

Kumar GA, Pokhrel M, Martinez A, Dennis RC, Villegas IL, Sardar DK (2012) Synthesis and spectroscopy of color tunable Y2O2S:Yb3+,Er3+ phosphors with intense emission. *Journal of Alloys and Compounds* 513:559-565.

Li H, Zhang Y, Chen B, Wang Y, Teh C, Ng GHB, Meng J, Huang Z, Dong W, Tan MY, Sun X, Sun X, Li X, Li J (2019) J-Aggregation of Perylene Diimides in Silica Nanocapsules for Stable Near-Infrared Photothermal Conversion. *ACS Applied Bio Materials* 2(4):1569-1577.

Liu M, Lai Y, Marquez M, Vetrone F, Liang J (2024b) Short-Wave Infrared Photoluminescence Lifetime Mapping of Rare-Earth Doped Nanoparticles Using All-optical Streak Imaging. *Adv. Sci.* 11(11):2305284-2305292.

Liu X, Skripka A, Lai Y, Jiang C, Liu J, Vetrone F, Liang J (2021b) Fast Wide-Field Upconversion Luminescence Lifetime Thermometry Enabled by Single-Shot Compressed Ultrahigh-Speed Imaging. *Nat. Commun.* 12(1):6401-6409.

Lucchini G, Speghini A, Canton P, Vetrone F, Quintanilla M (2019) Engineering Efficient Upconverting Nanothermometers using Eu^{3+} ions. *Nanoscale Adv.* 1(2):757-764.

Ma CG, Brik MG, Liu DX, Feng B, Tian Y, Suchocki A (2016) Energy level schemes of fN electronic configurations for the di-, tri-, and tetravalent lanthanides and actinides in a free state. *Journal of Luminescence* 170:369-374.

Marciniak L, Bednarkiewicz A, Stefanski M, Tomala R, Hreniak D, Strek W (2015) Near Infrared Absorbing Near Infrared Emitting Highly-Sensitive Luminescent Nanothermometer Based on Nd^{3+} to Yb^{3+} Energy Transfer. *Phys. Chem. Chem. Phys.* 17(37):24315-24321.

Martínez A, Morales J, Díaz-Torres LA, Salas P, De la Rosa E, Oliva J, Desirena H (2010) Green and red upconverted emission of hydrothermal synthesized Y2O3: Er3+–Yb3+ nanophosphors using different solvent ratio conditions. *Materials Science and Engineering: B* 174(1):164-168.

Martínez ED, Brites CDS, Carlos LD, García-Flores AF, Urbano RR, Rettori C (2019) Electrochromic Switch Devices Mixing Small- and Large-Sized Upconverting Nanocrystals. *Adv. Funct. Mater.* 29(8):1807758-1807769.

Matulionyte M, Skripka A, Ramos-Guerra A, Benayas A, Vetrone F (2023) The Coming of Age of Neodymium: Redefining Its Role in Rare Earth Doped Nanoparticles. *Chem. Rev.* 123(1):515-554.

Mialon G, Türkcan S, Dantelle G, Collins DP, Hadjipanayi M, Taylor RA, Gacoin T, Alexandrou A, Boilot J-P (2010) High Up-Conversion Efficiency of YVO4:Yb,Er Nanoparticles in Water down to the Single-Particle Level. *The Journal of Physical Chemistry C* 114(51):22449-22454.

Miyakawa T, Dexter DL (1970) Phonon Sidebands, Multiphonon Relaxation of Excited States, and Phonon-Assisted Energy Transfer between Ions in Solids. *Phys. Rev. B* 1(7):2961-2969.

Nsubuga A, Morice K, Fayad N, Pini F, Josserand V, Le Guével X, Alhabi A, Henry M, Puchán Sánchez D, Plassais N, Josse P, Boixel J, Blanchard P, Cabanetos C, Hildebrandt N (2024) Sub 20 nm Upconversion Photosensitizers for Near-Infrared Photodynamic Theranostics. *Advanced Functional Materials* 10.1002/adfm.202410077.

Okabe K, Inada N, Gota C, Harada Y, Funatsu T, Uchiyama S (2012) Intracellular Temperature Mapping with a Fluorescent Polymeric Thermometer and Fluorescence Lifetime Imaging Microscopy. *Nat. Commun.* 3:705-713.

Ortgies DH, Tan M, Ximendes EC, Del Rosal B, Hu J, Xu L, Wang X, Martin Rodriguez E, Jacinto C, Fernandez N, Chen G, Jaque D (2018) Lifetime-Encoded Infrared-Emitting Nanoparticles for in Vivo Multiplexed Imaging. *ACS Nano* 12(5):4362-4368.

Pérez-Rodríguez C, Martín LL, León-Luis SF, Martín IR, Kumar KK, Jayasankar CK (2014) Relevance of Radiative Transfer Processes on Nd^{3+} Doped Phosphate Glasses for Temperature Sensing by Means of the Fluorescence Intensity Ratio Technique. *Sensors and Actuators B: Chemical* 195:324-331.

Pickel AD, Teitelboim A, Chan EM, Borys NJ, Schuck PJ, Dames C (2018a) Apparent Self-Heating of Individual Upconverting Nanoparticle Thermometers. *Nat. Commun.* 9(1):4907-4918.

Qiu X, Zhou Q, Zhu X, Wu Z, Feng W, Li F (2020) Ratiometric Upconversion Nanothermometry with Dual Emission at the Same Wavelength Decoded via a Time-Resolved Technique. *Nat. Commun.* 11(1):4.

Rodriguez-Sevilla P, Marin R, Ximendes E, Del Rosal B, Benayas A, Jaque D (2022) Luminescence Thermometry for Brain Activity Monitoring: A Perspective. *Front. Chem.* 10:941861-941869.

Rohani S, Quintanilla M, Tuccio S, De Angelis F, Cantelar E, Govorov AO, Razzari L, Vetrone F (2015) Enhanced Luminescence, Collective Heating, and Nanothermometry in an Ensemble System Composed of Lanthanide-Doped Upconverting Nanoparticles and Gold Nanorods. *Adv. Optical Mater.* 3(11):1606-1613.

Savchuk OA, Carvajal JJ, Brites CDS, Carlos LD, Aguilo M, Diaz F (2018) Upconversion Thermometry: A New Tool to Measure the Thermal Resistance of Nanoparticles. *Nanoscale* 10(14):6602-6610.

Sen R, Hirvonen LM, Zhdanov A, Svihra P, Andersson-Engels S, Nomerotski A, Papkovsky D (2020) New Luminescence Lifetime Macro-Imager Based on A Tpx3Cam Optical Camera. *Biomed. Opt. Express* 11(1):77-88.

Shen Y, Lifante J, Fernandez N, Jaque D, Ximendes E (2020) In Vivo Spectral Distortions of Infrared Luminescent Nanothermometers Compromise Their Reliability. *ACS Nano* 14(4):4122-4133.

Shen Y, Lifante J, Zabala-Gutierrez I, de la Fuente-Fernandez M, Granado M, Fernandez N, Rubio-Retama J, Jaque D, Marin R, Ximendes E, Benayas A (2022a) Reliable and Remote Monitoring of Absolute Temperature during Liver Inflammation via Luminescence-Lifetime-Based Nanothermometry. *Adv. Mater.* 34(7):2107764-2107773.

Skripka A, Benayas A, Marin R, Canton P, Hemmer E, Vetrone F (2017) Double rare-earth nanothermometer in aqueous media: opening the third optical transparency window to temperature sensing. *Nanoscale* 9(9):3079-3085.

Skripka A, Karabanovas V, Jarockyte G, Marin R, Tam V, Cerruti M, Rotomskis R, Vetrone F (2019a) Decoupling Theranostics with Rare Earth Doped Nanoparticles. *Adv. Funct. Mater.* 29(12):1807105-1807116.

Skripka A, Morinvil A, Matulionyte M, Cheng T, Vetrone F (2019b) Advancing Neodymium Single-Band Nanothermometry. *Nanoscale* 11(23):11322-11330.

Sun L-D, Dong H, Zhang P-Z, Yan C-H (2015) Upconversion of Rare Earth Nanomaterials. *Annual Review of Physical Chemistry* 66(Volume 66, 2015):619-642.

Suta M, Meijerink A (2020) A Theoretical Framework for Ratiometric Single Ion Luminescent Thermometers—Thermodynamic and Kinetic Guidelines for Optimized Performance. *Adv. Theory Simul.* 3(12):2000176-2000207.

Tan M, Li F, Cao N, Li H, Wang X, Zhang C, Jaque D, Chen G (2020a) Accurate In Vivo Nanothermometry Through NIR-II Lanthanide Luminescence Lifetime. *Small* 16(48):2004118-2004127.

van Swieten TP, Meijerink A, Rabouw FT (2022) Impact of Noise and Background on Measurement Uncertainties in Luminescence Thermometry. *ACS Photonics* 9(4):1366-1374.

Vetrone F, Naccache R, Zamarrón A, Juarranz de la Fuente A, Sanz-Rodríguez F, Martinez Maestro L, Martín Rodriguez E, Jaque D, García Solé J, Capobianco JA (2010) Temperature Sensing Using Fluorescent Nanothermometers. *ACS Nano* 4(6):3254-3258.

Wang F, Zhong Y, Bruns O, Liang Y, Dai H (2024a) In vivo NIR-II fluorescence imaging for biology and medicine. *Nature Photonics* 18(6):535-547.

Wang XD, Wolfbeis OS, Meier RJ (2013b) Luminescent Probes and Sensors for Temperature. *Chem. Soc. Rev.* 42(19):7834-7869.

Wen S, Zhou J, Zheng K, Bednarkiewicz A, Liu X, Jin D (2018) Advances in highly doped upconversion nanoparticles. *Nature Communications* 9(1):2415.

Werts MHV, Jukes RTF, Verhoeven JW (2002) The emission spectrum and the radiative lifetime of Eu3+ in luminescent lanthanide complexes. *Physical Chemistry Chemical Physics* 4(9):1542-1548.

Wiesholler LM, Frenzel F, Grauel B, Würth C, Resch-Genger U, Hirsch T (2019) Yb,Nd,Er-doped upconversion nanoparticles: 980 nm versus 808 nm excitation. *Nanoscale* 11(28):13440-13449.

Wolfbeis OS (2015) An overview of nanoparticles commonly used in fluorescent bioimaging. *Chem Soc Rev* 44(14):4743-4768.

Xie X, Liu X (2012) Photonics: Upconversion Goes Broadband. *Nat. Mater.* 11(10):842-843.

Ximendes EC, Santos WQ, Rocha U, Kagola UK, Sanz-Rodriguez F, Fernandez N, Gouveia-Neto Ada S, Bravo D, Domingo AM, del Rosal B, Brites CD, Carlos LD, Jaque D, Jacinto C (2016a) Unveiling In Vivo Subcutaneous Thermal Dynamics by Infrared Luminescent Nanothermometers. *Nano Lett.* 16(3):1695-1703.

Yin D, Wang C, Ouyang J, Song K, Liu B, Cao X, Zhang L, Han Y, Long X, Wu M (2014) Enhancing upconversion luminescence of NaYF4:Yb/Er nanocrystals by Mo3+ doping and their application in bioimaging. *Dalton Transactions* 43(31):12037-12043.

Zhao Q, Shao B, Lü W, Jia Y, Lv W, Jiao M, You H (2013) Doping alkaline-earth: a strategy of stabilizing hexagonal GdF3 at room temperature. *Dalton Transactions* 42(43):15482-15488.

Zhong Y, Ma Z, Zhu S, Yue J, Zhang M, Antaris AL, Yuan J, Cui R, Wan H, Zhou Y, Wang W, Huang NF, Luo J, Hu Z, Dai H (2017b) Boosting the down-shifting luminescence of rare-earth nanocrystals for biological imaging beyond 1500 nm. *Nat. Commun.* 8(1):737.

Zhou B, Tang B, Zhang C, Qin C, Gu Z, Ma Y, Zhai T, Yao J (2020a) Enhancing multiphoton upconversion through interfacial energy transfer in multilayered nanoparticles. *Nature Communications* 11(1):1174.

Zhou B, Tang B, Zhang C, Qin C, Gu Z, Ma Y, Zhai T, Yao J (2020b) Enhancing multiphoton upconversion through interfacial energy transfer in multilayered nanoparticles. *Nat Commun* 11(1):1174.

Zhou J, Del Rosal B, Jaque D, Uchiyama S, Jin D (2020d) Advances and Challenges for Fluorescence Nanothermometry. *Nat. Methods* 17(10):967-980.

Zhou J, Liu Q, Feng W, Sun Y, Li F (2015) Upconversion Luminescent Materials: Advances and Applications. *Chemical Reviews* 115(1):395-465.

Zhou J, Wen S, Liao J, Clarke C, Tawfik SA, Ren W, Mi C, Wang F, Jin D (2018) Activation of the Surface Dark-Layer to Enhance Upconversion in A Thermal Field. *Nat. Photonics* 12(3):154-158.

2 MATERIALS AND METHODS

2.1 RENPs synthesis

2.1.1 Materials

Table 2.1 Chemicals employed in the preparation of the precursors and synthesis of RENPs.

Name	Abbreviation/Formula	Purity	Manufacture
Erbium oxide	Er_2O_3	99.999%	Alfa Aesar
Holmium oxide	Ho_2O_3	99.997%	Alfa Aesar
Ytterbium oxide	Yb_2O_3	99.998%	Alfa Aesar
Gadolinium oxide	Gd_2O_3	99.99%	Alfa Aesar
Yttrium oxide	Y_2O_3	99.999%	Alfa Aesar
Lutetium oxide	Lu_2O_3	999%	Alfa Aesar
Cerium carbonate	$Ce_2(CO_3)_3 \cdot XH_2O$	99.9%	Alfa Aesar
Sodium trifluoroacetate	CF_3COONa	98%	Alfa Aesar
Lithium trifluoroacetate	CF_3COOLi	97%	Alfa Aesar
Trifluoracetic acid	TFA	99%	Sigma-Aldrich
Milli-Q water	H_2O	Distilled and filtered	MilliporeSigma
Heavy water	D_2O	99.9%	MilliporeSigma
Oleic acid	OA	90%	Alfa Aesar
Oleylamine	OM	70%	Sigma-Aldrich
1-Octadecene	ODE	90%	Alfa Aesar

All chemicals were used as received.

2.1.2 Preparation of precursors

RE^{3+}-trifluoroacetate $(CF_3COO)_3RE$ precursors are prepared from stoichiometric amounts of RE_2O_3 and $RE_2(CO_3)_3$. The aimed starting materials are selectively mixed with 5 mL trifluoroacetic acid and 5 mL distilled water in a 50 mL three-neck round bottom flask. The mixture is kept at 80 °C under vigorous stirring until the solution became clear. The temperature

is then reduced to 60 °C to evaporate the residual trifluoroacetic acid and water, and the $(CF_3COO)_3RE$ precursors in the powder are obtained.

2.1.3 Thermal decomposition

Thermal decomposition of $(CF_3COO)_3RE$ precursors has been applied to prepare all of the RENPs in this thesis. Na-based RENPs are synthesized by one-step thermolysis and Li-based RENPs are synthesized by stabilization of the first nuclei (FN). More details are given in chapter 3 to chapter 5.

In typical one-step thermolysis, 2.5 mmol $(CF_3COO)_3RE$ precursors and 2.5 mmol CF_3COONa, are first dissolved in a mixture (solution A) of 7.5 mL OA and 7.5 mL ODE under vacuum at 125 °C for 30 min under vigorous stirring. Solution B is the mixture of 12.5 mL OA and 12.5 mL ODE and the temperature is then increased to 315 °C. Once the temperature of solution B is stable, solution A is injected into solution B at a rate of 1.5 mL min^{-1} (Harvard Apparatus Pump 11 Elite). The final solution is kept at 315 °C under an argon atmosphere for 1 hour to get core RENPs.

Synthesis of FN: 2.5 mmol $(CF_3COO)_3RE$ precursors and 2.5 mmol CF_3COONa, are mixed with 3 mL OA and 6 mL ODE (solution A) and then degassed at 125 °C for 30 min. When the precursors are dissolved, 3 mL of OM is then added in solution A and left to degas for 5 min. Meanwhile, a mixture (solution B) of 7 mL OA, 7 mL OM and 14 mL ODE is degassed at 110 °C for 15 min and then heated to 330 °C under an argon atmosphere. Once the temperature of solution B is stable, solution A is then injected into solution B at a rate of 1.5 mL min^{-1} (Harvard Apparatus Pump 11 Elite). The final solution is kept at 330 °C under an argon atmosphere for 1 hour to get FN RENPs.

Stabilization of FN: 1.25 mmol FN is mixed with 16 mL of OA and 16 7 mL of ODE in a 100 mL three-neck round bottom flask. The solution is degassed at 110 °C for 30 minutes and backfilled with argon gas. The temperature is raised to 315 °C, after which the reaction is continued for 1 hour.

Core-shell RENPs are prepared via epitaxial growth of the shell on the core. In solution A, shell precursors are mixed with CF_3COONa/CF_3COOLi and OA, ODE. The mixed solution is 15 mL in total. Solution A is degassed at 110 °C for 30 min. Solution B is 25 mL mixed from core RENPs, OA, and ODE (The volume ratio of OA and ODE is 1:1). After degassing, temperature of solution B is raised to 315 °C under argon. Solution A is then injected into solution B at a rate of

1 mL min^{-1}. The mixed solution is reacted at 315 °C for 1 hour. After cooling down to room temperature, the final product is washed with hexane/ethanol (1:3) three times and re-dispersed in hexane.

2.2 Ligand removal

The OA ligand on the surface of RENPs is stripped with the assistance of nitrosyl tetrafluoroborate ($NOBF_4$). A total of 25 mg RENPs dispersed in 5 mL hexane is mixed with 5 mL dichloromethane solution of $NOBF_4$ (0.01 mol/L). The mixed solution is then shaken for 5 min until the precipitation of RENPs is clearly observed. The supernatant is removed after centrifugation. The precipitated RENPs are washed with a toluene and hexane mixture (1:1 by volume) once, followed by one wash in water. The final RENPs are redispersed in H_2O or D_2O for spectral measurements.

2.3 Structural characterization

The crystallinity and phase of all RENPs are determined via X-ray powder diffraction (XRD) analysis on a Bruker D8 Advance Diffractometer using Cu Kα radiation (λ=1.5418 Å) and a step size of 0.05 degree. The morphology and size distribution of RENPs are investigated by transmission electron microscopy (TEM; Philips Tecnai 12, USA) working at the accelerating voltage of 80 kV. The particle size is determined from TEM images using ImageJ software. High-resolution TEM images, high-angle annular darkfield scanning transmission electron microscopy (HAADF-STEM) images, and energy-dispersive X-ray spectrometry (EDS) line scanning are taken on Jeol JEM-2100F TEM (JEOL), carried out by Dr. Jean-Philippe Masse at the Polytechnique Montreal, Canada.

2.4 Optical characterization

Upconversion and downshifting spectra of RENPs are obtained under laser diode excitation of 980 nm (MDL-SN-980-10W, CNI). The upconverting emission is recorded with an Avaspec-ULS2048L spectrometer (Avantes, The Netherlands). Stray light from the excitation source is removed with a short-pass 830 nm filter. The downshifting spectrum was collected with a Shamrock 500i monochromator (Andor, Ireland) equipped with an iDus InGaAs 1.7 NIR detector (Andor, Ireland). A long-pass 980 nm filter is used to remove any stray light from the excitation source. Time-resolved NIR emission intensity profile is measured by a home-built NIR

photoluminescence lifetime imaging microscopy using an all-optical streak camera (SWIR-PLIMASC developed in chapter 3).

The thermal response of RENPs is measured from 20 to 45 ºC in 5 ºC increments. The temperature is changed using a temperature-controlled cuvette holder (qpod 2e by Quantum Northwest, Washington, USA).

3 SHORT-WAVE INFRARED PHOTOLUMINESCENCE LIFETIME MAPPING OF RARE-EARTH DOPED NANOPARTICLES USING ALL-OPTICAL STREAK IMAGING

Short-wave infrared photoluminescence lifetime mapping of rare-earth doped nanoparticles using all-optical streak imaging

Cartographie de la durée de vie de la photoluminescence dans l'infrarouge à ondes courtes des nanoparticules dopées aux terres rares à l'aide d'une imagerie par caméra à balayage totalement optique

Auteurs :

Miao Liu, Yingming Lai, Miguel Marquez, Fiorenzo Vetrone*, Jinyang Liang*

Centre Énergie Matériaux Télécommunications, Institut National de la Recherche Scientifique, Université du Québec, 1650 boulevard Lionel-Boulet, Varennes, Québec J3X 1P7, CANADA

Publication:

Advanced Science Vol. 11, Issue 11, pp 2305284-2305292

Submitted 1 August 2023, accepted 20 March 2024

https://doi.org/10.1002/advs.202305284

Contribution des auteurs:

Miao Liu built the system, conducted the experiments, analyzed the data, and wrote the manuscript. Yingming Lai helped in designing the system. Yingming Lai and Miguel Marquez helped with software development and data analysis. Fiorenzo Vetrone and Jinyang Liang initiated the project, proposed the concept, contributed to experimental design, and supervised the project.

Abstract

The short-wave infrared (SWIR) or NIR photoluminescence lifetimes of rare-earth doped nanoparticles have found diverse applications in fundamental and applied research. Despite dazzling progress in the novel design and synthesis of RENPs with attractive optical properties, existing optical systems for SWIR photoluminescence lifetime imaging are still considerably restricted by inefficient photon detection, limited imaging speed, and low sensitivity. To overcome these challenges, we develop SWIR photoluminescence lifetime imaging microscopy using an all-optical streak camera (PLIMASC). Synergizing scanning optics and a high-sensitivity InGaAs CMOS camera, SWIR-PLIMASC has a one-dimensional (1D) imaging speed of up to 138.9 kHz in the spectral range of 900–1700 nm, which quantifies the photoluminescence lifetime of RENPs in a single shot. A two-dimensional photoluminescence lifetime map can be acquired by 1D scanning of the sample. To showcase the power of SWIR-PLIMASC, we synthesize a series of core-shell RENPs with distinct SWIR photoluminescence lifetimes. In particular, using Er^{3+}-doped RENPs, SWIR-PLIMASC enables multiplexed anti-counterfeiting. Leveraging Ho^{3+}-doped RENPs as temperature indicators, this system is applied to SWIR photoluminescence lifetime-based thermometry. Opening up a new avenue for efficient SWIR photoluminescence lifetime mapping, this work is envisaged to contribute to advanced materials characterization, information science, and biomedicine.

3.1 Introduction

RENPs have provoked widespread curiosity for their applicability in a plethora of fields, including nanomedicine, bioimaging, security authentication, and sensing.(Hemmer *et al.*, 2016a; Matulionyte *et al.*, 2023; Ren *et al.*, 2020) Their popularity is mostly attributed to their diverse photoluminescence properties that span multiple excitation wavelengths and emission possibilities.(Wang *et al.*, 2009) Of significant interest, many RENPs can be excited by short-wave infrared (SWIR) light (also referred to as near-infrared light). In biomedicine, SWIR excitation light (in the biological windows (Goh *et al.*, 2022; Golovynskyi *et al.*, 2018; Ma *et al.*, 2019; Roy *et al.*, 2022; Smith *et al.*, 2009a)) mitigates the drawbacks associated with ultraviolet (UV) and/or visible light excitation, such as strong scattering by tissue and large absorption of biomolecules, which enables deep tissue imaging.(Chen *et al.*, 2023b; Hong *et al.*, 2012; Kenry *et al.*, 2018; Zhou *et al.*, 2021). Invisible to the naked eye, SWIR light is also well-suited for defense and surveillance.(Malchow *et al.*, 2007) The emission of RENPs also presents remarkable properties. After multiphoton excitation, RENPs can convert the SWIR light to the UV and visible ranges, a process known as upconversion.(Haase *et al.*, 2011; Jalani *et al.*, 2015) Meanwhile, via single-photon excitation, RENPs can also emit in the SWIR range through downshifting emission (Wawrzynczyk *et al.*, 2012; Zhong *et al.*, 2017a), which has better penetration ability compared to the upconverting counterpart and avoids interference of background light. Thus, RENPs, which are excited in the SWIR region and can simultaneously emit in the UV, visible, and SWIR ranges, offer an attractive nanoplatform for both fundamental and applied research.

Among the SWIR optical properties of RENPs, the photoluminescence lifetime has recently ignited a surge of interest. The lifetime is an intrinsic characteristic of rare-earth photoluminescence that provides valuable information regarding the photophysical properties of the RENPs, e.g., energy transfer processes (Supplementary Note 1) and the photoluminescence efficiency.(Rabouw *et al.*, 2018; Skripka *et al.*, 2020a; Walsh *et al.*, 1998) In practice, photoluminescence lifetime does not vary with the concentration of RENPs and the penetration depth. It is minimally affected by many circumstances even the exterior conditions.(Fan *et al.*, 2018; Tan *et al.*, 2020b) Circumventing many problems in intensity-based measurements, photoluminescence lifetime imaging and sensing enables a reliable detection method,(Fan *et al.*, 2018; Li *et al.*, 2020a; Ortgies *et al.*, 2018; Tan *et al.*, 2020b) which is particularly beneficial for accuracy-demanding applications, such as secured information storage and temperature monitoring.(Pickel *et al.*, 2018b; Shen *et al.*, 2022b; Wu *et al.*, 2023)

Meanwhile, the study of photoluminescence lifetime can, in turn, aid in the understanding of the luminescence process and, thus, in the design of new RENPs with improved optical properties, including a high quantum yield and a tunable photoluminescence lifetime.(Kong *et al.*, 2019; Liu *et al.*, 2018b)

Existing photoluminescence lifetime imaging techniques still encounter various limitations in the SWIR range. The most common technique is time-correlated single-photon counting (TCSPC) using an InGaAs single-photon avalanche diode (SPAD).(Bruschini *et al.*, 2019; Maeda *et al.*, 2021; Parfenov *et al.*, 2020; Zhang *et al.*, 2015) Despite having a high signal-to-noise ratio (SNR), this method requires a large number of repeated excitations to the same location because the detector can only process a limited number of photons for each excitation. The long SWIR photoluminescence lifetimes of RENPs (i.e., from hundreds of microseconds to several milliseconds) restrict the excitation's repetition rate, which results in much extended pixel dwelling time to build the photoluminescence intensity decay curve. To accelerate data acquisition, many technical innovations have explored spatial parallelism and real-time (i.e., the time during which an event occurs) detection.(Liu *et al.*, 2019) The former strategy is represented by the invention of SPAD arrays(Homulle *et al.*, 2016) and the performance enhancement of SWIR CCD/CMOS cameras.(Krishnan *et al.*, 2003a; Wang *et al.*, 2020a) Nonetheless, SPAD arrays confront the same limitations as their point-detection counterpart. (Pavia *et al.*, 2014; Zappa *et al.*, 2007) SWIR CCD/CMOS cameras enjoy a high detection sensitivity. However, their pixel structures and readout mechanisms inevitably limit their frame rates to around 100 frames per second (fps), falling short of directly recording the dynamics of SWIR emission on the microsecond time scale. The required speed can be provided by image-converter streak cameras, which convert time to space by deflecting photoelectrons to different spatial locations.(Krishnan *et al.*, 2003b) Although capable of recording photoluminescence intensity decay in real time using a single excitation pulse, these instruments have exceptionally low sensitivity because the low energy of SWIR photons diminishes the generation of photoelectrons in the photocathode.(Liang *et al.*, 2018; Wang *et al.*, 2020b) Thus far, imaging techniques have not kept up to provide technical specifications tailored for highly efficient SWIR photoluminescence lifetime acquisition.

To surmount this challenge, we develop SWIR photoluminescence lifetime imaging microscopy using an all-optical streak camera (PLIMASC), which combines scanning optics with a high-sensitivity InGaAs CCD camera for one-dimensional (1D) ultrahigh-speed imaging at a speed of up to 138.9 kHz. By 1D scanning of the sample, SWIR-PLIMASC maps the 2D SWIR

photoluminescence lifetime distribution. To evaluate the system and assess its potential in two important applications, a series of Er^{3+} (or Ho^{3+})-doped RENPs with distinct SWIR photoluminescence decay lifetimes are prepared. The SWIR-PLIMASC system is applied to multiplexed SWIR anti-counterfeiting using the Er^{3+}-doped RENPs while it is implemented in SWIR photoluminescence lifetime-based thermometry using the Ho^{3+}-RENPs as nanothermometers.

3.2 Results

3.2.1 Preparation of RENPs

To tune the photoluminescence lifetimes of RENPs, we varied the host material, particle size, shell thickness, and dopant (activator) ions. All RENPs (i.e., Er^{3+} and Ho^{3+}-doped RENPs) were synthesized using the thermal decomposition method previously described.(Cheng *et al.*, 2018b) First, a series of Er^{3+} (2 mol%)-doped RENPs were prepared and their photoluminescence lifetimes were tuned by changing the host matrix from $NaGdF_4$ to $LiLuF_4$ and $LiYbF_4$. The Yb^{3+} ion was selected as the sensitizer (to increase 980 nm photon absorption),(Chen *et al.*, 2015b) and the concentration was kept at 18 mol% (in the case of $LiLuF_4$ and $NaGdF_4$ where it is added as a co-dopant) while for $LiYbF_4$, the Yb^{3+} sensitizer was part of the host matrix. The first three panels in Figure 3.1a show the transmission electron microscopy (TEM) images of the core $NaGdF_4$:Yb^{3+}, Er^{3+}, $LiLuF_4$:Yb^{3+}, Er^{3+}, and $LiYbF_4$:Er^{3+} RENPs, respectively. All the core RENPs are uniform and monodispersed with estimated diameters to be about 40 nm, 11 nm, and 15 nm, respectively (Figure 3.1b). Subsequently, the luminescent core RENPs were coated with an inert shell to decrease the surface defects and external quenching. The final core-shell structures shown in the first three panels in Figure 3.1c are $NaGdF_4$:Yb^{3+}, Er^{3+}@$NaGdF_4$ (Gd:Er@Gd), $LiLuF_4$:Yb^{3+}, Er^{3+}@$LiLuF_4$ (Lu:Er@Lu), and $LiYbF_4$:Er^{3+}@$LiYF_4$ (Yb:Er@Y), respectively. The shell thickness varies from 3 nm, 5 nm, and 11 nm, respectively, to minimize the surface quenching and increase the overall photoluminescence intensity (see Figure S3.1).(Cheng *et al.*, 2018b; Pini *et al.*, 2023; Wurth *et al.*, 2018) For further analysis of these core-shell RENPs, their crystal phases were examined using X-ray diffraction (XRD) measurements (Figure S3.2). All the diffraction peaks matched well with the standard diffraction patterns.

Under 980 nm laser excitation, the three Er^{3+}-doped core-shell RENPs showed SWIR emission centered at around 1535 nm (Figure 3.1d), corresponding to the transition of $^4I_{13/2} \rightarrow {}^4I_{15/2}$. The energy level diagram (showing the excited states of interest) is shown in Figure 3.1e. Amongst

all the various processes to populate the Er^{3+} excited states, the most dominant one likely involves Yb^{3+} to Er^{3+} energy transfer. In particular, excited Yb^{3+} ions transfer their absorbed energy to the adjacent Er^{3+} ions that are subsequently excited to the $^4I_{11/2}$ state via ground state absorption. The emitting $^4I_{13/2}$ state is populated after a multiphonon relaxation process from the $^4I_{11/2}$ state, leading to the following SWIR emission. The SWIR spectra of Lu:Er@Lu and Yb:Er@Y materials are similar—both spectra present multiple fine emission peaks. In contrast, the Gd:Er@Gd RENPs show broadband emission, which is consistent with previous studies.(Hazra *et al.*, 2020b; Jiang *et al.*, 2016) The multiple emission peaks in the $LiLuF_4$ or $LiYbF_4$ samples are attributed to the pronounced Stark splitting of Er^{3+} in these matrices, which exert high crystal field strengths on the dopants.(Auzel *et al.*, 1983; Jiang *et al.*, 2016) Alongside the downshifting emission, upconversion emissions at around 520/540 nm and 660 nm were also observed (Figure S3.3), which are assigned to the transitions of $^2H_{11/2}$ / $^4S_{3/2} \rightarrow {}^4I_{15/2}$ and $^4F_{9/2} \rightarrow {}^4I_{15/2}$, respectively.

Another activator ion, Ho^{3+}, was also investigated as a dopant for the RENPs. While its photoluminescence properties in the visible region (upconversion) are similar to Er^{3+}, its emission in the SWIR is different, which can be used to showcase the system's viability. Specifically, we synthesized $LiYbF_4$:Ho^{3+} core and $LiYbF_4$:Ho^{3+}@$LiYF_4$ (Yb:Ho@Y) core-shell RENPs. The TEM images (the last panels in Figures 3.1a, c) show uniform nanoparticles with distributions of about 16 nm and 41 nm in diameter (Figure 3.1b) for the core and core-shell structures, respectively. The crystal structure was confirmed by the XRD measurement (Figure S3.2). The downshifting photoluminescence spectrum of Yb:Ho@Y was collected, as shown in Figure 3.1d. The SWIR emission at around 1154 nm is attributed to the Ho^{3+} $^5I_6 \rightarrow {}^5I_8$ transition. Besides, the upconversion emissions at approximately 540 nm, 650 nm, and 750 nm were also observed (Figure S3.3), assigned to the radiative transitions of $^5S_2/^5F_4 \rightarrow {}^5I_8$, $^5F_5 \rightarrow {}^5I_8$, and $^5S_2/^5F_4 \rightarrow {}^5I_7$, respectively.

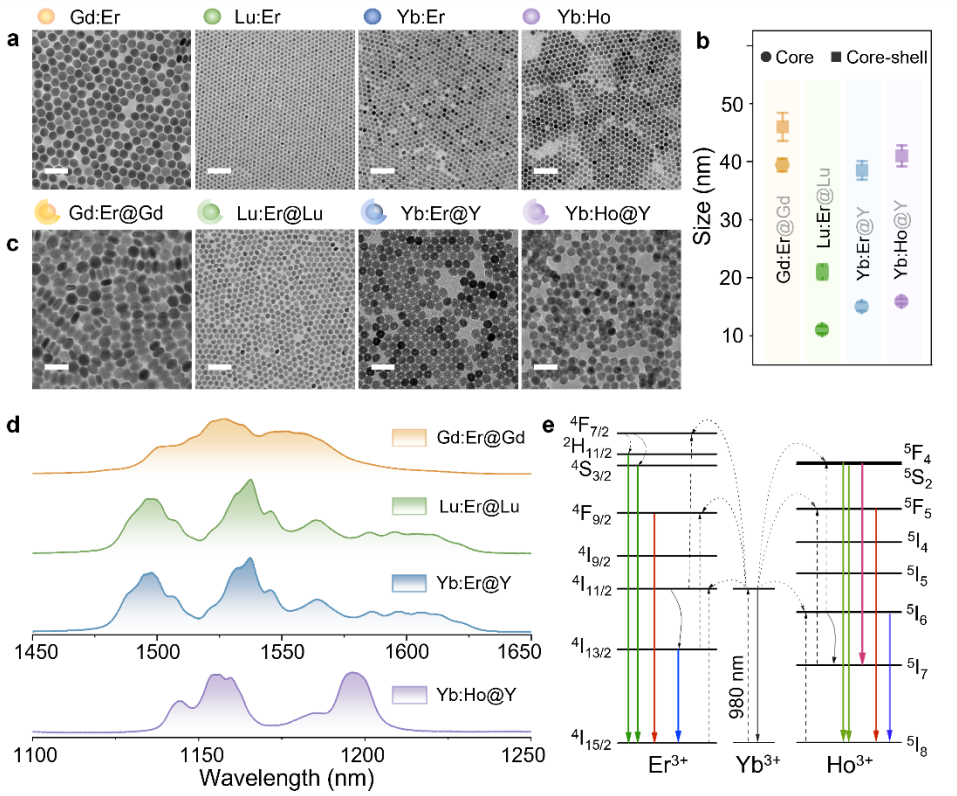

Figure 3.1 Morphology and downshifting photoluminescence of the prepared RENPs.

(a) Transmission electron microscopy images of four types of core RENPs. (b) Size distributions of all the core and core-shell RENPs. (c) As (a), but showing core-shell RENPs. (d) SWIR photoluminescence spectra of the four types of core-shell RENPs under 980 nm excitation. (e) Energy level diagrams of Er^{3+}-doped RENPs and Ho^{3+}-doped RENPs under 980 nm excitation. Scale bar in (a, c): 100 nm.

3.2.2 Operating principle of SWIR-PLIMASC

The schematic of the SWIR-PLIMASC is shown in Figure 3.2a. A 980 nm laser, controlled by an external trigger, generates microsecond-level pulses for illumination. A 200-mm-focal-length plano-convex lens (Thorlabs, LA1708-B-ML, marked as L0) focuses the pulse onto the sample plane. The visible and SWIR emissions of the RENPs are collected by a 20× objective lens (Mitutoyo, 378-824-16, 0.4 numerical aperture). The light passes through a mirror, a tube lens, and a band-pass filter (Semrock BLP01-1064R-25). In this way, both the upconversion emission and the back-scattered excitation light are filtered out, and an image of the object with the targeted SWIR emission band is formed at the intermediate image plane. There, a slit (100 μm × 2 mm, Fineline Imaging) is placed to limit the field of view to one dimension. Then, the slit image is relayed to a SWIR CMOS camera (Xenics, Cheetah-640CL TE3) by a 4*f* imaging system composed of two 100-mm-focal-length lenses (Thorlabs, AC254-100-C, marked as L1 and L2 in Figure 3.2a). A galvanometer scanner (GS), placed at the Fourier plane and driven by

a triangular wave, temporally shears the dynamic slit images along its width (i.e., x) direction. Thus, each image captured by the camera records the y-t information within the exposure time. The 1D imaging speed, denoted by γ_1, is determined by

$$\gamma_1 = \frac{\gamma V_{\mathrm{g}} f_2}{t_{\mathrm{tri}} d} \,. \tag{3.1}$$

Here, γ is a constant that links the deflection angle and the voltage of the input waveform on GS (i.e., V_{g}).(Liu *et al.*, 2021a) $f_2 = 100$ mm is the focal length of lens L2. t_{tri} is the period of the triangular waveform. $d = 20$ μm is the pixel size of the camera. In addition, the exposure time, denoted by t_{e}, determines the number of time bins in each y-t plot by $N_t = r_{\mathrm{l}} t_{\mathrm{e}}$. Finally, the sample is scanned in the x direction by a motorized translation stage (Physik Instrumente, L-509.10SD00) synchronized with the laser, the GS, and the camera (see the inset of Figure 3.2a). It is worth noting that the frequency of the trigger on the laser is the same as on the camera to ensure there is only one pulse excitation during the exposure time. In this way, SWIR-PLIMASC efficiently records the full photoluminescence intensity decay in a single shot.

The system performance of SWIR-PLIMASC was characterized by the following three aspects. First, to assess the system's spatial resolution, we covered the Gd:Er@Gd core-shell RENPs with a negative USAF resolution target (Edmund Optics, 55-622). Figures 3.2b–c show a reference image (i.e., a wide-field snapshot with no slit) and the local line-scanning result of Group 7 with the slit. The averaged intensity profile of Element 1–6 of the line-scanning result is plotted in Figure 3.2d, showing good contrast for all elements. The spatial resolution, quantified by analyzing an edge spread function (Figure S3.4), was determined to be 2.27 μm, which closely matched the theoretical value. Second, to accommodate the varied photoluminescence lifetimes of the RENPs, the imaging speed and time bins of SWIR-PLIMASC were tuned by changing the period and the voltage of the triangular waveform applied to the GS as well as the exposure time of the camera. In particular, for Er^{3+}-doped RENPs, $t_{\mathrm{tri}} = 200\ \mathrm{ms}$, $V_{\mathrm{g}} = 3\ \mathrm{V}$, and $t_{\mathrm{e}} = 50\ \mathrm{ms}$. For Ho^{3+}-doped RENPs, $t_{\mathrm{tri}} = 50\ \mathrm{ms}$, $V_{\mathrm{g}} = 10\ \mathrm{V}$, and $t_{\mathrm{e}} = 4\ \mathrm{ms}$. Figure 3.2e shows the static image of the slit and the streak images of the slit under these two configurations from steady emission under continuous-wave 980 nm excitation. The intensity profiles of the slit in Figure 3.2e, averaged in the y direction, are plotted in Figure 3.2f, which yielded r_{l}=10.3 kHz (corresponding to 97.6 μs/pixel) for Er^{3+}-doped RENPs and r_{l}=138.9 kHz (corresponding to 7.2 μs/pixel) for Ho^{3+}-doped RENPs. Finally, to examine the linearity in the temporal shearing operation, we varied the exposure time from 0.2 ms to 50 ms and recorded the width of the streak images. The results were fitted with a linear function (Figure 3.2g). The slopes of the

fitted curves were quantified to be 10.4 kHz and 139.8 kHz. The deviation was attributed to pixel counting error and different shutter responses for various exposure times, which exerted a larger impact for higher imaging speed. For the ensuing experiment, the exposure times were set to 50 ms for the Er^{3+}-doped RENPs and 4 ms for the Ho^{3+}-doped RENPs.

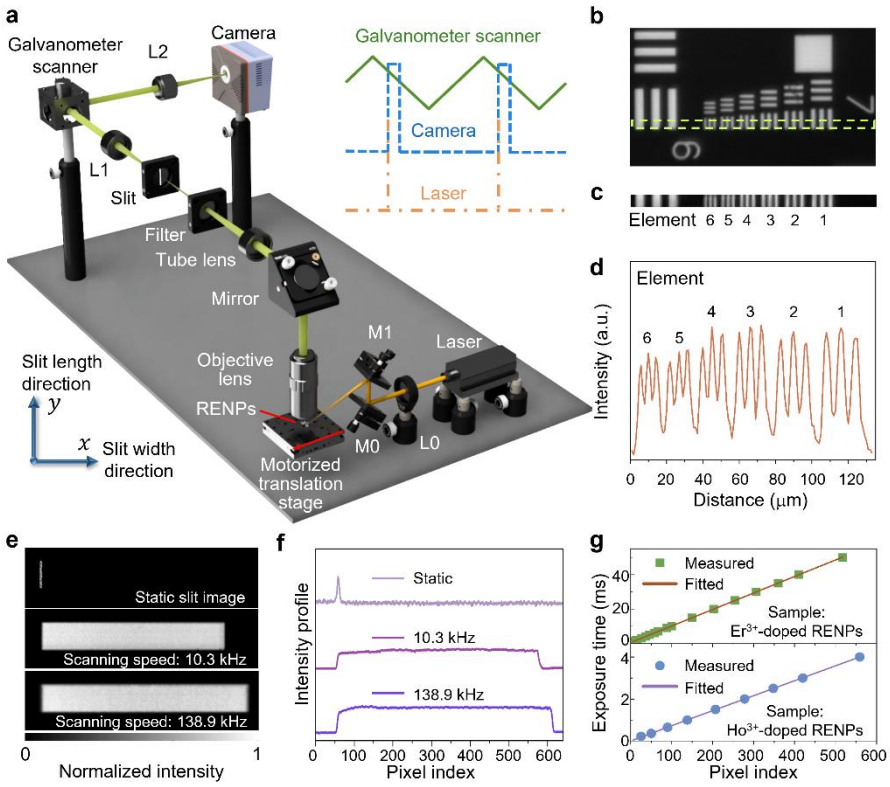

Figure 3.2 Short-wave infrared photoluminescence lifetime imaging microscopy using an all-optical streak camera (SWIR-PLIMASC).

(a) Schematic. M0–M1, Mirror; L0–L2, Lens. Inset: Diagram of synchronization of the galvanometer scanner's triangular control signal (green solid line), the camera's exposure (blue dashed line), and the laser pulses (orange dash-dotted line). (b) Reference image of a USAF resolution target. (c) Local line-scanning image of Group 7 elements on the USAF resolution target. (d) Averaged intensity profile of Element 1–6 of Group 7 in (c). (e) Static image and streak images of the slit under two different imaging configurations. (f) Averaged intensity profiles of the slit images in (e). (g) Linearity test at two imaging speeds. RENPs: Rare-earth doped nanoparticles.

SWIR-PLIMASC presents several attractive advantages in characterizing the photoluminescence lifetime of the RENPs. First, the system is responsive to a wide spectral range from 900 nm to 1700 nm and thus photoluminescence at different wavelengths and/or spectral bands can be detected by changing the band-pass filter. To the best of our knowledge, SWIR-PLIMASC marks the first of its kind in high-sensitivity, ultrahigh-speed SWIR imaging. Second, the system offers high tunability in 1D imaging speed from 10.3 kHz to 138.9 kHz. Benefiting from this ability, SWIR photoluminescence lifetimes from microseconds to

milliseconds can be directly captured using the same system. Moreover, the shearing operation allocates temporal information in photoluminescence to different spatial positions, so that the entire process of the 1D photoluminescence intensity decay can be recorded in a snapshot. Circumventing the dead time in photon processing, SWIR-PLIMASC has a higher light throughput compared with the TCSPC and SPAD techniques.

3.2.3 Anti-counterfeiting using SWIR-PLIMASC

Anti-counterfeiting has become an essential practice to protect valuable commodities.(Fincham, 2014; Fink *et al.*, 2015; Yoon *et al.*, 2013) Among existing techniques, luminescent RENPs are becoming widely studied as advanced anti-counterfeiting materials due to their attractive properties, such as excellent photostability and high compatibility with printing techniques.(Tan *et al.*, 2019; Zhang *et al.*, 2010; Ziniuk *et al.*, 2021) While photoluminescence spectrum-based anti-counterfeiting coding has a lower security level due to the well-defined and known positions of RENPs' spectral bands, photoluminescence lifetime-based anti-counterfeiting patterns offer better protection owing to its transience in emission, fine tunability, and demand of specialized examination tools. Storing encrypted information in the time domain, photoluminescence lifetime-based anti-counterfeiting can avoid photoluminescence overlap in the spectrum and background interference.(Lu *et al.*, 2013; Zhu *et al.*, 2022) Thus, using SWIR-PLIMASC, we explored anti-counterfeiting by SWIR photoluminescence lifetime mapping of RENPs. Under an imaging speed of $r_1 = 10.3$ kHz, the streak images of the three types of Er^{3+}-doped core-shell RENPs are shown in Figure 3.3a. By averaging the intensity in the y direction, the normalized photoluminescence intensity decay curves are plotted in Figure 3.3b. The photoluminescence lifetime was extracted by synthetically considering the finite width of the slit and the finite duration of the excitation pulse (Supplementary Note 3.2 and Figure S3.5). Using this method, the photoluminescence lifetimes (denoted by τ) at around 1535 nm in Gd:Er@Gd, Lu:Er@Lu, and Yb:Er@Y RENPs were calculated to be 3.59 ms, 5.78 ms, and 6.26 ms, respectively. Then, we covered these RENP samples with a transparency of a flower. Their photoluminescence lifetime maps are shown in Figure 3.3c, and the histograms of photoluminescence lifetimes in each case are shown in Figure S3.6.

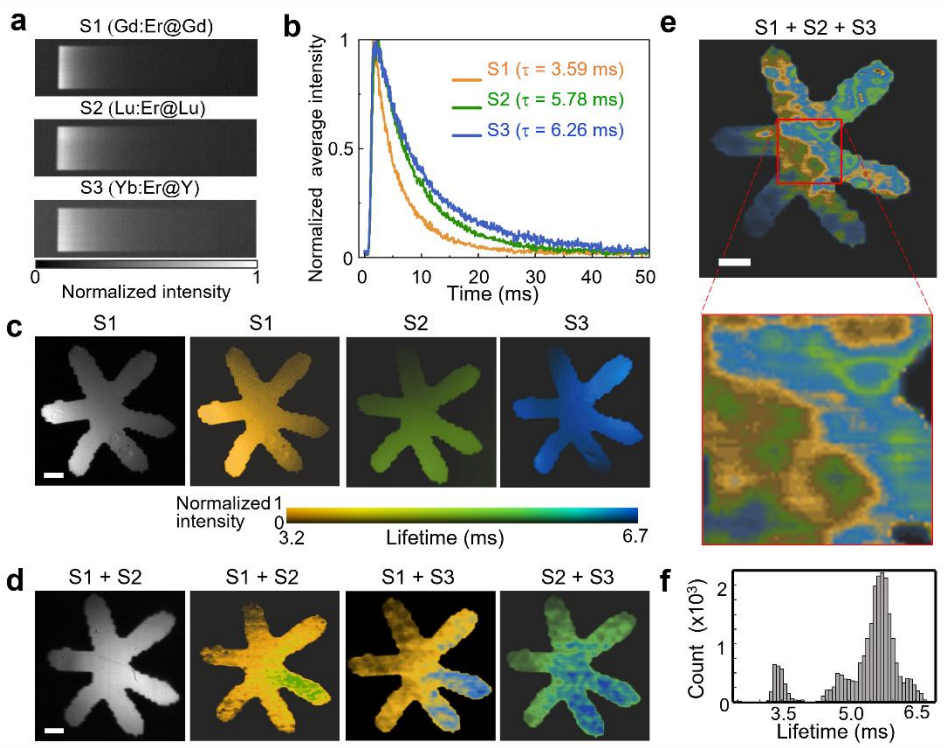

Figure 3.3 Photoluminescence lifetime-based anti-counterfeiting using SWIR-PLIMASC with Er^{3+}-doped core-shell RENPs.

(a) Streak images of three types of Er^{3+}-doped core-shell RENPs, denoted by S1–S3. (b) Normalized average photoluminescence intensity decay curves of S1–S3 plotted from the corresponding images in (a). (c) Intensity image and photoluminescence lifetime images of the three types of Er^{3+}-doped core-shell RENPs covered by a transparency of a flower. (d) Photoluminescence lifetime images of the mixture of two types of RENPs. (e) Photoluminescence lifetime image of mixed three types of RENPs with a zoom-in view of a local area. (f) Histogram of photoluminescence lifetimes in the flower pattern shown in (e). Scale bar in (c, d, e): 50 μm.

These Er^{3+}-doped core-shell RENPs, which had similar photoluminescence spectra but different photoluminescence lifetimes, provided temporal codes for SWIR anti-counterfeiting. First, we mixed two of the three different types of RENPs. A different type of RENP was used in one or two petals of the flower pattern to encrypt the spatially heterogeneous photoluminescence lifetimes (Figure 3.3d). While the intensity image, as a camouflage, shows similar brightness of these petals with the surrounding ones (see the first panel of Figure 3.3d as well as Figure S3.7), SWIR-PLIMASC reveals the encrypted content—the different photoluminescence lifetimes in the designated locations. To further test SWIR-PLIMASC's ability to decrypt complex photoluminescence lifetime information, we mixed all three types of RENPs dispersed in hexane. A drop containing S1 was deposited and dried on the glass slide. Using this protocol, the second and third drops containing S2 and S3 were applied to the same location. The 2D photoluminescence lifetime distribution of this sample is shown in Figure 3.3e. Interestingly, the

complex photoluminescence lifetime distribution resembles water stains, reflecting the flow and drying of the hexane solvent during sample preparation. Finally, by analyzing these 2D photoluminescence lifetime images (e.g., Figures 3.3d, e), the photoluminescence lifetime histogram in each sample was extracted (see Figure S3.8 and Figure 3.3f). Compared with the histograms in Figure S3.6, the broadened ranges and larger overlaps of photoluminescence lifetimes in the histogram in Figure 3.3f were likely attributed to the mixture of the RENPs. Considering the difficult-to-reproduce nature of the all-mixed sample, SWIR-PLIMASC is poised to accurately decrypt complex photoluminescence lifetime-coded information. Benefiting from this delicate topology composed of only three types of RENPs, this anti-counterfeiting design shows potential for a SWIR photoluminescence lifetime-based taggant with a high-security level

3.2.4 Photoluminescence thermometry using SWIR-PLIMASC

The Boltzmann-coupled emission bands in RENPs are highly sensitive to temperature changes.(Avram *et al.*, 2021; Brites *et al.*, 2018b) Leveraging this photoluminescence property, RENPs, as temperature indicators, were teamed up with advanced imaging modalities for remote-detection, minimally invasive, and high-resolution photoluminescence thermometry.(Liu *et al.*, 2021c; Qiu *et al.*, 2020) These advances inspired us to apply SWIR-PLIMASC to photoluminescence lifetime-based thermometry. In particular, the large energy mismatch between Yb^{3+} ($^2F_{5/2}$) and Ho^{3+} ($^5I_6$) provides a strong temperature-induced variation of the phonon-assisted energy transfer from Yb^{3+} to Ho^{3+},(Wortmann *et al.*, 2018) making Yb:Ho@Y RENPs ideal sensitive temperature indicators for SWIR photoluminescence lifetime-based thermometry.

The experimental setup is shown in Figure 3.4a. The temperature of the sample was controlled by a heating plate and double-checked by a Type K thermocouple (Omega, HH306A). SWIR-PLIMASC was applied with a 1D imaging speed of $r_1 = 138.9$ kHz. In the proof-of-concept experiment, SWIR-PLIMASC captured the intensity decay of the Ho^{3+}-doped core-shell RENPs without scattering medium (Figure S3.9). The same analysis applied to the experiments of Er^{3+}-doped RENPs was used here to extract the photoluminescence lifetime of Yb:Ho@Y RENPs. As shown in Figure 3.4b, the photoluminescence lifetime monotonically decreases with temperature from 651.4 μs at 10 °C to 505.0 μs at 60 °C, which is fitted with a linear curve with a slope of S_a = –2.9 μs $°C^{-1}$ and an intercept of 680.0 μs, where S_a denotes the absolute temperature sensitivity (Figure 3.4c). Moreover, we calculated the relative sensitivity S_r (Figure S3.10) and quantified the measured lifetime uncertainty of the optical system (0.32–1.29 % at

room temperature). The details are provided in Supplementary Note 3.3. Finally, to validate the reliability of this technique, we conducted a longitudinal monitoring of temperature cycled between 20 °C to 50 °C for over 30 minutes. As shown in Figure 3.4d, the measured temperatures are in good agreement with the temperature change measured by the thermocouple as the gold standard.

To test SWIR-PLIMASC in a biological environment, a piece of beef tissue with a varied thickness up to 0.94 mm as the absorbing and scattering medium was placed at 1.0 mm above the sample. As shown in Figure 3.4e, SWIR-PLIMASC can accurately image temperature distribution beneath biological tissue. Moreover, we recorded the cooling process of the sample covered by 0.5 mm-thick beef tissue. The temperature of the sample was first increased to about 70 °C. Then, the heating plate was turned off. The SWIR-PLIMASC system continuously captured 80 images to record the photoluminescence lifetime/temperature change. Besides SWIR-PLIMASC, a thermal camera was also used to monitor the temperature evolution. The lifetime/temperature map captured by SWIR-PLIMASC is shown in Figure 3.4f. The averaged curve is plotted in Figure 3.4g, which shows a drastic temperature decrease from 70 °C to 37 °C in the first minute, followed by a much slower decrease to 29 °C as the sample approaches room temperature in 4 minutes. The result also shows excellent agreement with the temperature measured by the thermocouple. In contrast, the measurement from the thermal camera shows considerable errors of up to 40 °C. Detached from the sample, the covered beef tissue was not heated up but was almost kept at room temperature. Only capable of surface temperature sensing, the thermal camera failed to report the temperature of RENPs located beneath the beef tissue. The biological phantom in this experiment served as an analogy to the temperature difference between the skin and the core body. The accurate temperature sensing showcases SWIR-PLIMASC’s advantage over thermal camera-based temperature measurement, indicating the prospect of deep tissue temperature monitoring for potential applications in early cancer theranostics.

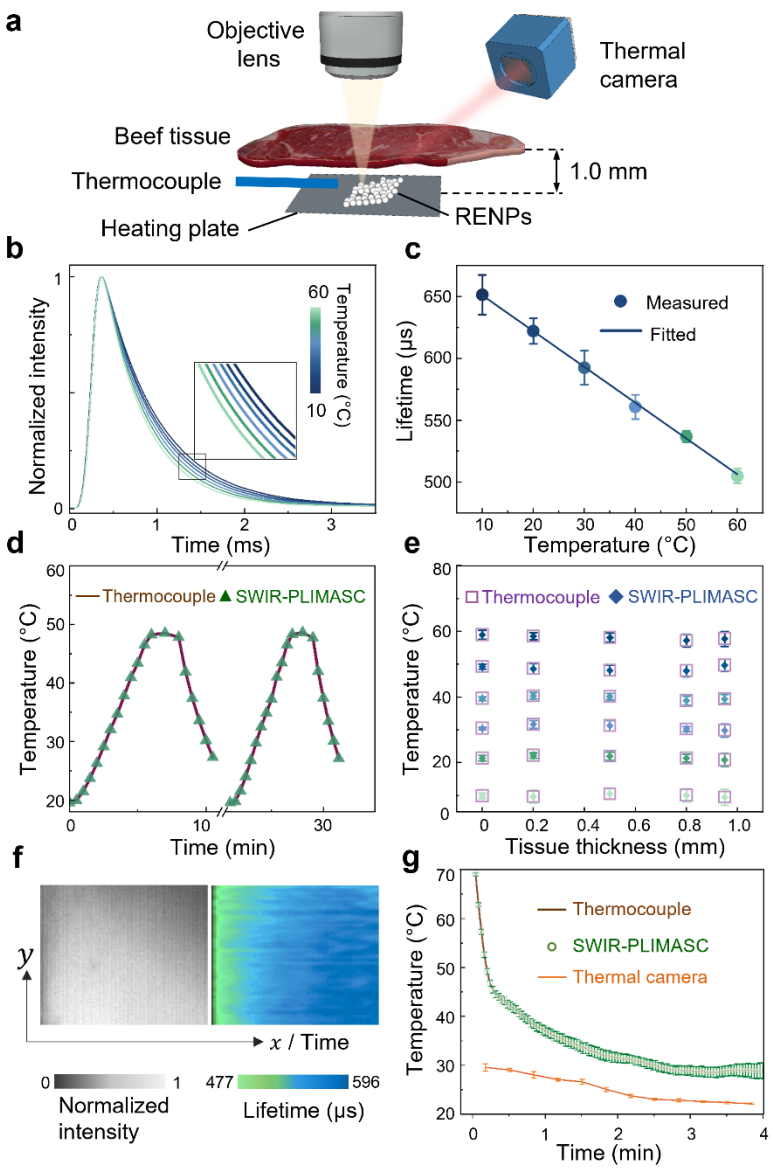

Figure 3.4 Photoluminescence thermometry using SWIR-PLIMASC with $LiYbF_4:Ho^{3+}@LiYF_4$ RENPs.

(a) Schematic representation of the experimental setup. (b) Normalized photoluminescence intensity decays of RENPs from 10 °C to 60 °C. (c) Temperature dependence of the average photoluminescence lifetime of RENPs with linear fitting. (d) Longitudinal temperature monitoring. (e) Temperature sensing from 10 °C to 60 °C underneath beef tissue with different thicknesses. (f) Dynamic temperature mapping through 0.5 mm-thick beef tissue during the cooling of the heating plate. (g) Comparison of temperature sensing ability of SWIR-PLIMASC with the thermal camera. Error bars in (c, e, g): standard deviation.

3.3 Discussion

In summary, we develop SWIR-PLIMASC—an efficient photoluminescence lifetime mapping platform specialized for RENPs in the SWIR spectral range. The implementation of scanning optics endows the InGaAs CMOS camera with a 1D ultrahigh imaging speed of up to 138.9 kHz while allowing it to retain its high sensitivity in the SWIR spectral range, which enables efficient quantification of RENPs' SWIR photoluminescence lifetimes. Combined with the Er^{3+}-doped RENPs, this technique reveals complex topology in photoluminescence lifetime-based taggants, which shows great potential in high-security anti-counterfeiting. Using Ho^{3+}-doped RENPs that present strong temperature dependence, we implement SWIR-PLIMASC in accurate temperature sensing in a biological phantom, demonstrating its superior detection ability compared to conventional thermal imaging.

In the experiments, we have taken the following precautions to minimize the impacts of various photonic effects on the measurement accuracy in SWIR-PLIMASC. First, the results could be affected by noises (e.g., shot noise and readout noise) and background.(Hirsch *et al.*, 2013; van Swieten *et al.*, 2022) To reduce the impact of the shot noise, we optimized the excitation laser power for high SNR acquisition. To mitigate the readout noise, we used 14-bit quantization, a moderate gain in data acquisition, and a relatively low readout bandwidth. We also leveraged three-stage thermoelectric cooling implemented on the camera. To avoid the background, we performed the experiments in a dark room and covered the beam path to eliminate the stray light. Second, the results could be influenced by the local density of optical states (LDOS).(Senden *et al.*, 2015; Vonk *et al.*, 2023) Nonetheless, we used thick RENP layers as the sample, which should largely average any photonic distortions induced by the varying LDOS. Moreover, neither a reflector nor inhomogeneity was present in the vicinity of RENPs to confound the results. Finally, temperature was exacted from the intensity decay of emission, not by the intensity ratio of two emission bands. Thus, considering the photonic artifacts induced by SWIR-emitting RENPs in ratiometric thermometry, SWIR-PLIMASC presents a more suitable modality to accommodate these RENPs for accurate measurement, which can thus fully leverage their deeper penetration advantages in biomedical applications.(Labrador-Páez *et al.*, 2018; Shen *et al.*, 2020; Smith *et al.*, 2009b; van Swieten *et al.*, 2022; van Swieten *et al.*, 2021; Vonk *et al.*, 2023)

The consideration of these photonic effects points to attractive future research directions. First, they could guide the system design and equipment selection to minimize the photonic distortions. Meanwhile, they would be further leveraged in *in-situ* calibration for the temperature

readout in an inhomogeneous environment.(Baffou, 2021; van Swieten *et al.*, 2021) Finally, they could propel the design and fabrication of innovative RENPs with tunable SWIR photoluminescence lifetimes. All these efforts will aid SWIR-PLIMASC, as an advanced characterization technique, for broad applications in information science and biomedicine.

3.4 Experimental methods

Preparation of RENPs precursors. Stoichiometric amounts of RE_2O_3 (RE = Lu, Gd, Yb, Er, Ho) were selectively mixed with 5 mL trifluoroacetic acid and 5 mL distilled water in a 50 mL three-neck round bottom flask. The mixture was kept at 80 °C under vigorous stirring until the solution became clear. The temperature was then reduced to 60 °C to evaporate the residual trifluoroacetic acid and water.

Synthesis of $NaGdF_4$:18% Yb^{3+}, 2% Er^{3+}@$NaGdF_4$. $NaGdF_4$:18% Yb^{3+}, 2% Er^{3+} core RENPs were synthesized via the hot injection thermolysis approach. Specifically, the precursor $(CF_3COO)_3RE$ (RE = Gd/Yb/Er) and CF_3COONa were dispersed in Solution A0 [containing 7.5 mL of 1-octadecene (ODE) and 7.5 mL of oleic acid (OA)] and degassed at 125 °C under vigorous stirring. Then, Solution A0 was injected into the preheated mixture of 12.5 mL of OA and 12.5 mL of ODE (Solution B0) at a rate of 1.5 mL min^{-1} (Harvard Apparatus Pump 11 Elite). The final solution was kept at 315 °C under an argon atmosphere for 1 hour to get core RENPs. The core-shell structure was prepared by epitaxial growth of the shell on the performed cores. 0.5 mmol of core RENPs were mixed with 10 mL of OA and 10 mL of ODE (Solution A1). 2 mmol shell precursors $(CF_3COO)_3Gd$ together with CF_3COOLi were mixed with 10 mL of OA and 10 mL of ODE (Solution B1). Solution A1 and B1 were both degassed at 110 °C for 30 minutes. After degassing, Solution A1 was heated to 290 °C. Solution B1 was injected into Solution A1 at a 0.75 mL min^{-1} rate when the temperature of Solution A1 was stable. After cooling down to room temperature, the final product was washed with hexane/ethanol (1:3) three times and re-dispersed in hexane.

Synthesis of $LiYbF_4$:18% Yb^{3+}, 2% Er^{3+}/Ho^{3+}@$LiYF_4$ and $LiLuF_4$:18% Yb^{3+}, 2% Er^{3+}@$LiLuF_4$. These RENPs were prepared via a two-step thermal decomposition method from the first nuclei to the core RENPs. A mixture of 7 mL of OA, 7 mL of oleylamine (OM), and 14 mL ODE (Solution A2) was degassed at 110 °C for 15 min and then heated to 330 °C under an argon

atmosphere. Meanwhile, 2.5 mmol CF_3COOLi and $(CF_3COO)_3RE$ (RE = Lu/Yb, Er/Ho) were mixed with 3 mL OA and 6 mL ODE (Solution B2) and then degassed at 125 °C for 30 min. 3 mL of OM was added in Solution B2 and left to degas for 5 min. Once the temperature of Solution A2 was stable, Solution B2 was injected into Solution A2 with a rate of 1.5 mL min^{-1}. After a one-hour reaction at 330 °C, the preparation of the first nuclei was finished. Core RENPs were formed by stabilizing first nuclei with an excess of OA. 1.25 mmol first nuclei were mixed with 16 mL of OA and 16 mL of ODE in a 100 mL three-neck round bottom flask. The solution was degassed at 110 °C for 30 minutes and backfilled with argon gas. The temperature was raised to 315 °C, after which the reaction was continued for 1 hour.

Core-shell RENPs were prepared by using the same method mentioned above except for the rare-earth source. The only difference was the reaction time. After each ~7 mL injection of solution B1 to solution A1, the mixture was allowed to react for 40 minutes.

Supporting Information

Supporting Information is available from the Wiley Online Library or the authors.

Acknowledgements

This work was supported in part by Natural Sciences and Engineering Research Council of Canada (RGPIN-2017-05959, RGPIN-2018-06217, RGPAS-2017-507845, RGPAS-2018-522650, I2IPJ-555593-20); Canada Research Chair Programs (CRC-2022-00119); Canada Foundation for Innovation and Ministère de l'Économie et de l'Innovation du Québec (37146); Canadian Cancer Society (707056); New Frontiers in Research Fund (NFRFE-2020-00267); Fonds de Recherche du Québec–Nature et Technologies (203345–Centre d'Optique, Photonique, et Lasers; 203321-Centre québécois sur les matériaux fonctionnels/Québec Centre for Advanced Materials; 255545-Projet de recherche en équipe); Fonds de Recherche du Québec–Santé (267406, 280229).

Conflict of Interest

The authors declare no conflict of interest.

Data Availability Statement

The data that support the findings of this study are available from the corresponding author upon reasonable request.

Keywords

short-wave infrared, rare-earth doped nanoparticles, anti-counterfeiting, lifetime-based photoluminescence nanothermometry, ultrahigh-speed imaging

3.5 References

Auzel F, Malta OL (1983) A scalar crystal field strength parameter for rare-earth ions : meaning and usefulness. *J. Phys. France* 44(2):201-206.

Avram D, Porosnicu I, Patrascu A, Tiseanu C (2021) Real-Time Thermal Imaging based on the Simultaneous Rise and Decay Luminescence Lifetime Thermometry. *Adv. Photonics Res.* 3(6).

Baffou G (2021) Anti-Stokes Thermometry in Nanoplasmonics. *ACS Nano* 15(4):5785-5792.

Brites CDS, Balabhadra S, Carlos LD (2018b) Lanthanide-Based Thermometers: At the Cutting-Edge of Luminescence Thermometry. *Adv. Opt. Mater.* 7(5).

Bruschini C, Homulle H, Antolovic IM, Burri S, Charbon E (2019) Single-photon avalanche diode imagers in biophotonics: review and outlook. *Light Sci. Appl.* 8:87.

Chen G, Ågren H, Ohulchanskyy TY, Prasad PN (2015b) Light upconverting core–shell nanostructures: nanophotonic control for emerging applications. *Chem. Soc. Rev.* 44(6):1680-1713.

Chen Y, Wang S, Zhang F (2023b) Near-infrared luminescence high-contrast in vivo biomedical imaging. *Nat. Rev. Bioeng.* 1(1):60-78.

Cheng T, Marin R, Skripka A, Vetrone F (2018b) Small and Bright Lithium-Based Upconverting Nanoparticles. *J. Am. Chem. Soc.* 140(40):12890-12899.

Fan Y, Wang P, Lu Y, Wang R, Zhou L, Zheng X, Li X, Piper JA, Zhang F (2018) Lifetime-Engineered NIR-II Nanoparticles Unlock Multiplexed In Vivo Imaging. *Nat. Nanotechnol.* 13(10):941-946.

Fincham JE (2014) Counterfeit Medications and Their Negative Impacts on Health Care. *Am. J. Pharm. Educ.* 78(3):48.

Fink C, Maskus KE, Qian Y (2015) The Economic Effects of Counterfeiting and Piracy: A Review and Implications for Developing Countries. *The World Bank Research Observer* 31(1):1-28.

Goh Y, Kim J, Park HS, Jung T, Hong KS, Nam SH, Suh YD, Lee KT (2022) Visualization of intercellular cargo transfer using upconverting nanoparticles. *Nanoscale* 14(38):14008-14013.

Golovynskyi S, Golovynska I, Stepanova LI, Datsenko OI, Liu L, Qu J, Ohulchanskyy TY (2018) Optical windows for head tissues in near-infrared and short-wave infrared regions: Approaching transcranial light applications. *J Biophotonics* 11(12):e201800141.

Haase M, Schafer H (2011) Upconverting nanoparticles. *Angew. Chem. Int. Ed.* 50(26):5808-5829.

Hazra C, Skripka A, Ribeiro SJL, Vetrone F (2020b) Erbium Single-Band Nanothermometry in the Third Biological Imaging Window: Potential and Limitations. *Adv. Opt. Mater.* 8(23).

Hehlen MP, Brik MG, Krämer KW (2013) 50th anniversary of the Judd–Ofelt theory: An experimentalist's view of the formalism and its application. *J. Lumin.* 136:221-239.

Hemmer E, Benayas A, Légaré F, Vetrone F (2016a) Exploiting the biological windows: current perspectives on fluorescent bioprobes emitting above 1000 nm. *Nanoscale Horiz.* 1(3):168-184.

Hirsch M, Wareham RJ, Martin-Fernandez ML, Hobson MP, Rolfe DJ (2013) A stochastic model for electron multiplication charge-coupled devices--from theory to practice. *PLoS One* 8(1):e53671.

Homulle HA, Powolny F, Stegehuis PL, Dijkstra J, Li DU, Homicsko K, Rimoldi D, Muehlethaler K, Prior JO, Sinisi R, Dubikovskaya E, Charbon E, Bruschini C (2016) Compact solid-state CMOS single-photon detector array for in vivo NIR fluorescence lifetime oncology measurements. *Biomed. Opt. Express* 7(5):1797-1814.

Hong G, Lee JC, Robinson JT, Raaz U, Xie L, Huang NF, Cooke JP, Dai H (2012) Multifunctional in vivo vascular imaging using near-infrared II fluorescence. *Nat. Med.* 18(12):1841-1846.

Jalani G, Naccache R, Rosenzweig DH, Lerouge S, Haglund L, Vetrone F, Cerruti M (2015) Real-time, non-invasive monitoring of hydrogel degradation using LiYF4:Yb3+/Tm3+ NIR-to-NIR upconverting nanoparticles. *Nanoscale* 7(26):11255-11262.

Jiang X, Cao C, Feng W, Li F (2016) Nd3+-doped LiYF4 nanocrystals for bio-imaging in the second near-infrared window. *J. Mater. Chem. B* 4(1):87-95.

Judd BR (1962a) Optical Absorption Intensities of Rare-Earth Ions. *Phys. Rev.* 127:750-761.

Kenry, Duan Y, Liu B (2018) Recent Advances of Optical Imaging in the Second Near-Infrared Window. *Adv. Mater.* 30(47):e1802394.

Kong M, Gu Y, Liu Y, Shi Y, Wu N, Feng W, Li F (2019) Luminescence Lifetime-Based In Vivo Detection with Responsive Rare Earth-Dye Nanocomposite. *Small* 15(46):e1904487.

Krishnan RV, Biener E, Zhang J-H, Heckel R, Herman B (2003a) Probing subtle fluorescence dynamics in cellular proteins by streak camera based fluorescence lifetime imaging microscopy. *Appl. Phys. Lett.* 83(22):4658-4660.

Krishnan RV, Saitoh H, Terada H, Centonze VE, Herman B (2003b) Development of a multiphoton fluorescence lifetime imaging microscopy system using a streak camera. *Rev. Sci. Instrum.* 74(5):2714-2721.

Labrador-Páez L, Pedroni M, Speghini A, García-Solé J, Haro-González P, Jaque D (2018) Reliability of rare-earth-doped infrared luminescent nanothermometers. *Nanoscale* 10(47):22319-22328.

Li H, Tan M, Wang X, Li F, Zhang Y, Zhao L, Yang C, Chen G (2020a) Temporal Multiplexed in Vivo Upconversion Imaging. *J. Am. Chem. Soc.* 142(4):2023-2030.

Liang J, Zhu L, Wang LV (2018) Single-shot real-time femtosecond imaging of temporal focusing. *Light Sci. Appl.* 7:42.

Liu G (2015) Advances in the theoretical understanding of photon upconversion in rare-earth activated nanophosphors. *Chem. Soc. Rev.* 44(6):1635-1652.

Liu M, Shi Z, Wang X, Zhang Y, Mo X, Jiang R, Liu Z, Fan L, Ma CG, Shi F (2018b) Simultaneous enhancement of red upconversion luminescence and CT contrast of NaGdF(4):Yb,Er nanoparticles via Lu(3+) doping. *Nanoscale* 10(43):20279-20288.

Liu X, Lin D, Becker W, Niu J, Yu B, Liu L, Qu J (2019) Fast fluorescence lifetime imaging techniques: A review on challenge and development. *J. Innov. Opt. Heal. Sci.* 12(05).

Liu X, Monteiro J, Albuquerque I, Lai Y, Jiang C, Zhang S, Falk TH, Liang J (2021a) Single-shot real-time compressed ultrahigh-speed imaging enabled by a snapshot-to-video autoencoder. *Photon. Res.* 9(12).

Liu X, Skripka A, Lai Y, Jiang C, Liu J, Vetrone F, Liang J (2021c) Fast wide-field upconversion luminescence lifetime thermometry enabled by single-shot compressed ultrahigh-speed imaging. *Nat. Commun.* 12(1):6401.

Lu Y, Zhao J, Zhang R, Liu Y, Liu D, Goldys EM, Yang X, Xi P, Sunna A, Lu J, Shi Y, Leif RC, Huo Y, Shen J, Piper JA, Robinson JP, Jin D (2013) Tunable lifetime multiplexing using luminescent nanocrystals. *Nat. Photon.* 8(1):32-36.

Ma Y, Bao J, Zhang Y, Li Z, Zhou X, Wan C, Huang L, Zhao Y, Han G, Xue T (2019) Mammalian Near-Infrared Image Vision through Injectable and Self-Powered Retinal Nanoantennae. *Cell* 177(2):243-255 e215.

Maeda T, Oishi K, Ishii H, Chang WH, Shimizu T, Endoh A, Fujishiro H, Koida T (2021) High and broadband sensitivity front-side illuminated InGaAs photo field-effect transistors (photoFETs) with SWIR transparent conductive oxide (TCO) gate. *Appl. Phys. Lett.* 119(19).

Malchow D, Battaglia J, Brubaker R, Ettenberg M (2007) High speed short wave infrared (SWIR) imaging and range gating cameras. in *Thermosense XXIX*).

Matulionyte M, Skripka A, Ramos-Guerra A, Benayas A, Vetrone F (2023) The Coming of Age of Neodymium: Redefining Its Role in Rare Earth Doped Nanoparticles. *Chem. Rev.* 123(1):515-554.

Ofelt GS (2004) Intensities of Crystal Spectra of Rare-Earth Ions. *J. Chem. Phys.* 37(3):511-520.

Ortgies DH, Tan M, Ximendes EC, Del Rosal B, Hu J, Xu L, Wang X, Martin Rodriguez E, Jacinto C, Fernandez N, Chen G, Jaque D (2018) Lifetime-Encoded Infrared-Emitting Nanoparticles for in Vivo Multiplexed Imaging. *ACS Nano* 12(5):4362-4368.

Parfenov PS, Litvin AP, Onishchuk DA, Gonchar KA, Berwick K, Fedorov AV, Baranov AV (2020) The Effect of High Background and Dead Time of an InGaAs/InP Single-Photon Avalanche Photodiode on the Registration of Microsecond Range Near-Infrared Luminescence. *Opt. Spectrosc.* 128(5):674-677.

Pavia JM, Wolf M, Charbon E (2014) Measurement and modeling of microlenses fabricated on single-photon avalanche diode arrays for fill factor recovery. *Opt. Express* 22(4):4202-4213.

Pickel AD, Teitelboim A, Chan EM, Borys NJ, Schuck PJ, Dames C (2018b) Apparent self-heating of individual upconverting nanoparticle thermometers. *Nat. Commun.* 9(1):4907.

Pini F, Frances-Soriano L, Andrigo V, Natile MM, Hildebrandt N (2023) Optimizing Upconversion Nanoparticles for FRET Biosensing. *ACS Nano* 17(5):4971-4984.

Qiu X, Zhou Q, Zhu X, Wu Z, Feng W, Li F (2020) Ratiometric Upconversion Nanothermometry with Dual Emission at the Same Wavelength Decoded via a Time-Resolved Technique. *Nat. Commun.* 11(1):4.

Rabouw FT, Prins PT, Villanueva-Delgado P, Castelijns M, Geitenbeek RG, Meijerink A (2018) Quenching Pathways in NaYF(4):Er(3+),Yb(3+) Upconversion Nanocrystals. *ACS Nano* 12(5):4812-4823.

Ren W, Lin G, Clarke C, Zhou J, Jin D (2020) Optical Nanomaterials and Enabling Technologies for High-Security-Level Anticounterfeiting. *Adv. Mater.* 32(18):e1901430.

Riseberg LA, Moos HW (1968) Multiphonon Orbit-Lattice Relaxation of Excited States of Rare-Earth Ions in Crystals. *Phys. Rev.* 174(2):429-438.

Roy S, Curry SD, Corbella Bagot C, Mueller EN, Mansouri AM, Park W, Cha JN, Goodwin AP (2022) Enzyme Prodrug Therapy with Photo-Cross-Linkable Anti-EGFR Affibodies Conjugated to Upconverting Nanoparticles. *ACS Nano* 16(10):15873-15883.

Senden T, Rabouw FT, Meijerink A (2015) Photonic Effects on the Radiative Decay Rate and Luminescence Quantum Yield of Doped Nanocrystals. *ACS Nano* 9(2):1801-1808.

Shen Y, Lifante J, Fernandez N, Jaque D, Ximendes E (2020) In Vivo Spectral Distortions of Infrared Luminescent Nanothermometers Compromise Their Reliability. *ACS Nano* 14(4):4122-4133.

Shen Y, Lifante J, Zabala-Gutierrez I, de la Fuente-Fernandez M, Granado M, Fernandez N, Rubio-Retama J, Jaque D, Marin R, Ximendes E, Benayas A (2022b) Reliable and Remote Monitoring of Absolute Temperature during Liver Inflammation via Luminescence-Lifetime-Based Nanothermometry. *Adv. Mater.* 34(7):e2107764.

Skripka A, Benayas A, Brites CDS, Martin IR, Carlos LD, Vetrone F (2020a) Inert Shell Effect on the Quantum Yield of Neodymium-Doped Near-Infrared Nanoparticles: The Necessary Shield in an Aqueous Dispersion. *Nano Lett.* 20(10):7648-7654.

Smith AM, Mancini MC, Nie S (2009a) Bioimaging: second window for in vivo imaging. *Nat. Nanotechnol.* 4(11):710-711.

Smith AM, Mancini MC, Nie S (2009b) Bioimaging: second window for in vivo imaging. *Nat Nanotechnol* 4(11):710-711.

Tan H, Gong G, Xie S, Song Y, Zhang C, Li N, Zhang D, Xu L, Xu J, Zheng J (2019) Upconversion Nanoparticles@Carbon Dots@Meso-SiO(2) Sandwiched Core-Shell Nanohybrids with Tunable Dual-Mode Luminescence for 3D Anti-Counterfeiting Barcodes. *Langmuir* 35(35):11503-11511.

Tan M, Li F, Cao N, Li H, Wang X, Zhang C, Jaque D, Chen G (2020b) Accurate In Vivo Nanothermometry through NIR-II Lanthanide Luminescence Lifetime. *Small* 16(48):e2004118.

van Swieten TP, Meijerink A, Rabouw FT (2022) Impact of Noise and Background on Measurement Uncertainties in Luminescence Thermometry. *ACS Photonics* 9(4):1366-1374.

van Swieten TP, van Omme T, van den Heuvel DJ, Vonk SJW, Spruit RG, Meirer F, Garza HHP, Weckhuysen BM, Meijerink A, Rabouw FT, Geitenbeek RG (2021) Mapping

Elevated Temperatures with a Micrometer Resolution Using the Luminescence of Chemically Stable Upconversion Nanoparticles. *ACS Appl Nano Mater* 4(4):4208-4215.

Vonk SJW, van Swieten TP, Cocina A, Rabouw FT (2023) Photonic Artifacts in Ratiometric Luminescence Nanothermometry. *Nano Lett* 23(14):6560-6566.

Walsh BM, Barnes NP, Di Bartolo B (1998) Branching ratios, cross sections, and radiative lifetimes of rare earth ions in solids: Application to Tm3+ and Ho3+ ions in LiYF4. *J. Appl. Phys.* 83(5):2772-2787.

Wang C, Cheng Z, Gan W, Cui M (2020a) Line scanning mechanical streak camera for phosphorescence lifetime imaging. *Opt. Express* 28(18):26717-26723.

Wang F, Liu X (2009) Recent advances in the chemistry of lanthanide-doped upconversion nanocrystals. *Chem. Soc. Rev.* 38(4):976-989.

Wang P, Liang J, Wang LV (2020b) Single-shot ultrafast imaging attaining 70 trillion frames per second. *Nat. Commun.* 11(1):2091.

Wang X-d, Wolfbeis OS, Meier RJ (2013a) Luminescent probes and sensors for temperature. *Chem. Soc. Rev.* 42(19):7834-7869.

Wawrzynczyk D, Bednarkiewicz A, Nyk M, Strek W, Samoc M (2012) Neodymium(iii) doped fluoride nanoparticles as non-contact optical temperature sensors. *Nanoscale* 4(22):6959-6961.

Wortmann L, Suyari S, Ube T, Kamimura M, Soga K (2018) Tuning the thermal sensitivity of β-NaYF4: Yb3+, Ho3+, Er3+ nanothermometers for optimal temperature sensing in OTN-NIR (NIR II/III) biological window. *J. Lumin.* 198:236-242.

Wu L, Jia M, Li D, Chen G (2023) Shell Engineering on Thermal Sensitivity of Lifetime-Based NIR Nanothermometers for Accurate Temperature Measurement in Murine Internal Liver Organ. *Nano Letters* 23(7):2862-2869.

Wurth C, Fischer S, Grauel B, Alivisatos AP, Resch-Genger U (2018) Quantum Yields, Surface Quenching, and Passivation Efficiency for Ultrasmall Core/Shell Upconverting Nanoparticles. *J. Am. Chem. Soc.* 140(14):4922-4928.

Yoon B, Lee J, Park IS, Jeon S, Lee J, Kim J-M (2013) Recent functional material based approaches to prevent and detect counterfeiting. *J. Mater. Chem. C* 1(13):2388-2403.

Zappa F, Tisa S, Tosi A, Cova S (2007) Principles and features of single-photon avalanche diode arrays. *Sensors and Actuators A* 140(1):103-112.

Zhang C, Zhou HP, Liao LY, Feng W, Sun W, Li ZX, Xu CH, Fang CJ, Sun LD, Zhang YW, Yan CH (2010) Luminescence modulation of ordered upconversion nanopatterns by a photochromic diarylethene: rewritable optical storage with nondestructive readout. *Adv. Mater.* 22(5):633-637.

Zhang J, Itzler MA, Zbinden H, Pan J-W (2015) Advances in InGaAs/InP single-photon detector systems for quantum communication. *Light Sci. Appl.* 4(5):e286-e286.

Zhong Y, Ma Z, Zhu S, Yue J, Zhang M, Antaris AL, Yuan J, Cui R, Wan H, Zhou Y, Wang W, Huang NF, Luo J, Hu Z, Dai H (2017a) Boosting the down-shifting luminescence of rare-earth nanocrystals for biological imaging beyond 1500 nm. *Nat. Commun.* 8(1):737.

Zhou T, Ohulchanskyy TY, Qu J (2021) Effect of NIR light on the permeability of the blood-brain barriers in in vitro models. *Biomedical Optics Express* 12(12):7544-7555.

Zhu X, Wang X, Zhang H, Zhang F (2022) Luminescence Lifetime Imaging Based on Lanthanide Nanoparticles. *Angew. Chem. Int. Ed.* 61(42):e202209378.

Ziniuk R, Yakovliev A, Li H, Chen G, Qu J, Ohulchanskyy TY (2021) Real-Time Imaging of Short-Wave Infrared Luminescence Lifetimes for Anti-counterfeiting Applications. *Front. Chem.* 9:659553.

Supporting Information

Short-wave infrared photoluminescence lifetime mapping of rare-earth doped nanoparticles using all-optical streak imaging

Miao Liu, Yingming Lai, Miguel Marquez, Fiorenzo Vetrone, Jinyang Liang**

Centre Énergie Matériaux Télécommunications, Institut National de la Recherche Scientifique, Université du Québec, 1650 boulevard Lionel-Boulet, Varennes, Québec J3X 1P7, CANADA

Corresponding authors: Fiorenzo.Vetrone@inrs.ca (F.V.), Jinyang.Liang@inrs.ca (J.L.)

Materials

Gd_2O_3 (REacton 99.999%), Lu_2O_3 (REacton, 99.999%), Yb_2O_3 (REacton, 99.998%), Er_2O_3 (REacton, 99.99%), Ho_2O_3 (REacton, 99.997%), 1-octadecene (ODE, 90%), and oleic acid (OA, 90%) were purchased from Alfa Aesar (USA). Lithium trifluoroacetate (98%), sodium trifluoroacetate (98%), oleylamine (OM, 70%), and trifluoroacetic acid (TFA, 99%) were purchased from Sigma-Aldrich. All chemicals were used as received.

Characterization

Structural Characterization. The crystallinity and phases of the core and core-shell rare-earth doped nanoparticles (RENPs) were determined via X-ray powder diffraction analysis on a Bruker D8 Advance Diffractometer (USA) using Cu Kα radiation (l=1.5418 Å). The morphology and size distribution of the core and core-shell structures were further investigated by transmission electron microscopy (TEM, Philips Tecnai 12, USA). The particle size was determined from TEM images using ImageJ software with a minimal set size of 100 particles.

Optical Characterization. Upconversion and downshifting spectra of oleate-capped RENPs in hexane were obtained at room temperature under the excitation of a 980-nm laser (MDL-SN-980-10W, CNI, China). Laser power and power density were about 490 mW and 8.0 W/cm^2, respectively. All spectra were measured in a quartz cuvette of 1 cm optical path, filled with 2 mL of RENPs at 10 mg/mL concentration. The upconversion emission was recorded with an Avaspec-ULS2048L spectrometer (Avantes, The Netherlands). Stray light from the excitation

source was removed with an 830-nm short-pass filter. The downshifting emission was collected with a Shamrock 500i monochromator (Andor, Ireland) equipped with an iDus InGaAs 1.7 NIR detector (Andor, Ireland). A 980-nm long-pass filter was used to remove any stray light from the excitation source.

Supplementary Note 3.1: Background of the photoluminescence lifetime of rare-earth doped nanoparticles

The photoluminescence lifetime of RENPs, denoted by τ, is determined by

$$\tau = \frac{1}{W_{\mathrm{R}} + W_{\mathrm{NR}}}. \tag{S3.1}$$

Here, W_{R} is the radiative transition rate, and W_{NR} refers to the non-radiative transition rate.

According to the Judd-Ofelt theory, the rate of relaxation from an initial state J to the final state J' through the radiative transition is determined by (Liu, 2015)

$$W_{\mathrm{R}}(J, J') = \frac{64\pi^2\Delta^3}{3h(2J+1)}(\chi\bar{F}^2 + n^3\bar{M}^2). \tag{S3.2}$$

Here, Δ is the energy gap between J and J'. h is the Planck constant. $\chi = n(n^2+2)^2/9$ is the Lorentz correction for the local field with n being the refractive index of the host material. $\bar{F}^2$ and $\bar{M}^2$ are the matrix elements of the electric dipole and magnetic dipole moments, respectively (Hehlen *et al.*, 2013; Judd, 1962a; Ofelt, 2004).

The non-radiative transition rate W_{NR} is related to temperature T via the Arrhenius equation (Riseberg *et al.*, 1968; Wang *et al.*, 2013a)

$$W_{\mathrm{NR}} \propto \exp(-\Delta E/kT). \tag{S3.3}$$

Here, ΔE is the energy gap between the lowest level of the excited states and a possible non-radiative decay state. k is the Boltzmann constant.

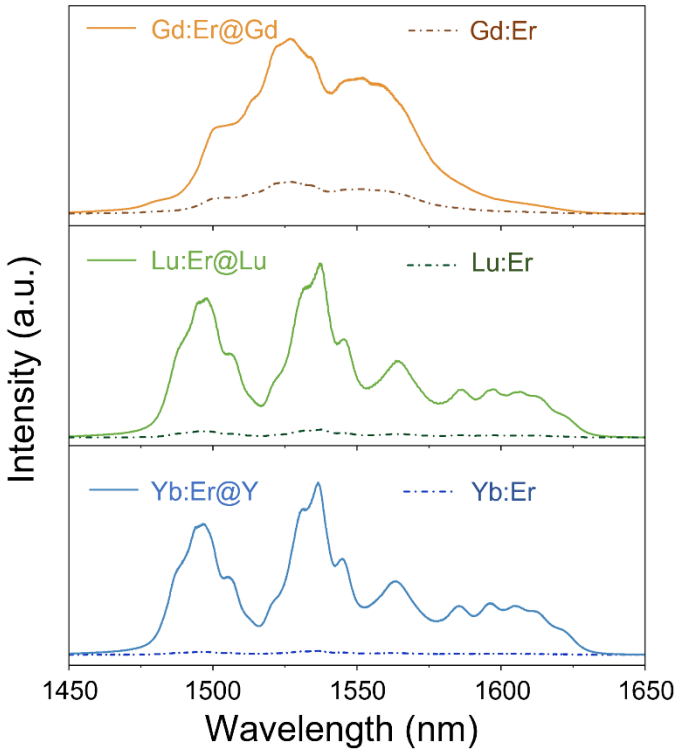

Figure S3.1 **Short-wavelength infrared (SWIR) spectra of the core and the corresponding core-shell RENPs under 980-nm excitation.**

$NaGdF_4$:Yb^{3+}, Er^{3+} (Gd:Er); $NaGdF_4$:Yb^{3+}, Er^{3+}@$NaGdF_4$ (Gd:Er@Gd); $LiLuF_4$:Yb^{3+}, Er^{3+} (Lu:Er); $LiLuF_4$:Yb^{3+}, Er^{3+}@$LiLuF_4$ (Lu:Er@Lu); $LiYbF_4$:Er^{3+} (Yb:Er); $LiYbF_4$:Er^{3+}@$LiYF_4$ (Yb:Er@Y).

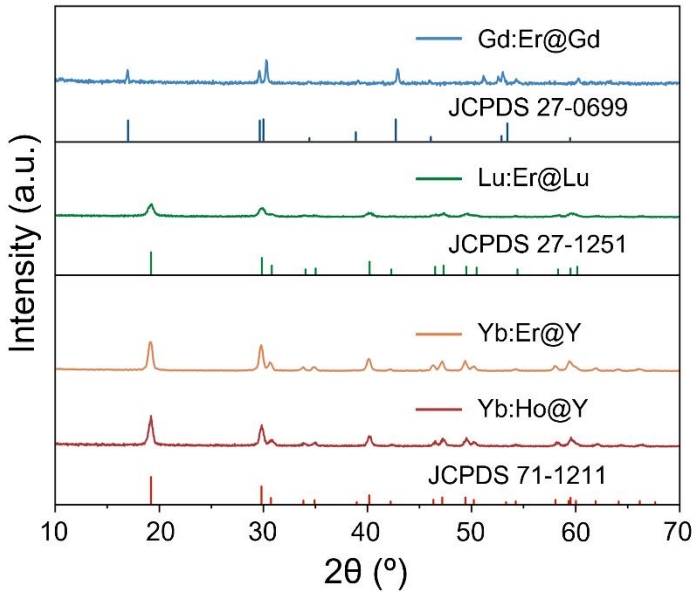

Figure S3.2 **X-ray diffraction patterns of the core-shell RENPs.**

$NaGdF_4$:Yb^{3+}, Er^{3+}@$NaGdF_4$ (Gd:Er@Gd); $LiLuF_4$:Yb^{3+}, Er^{3+}@$LiLuF_4$ (Lu:Er@Lu); $LiYbF_4$:Er^{3+}@$LiYF_4$ (Yb:Er@Y); $LiYbF_4$:Ho^{3+}@$LiYF_4$ (Yb:Ho@Y).

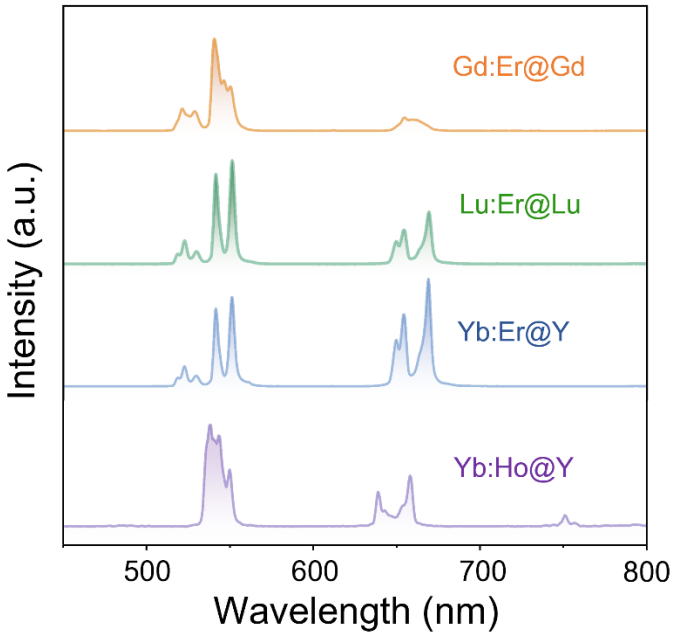

Figure S3.3 **Upconversion photoluminescence spectra of core-shell RENPs under 980-nm excitation.** **$NaGdF_4:Yb^{3+}$, Er^{3+}@$NaGdF_4$ (Gd:Er@Gd); $LiLuF_4:Yb^{3+}$, Er^{3+}@$LiLuF_4$ (Lu:Er@Lu); $LiYbF_4:Er^{3+}$@$LiYF_4$ (Yb:Er@Y); $LiYbF_4:Ho^{3+}$@$LiYF_4$ (Yb:Ho@Y).**

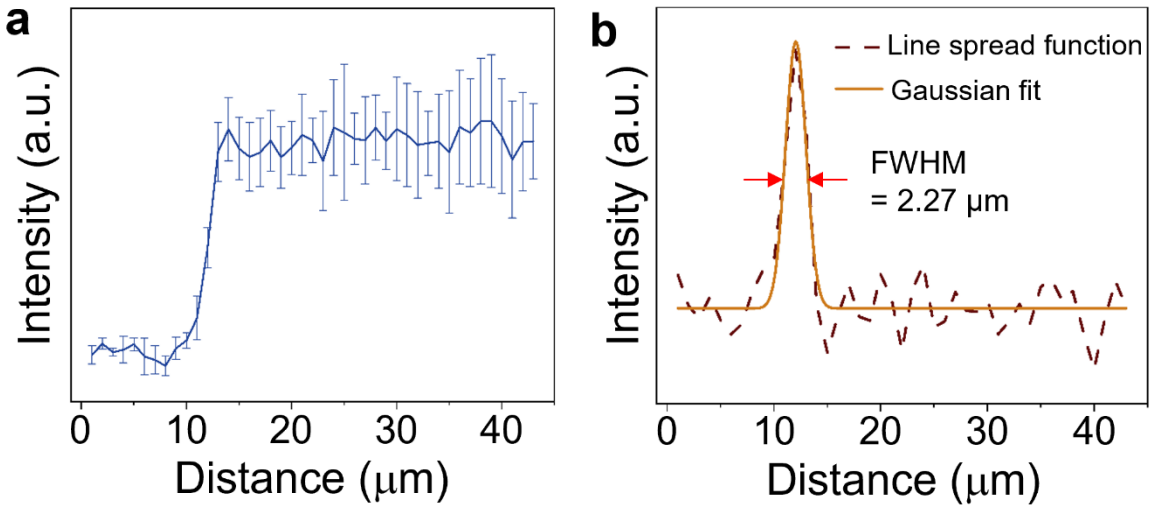

Figure S3.4 **Quantification of spatial resolution of SWIR photoluminescence lifetime imaging microscopy using an all-optical streak camera (PLIMASC).**

(a) Edge spread function extracted from an edge on a USAF resolution target. Error bar: standard deviation. (b) Line spread function produced from (a) with a Gaussian fit. FWHM: Full width at half maximum.

Supplementary Note 3.2: Determination of the photoluminescence lifetime of the RENP sample

The determination of photoluminescence lifetimes synthetically considers the excitation pulse profile [denoted by $I_{\mathrm{pulse}}(t)$] and the finite width of the slit [denoted by $I_{\mathrm{slit}}(t)$]. In particular, the measured intensity decay can be deduced from the convolution

$$I(t) = I_{\mathrm{pulse}}(t) * I_{\mathrm{slit}}(t) * O(t), \tag{S3.4}$$

where $O(t) = \exp(-t/\tau)$ represents the mono-exponential function with a lifetime of τ. In this work, $I_{\mathrm{pulse}}(t)$ is measured by a photodiode, and $I_{\mathrm{slit}}(t)$ is extracted from the static slit image. Then, $I(t)$ is computed and used to fit the experimental result.

Figure S3.5 shows the photoluminescence lifetime extraction. The excitation pulse width was measured to be 200 μs. $I_{\mathrm{pulse}}(t)$ was produced after filtering the noise and cleaning the background (Figure S3.5a). In addition, the static slit image was averaged in the y direction (see an example in Figure 3.2e in Main Text) to produce a line profile (Figure S3.5b). Using the shearing relation [i.e., 97.6 μs/pixel (see Section 3.2.2 in Main Text)], the spatial pixels were converted to time bins, which produced $I_{\mathrm{slit}}(t)$. As an example, the normalized average photoluminescence intensity decay curve of Gd:Er@Gd (see Figure 3.3b in Main Text) and the fit are plotted in Figure S3.5c. Its corresponding semi-log plot is shown in Figure S3.5d. The lifetime of Gd:Er@Gd was determined by the fitted $I(t)$ that gave the highest R-squared value. For this sample, its photoluminescence lifetime was determined to be 3.59 ms (with R^2 = 0.9821). Finally, the semi-log plots of the normalized average photoluminescence intensity decay of Lu:Er@Lu, and Yb:Er@Y RENPs (see Figure 3.3b in Main Text) are shown in Figures S3.5e–f.

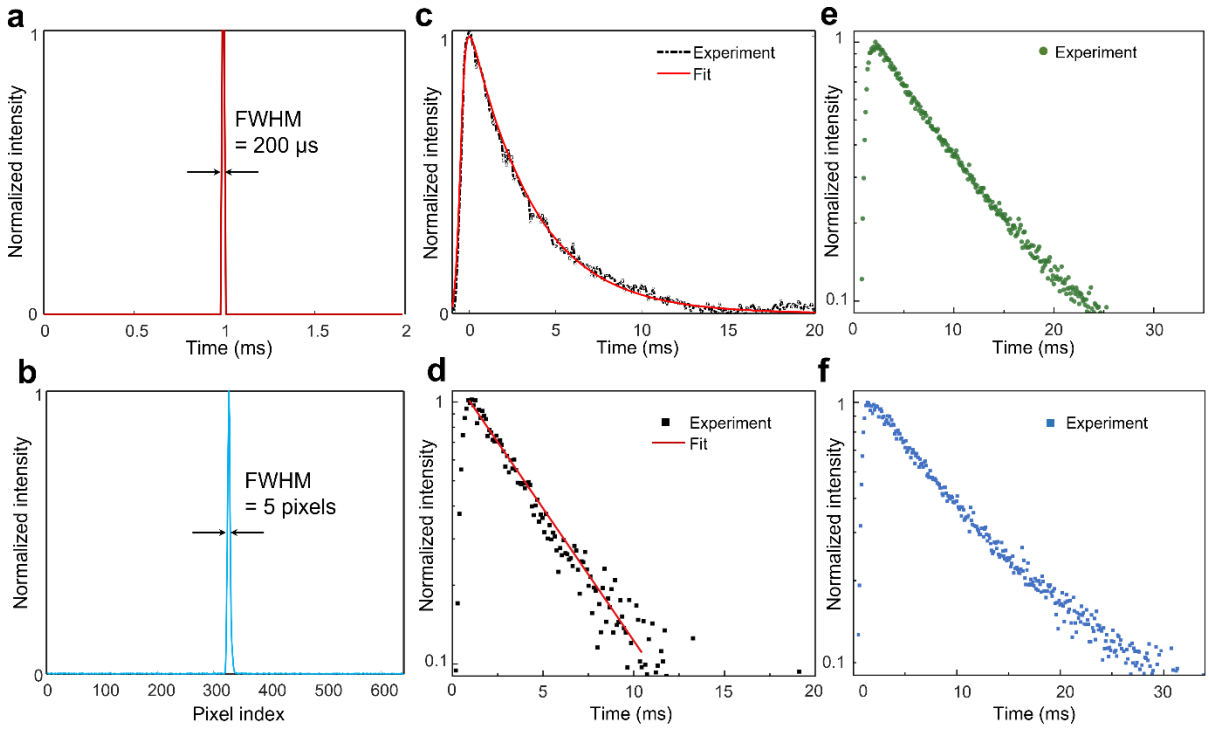

Figure S3.5 Determination of photoluminescence lifetime for Gd:Er@Gd RENP samples.

(a) Normalized excitation pulse profile. (b) Averaged spatial profile of the slit. (c) Measured photoluminescence intensity decay of Gd:Er@Gd with the fit. (d) As (c), but plotted in the logarithmic scale. (e)–(f) As (d), but showing the results of Lu:Er@Lu (e) and Yb:Er@Y (f).

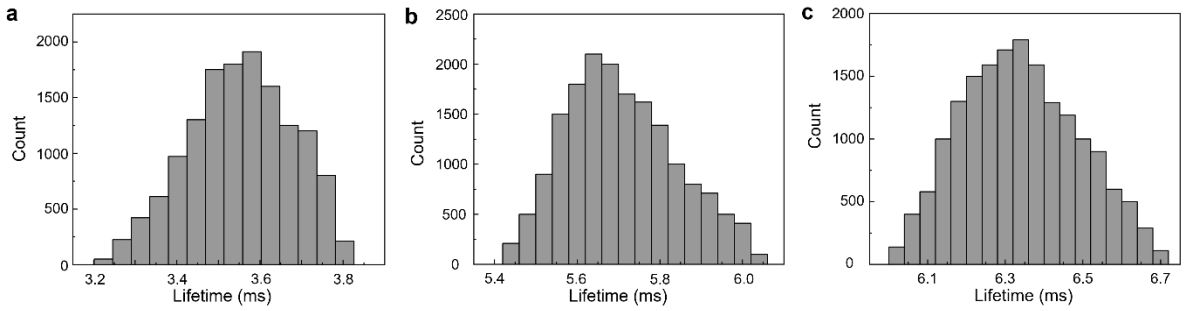

Figure S3.6 Photoluminescence lifetime histograms of RENPs corresponding to Figure 3c.

(a) Gd:Er@Gd (i.e., S1). (b) Lu:Er@Lu (i.e., S2). (c) Yb:Er@Y (i.e., S3).

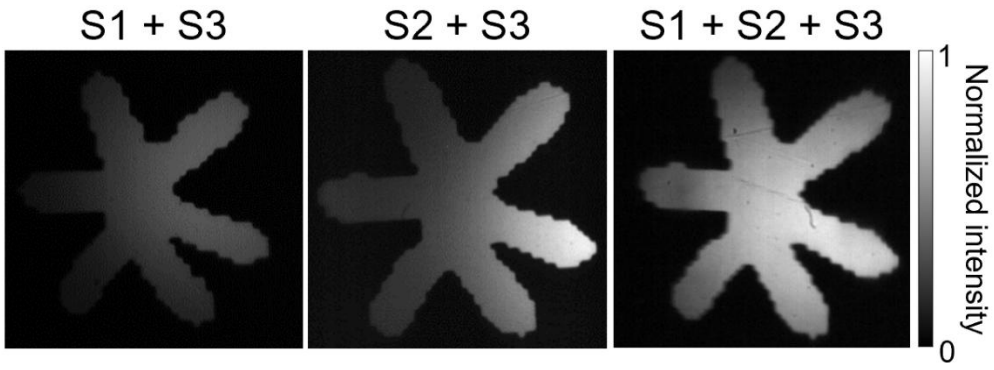

Figure S3.7 SWIR intensity images.

SWIR intensity images of the samples composed of the mixture of Gd:Er@Gd (i.e., S1), Lu:Er@Lu (i.e., S2), and Yb:Er@Y (i.e., S3) RENPs.

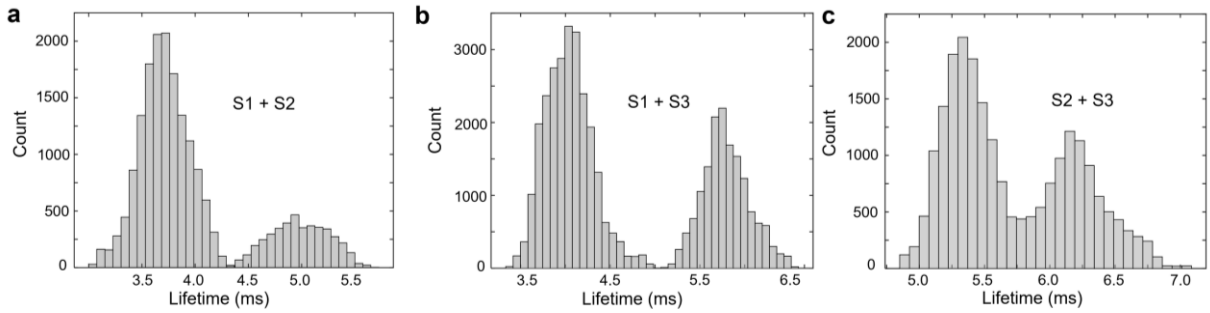

Figure S3.8 Photoluminescence lifetime histograms.

Photoluminescence lifetime histograms of RENPs corresponding to Figure 3d. (a) S1 + S2. (b) S1 + S3. (c) S2 + S3.

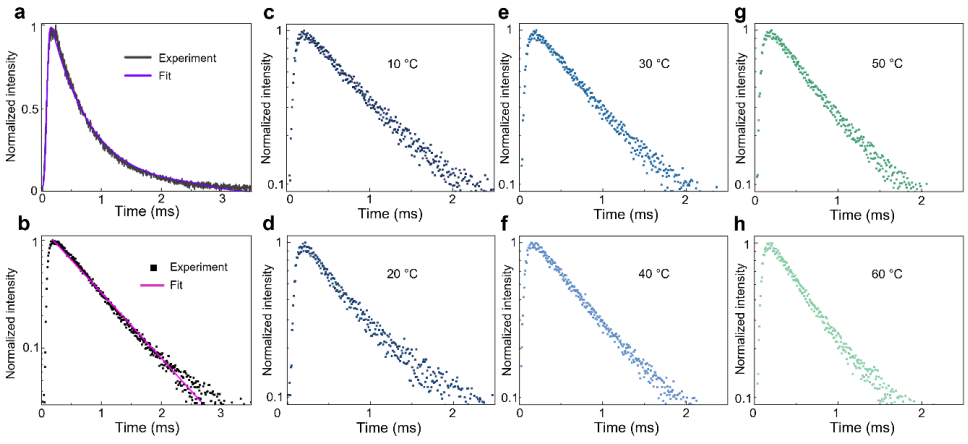

Figure S3.9 Photoluminescence intensity decay of $LiYbF_4:Ho^{3+}@LiYF_4$ RENPs.

(a) Normalized average intensity decay curve at room temperature with the fit. (b) As (a), but plotted in the logarithmic scale. (c-h) As (b), but showing the photoluminescence intensity decays at six different temperatures.

Supplementary Note 3.3: Performance of photoluminescence lifetime-based luminescence thermometry

Relative sensitivity. The photoluminescence lifetime-based relative sensitivity S_r is calculated as follows:

$$S_r = \left|\frac{1}{\tau}\frac{\partial \tau}{\partial T}\right|. \quad (S3.5)$$

Here, S_r demonstrates the percentage change of the photoluminescence lifetime per unit temperature.

Thermal uncertainty. Thermal uncertainty δT is calculated by

$$\delta T = \frac{1}{S_r}\frac{\delta \tau}{\tau}. \quad (S3.6)$$

Equation (S3.6) shows that the temperature uncertainty of the RENPs is influenced by the performance of the nanoparticles themselves and the photoluminescence lifetime fluctuation measured by the optical system. In this work, the standard deviation of the lifetimes was quantified to be 3.86 μs in 40 repeated measurements.

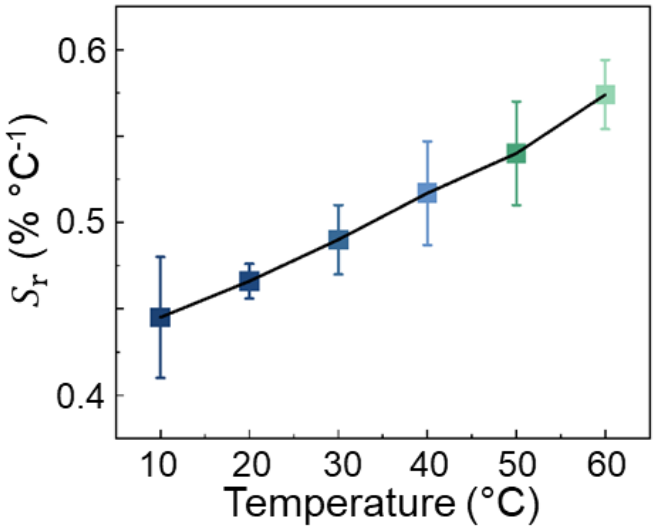

Figure S3.10 Relative sensitivity of $LiYbF_4$:Ho^{3+}@$LiYF_4$ RENPs.

4 INCREASING DOWNSHIFTING (DS) LUMINESCENCE INTENSITY THROUGH AN EXTENDED ACTIVE LAYER

Increasing Downshifting Luminescence Intensity Through an Extended Active Layer

Augmentation de l'intensité de la luminescence de décalage vers le rouge grâce à une couche active étendue

Auteurs :

Miao Liu, Jinyang Liang*, Fiorenzo Vetrone*

Centre Énergie Matériaux Télécommunications, Institut National de la Recherche Scientifique, Université du Québec, 1650 boulevard Lionel-Boulet, Varennes, Québec J3X 1P7, CANADA

Submitted to Advanced Materials on 20 December 2024, current status: under review

Contribution des auteurs:

Miao Liu proposed the concept, conducted the experiments, analyzed the data, and wrote the manuscript. Jinyang Liang and Fiorenzo Vetrone initiated the project, contributed to manuscript revision, and supervised the project.

Abstract

NIR emission of RENPs, known as downshifting luminescence, has been extensively investigated in diverse applications from information technology to biomedicine. In promoting brightness and enriching the functionalities of the downshifting luminescence of RENPs, numerous studies have exploited inert shell to protect rare-earth dopants from surface quenchers. However, internal concentration quenching remains an unsolved puzzle when using higher dopant concentrations of rare-earth ions in an attempt to obtain brighter emission. Following a plethora of research involving core-shell structures, the interface has shown to be controllable, ranging from a well-defined, abrupt boundary to an obscure one with cation intermixing. By utilizing this inter-mixed core-shell property for the first time, we design a new architecture to create a homogeneous double-layer core-shell interface to extend the active layer, allowing more luminescent centers without severe concentration quenching. By systematically deploying the crystallinity of the starting core, shell growth dynamics, and dopant concentrations, the downshifting luminescence intensity of new architecture achieves a 12-fold enhancement surpassing the traditional core-shell structure. These results provide deeper insight into the potential benefits of the intermixed core-shell structure, offering an effective approach to tackling the internal concentration quenching effect for highly boosted NIR optical performance.

4.1 Introduction

NIR region, spanning from 900 to 1700 nm, offers numerous advantages in both fundamental research and frontier applications. (Feng *et al.*, 2023; Li *et al.*, 2024a; Zhong *et al.*, 2017b) Invisible to the naked eye, NIR light allows for the embedding of features in high-security information storage. (Liu *et al.*, 2024c) In optical communications, the use of 1550 nm has been standardized due to its low attenuation and high transparency in optical fibers, which ensures minimal energy loss during transmission. (Avesani *et al.*, 2021; Müller *et al.*, 2018; Zhou *et al.*, 2017) In biomedicine, NIR emission wavelengths that fall within the biological imaging windows hold the potential for deep penetration owing to their low scattering and low absorption by tissues. (Wang *et al.*, 2024a) Notably, NIR-IIb (1500-1700 nm) shows reduced scattering and near-zero autofluorescence, which further enhances spatial resolution and the signal-to-noise ratio in bioimaging. (Li *et al.*, 2020b) Additionally, NIR light is well-suited for transmitting through turbid or colored media, such as murky water, fog, and blood, and thus can be exploited for non-invasive sensing and analysis. (Chen *et al.*, 2023a; Duthon *et al.*, 2019; Zeng *et al.*, 2018)

A variety of nanoscale materials have been studied for their NIR luminescence, for example, lead sulfide/silver sulfide quantum dots, single-walled carbon nanotubes, and organic fluorophores.(Feng *et al.*, 2023; Kwon *et al.*, 2016) Among these studied luminescent materials, rare-earth doped nanoparticles (RENPs) have shown great promise for their unique optical properties, such as fixed transition bandwidths, long photoluminescence lifetimes, high photostability, and low toxicity.(Gai *et al.*, 2014; Matulionyte *et al.*, 2023) Most importantly, the abundant energy levels of the rare-earth ions allow RENPs to emit across multiple regions of the NIR spectrum, e.g., 980 nm from Yb^{3+}, 1060 nm and 1310 nm from Nd^{3+}, 1150 nm from Ho^{3+}, 1475 nm from Tm^{3+}, and 1525 nm from Er^{3+}. (Zhou *et al.*, 2020c) In particular, Er^{3+}-doped RENPs, which emit in the NIR-IIb range, have been reported as promising candidates for deep tissue bioimaging and temperature sensing. (Hazra *et al.*, 2020a; Hemmer *et al.*, 2016b) While a great deal of work has focused on improving the upconversion luminescence intensity (Liu *et al.*, 2018a), improving the downshifting performance, despite its various advantages and applications, is still largely unexplored. Developing bright, downshifting emissions with low excitation thresholds is still of significant importance since future applications of RENPs crucially hinge on their optical performance.

The emission in RENPs originates from the rare-earth ions doped within the host lattice.(Zheng *et al.*, 2022) In principle, a high concentration of dopant ions provides more possibilities for the absorption of excitation photons and energy transfer to the activator ions (luminescent centers)

to reach a higher intensity. (Wen *et al.*, 2018) However, excessively dense distribution of activator ions in a host can also promote concentration quenching pathways such as non-radiative energy migration to surface quenchers and non-radiative, cross-relaxation energy loss.(Wang *et al.*, 2010; Wen *et al.*, 2018) To date, significant efforts have been devoted to mitigating concentration quenching in RENPs. On the one hand, constructing an inert shell on the luminescent core to block the energy migration to surface quenchers is one of the most common and well-accepted approaches. (Dühnen *et al.*, 2015; Fischer *et al.*, 2016; Hu *et al.*, 2019; Skripka *et al.*, 2020b) Nonetheless, the inert shell can only protect the activator ions from the surface quenchers while internal cross-relaxation remains a problem that hinders the high dopant concentration of activator ions. On the other hand, the integrity and heterogeneity of the widely employed core-shell structure are much clearer than before. Compelling evidence has been put forth that cation intermixing between the core and shell layer occurs such that the interfacial region is not characterized by a simple sharp separation. (Bastian *et al.*, 2021; Dong *et al.*, 2009; Hudry *et al.*, 2017; Hudry *et al.*, 2021) For instance, due to the activator ions readily diffusing from the core into the shielding shell, a rather thick shell outer layer is required to properly protect the luminescent ions in the core. (Abel *et al.*, 2011; Johnson *et al.*, 2017) While a great deal of research has been focused on how to suppress cation intermixing to the shielding layer, (Bastian *et al.*, 2020; Bastian *et al.*, 2021; Huang *et al.*, 2023) utilization of the diffused elements at the interface to reach a high dopant concentration of activator ions has not yet been explored.

Here, we develop a novel approach to realize high Er^{3+} doping through dopant ion diffusion at the extended interface for efficient downshifting luminescence by exploiting an inert core-active shell-inert shell architecture. Specifically, we rationally design a new structure, namely $LiLuF_4$@$LiLuF_4$:Ce^{3+}, Yb^{3+}, Er^{3+}@$LiLuF_4$ RENPs (Figure 4.1). To avoid host structure-induced lattice mismatch between the core and shell layers, the same composition is preferred throughout the architecture. Moreover, a homogeneous core-shell interface makes it easier for cation intermixing. A lutetium host lattice is employed compared with the more common yttrium ion host lattice given that it is better matched in size and mass with the heavy rare earth dopants. (Comer *et al.*, 2013) Utilizing an homogeneous inert core and inert shell to construct a double-layer interface for dopant ions diffusion, the active shell layer is extended allowing for more active ions to be doped without severe concentration quenching. The size of the inert core as well as the crystal growth dynamics of the core-shell architecture have been investigated to maximize ion diffusion at the interface, which helps to better control the interface structure for enhanced downshifting luminescence intensity. By optimizing the structure, the downshifting

intensity shows a dramatic enhancement compared with the conventional core-shell structure. The innovative RENPs have been successfully deployed to transmit NIR signals through obstacles including plastic and paper boxes, showcasing their exceptional capability in overcoming barriers for signal detection.

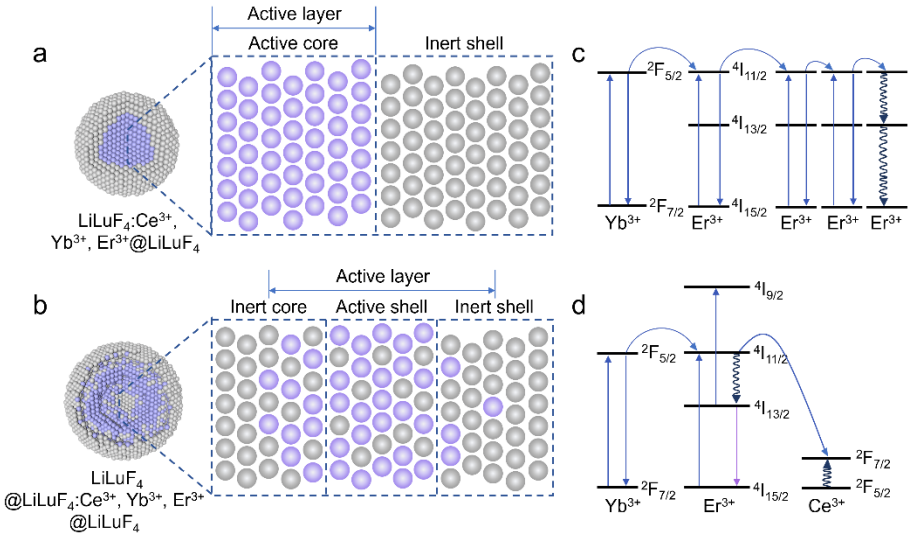

Figure 4.1 Schematic of conventional core-shell structure and inert core-active shell-inert shell architecture with extended active layer.

(a) Conventional $LiLuF_4:Ce^{3+}$, Yb^{3+}, $Er^{3+}@LiLuF_4$ architecture with limited active layer. (b) $LiLuF_4@LiLuF_4:Ce^{3+}$, Yb^{3+}, $Er^{3+}@LiLuF_4$ inert core-active shell-inert shell structure. The extended active layer is in the middle (purple color) of the entire architecture. (c) Concentration quenching at highly Er^{3+}-doped conventional core-shell structure. (d) Normal energy transfer process in highly Er^{3+}-doped RENPs with Ce^{3+} co-dopant to enhance downshifting emission intensity.

4.2 Results and discussion

4.2.1 Er^{3+} dopant concentration

A strategy of doping Ce^{3+} to the matrix was used to obtain enhanced NIR downshifting emission.(Hazra *et al.*, 2020a; Huang *et al.*, 2008; Zhong *et al.*, 2017b) Initially, different concentrations of Ce^{3+} were doped in the $LiLuF_4@LiLuF_4$: *x* mol% Ce^{3+}, Yb^{3+}, *y* mol% $Er^{3+}@LiLuF_4$ (*x* = 0, 1, 2 and *y* = 2, 3, 4, 5, 6, 8) architecture where the concentrations of Er^{3+} and Yb^{3+} were fixed at 2 and 18 mol%, respectively. The morphology and size distribution were characterized by transmission electron microscopy (TEM), as shown in Figure S4.1. The inert-core (IC) with a size of *d* nm, active-shell (AS) with dopant concentrations of Ce^{3+} (*x*) or Er^{3+} (*y*), and inert-shell (IS) are denoted by $IC_{d\text{nm}}$, $IC_{d\text{nm}}\text{-}AS_{x\text{Ce}/y\text{Er}}$, and $IC_{d\text{nm}}\text{-}AS_{x\text{Ce}/y\text{Er}}\text{-}IS$, respectively. To avoid size-effect induced variations on the optical performance, the same inert core with a size of about 5 nm was used and the $LiLuF_4$:*x* mol% Ce^{3+}, Yb^{3+}, Er^{3+} shell thicknesses were kept

constant at about 5-8 nm. An inert $LiLuF_4$ outer shell of about 5 nm was grown as a protective layer to prevent surface quenching. All the core-shell or core-shell-shell architectures displayed a bi-pyramidal shape, indicative of the tetragonal crystal structure, which was confirmed by X-ray diffraction (XRD), as shown in Figure S4.2.

In RENPs doped with only Yb^{3+} and Er^{3+}, the Yb^{3+} ion acts as a sensitizer to harvest the excitation photons and then effectively transfer the energy to adjacent Er^{3+} ions (the activator) following 980 nm excitation, Thus, the $^4I_{11/2}$ excited state of Er^{3+} is subsequently populated via ground state ($^4I_{15/2}$) absorption followed by nonradiative decay to the lower lying $^4I_{13/2}$ state that ultimately leads to the 1550 nm downshifting emission ascribed to the $^4I_{13/2}$ ® $^4I_{15/2}$ transition. When Ce^{3+} is added to the matrix, an additional pathway accelerates the accumulation of Er^{3+} ions at the $^4I_{13/2}$ level. According to the classic Dieke energy level diagram, the energy gap between the $^2F_{5/2}$ and $^2F_{7/2}$ levels of Ce^{3+} is about 2300 cm^{-1} (*ca*. 0.29 eV), which shows a small mismatch with the energy difference between the $^4I_{11/2}$ and $^4I_{13/2}$ states of Er^{3+} (around 3700 cm^{-1}, *ca*. 0.46 eV).(Huang *et al.*, 2008; Zhong *et al.*, 2017b) Hence, when Ce^{3+} is present, following the 980 nm excitation, ions in the $^4I_{11/2}$ state will easily decay to the $^4I_{13/2}$ state due to the cross-relaxation between Er^{3+} and Ce^{3+} ($^4I_{11/2}$ + $^2F_{5/2}$ ® $^4I_{13/2}$ + $^2F_{7/2}$) although phonon-assisted process is necessary for the energy transfer (Figure 4.1d). (Dieke *et al.*, 1963) The influence of Ce^{3+} dopant on the downshifting emission of $^4I_{11/2}$ ® $^4I_{13/2}$ transition from Er^{3+} under excitation of 980 nm laser is demonstrated in Figure S4.3. The multiple emission peaks within the 1550 nm manifold arise from the Stark sublevels of the $^4I_{13/2}$ and $^4I_{15/2}$ states of Er^{3+} (Figure S4.4), which result from the splitting of those states due to the high crystal field strength from the $LiLuF_4$ host lattice. (Auzel, 1984; Hazra *et al.*, 2020a) As shown in Figure S4.3, 1 mol% Ce^{3+} doped RENPs have a contrasting effect on downshifting emission enhancement independent of the architecture (IC_{5nm}-AS_{xCe} or IC_{5nm}-S_{xCe}-S). However, a higher Ce^{3+} dopant inhibits the NIR downshifting emission, indicating a limitation to the desensitization of $^4I_{13/2}$ of Er^{3+}. 1 mol% Ce^{3+} is thus chosen as the optimum concentration for subsequent experiments.

Although the cation intermixing phenomenon at the core-shell interface has been reported from the structural perspective, there is no further demonstration of using the extended core-shell interface for higher dopant concentration and thus increased downshifting emission. (Bastian *et al.*, 2021; Dühnen *et al.*, 2015; Hudry *et al.*, 2017; Hudry *et al.*, 2021) To verify the dilution effect of dopant ions at the core-shell interface, the concentration of Er^{3+} was tuned from 2 mol% to 8 mol%. If the diffusion phenomenon does occur at the interface, a higher dopant concentration should be tolerable without severe concentration quenching. As a proof of concept, a series of

$LiLuF_4$@$LiLuF_4$:1 mol% Ce^{3+}, 18 mol% Yb^{3+}, *y* mol% Er^{3+}@$LiLuF_4$ were then developed. The prepared inert core-active shell $LiLuF_4$@$LiLuF_4$:1 mol% Ce^{3+}, Yb^{3+}, *y* mol% Er^{3+} (IC_{5nm}-AS_{yEr}), and inert core-active shell-inert shell $LiLuF_4$@$LiLuF_4$:1 mol% Ce^{3+}, Yb^{3+}, *y* mol% Er^{3+} (IC_{5nm}-AS_{yEr}-IS) RENPs are shown in Figure 4.2a-b. The size of IC_{5nm}-AS_{yEr} and IC_{5nm}-AS_{yEr}-IS were measured to be around 17 ± 3 nm and 27 ± 3 nm, respectively (Figure S4.5). All the RENPs were monodispersed and had a uniform size distribution, confirming the well-controlled preparation of high-quality RENPs. The radius of the core was close to the thickness of the shell, which ensured that the diameter of the optically active domain was identical when tuning the Er^{3+} dopant concentration. A typical high-angle annular dark-field image in scanning transmission electron microscopy (HAADF-STEM) of IC_{5nm}-AS_{yEr}-IS is shown in Figure 4.2c with a size of 30 nm (Figure 4.2d). The high-resolution TEM (HRTEM) image displays lattice fringes with an interplanar spacing of 0.46 nm (Figure 4.2e), which matches the (101) lattice planes of tetragonal phase $LiLuF_4$ (JCPDS: 027-1251). The XRD diffractograms (Figure S4.6-7) further demonstrate the excellent crystallinity of the synthesized RENPs as well as the tetragonal phase.

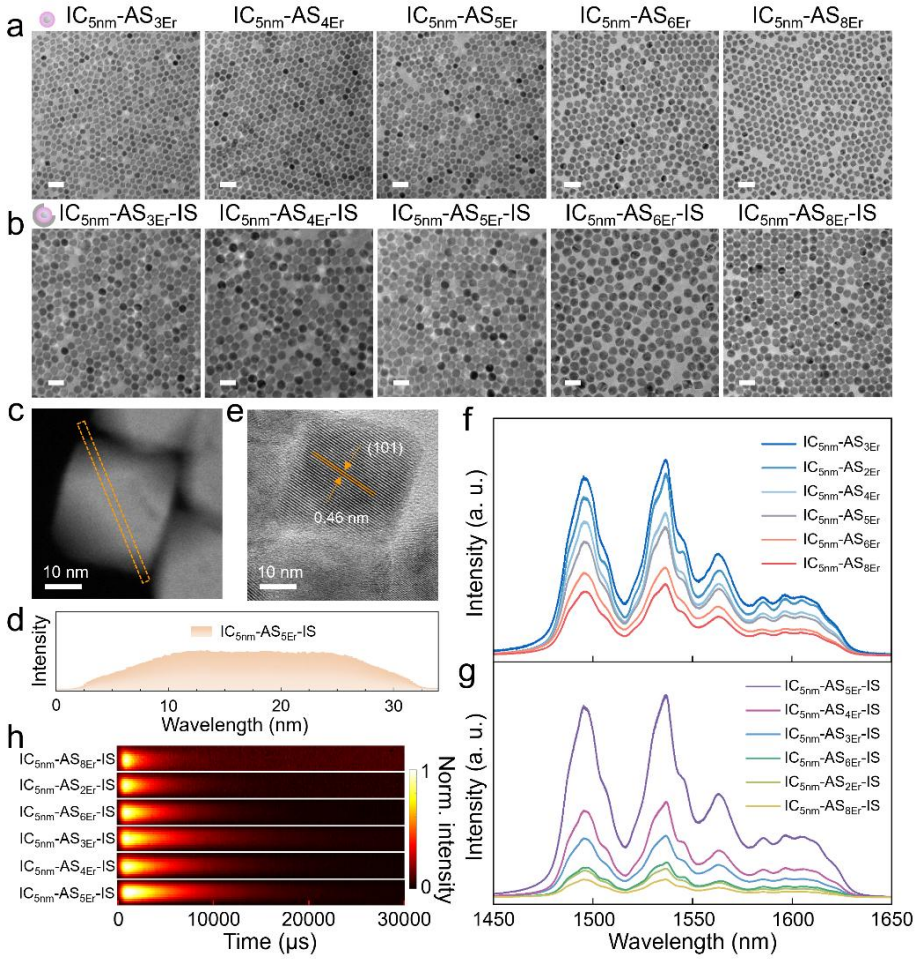

Figure 4.2 Dilution effect at the core-shell interface for higher Er^{3+} dopant concentrations.

TEM images of prepared RENPs with an inert core of 5 nm and varied Er^{3+} dopant concentrations with the structure of (a) inert core-active shell (IC_{5nm}-AS_{yEr}) and (b) inert core-active shell-inert shell (IC_{5nm}-AS_{yEr}-IS). (c) HAADF STEM image of a single IC_{5nm}-AS_{5Er}-IS RENP. (d) Intensity distribution along the orange bar in (c). (e) HRTEM of IC_{5nm}-AS_{5Er}-IS. (f) Downshifting spectra of IC_{5nm}-AS_{yEr} and (g) IC_{5nm}-AS_{yEr}-IS under 980 nm laser excitation. (h) Downshifting emission intensity decay of IC_{5nm}-AS_{yEr}-IS. Scale bar in (a-b): 50 nm and *y* = 2, 3, 4, 5, 6, 8.

Figure 4.2f shows the downshifting spectrum of the IC_{5nm}-AS_{yEr} RENPs doped with different concentrations of Er^{3+} under 980 nm laser excitation. RENPs with 3 mol% Er^{3+} dopant (IC_{5nm}-AS_{3Er}) perform best among the different dopant concentrations. However, further increasing the Er^{3+} dopant concentration (higher than 3 mol%) in IC_{5nm}-AS_{yEr} resulted in decreased emission intensities. It should be noted that there is no outermost shell protection here and the emission of IC_{5nm}-AS_{yEr} RENPs is hindered by a strong surface quenching effect. This is especially true at higher Er^{3+} concentrations where more Er^{3+} ions in the shell layer are closer to the surface and ultimately exposed to the environment. Therefore, the comparison of emission intensity in the IC_{5nm}-AS_{yEr} RENPs cannot totally prove the dilution phenomenon at the interface. An outermost

inert shell layer was then epitaxially grown on these RENPs. The downshifting emission spectra of IC_{5nm}-AS_{yEr}-IS are shown in Figure 4.2g. The downshifting luminescence intensity shows an initial increase from 2 mol% to 5 mol% Er^{3+} dopant and then a sharp drop at 6 mol% and 8 mol%. It is noteworthy that the intensity of IC_{5nm}-AS_{yEr}-IS at y = 3, 4, 5, 6 mol% are all higher than the conventional 2 mol% dopant concentration. The tolerable high dopant concentration of Er^{3+} for intense downshifting emission shows direct optical evidence of the cation intermixing and thus dilution effect at the interface. However, concentration quenching still plays a dominant role when the Er^{3+} concentration is too high (8 mol%). The integrated intensity of IC_{5nm}-AS_{yEr} and IC_{5nm}-AS_{yEr}-IS at around 1550 nm is demonstrated in Figure S4.8. The enhanced downshifting intensity of IC_{5nm}-AS_{yEr}-IS compared with IC_{5nm}-AS_{yEr} verified the successful depletion of the surface quenching. Interestingly, with the same outermost protection thickness, a significant enhancement (40 times) was realized by doping 5 mol% Er^{3+} in the active shell layer while the conventional 2 mol% Er^{3+} only has 4 times increment. Considering the same inert core, same active layer thickness as well as the same outermost layer thickness, the dramatic enhancement at 5 mol% Er^{3+} further indicates the crucial role of the interface in high dopant concentration RENPs. Owing to the double-layer core-shell interface, Er^{3+} ions dilute to both the inert core and the inert shell, so concentration quenching is weakened. The downshifting luminescence lifetimes of IC_{5nm}-AS_{yEr}-IS were characterized using an NIR luminescence lifetime imaging microscope developed in-house. (Liu *et al.*, 2024c) The time-resolved luminescence process of IC_{5nm}-AS_{yEr}-IS RENPs can be directly captured within a 30 ms exposure window in a single shot. As shown in Figure 4.2h, the intensity decay difference among all RENPs is clearly observed in the image. 5 mol% Er^{3+} doped IC_{5nm}-AS_{5Er}-IS presents the longest lifetime followed by 4 mol%, 3 mol%, 6 mol%, 2 mol% and 8 mol% being the shortest one, which is consistent with the downshifting spectrum result. The normalized luminescence intensity decay curves are plotted in Figure S4.9 with fitted lifetimes from 1.65 ms to 6.22 ms. The long lifetime of the $^4I_{13/2}$ ® $^4I_{15/2}$ transition indicates that the ions remain in the excited state ($^4I_{13/2}$) for a long time before decaying to the $^4I_{15/2}$ ground state, which also proves the depressed concentration quenching in 5 mol% Er^{3+} highly doped IC_{5nm}-AS_{5Er}-IS.

To further reveal the effect of the interface on the optical properties, the upconversion emission spectra of IC_{5nm}-AS_{yEr}-IS were also studied in Figure S4.10. All the samples presented two characteristic visible emission bands centered at 525/545 and 660 nm, which are attributed to the radiative transitions of the $^2H_{11/2}$/$^4S_{3/2}$, and $^4F_{9/2}$ excited states to the $^4I_{15/2}$ ground state, respectively. The results revealed that the 5% Er^{3+} doped IC_{5nm}-AS_{5Er}-IS sample, still possessed the highest upconversion emission intensity among the samples studied. Nonetheless, the

difference in the upconversion emission intensity among the varied Er^{3+} dopant concentrations was not as obvious as in the downshifting emission. It is noted that upconversion and downshifting emission intensities are highly related to the population of the $^4I_{11/2}$ excited state where the two processes (i.e., upconversion or downshifting) are actually in competition with each other. In our case, the addition of Ce^{3+} promoted phonon-assisted energy transfer from $^4I_{11/2}$ of Er^{3+} to Ce^{3+} resulting in the inevitable suppression of the upconversion emission.

4.2.2 Inert core

In addition to the dopant concentration, it is also meaningful to explore the influence of the existence of the inert core and its size on the interface dilution effect. It has been reported that the size of the starting core can change the diffusion length to affect the cation intermix . (Chen *et al.*, 2014a; Hudry *et al.*, 2017) Here, we tuned the inert core from 5 nm to 10 nm. A series of RENPs with an inert core of 10 nm (IC_{10nm}), active-shell layers doped with 2 mol% Er^{3+} (AS_{2Er}), and 5 mol% Er^{3+} (AS_{5Er}) are shown in Figure 4.3b-c. The size (Figure S4.11) of the active shell, and outermost shell were kept similar at around 5 nm. Besides, the conventional active core and core-shell structures are shown in Figure 4.3d for comparison. To ensure the same diameter of the optically active domain in the final structure, the thickness of the active shell in IC_{5nm}-$AS_{y\mathrm{Er}}$-IS and IC_{10nm}-$AS_{y\mathrm{Er}}$-IS was set to be as close as the radius of the conventional core. The size difference between the two adjacent architectures only came from the inert core and was thus expected to be 5 nm (as confirmed in Figure 4.3e). Furthermore, the clear lattice fringes observed over the entire architecture in the HRTEM images of the AC_{2Er}-IS, IC_{5nm}-AS_{2Er}-IS, and IC_{10nm}-AS_{2Er}-IS samples (Figure S4.12) demonstrate their excellent crystallinity and the tetragonal phase (Figure S4.13).

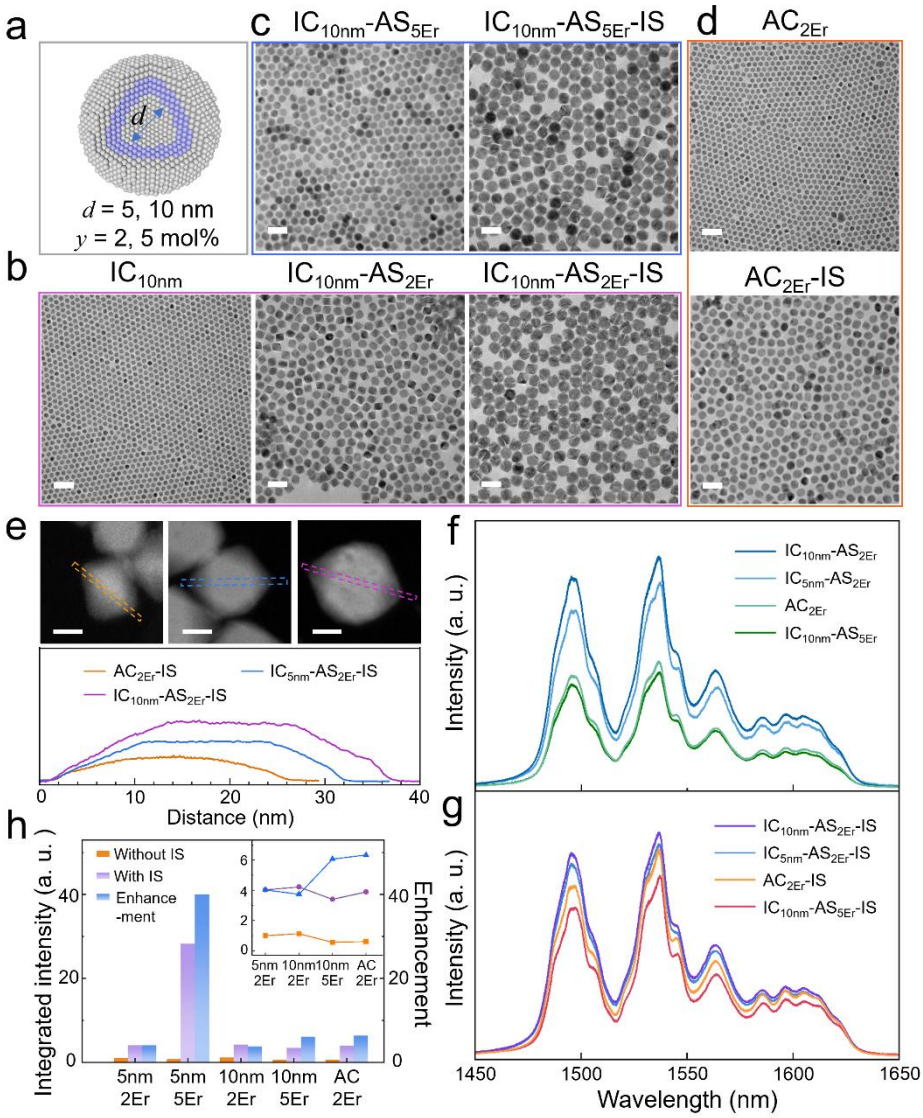

Figure 4.3 Influence of the inert core on the downshifting emission intensity.

(a) Schematic of the inert core-active shell-inert shell architecture. (b-d) TEM images of explored RENP structures: (b) inert core (IC_{10nm}), inert core-active shell (IC_{10nm}-AS_{2Er}), and inert core-active shell-inert shell (IC_{10nm}-AS_{2Er}-IS) with an inert core of 10 nm and 2 mol% Er^{3+} dopant concentration; (c) inert core-active shell (IC_{10nm}-AS_{5Er}) and inert core-active shell-inert shell (IC_{10nm}-AS_{5Er}-IS) with an inert core of 10 nm and 5 mol% Er^{3+} dopant concentration; (d) active core (AC_{2Er}) and active core-inert shell (AC_{2Er}-IS) with 2 mol% Er^{3+} dopant concentration. (e) HAADF-STEM images of AC_{2Er}-IS, IC_{5nm}-AS_{2Er}-IS, IC_{10nm}-AS_{2Er}-IS, and the corresponding averaged intensity distribution along the selected area. Downshifting emission spectra of (f) AC_{2Er} and IC_{dnm}-AS_{yEr} with d = 5, 10 nm and y = 2 mol% and 5 mol%, (g) similar to (f) but the structure has the outermost inert shell coating. (h) Integrated NIR downshifting intensity in (f-g) and the enhancement factor of the outermost shell protection. The inset is a magnified plot of (h) without the 5nm/5Er set. Scale bar: 50 nm in (a-b), 10 nm in (e).

The downshifting spectra of RENPs without the outermost shell layer are shown in Figure 4.3f. For IC_{dnm}-AS_{yEr} with the same Er^{3+} concentration but different size of the inert core, IC_{10nm}-AS_{2Er} shows higher emission intensity than IC_{5nm}-AS_{2Er} and AC_{2Er} due to its larger size, smaller

surface-to-volume ratio and thus relatively fewer surface quenching centers. For $IC_{d\text{nm}}$-$AS_{y\text{Er}}$ with different Er^{3+} concentrations but the same inert core, the downshifting intensity of $IC_{10\text{nm}}$-$AS_{5\text{Er}}$ is lower than $IC_{10\text{nm}}$-$AS_{2\text{Er}}$, indicating the strong concentration quenching in $IC_{10\text{nm}}$-$AS_{5\text{Er}}$. After outermost-shell protection, the intensity order in Figure 4.3g is the same as it is in Figure 4.3f without the outermost-shell. The integrated intensities of the RENPs are normalized according to $IC_{5\text{nm}}$-$AS_{2\text{Er}}$ (Figure 4.3h). Surprisingly, despite the significantly high intensity of $IC_{5\text{nm}}$-$AS_{5\text{Er}}$-IS, $IC_{10\text{nm}}$-$AS_{5\text{Er}}$-IS shows even lower intensity than the conventional core-shell structure, which means the contribution of double layer interface for enhancing the NIR intensity in $IC_{10\text{nm}}$-$AS_{5\text{Er}}$-IS is limited (Figure S4.14-15) and also the dilution effect at the interface is not obvious.

To explore the possible influence of the crystal structure of the starting cores on the NIR downshifting emission intensity, we performed energy-dispersive X-ray spectroscopy (EDS) line-scanning for $AC_{2\text{Er}}$-IS, $IC_{5\text{nm}}$-$AS_{2\text{Er}}$-IS and $IC_{10\text{nm}}$-$AS_{2\text{Er}}$-IS (Figure S4.16). Under identical measurement conditions, the $IC_{5\text{nm}}$-$AS_{2\text{Er}}$-IS sample was damaged after line scanning while $AC_{2\text{Er}}$-IS and $IC_{10\text{nm}}$-$AS_{2\text{Er}}$-IS kept their original morphology. The elemental distribution of Lu and F both present a decreasing trend in the center of $IC_{5\text{nm}}$-$AS_{2\text{Er}}$-IS crystal indicating that the damage mainly occurs at the center of the crystal. Following this, the same characterization condition was also conducted on $IC_{5\text{nm}}$. Compared with the HAADF image before line scanning, the $IC_{5\text{nm}}$ crystal shows obvious damage after line scanning (Figure S4.18a-b), which can also be observed in the HRTEM image (Figure S4.18d) where two circled RENPs show the variation. The fragile structure of $IC_{5\text{nm}}$ suggests its instability under high-energy electron beam irradiation in HAADF. The crystallinity of $IC_{5\text{nm}}$ was then investigated by XRD (Figure S4.17). First, the diffraction peaks of the core match well with the tetragonal phase $LiLuF_4$ regardless of its size. However, the peak patterns of $IC_{5\text{nm}}$ are not sharp and narrow compared with the $AC_{10\text{nm}}$ and $IC_{10\text{nm}}$, implying the poor crystallinity of $IC_{5\text{nm}}$. The instability and low crystallinity of such ultra-small RENPs have also been observed in previous research. (Cheng *et al.*, 2018a) Moreover, in a typical synthesis procedure, stabilization of the 5 nm-sized core is necessary to get a chemically stable structure. (Cheng *et al.*, 2018a) However, in our specific case, the stabilization step of the 5 nm inert core was bypassed to obtain the required small size.

From the downshifting emission intensity and structure properties, we determined that a smaller un-stabilized inert core, $IC_{5\text{nm}}$, was easier for cation intermixing at the interface, which was attributed to its instability and poor crystallinity. Previous reports have shown that 8 nm starting cores (in $NaEuF_4$@$NaGdF_4$) demonstrated more significant cation intermixing than starting cores of 40 nm (in $NaYF_4$:Ce@$NaYF_4$:Tb). (Chen *et al.*, 2015a; Dühnen *et al.*, 2015) Meanwhile,

Hudry *et al*. discussed the interface structure in detail, concluding that smaller starting cores had a higher probability of losing the chemical integrity of the starting core domain. (Hudry *et al.*, 2021; Hudry *et al.*, 2019) On the contrary, while the larger inert core (IC_{10nm}) presented more stable crystallinity, it was more difficult for the diffusion process to occur and thus a well-defined and abrupt interface was prone to be created. The highly doped Er^{3+} ions in IC_{10nm}-AS_{5Er}-IS were confined in the middle layer, so the internal cross-relaxation was more severe, which was not ideal for the downshifting emission intensity.

4.2.3 Shell growth dynamics

For a better understanding of the diffusion process on the downshifting emission intensity, IC_{5nm}-AS_{5Er} RENPs were extracted at different reaction times (i.e., 10, 25, 40, and 60 min) after the hot injection of the shell precursors (Figure 4.4a). The downshifting emission spectra and integrated intensity (Figure 4.4e, g) show that IC_{5nm}-AS_{5Er} at 25 min performs better. The same phenomenon was also observed in the RENPs with a lower Er^{3+} doping concentration in the active shell, IC_{5nm}-AS_{2Er} (Figure S4.19). The sizes of IC_{5nm}-AS_{5Er} at different reaction times (Figure 4.4c) were similar, indicating that the formation of the $LiLuF_4$ shell was quite fast. However, a subtle decreasing trend can also be seen from 10 min to 25 min, indicating the dissolution of the architecture. At the same time, the narrowed size distribution at 40 min and 60 min implies the re-growth to more uniform morphology during the core-shell synthesis. Heating of RENPs is known to induce the Ostwald ripening process in which small RENPs are dissolved (from 10 min to 25 min) into monomers until the concentration of the monomers in solution becomes so high that the particles stop dissolving and start to grow (from 25 min to 60 min). The consumed monomers in the solution will be further replenished to keep the thermodynamic balance.(Lahtinen *et al.*, 2017) In consequence, the dissolution of IC_{5nm} at 25 min was expected to be high and gradually decrease. Er^{3+} ions were redistributed in the architecture with a lower concentration in the active shell and thus the concentration quenching is suppressed. Similar results have also been observed in the literature: e.g., a low concentration of Eu^{3+} ions is found in the shell layer of the $NaEuF_4$@$NaGdF_4$ architecture, Yb^{3+} ions are spatially diluted within the whole volume of the $NaYF_4$:Yb^{3+}, Er^{3+}@$NaYF_4$ RENP according to the EDS maps. (Arteaga Cardona *et al.*, 2023b; Dühnen *et al.*, 2015) In the case of IC_{5nm}-AS_{2Er}-IS, the inert shell should first dissolve into the active shell to dilute the concentration of Er^{3+} ions, followed by growth with high crystallinity to block the surface quenchers. In Figure 4.4d, 40 min reaction time with a narrow size distribution was the expected reaction time, and the NIR emission intensity (Figure 4.4f, g) further proved the expectation.

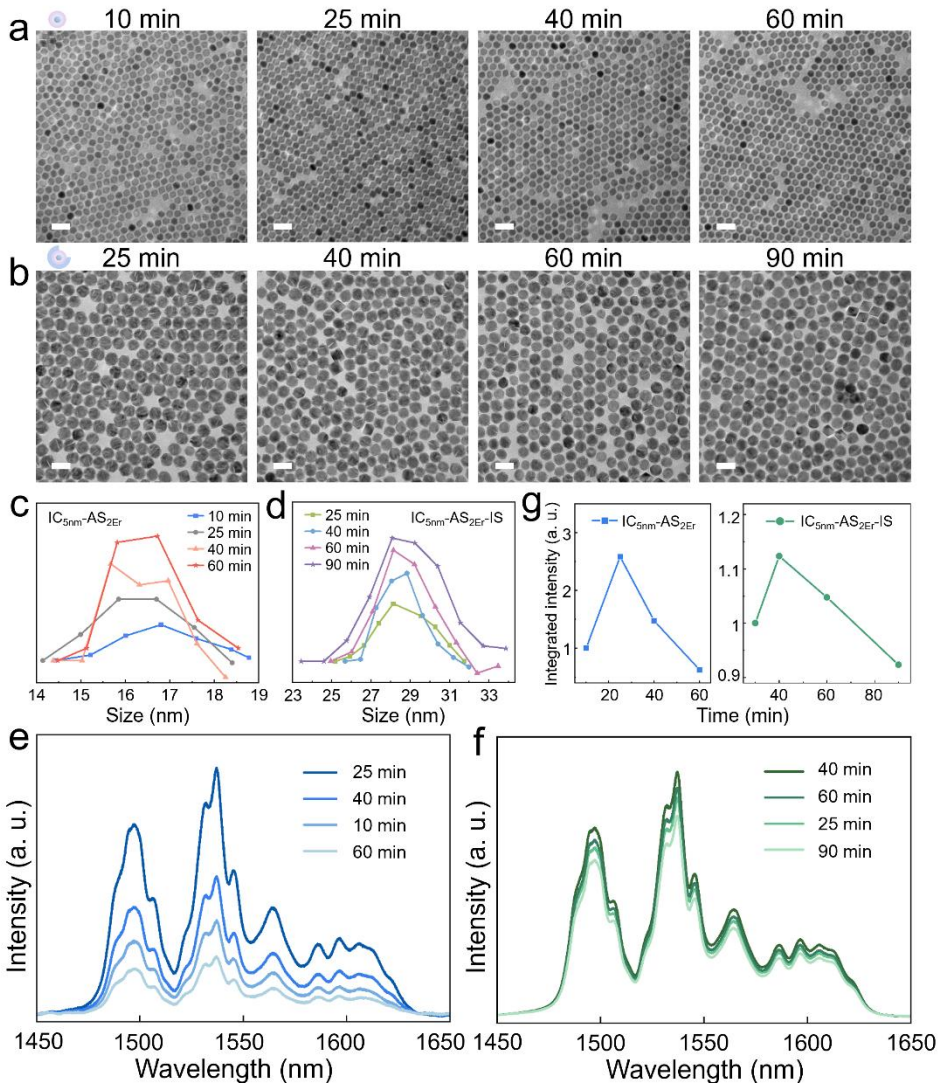

Figure 4.4 **Morphology and downshifting emission intensity of IC_{5nm}-AS_{5Er} and IC_{5nm}-AS_{5Er}-IS extracted at different reaction times during the shell growth.**

(a-b) TEM images of (a) IC_{5nm}-AS_{5Er} reacted at 10, 25, 40, 60 mins and (b) IC_{5nm}-AS_{5Er}-IS extracted at 25, 40, 60, 90 mins. (c-d) Size distribution of the RENPs in the images in (a-b). (e) Downshifting emission spectra of the samples in (a). (f) As (e) but for the samples in (b). (g) Normalized integrated intensity of samples in (a-b). Scale bar in (a-b): 50 nm.

4.2.4 NIR image and application

By finely tuning the parameters including the size of the inert core, the dopant concentration of Er^{3+}, and the reaction time of shell growth, the downshifting luminescence intensity of these newly designed IC_{5nm}-AS_{5Er}-IS RENPs is 12 times higher than the conventional core-shell structure AS_{2Er}-IS (Figure S4.20). It is noteworthy that the main contribution to this remarkable 12-times enhancement is the 5 nm inert core-active shell-inert shell architecture which allows for a high (5 mol%) Er^{3+} high dopant concentration. To give a direct impression of enhancement in

the NIR intensity, the NIR images of newly developed IC_{5nm}-AS_{5Er}-IS RENPs and conventional AC_{2Er}-IS RENPs covered with an “INRS” transparency are shown in Figure 4.5a-b. The different optical performance in the NIR intensity as well as the lifetime of IC_{5nm}-AS_{5Er}-IS and AC_{2Er}-IS is further demonstrated by lifetime imaging microscopy (Liu *et al.*, 2024c). We first mixed the two samples as follows: hexane solution containing AC_{2Er}-IS RENPs was deposited on the glass slide in a relatively large area. Using the same protocol, IC_{5nm}-AS_{5Er}-IS hexane solution was then dropped at the center of the same area. In Figure 4.5c, brighter NIR intensity along with the longer lifetime in the middle of the mixture comes from the emission of IC_{5nm}-AS_{5Er}-IS while the surrounding part is mainly the distribution of AC_{2Er}-IS RENPs. To showcase the significance of the enhanced NIR downshifted intensity in signal detection, we applied the optimized IC_{5nm}-AS_{5Er}-IS RENPs to investigate their capabilities to transmit their NIR luminescence through (diverse) obstacles. As shown in Figure 4.5d, the visible image presents no useful information underneath the obstacle, cellulose paper, while the NIR image (Figure 4.5e) depicts the “A” letter which is the transparency covered on IC_{5nm}-AS_{5Er}-IS RENPs. In contrast, nearly no hint of the shape of the letter underneath the obstacles can be obtained from the NIR image (Figure 4.5f) of conventional structure, AC_{2Er}-IS RENPs. The low intensity of AC_{2Er}-IS induced low signal-to-noise ratio so that the useful information was submerged into the background (Figure 4.5g). The capiliblтiy of the high NIR intensity of IC_{5nm}-AS_{5Er}-IS RENPs was further demonstrated using diverse opaque obstacles (Figure S4.21): polyethylene terephthalate; polypropylene with acrylic adhesive; cellulose paper. Without covering any obstacles, a clear image with sharp boundaries of the covered “C”, “A”, and “N” letters could be observed (Figure S4.21a). The uneven intensity distribution is from the height difference of the powder sample so that only part of the area was focused. By covering diverse opaque obstacles: polyethylene terephthalate (Figure S4.21e); polypropylene with acrylic adhesive (Figure S4.21f); cellulose paper (Figure S4.21g), the image of “C” “A” “N” letters are blurred with decreased intensity (Figure S4.21b-d) which mainly due to the scattering and absorption of the medium. Nonetheless, the shape can still be seen to discern the pattern even when the signal is low and the covered material has different colors (Figure S4.22). The newly designed IC_{5nm}-AS_{5Er}-IS with the dramatic 12 times enhanced NIR intensity shows its irreplaceable role in signal detection.

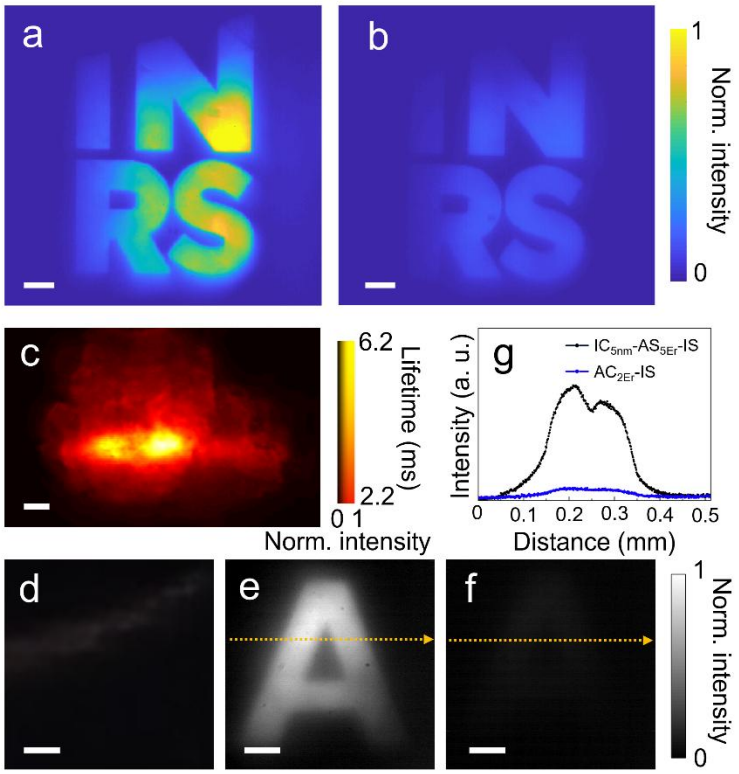

Figure 4.5 Enhanced NIR intensity of IC_{5nm}-AS_{5Er}-IS and its application in signal detection through obstacles.

Normalized NIR intensity image of (a) IC_{5nm}-AS_{5Er}-IS and (b) AC_{2Er}-IS under 980 nm excitation. (c) NIR intensity and lifetime distribution of the mixed sample of IC_{5nm}-AS_{5Er}-IS and AC_{2Er}-IS. (d) Visible image and NIR intensity image of the (e) IC_{5nm}-AS_{5Er}-IS and (f) AC_{2Er}-IS covered with cellulose paper. (g) Intensity profile of the marked place in (e and f). Scale bar: 50 mm.

4.3 Conclusion

In summary, we have developed a novel RENP architecture, based on an inert core-active shell-inert shell structure, specifically $LiLuF_4$@$LiLuF_4$:Ce^{3+}, Yb^{3+}, Er^{3+}@$LiLuF_4$ in which the Er^{3+} dopant concentration can be increased to 5% yielding 12 times enhanced NIR downshifting emission intensity at around 1550 nm compared to conventional active core-inert shell architecture. The enhancement mechanism was further studied by tuning the size/crystallinity of the inert core (5 nm and 10 nm) as well as the shell growth dynamics. The ultra-small unstable inert core allowed for easier intermixing with the shell layers. Meanwhile, the double interfaces in the $LiLuF_4$@$LiLuF_4$:Ce^{3+}, Yb^{3+}, Er^{3+}@$LiLuF_4$ core-shell-shell architecture provided an extended layer for Er^{3+} doping to overcome the concentration quenching effect that normally occurs in the conventional core-shell structure. Our method suggests a general way to suppress concentration quenching to further increase not only NIR downshifting emission intensity but

also visible emissions. The optimized structure IC_{5nm}-AS_{5Er}-IS has been successfully applied in signal detection through opaque obstacles.

4.4 Experimental methods

Preparation of RENPs precursors. Stoichiometric amounts of RE_2O_3 (RE = Lu, Yb, Er) and $Ce_2(CO_3)_3$ were selectively mixed with 5 mL trifluoroacetic acid and 5 mL distilled water in a 50 mL three-neck round bottom flask. The mixture was kept at 80 °C under vigorous stirring until the solution became clear. The temperature was then reduced to 60 °C to evaporate the residual trifluoroacetic acid and water.

Synthesis of 5 nm $LiLuF_4$. Unstabilized $LiLuF_4$ core RENPs were synthesized via the hot injection thermolysis approach. Solution A0: 7 mL of oleic acid (OA), 7 mL of oleylamine (OM), and 14 mL 1-octadecene (ODE), were degassed at 110 °C for 15 min and then heated to 330 °C under an argon atmosphere. Solution B0: 2.5 mmol CF_3COOLi and $(CF_3COO)_3RE$ (RE = Lu/Yb, Er) were mixed with 3 mL OA and 6 mL ODE, and was degassed at 125 °C for 30 min. 3 mL of OM was added in Solution B0 and degassed for 5 min. Solution B0 was then injected into Solution A0 with a rate of 1.5 mL min^{-1}. After reacting at 330 °C for 1 h, the preparation of ultra-small $LiLuF_4$ was finished.

Synthesis of 10 nm $LiLuF_4$ and conventional core $LiLuF_4$:1 mol% Ce^{3+}, 18 mol% Yb^{3+}, 2 mol% Er^{3+}. Core RENPs were formed by the stabilization of the first nuclei, ultra-small $LiLuF_4$, with an excess of OA. 1.25 mmol first nuclei were mixed with 16 mL of OA and 16 mL of ODE in a 100 mL three-neck round bottom flask. The solution was degassed at 110 °C for 30 min and backfilled with argon gas. The temperature was raised to 315 °C following which the reaction was continued for 1 h. conventional core $LiLuF_4$:1% Ce^{3+}, 18% Yb^{3+}, 2% Er^{3+} was synthesized using same procedure as 10 nm $LiLuF_4$ with extra addition of Yb^{3+}, Er^{3+}, and Ce^{3+} source in Solution B.

Synthesis of $LiLuF_4$@ $LiLuF_4$:x mol% Ce^{3+}, 18 mol% Yb^{3+}, y mol% Er^{3+}@$LiLuF_4$ (x = 0, 1, 2; y = 2, 3, 4, 5, 6, 8). The core-shell structure was prepared by epitaxial growth of the shell on the performed cores. 0.5 mmol of $LiLuF_4$ inert core RENPs (size of the inert core: 5/10 nm) were mixed with 10 mL of OA and 10 mL of ODE (Solution A1). 2 mmol shell precursors

$(CF_3COO)_3RE$ (RE = Lu/Yb/ Er/Ce) together with CF_3COOLi were mixed with 10 mL of OA and 10 mL of ODE (Solution B1). Solution A1 and B1 were both degassed at 110 °C for 30 min. After degassing, Solution A1 was heated to 315 °C. Solution B1 was injected into Solution A1 at a 1.5 mL min^{-1} rate when the temperature of Solution A1 was stable. After cooling down to room temperature, the $LiLuF_4$@$LiLuF_4$:1 mol% Ce^{3+}, 18 mol% Yb^{3+}, 2 mol% Er^{3+} inert core-active shell RENPs were washed with hexane/ethanol (1:3) three times and re-dispersed in hexane. $LiLuF_4$@$LiLuF_4$:1% Ce^{3+}, 18% Yb^{3+}, 2% Er^{3+}@$LiLuF_4$ inert core-active shell-inert shell RENPs were prepared by epitaxial growth of the $LiLuF_4$ shell onto the inert core-shell structure. Conventional core-shell structure $LiLuF_4$:1 mol% Ce^{3+}, 18 mol% Yb^{3+}, 2 mol% Er^{3+}@$LiLuF_4$ was synthesized following the same protocol.

Supporting Information

Supporting Information is available from the Wiley Online Library or from the authors.

Acknowledgments

This work was supported in part by Natural Sciences and Engineering Research Council of Canada (RGPIN-2024-05551, I2IPJ 592655-24), Canada Research Chair Programs (CRC-2022-00119), INRS Chair in Nano-biophotonics, Canadian Cancer Society (707056); New Frontier in Research Fund (NFRFE-2020-00267); Fonds de Recherche du Québec–Nature et Technologies (203345–Centre d'Optique, Photonique, et Lasers); Fonds de Recherche du Québec–Santé (267406, 280229).

Conflict of Interest

The authors declare no conflict of interest.

Data Availability Statement

The data that support the findings of this study are available from the corresponding authors upon reasonable request.

Keywords

rare-earth doped nanoparticles, efficient downshifting emission, cation intermixing, core-shell interface, signal detection

4.5 References

Abel KA, Boyer J-C, Andrei CM, van Veggel FCJM (2011) Analysis of the Shell Thickness Distribution on NaYF4/NaGdF4 Core/Shell Nanocrystals by EELS and EDS. *The Journal of Physical Chemistry Letters* 2(3):185-189.

Arteaga Cardona F, Jain N, Popescu R, Busko D, Madirov E, Arús BA, Gerthsen D, De Backer A, Bals S, Bruns OT, Chmyrov A, Van Aert S, Richards BS, Hudry D (2023b) Preventing cation intermixing enables 50% quantum yield in sub-15 nm short-wave infrared-emitting rare-earth based core-shell nanocrystals. *Nature Communications* 14(1):4462.

Auzel F (1984) A Scalar Crystal Field Strength Parameter for Rare-Earth Ions: Meaning and Application to Energy Transfer. *Energy Transfer Processes in Condensed Matter*, Di Bartolo B (Édit.) Springer US, Boston, MA10.1007/978-1-4613-2407-2_10. p 511-520.

Avesani M, Calderaro L, Schiavon M, Stanco A, Agnesi C, Santamato A, Zahidy M, Scriminich A, Foletto G, Contestabile G, Chiesa M, Rotta D, Artiglia M, Montanaro A, Romagnoli M, Sorianello V, Vedovato F, Vallone G, Villoresi P (2021) Full daylight quantum-key-distribution at 1550 nm enabled by integrated silicon photonics. *npj Quantum Information* 7(1):93.

Bastian PU, Nacak S, Roddatis V, Kumke MU (2020) Tracking the Motion of Lanthanide Ions within Core–Shell–Shell NaYF4 Nanocrystals via Resonance Energy Transfer. *The Journal of Physical Chemistry C* 124(20):11229-11238.

Bastian PU, Robel N, Schmidt P, Schrumpf T, Günter C, Roddatis V, Kumke MU (2021) Resonance Energy Transfer to Track the Motion of Lanthanide Ions—What Drives the Intermixing in Core-Shell Upconverting Nanoparticles? *Biosensors* 11(12):515.

Chen B, Peng D, Chen X, Qiao X, Fan X, Wang F (2015a) Establishing the Structural Integrity of Core–Shell Nanoparticles against Elemental Migration using Luminescent Lanthanide Probes. *Angewandte Chemie International Edition* 54(43):12788-12790.

Chen D, Huang P (2014a) Highly intense upconversion luminescence in Yb/Er:NaGdF4@NaYF4 core–shell nanocrystals with complete shell enclosure of the core. *Dalton Transactions* 43(29):11299-11304.

Chen Y, Wang S, Zhang F (2023a) Near-infrared luminescence high-contrast in vivo biomedical imaging. *Nature Reviews Bioengineering* 1(1):60-78.

Cheng T, Marin R, Skripka A, Vetrone F (2018a) Small and Bright Lithium-Based Upconverting Nanoparticles. *Journal of the American Chemical Society* 140(40):12890-12899.

Comer S, McMillen CD, Kolis JW (2013) Hydrothermal growth of LiLuF4 crystals and new lithium lutetium fluorides LiKLuF5 and LiNaLu2F8. *Solid State Sciences* 17:90-96.

Dieke GH, Crosswhite HM (1963) The Spectra of the Doubly and Triply Ionized Rare Earths. *Applied Optics* 2:675-686.

Dong C, van Veggel FCJM (2009) Cation Exchange in Lanthanide Fluoride Nanoparticles. *ACS Nano* 3(1):123-130.

Dühnen S, Haase M (2015) Study on the Intermixing of Core and Shell in NaEuF4/NaGdF4 Core/Shell Nanocrystals. *Chemistry of Materials* 27(24):8375-8386.

Duthon P, Colomb M, Bernardin F (2019) Light Transmission in Fog: The Influence of Wavelength on the Extinction Coefficient. *Applied Sciences* 9(14):2843.

Feng Z, Li Y, Chen S, Li J, Wu T, Ying Y, Zheng J, Zhang Y, Zhang J, Fan X, Yu X, Zhang D, Tang BZ, Qian J (2023) Engineered NIR-II fluorophores with ultralong-distance molecular packing for high-contrast deep lesion identification. *Nature Communications* 14(1):5017.

Fischer S, Bronstein ND, Swabeck JK, Chan EM, Alivisatos AP (2016) Precise Tuning of Surface Quenching for Luminescence Enhancement in Core–Shell Lanthanide-Doped Nanocrystals. *Nano Letters* 16(11):7241-7247.

Gai S, Li C, Yang P, Lin J (2014) Recent Progress in Rare Earth Micro/Nanocrystals: Soft Chemical Synthesis, Luminescent Properties, and Biomedical Applications. *Chem. Rev.* 114(4):2343-2389.

Hazra C, Skripka A, Ribeiro SJL, Vetrone F (2020a) Erbium Single-Band Nanothermometry in the Third Biological Imaging Window: Potential and Limitations. *Adv. Opt. Mater.* 8(23):2001178.

Hemmer E, Benayas A, Légaré F, Vetrone F (2016b) Exploiting the biological windows: current perspectives on fluorescent bioprobes emitting above 1000 nm. *Nanoscale Horizons* 1(3):168-184.

Hu Y, Shao Q, Dong Y, Jiang J (2019) Energy Loss Mechanism of Upconversion Core/Shell Nanocrystals. *The Journal of Physical Chemistry C* 123(36):22674-22679.

Huang F, Bagheri N, Wang L, Ågren H, Zhang J, Pu R, Zhan Q, Jing Y, Xu W, Widengren J, Liu H (2023) Suppression of Cation Intermixing Highly Boosts the Performance of Core–Shell Lanthanide Upconversion Nanoparticles. *Journal of the American Chemical Society* 145(32):17621-17631.

Huang J, Chen Y, Lin Y, Gong X, Luo Z, Huang Y (2008) Enhanced efficiency of Er:Yb:Ce:NaGd(WO4)2 laser at 1.5–1.6 μm by the introduction of high-doping Ce3+ ions. *Optics Letters* 33(21):2548-2550.

Hudry D, Busko D, Popescu R, Gerthsen D, Abeykoon AMM, Kübel C, Bergfeldt T, Richards BS (2017) Direct Evidence of Significant Cation Intermixing in Upconverting Core@Shell Nanocrystals: Toward a New Crystallochemical Model. *Chemistry of Materials* 29(21):9238-9246.

Hudry D, De Backer A, Popescu R, Busko D, Howard IA, Bals S, Zhang Y, Pedrazo-Tardajos A, Van Aert S, Gerthsen D, Altantzis T, Richards BS (2021) Interface Pattern Engineering in Core-Shell Upconverting Nanocrystals: Shedding Light on Critical Parameters and Consequences for the Photoluminescence Properties. *Small* 17(47):2104441.

Hudry D, Popescu R, Busko D, Diaz-Lopez M, Abeykoon M, Bordet P, Gerthsen D, Howard IA, Richards BS (2019) Interface disorder in large single- and multi-shell upconverting nanocrystals. *Journal of Materials Chemistry C* 7(5):1164-1172.

Johnson NJJ, He S, Diao S, Chan EM, Dai H, Almutairi A (2017) Direct Evidence for Coupled Surface and Concentration Quenching Dynamics in Lanthanide-Doped Nanocrystals. *Journal of the American Chemical Society* 139(8):3275-3282.

Karayianis N (1971) Theoretical energy levels and g values for the 4I terms of Nd3+ and Er3+ in LiYF4. *Phys. Chem. Solids* 32(10):2385-2391.

Kwon H, Furmanchuk Ao, Kim M, Meany B, Guo Y, Schatz GC, Wang Y (2016) Molecularly Tunable Fluorescent Quantum Defects. *Journal of the American Chemical Society* 138(21):6878-6885.

Lahtinen S, Lyytikäinen A, Päkkilä H, Hömppi E, Perälä N, Lastusaari M, Soukka T (2017) Disintegration of Hexagonal NaYF4:Yb3+,Er3+ Upconverting Nanoparticles in Aqueous Media: The Role of Fluoride in Solubility Equilibrium. *The Journal of Physical Chemistry C* 121(1):656-665.

Li C, Du J, Jiang G, Gong J, Zhang Y, Yao M, Wang J, Wu L, Tang BZ (2024a) White-light activatable organic NIR-II luminescence nanomaterials for imaging-guided surgery. *Nature Communications* 15(1):5832.

Li Y, Cai Z, Liu S, Zhang H, Wong STH, Lam JWY, Kwok RTK, Qian J, Tang BZ (2020b) Design of AIEgens for near-infrared IIb imaging through structural modulation at molecular and morphological levels. *Nat Commun* 11(1):1255.

Liu M, Lai Y, Marquez M, Vetrone F, Liang J (2024c) Short-wave Infrared Photoluminescence Lifetime Mapping of Rare-Earth Doped Nanoparticles Using All-Optical Streak Imaging. *Advanced Science* 11(11):2305284.

Liu M, Shi Z, Wang X, Zhang Y, Mo X, Jiang R, Liu Z, Fan L, Ma C-g, Shi F (2018a) Simultaneous enhancement of red upconversion luminescence and CT contrast of NaGdF4:Yb,Er nanoparticles via Lu3+ doping. *Nanoscale* 10(43):20279-20288.

Matulionyte M, Skripka A, Ramos-Guerra A, Benayas A, Vetrone F (2023) The Coming of Age of Neodymium: Redefining Its Role in Rare Earth Doped Nanoparticles. *Chem. Rev.* 123(1):515-554.

Müller T, Skiba-Szymanska J, Krysa AB, Huwer J, Felle M, Anderson M, Stevenson RM, Heffernan J, Ritchie DA, Shields AJ (2018) A quantum light-emitting diode for the standard telecom window around 1,550 nm. *Nature Communications* 9(1):862.

Skripka A, Cheng T, Jones CMS, Marin R, Marques-Hueso J, Vetrone F (2020b) Spectral characterization of LiYbF4 upconverting nanoparticles. *Nanoscale* 12(33):17545-17554.

Wang F, Wang J, Liu X (2010) Direct evidence of a surface quenching effect on size-dependent luminescence of upconversion nanoparticles. *Angew. Chem. Int. Ed* 49(41):7456-7460.

Wang F, Zhong Y, Bruns O, Liang Y, Dai H (2024a) In vivo NIR-II fluorescence imaging for biology and medicine. *Nature Photonics* 18(6):535-547.

Wen S, Zhou J, Zheng K, Bednarkiewicz A, Liu X, Jin D (2018) Advances in highly doped upconversion nanoparticles. *Nature Communications* 9(1):2415.

Zeng X, Chu J, Cao W, Kang W, Zhang R (2018) Visible–IR transmission enhancement through fog using circularly polarized light. *Applied Optics* 57(23):6817-6822.

Zheng B, Fan J, Chen B, Qin X, Wang J, Wang F, Deng R, Liu X (2022) Rare-Earth Doping in Nanostructured Inorganic Materials. *Chemical Reviews* 122(6):5519-5603.

Zhong Y, Ma Z, Zhu S, Yue J, Zhang M, Antaris AL, Yuan J, Cui R, Wan H, Zhou Y, Wang W, Huang NF, Luo J, Hu Z, Dai H (2017b) Boosting the down-shifting luminescence of rare-earth nanocrystals for biological imaging beyond 1500 nm. *Nat. Commun.* 8(1):737.

Zhou B, Yan L, Huang J, Liu X, Tao L, Zhang Q (2020c) NIR II-responsive photon upconversion through energy migration in an ytterbium sublattice. *Nature Photonics* 14(12):760-766.

Zhou K, Zhao Q, Huang X, Yang C, Li C, Zhou E, Xu X, Wong KKY, Cheng H, Gan J, Feng Z, Peng M, Yang Z, Xu S (2017) kHz-order linewidth controllable 1550 nm single-frequency fiber laser for coherent optical communication. *Optics Express* 25(17):19752-19759.

Supporting information

Increasing Downshifting (DS) Luminescence Intensity Through an Extended Active Layer

Miao Liu, Jinyang Liang, Fiorenzo Vetrone**

Centre Énergie Matériaux Télécommunications, Institut National de la Recherche Scientifique, Université du Québec, 1650 boulevard Lionel-Boulet, Varennes, Québec J3X 1P7, CANADA

Corresponding authors: jinyang.liang@inrs.ca (J.L.), fiorenzo.vetrone@inrs.ca (F.V.)

Materials

Lu_2O_3 (REacton, 99.999%), Yb_2O_3 (REacton, 99.998%), Er_2O_3 (REacton, 99.99%), $Ce_2(CO_3)_3 \cdot xH_2O$ (REacton, 99.9%), 1-octadecene (ODE, 90%), and oleic acid (OA, 90%) were obtained from Alfa Aesar (USA); lithium trifluoroacetate (98%), oleylamine (OM, 70%), trifluoroacetic acid (TFA, 99%), were purchased from Sigma-Aldrich. All chemicals were used as received.

Characterization

Structural characterization: The crystallinity and phase of the core and core-shell RENPs were determined via X-ray powder diffraction (XRD) analysis on a Bruker D8 Advance Diffractometer using Cu Kα radiation (l = 1.5418 Å). The morphology and size distribution of the core, core-shell, and core-shell-shell were further investigated by TEM (Philips Tecnai 12). The particle size was determined from TEM images using ImageJ software with a minimal set size of 200 particles.

Optical characterization: Upconversion and downshifting spectra of oleate-capped RENPs in hexane were obtained at room temperature under laser diode excitation of 980 nm (MDL-SN-980-10W, CNI). Laser power and power density were about 490 mW and 8.0 W/cm^2, respectively. All spectra were measured in powder. The upconverting emission was recorded with an Avaspec-ULS2048L spectrometer (Avantes, The Netherlands). Stray light from the excitation source was removed with a short-pass 830 nm filter. The downshifting spectrum was collected with a Shamrock 500i monochromator (Andor, Ireland) equipped with an iDus InGaAs 1.7 NIR detector (Andor, Ireland). A long-pass 980 nm filter was used to remove any stray light from the excitation source. Time-resolved NIR emission intensity profile was measured by a

home-built NIR photoluminescence lifetime imaging microscopy using an all-optical streak camera. The excitation pulse had a pulse width of 200 μs, and the laser repetition rate was set to 10 Hz.

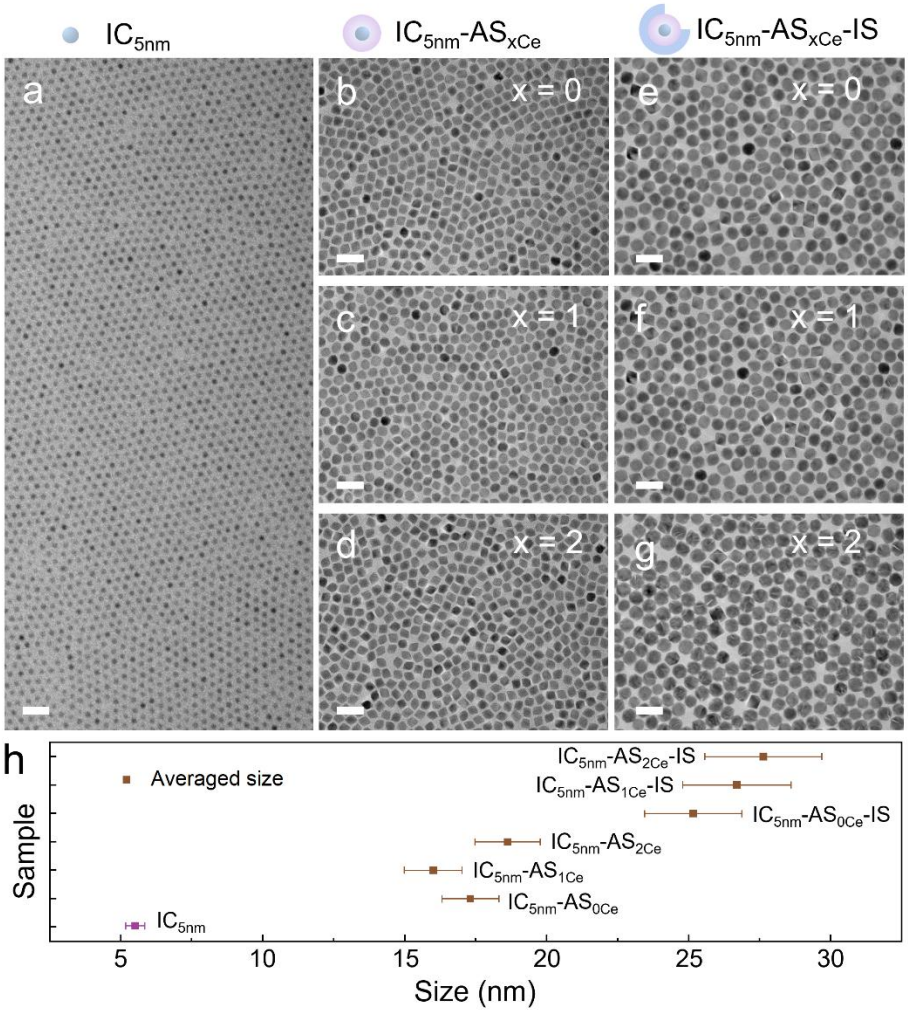

Figure S4.1 TEM images and averaged size distribution of all RENPs.

TEM images of (a) $LiLuF_4$ inert core of 5 nm (IC_{5nm}), (b-d) $LiLuF_4$@$LiLuF_4$:*x* mol% Ce^{3+}, Yb^{3+}, Er^{3+} inert core-active shell (IC_{5nm}-AS_{xCe}) with different doping concentrations of Ce^{3+} from *x* = 0 to 1 and 2, respectively. (e-g) $LiLuF_4$@$LiLuF_4$:*x* mol% Ce^{3+}, Yb^{3+}, Er^{3+}@$LiLuF_4$ inert core-active shell-inert shell structure (IC_{5nm}-AS_{xCe}-IS). (h) Averaged size distribution of all RENPs measured along major and minor axes. Scale bar: 20 nm in (a); 50 nm in (b-g).

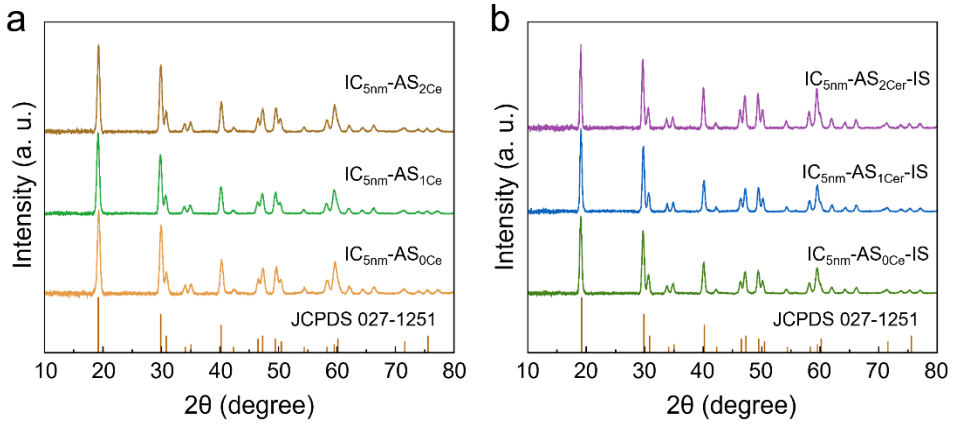

Figure S4.2 XRD patterns of RENPs.

XRD patterns of (a) $LiLuF_4$@$LiLuF_4$:*x* mol% Ce^{3+}, Yb^{3+}, Er^{3+} (*x* = 0, 1, 2) with the inert core of 5 nm and different Ce^{3+} concentration (IC_{5nm}-AS_{xCe}), (b) $LiLuF_4$@$LiLuF_4$:*x* mol% Ce^{3+}, Yb^{3+}, Er^{3+}@$LiLuF_4$ (IC_{5nm}-AS_{xCe}-IS) RENPs. The diffraction patterns of pure $LiLuF_4$ are shown.

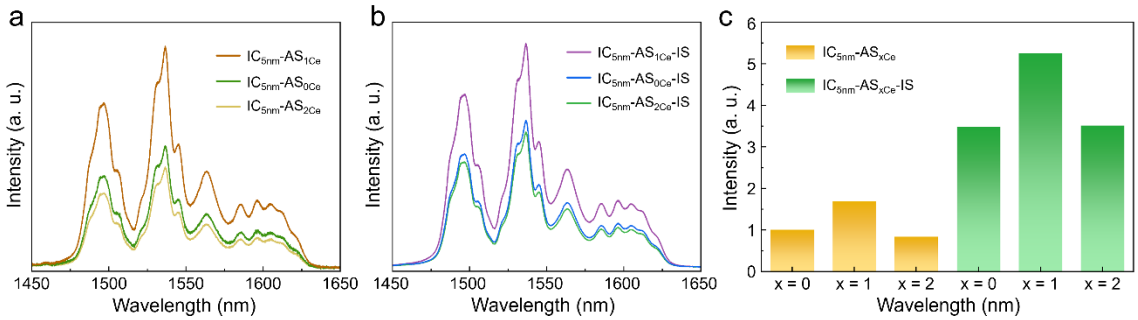

Figure S4.3 Downshifting performance corresponding to the $^4I_{13/2} \rightarrow {}^4I_{15/2}$ transition.

Downshifting spectra corresponding to the $^4I_{13/2} \rightarrow {}^4I_{15/2}$ transition of (a) $LiLuF_4$@$LiLuF_4$:*x* mol% Ce^{3+}, Yb^{3+}, Er^{3+} with inert core of 5 nm (IC_{5nm}-AS_{xCe}), (b) $LiLuF_4$@$LiLuF_4$:*x* mol% Ce^{3+}, Yb^{3+}, Er^{3+}@$LiLuF_4$ (IC_{5nm}-AS_{xCe}-IS) RENPs. (*x* = 0, 1, and 2). (c) Integrated intensity of the downshifting emission in spectrum (a) and (b). The integrated intensities are normalized according to the intensity of IC_{5nm}-AS_{0Ce}.

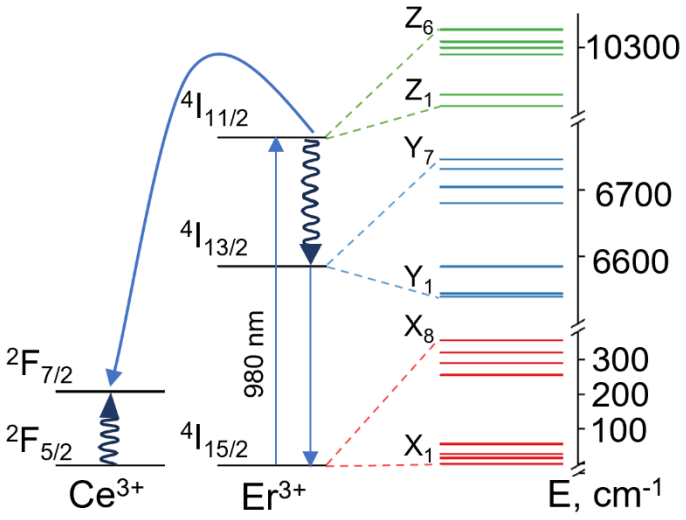

Figure S4.4 Energy level diagram of Er^{3+}, Ce^{3+} co-doped RENPs.

Energy level diagram of Er^{3+}, Ce^{3+} co-doped RENPs under excitation of 980 nm showing the Stark sublevels of the first three ^4I_J (J = 15/2, 13/2, and 11/2) manifolds and part of the energy transfer processes.(Karayianis, 1971).

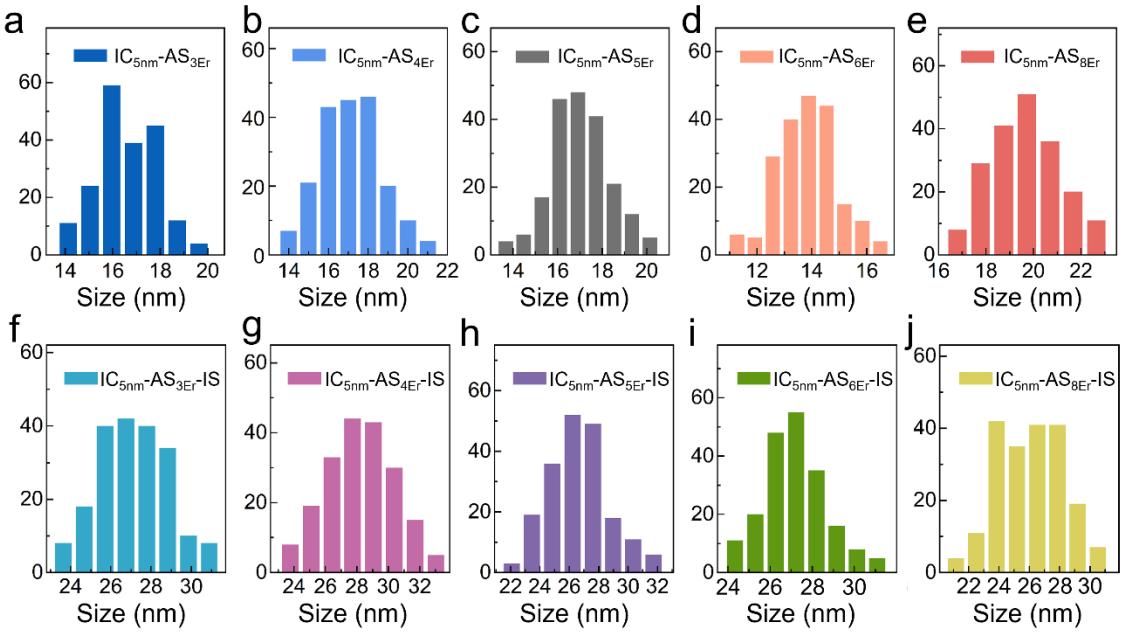

Figure S4.5 Size distribution of RENPs with an inert core of 5 nm.

Size distribution of (a-e) $LiLuF_4$@$LiLuF_4$:Ce^{3+}, Yb^{3+}, *y* mol% Er^{3+}@$LiLuF_4$ with an inert core of 5 nm (IC_{5nm}-AS_{yEr}, *y* = 3, 4, 5, 6, 8) and (f-g) $LiLuF_4$@$LiLuF_4$:Ce^{3+}, Yb^{3+}, *y* mol% Er^{3+}@$LiLuF_4$ (IC_{5nm}-AS_{yEr}-IS) RENPs.

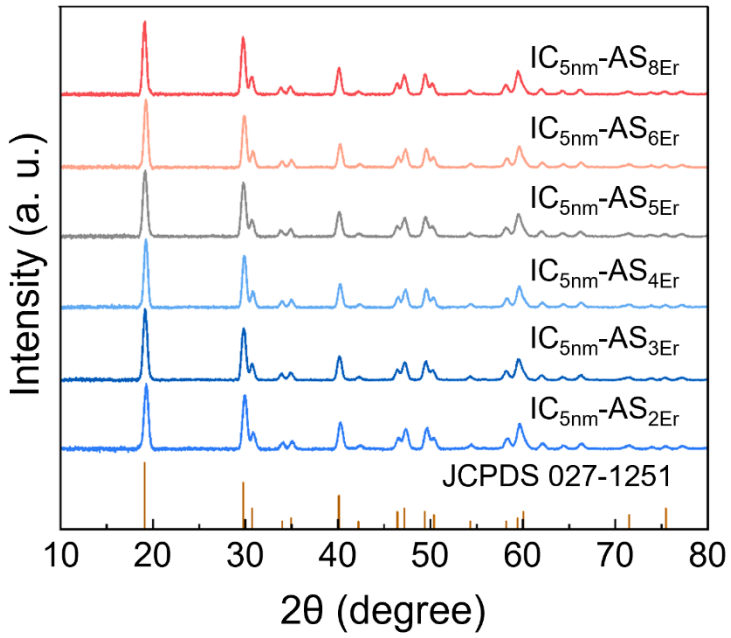

Figure S4.6 **XRD patterns of $LiLuF_4$@$LiLuF_4$:Ce^{3+}, Yb^{3+}, *y* mol% Er^{3+} with inert core of 5 nm (IC_{5nm}-AS_{yEr}, *y* = 2, 3, 4, 5, 6, 8) RENPs.**

Diffraction patterns of pure $LiLuF_4$ are shown.

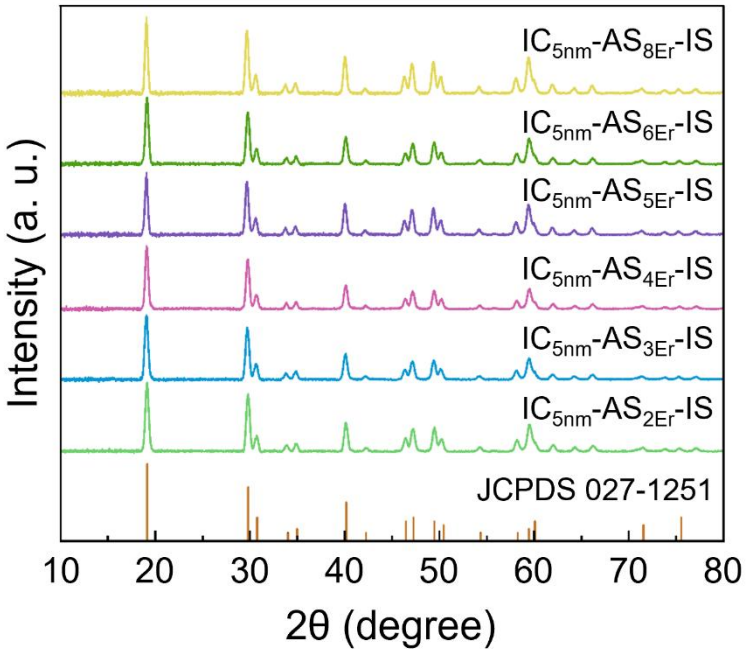

Figure S4.7 **XRD patterns of $LiLuF_4$@$LiLuF_4$:Ce^{3+}, Yb^{3+}, *y* mol% Er^{3+}@$LiLuF_4$ with the inert core of 5 nm (IC_{5nm}-AS_{yEr}-IS, *y* = 2, 3, 4, 5, 6, 8) RENPs.**

Diffraction patterns of pure $LiLuF_4$ are shown.

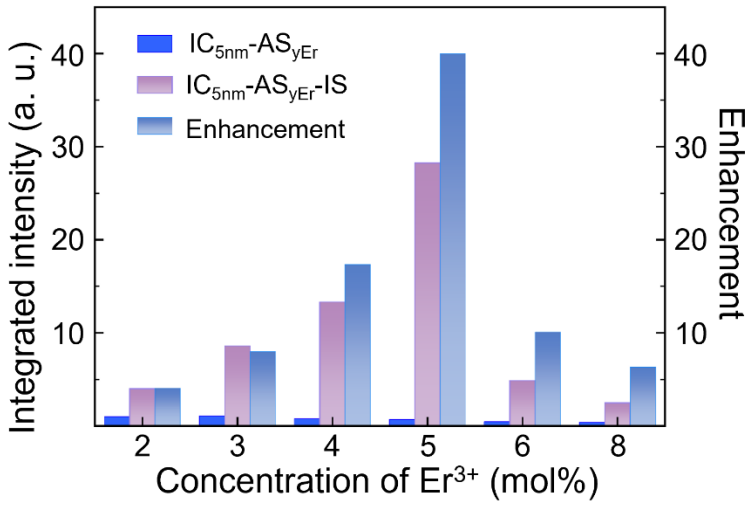

Figure S4.8 Integrated NIR intensity of RENPs.

Integrated NIR intensity of $LiLuF_4$@$LiLuF_4$:Ce^{3+}, Yb^{3+}, *y* mol% Er^{3+}@$LiLuF_4$ with inert core of 5 nm (IC_{5nm}-AS_{yEr}, *y* = 2, 3, 4, 5, 6, 8), $LiLuF_4$@$LiLuF_4$:Ce^{3+}, Yb^{3+}, *y* mol% Er^{3+}@$LiLuF_4$ (IC_{5nm}-AS_{yEr}-IS) and the enhancement factor from IC_{5nm}-AS_{yEr} to IC_{5nm}-AS_{yEr}-IS.

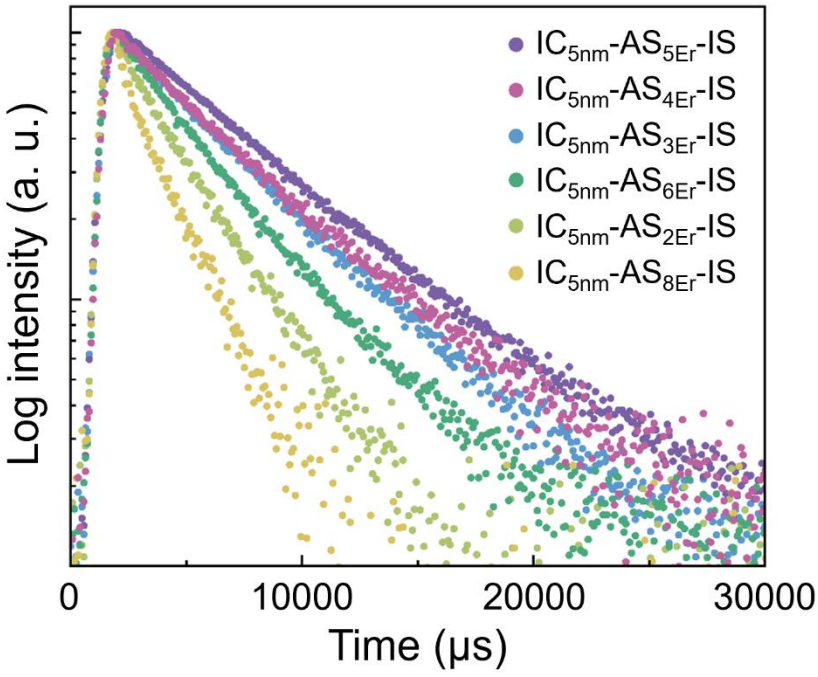

Figure S4.9 Normalized photoluminescence lifetime corresponding to $^4I_{13/2} \rightarrow {}^4I_{15/2}$ transition.

Normalized photoluminescence lifetime corresponding to $^4I_{13/2} \rightarrow {}^4I_{15/2}$ transition of $LiLuF_4$@$LiLuF_4$:Ce^{3+}, Yb^{3+}, *y* mol% Er^{3+}@$LiLuF_4$ with an inert core of 5 nm (IC_{5nm}-AS_{yEr}-IS, *y* = 2, 3, 4, 5, 6, 8).

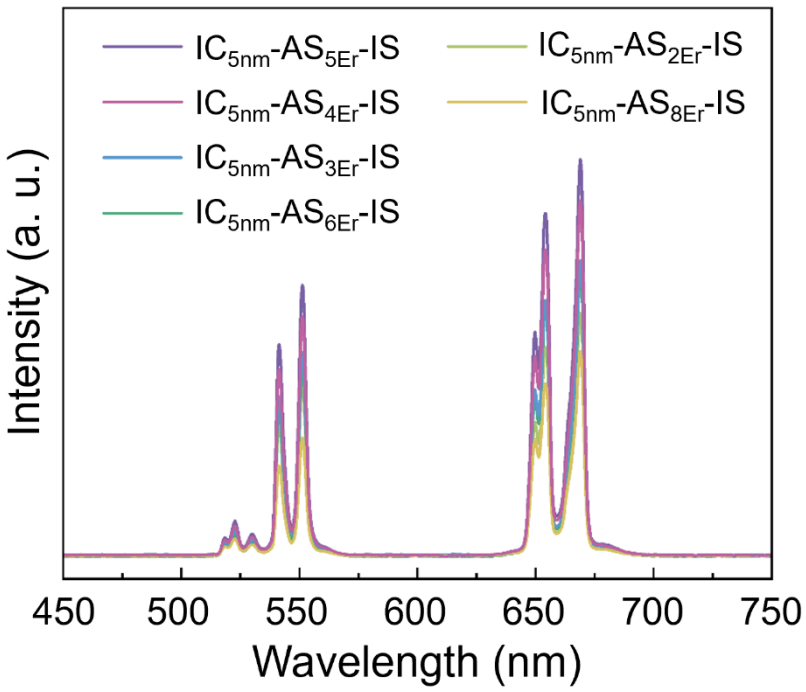

Figure S4.10 **Upconversion luminescence spectra of $LiLuF_4$@$LiLuF_4$:Ce^{3+}, Yb^{3+}, *y* mol% Er^{3+}@$LiLuF_4$ with an inert core of 5 nm (IC_{5nm}-AS_{yEr}-IS, *y* = 2, 3, 4, 5, 6, 8).**

Excitation: 980 nm laser. The emission centered at around 525/545 and 660 nm are attributed to the radiative transitions from $^2H_{11/2}$/$^4S_{3/2}$, and $^4F_{9/2}$ to the ground state $^4I_{15/2}$, respectively.

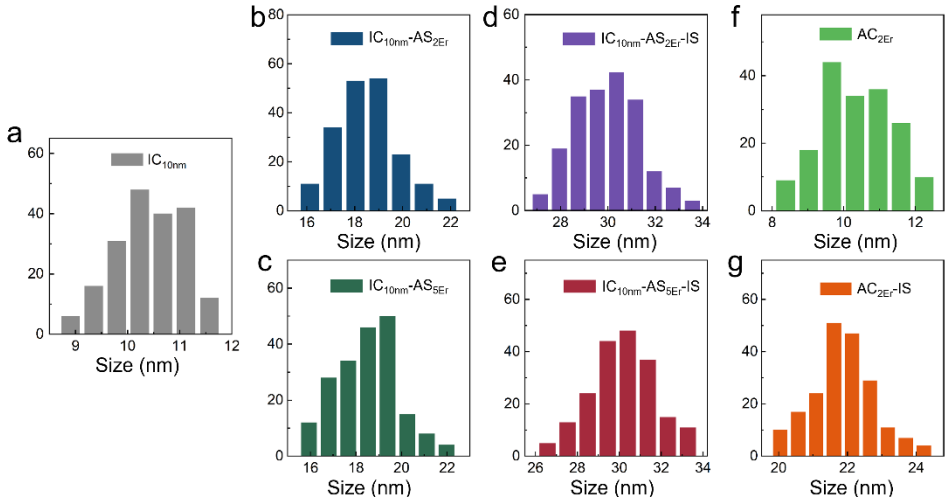

Figure S4.11 **Size distribution of RENPs with the inert core of 10 nm and active core.**

Size distribution of (a) $LiLuF_4$ with 10 nm (IC_{10nm}), (b-c) $LiLuF_4$@$LiLuF_4$:Ce^{3+}, Yb^{3+}, *y* mol% Er^{3+} (IC_{10nm}-AS_{yEr}, *y* = 2, 5), (d-e) $LiLuF_4$@$LiLuF_4$:Ce^{3+}, Yb^{3+}, *y* mol% Er^{3+}@$LiLuF_4$ (IC_{10nm}-AS_{yEr}, *y* = 2, 5) (f) $LiLuF_4$:Ce^{3+}, Yb^{3+}, Er^{3+} (AC_{2Er}) and (g) $LiLuF_4$:Ce^{3+}, Yb^{3+}, Er^{3+}@$LiLuF_4$ (AC_{2Er}-IS) RENPs.

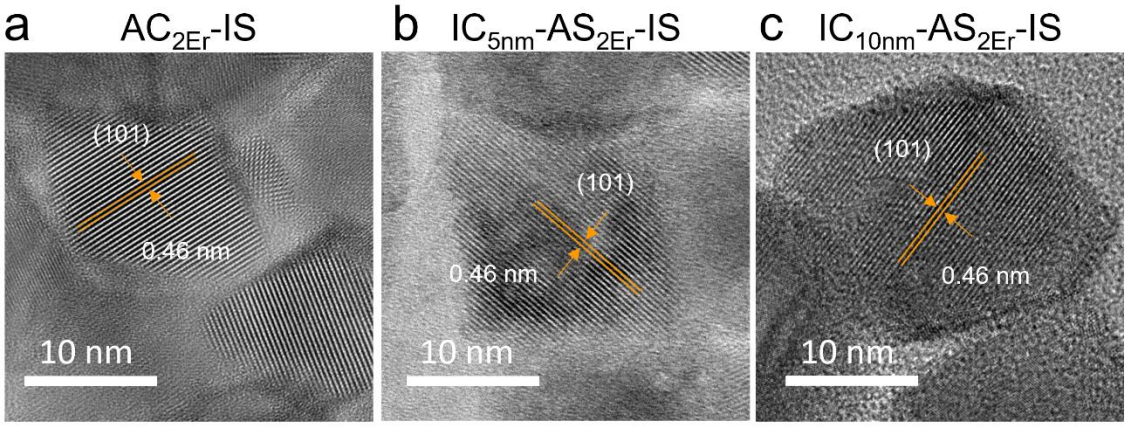

Figure S4.12 High-resolution TEM images.

High-resolution TEM images of (a) $LiLuF_4:Ce^{3+}$, Yb^{3+}, Er^{3+}@$LiLuF_4$ (AC_{2Er}-IS), and $LiLuF_4$@$LiLuF_4:Ce^{3+}$, Yb^{3+}, Er^{3+}@$LiLuF_4$ with varied sizes of the inert core (b) 5nm: IC_{5nm}-AS_{2Er}-IS, (c) IC_{10nm}-AS_{2Er}-IS.

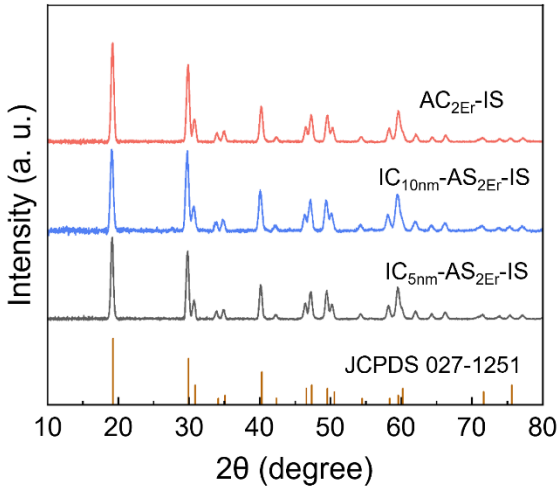

Figure S4.13 XRD patterns of RENPs with the inert core of 5, 10 nm, or active core.

XRD patterns of $LiLuF_4$@$LiLuF_4:Ce^{3+}$, Yb^{3+}, Er^{3+}@$LiLuF_4$ with varied inert core size 5 nm (IC_{5nm}-AS_{2Er}-IS), and 10 nm (IC_{10nm}-AS_{2Er}-IS) and $LiLuF_4:Ce^{3+}$, Yb^{3+}, Er^{3+}@$LiLuF_4$ (AC_{2Er}-IS) RENPs. Diffraction patterns of pure $LiLuF_4$ are also shown.

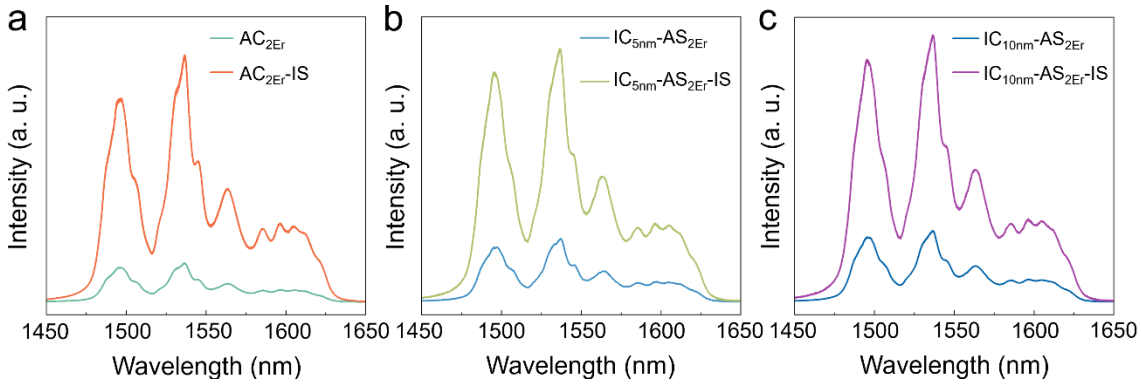

Figure S4.14 Downshifting photoluminescence intensity between core and core-shell RENPs.

Downshifting spectra of (a) AC_{2Er} active core, AC_{2Er}-IS active core-inert shell, and $LiLuF_4$@$LiLuF_4$:Ce^{3+}, Yb^{3+}, Er^{3+} inert core-active shell, $LiLuF_4$@$LiLuF_4$:Ce^{3+}, Yb^{3+}, Er^{3+}@$LiLuF_4$ inert core-active shell-inert shell with same 2 mol% Er^{3+} dopant concentration but varied size of the inert core of (b) 5 nm: IC_{5nm}-AS_{2Er} and IC_{5nm}-AS_{2Er}-IS, (c) 10 nm: IC_{10nm}-AS_{2Er} and IC_{10nm}-AS_{2Er}-IS. Comparison of the emission intensity to show the enhancement of the outermost shell in different structures with the same dopant concentration of 2 mol% Er^{3+}.

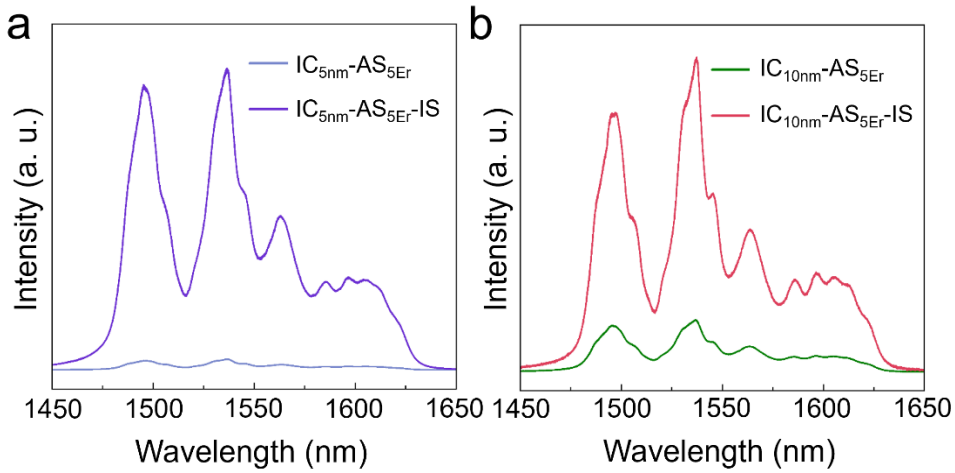

Figure S4.15 Downshifting photoluminescence intensity between core-shell and core-shell-shell RENPs.

Downshifting spectra of $LiLuF_4$@$LiLuF_4$:Ce^{3+}, Yb^{3+}, Er^{3+} inert core-active shell, and $LiLuF_4$@$LiLuF_4$:Ce^{3+}, Yb^{3+}, Er^{3+}@$LiLuF_4$ inert core-active shell-inert shell with same 5 mol% Er^{3+} dopant but with varied size of the inert core of (a) 5 nm: IC_{5nm}-AS_{5Er} and IC_{5nm}-AS_{5Er}-IS, (b) 10 nm: IC_{10nm}-AS_{5Er} and IC_{10nm}-AS_{5Er}-IS. Comparison of the emission intensity to show the enhancement of the outmost shell in different structures with the same doping concentration of 5 mol% Er^{3+}.

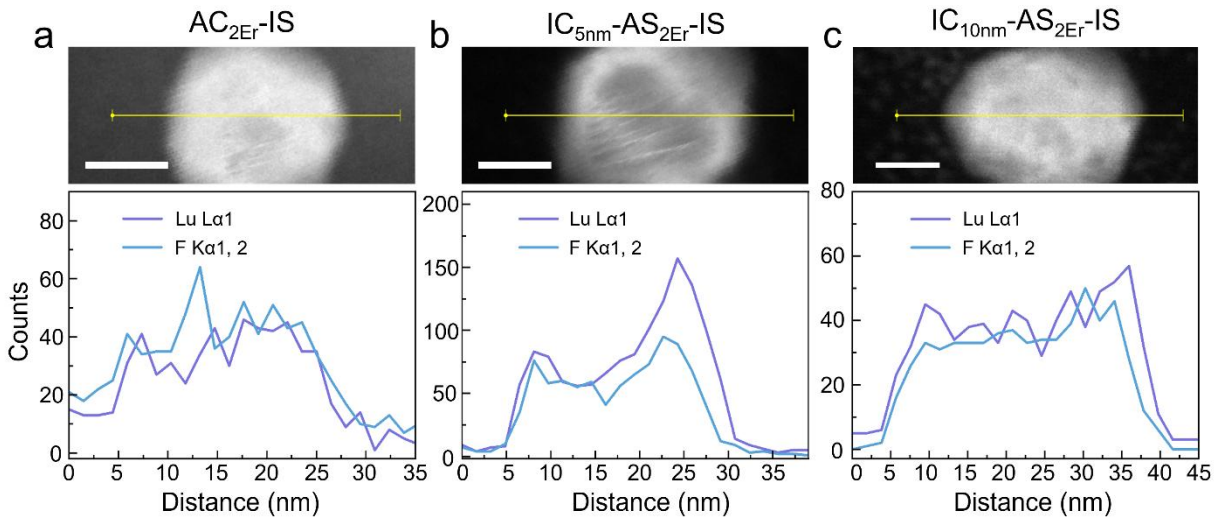

Figure S4.16 EDS line scanning of the inert core-active shell-inert shell and active core-inert shell RENPs.

EDS line scanning of (a) $LiLuF_4:Ce^{3+}$, Yb^{3+}, Er^{3+}@$LiLuF_4$ active core-inert shell (AC_{2Er}-IS), $LiLuF_4$@$LiLuF_4:Ce^{3+}$, Yb^{3+}, Er^{3+}@$LiLuF_4$ with same 2 mol% Er^{3+} dopant but varied size of the inert core of (b) 5 nm: IC_{5nm}-AS_{2Er}-IS, (c) IC_{10nm}-AS_{2Er}-IS. Scale bar: 10 nm.

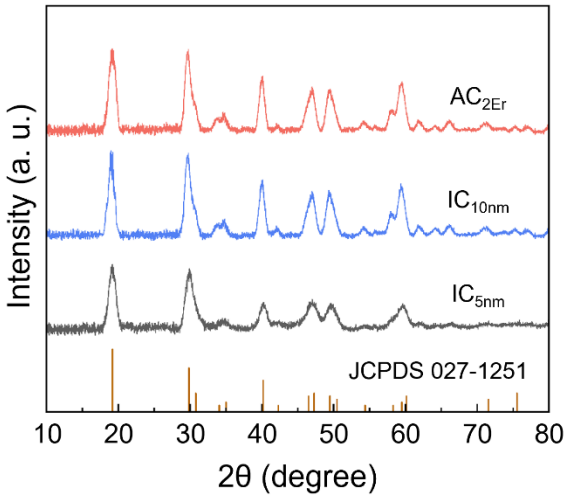

Figure S4.17 XRD patterns of inert core and active core RENPs.

XRD patterns of $LiLuF_4$ inert core with varied sizes of 5 nm (IC_{5nm}), 10 nm (IC_{10nm}) and $LiLuF_4:Ce^{3+}$, Yb^{3+}, Er^{3+} active core (AC_{2Er}) RENPs. Diffraction patterns of pure $LiLuF_4$ are also shown.

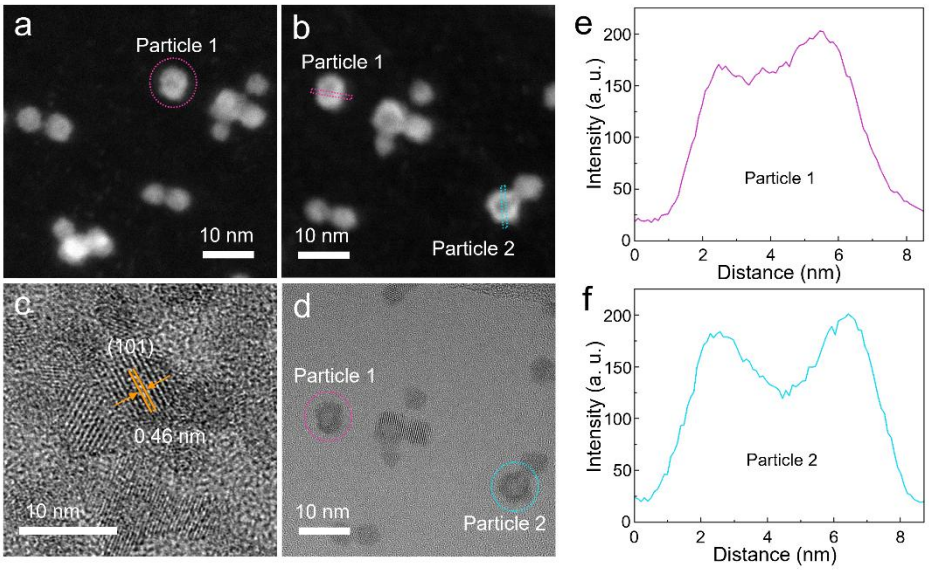

Figure S4.18 HAADF-STEM and HRTEM image of the inert core before and after experiment.

HAADF-STEM image of the inert core of 5 nm (IC_{5nm}) (a) before and (b) after line scanning. (c) HRTEM of IC_{5nm} without line scanning operation. (d) Same condition as (b) but showing the HRTEM image. (e-f) Intensity distribution along the selected area in (b) of particle 1 and particle 2.

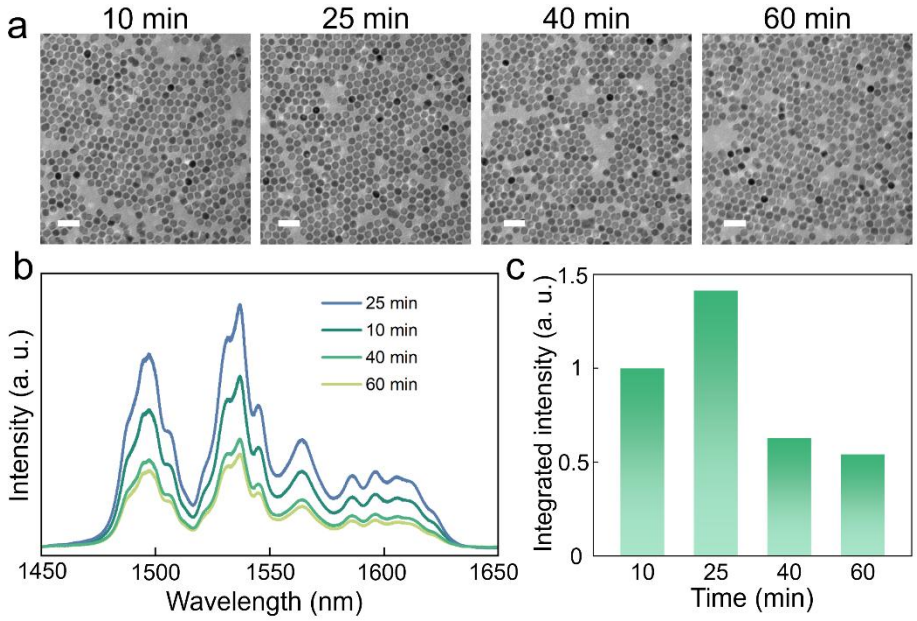

Figure S4.19 TEM image and NIR downshifting luminescence performance of IC_{5nm}-AS_{2Er} reacted at different time slots.

(a) TEM images of $LiLuF_4$@$LiLuF_4$:Ce^{3+}, Yb^{3+}, Er^{3+} (IC_{5nm}-AS_{2Er}) reacted at different time of 10 min, 25 min, 40 min to 60 min. (b) NIR downshifting luminescence spectra of IC_{5nm}-AS_{2Er} under 980 nm laser excitation and (c) the integrated intensity.

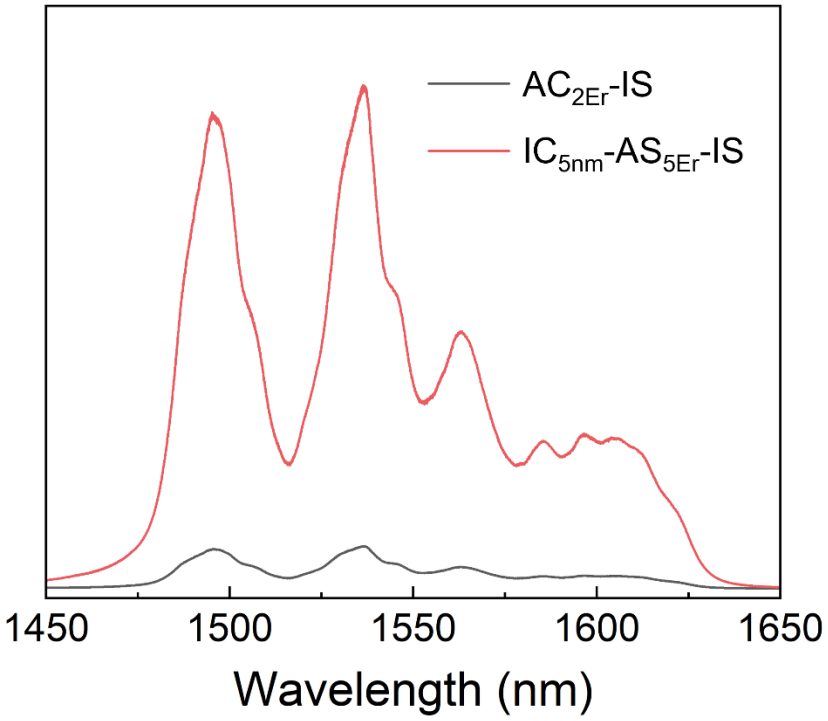

Figure S4.20 NIR photoluminescence spectrum comparison between the IC_{5nm}-AS_{2Er}-IS and AC_{2Er}-IS.

NIR spectra of optimized $LiLuF_4$@$LiLuF_4$:Ce^{3+}, Yb^{3+}, Er^{3+}@$LiLuF_4$ with the inert core size of 5 nm (IC_{5nm}-AS_{2Er}-IS) and @$LiLuF_4$:Ce^{3+}, Yb^{3+}, Er^{3+}@$LiLuF_4$ (AC_{2Er}-IS) under 980 nm laser excitation.

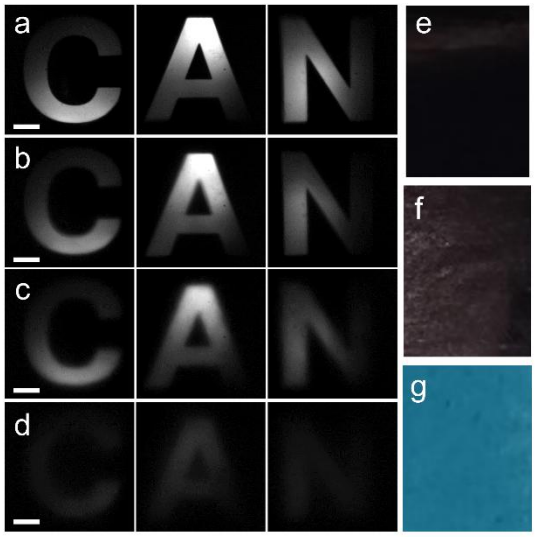

Figure S4.21 NIR image of the IC_{5nm}-AS_{5Er}-IS without or with with different obstacles.

NIR image of the IC_{5nm}-AS_{5Er}-IS (a) with no cover or covered with different obstacles: (b) polyethylene terephthalate film, (c) polypropylene with acrylic adhesive, (d) cellulose paper. Visible image of the covered obstacles: (e) polyethylene terephthalate film, (f) polyethylene terephthalate film, (g) cellulose paper Scale bar: 50 mm.

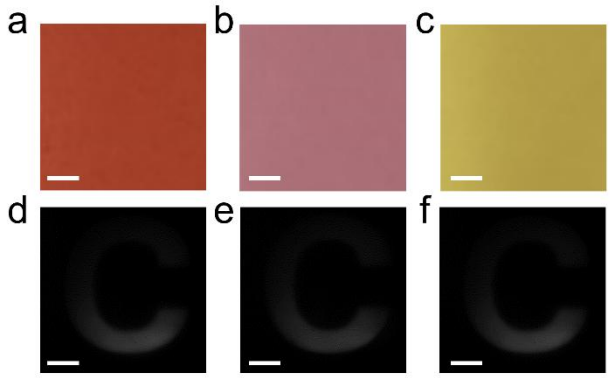

Figure S4.22 Visible images of cellulose papers and NIR image of IC_{5nm}-AS_{2Er}-IS through cellulose papers.

(a-c) Visible images of cellulose paper with different colors. (d-f) NIR images of IC_{5nm}-AS_{2Er}-IS covered by the different colors of cellulose paper. Scale bar: 50 µm.

5 EFFECT OF H_2O ON THE UPCONVERSION (UC) AND DOWNSHIFTING (DS) LUMINESCENCE NANOTHERMOMETRY

Effect of H_2O on the upconversion (UC) and downshifting (DS) luminescence nanothermometry

Effet de l'H2O sur la nanothermométrie par luminescence de conversion ascendante (UC) et de décalage vers le rouge (DS)

Auteurs :

Miao Liu[a], Paulina Rajchel-Mieldzioć[b], Piotr Fita[b], Jinyang Liang*[a], Fiorenzo Vetrone*[a]

[a]*Centre Énergie, Matériaux et Télécommunications, Institut National de la Recherche Scientifique, Université du Québec, 1650 boulevard Lionel-Boulet, Varennes, Québec J3X 1P7, CANADA*

[b]*Institute of Experimental Physics, Faculty of Physics, University of Warsaw, Pasteura 5, 02-093 Warsaw, Poland.*

Submitted to Nanoscale in 25 March 2025, current status: under review.

Contribution des auteurs:

Study conceptualization and design was conducted by Miao Liu and Fiorenzo. Material preparation, data collection, investigation and formal analysis were performed by Miao Liu and Paulina Rajchel-Mieldzioć. The first draft of the manuscript was written by Miao Liu and all authors commented on previous versions of the manuscript. All authors have read and approved the final manuscript.

Abstract

Owing to the noninvasive temperature sensing with high spatial resolution, luminescence nanothermometry has showcased its advantages and has been successfully applied in biomedical sciences. RENPs substantially aided this field due to their unique optical properties, which can be excited by low-energy photons to emit higher-energy (upconversion, UC) or lower-energy (downshifting, DS) photons. However, the luminescence properties of RENPs are affected by various factors such as excitation power density and surrounding media, potentially compromising the reliability of the measured temperature and limiting further applications. To gain deeper insights into the effect of water (H_2O) on the luminescence properties, RENPs with both UC and DS emissions were developed and then applied to sense temperature in a mixed solution of deuterium oxide (D_2O) and different volume ratios of H_2O. The H_2O-induced changes in UC and DS nanothermometry characteristics are presented, and the possible reasons are discussed in detail. Overall, this work paints a realistic outlook on the potential and pitfalls of UC and DS nanothermometry, which is critical for future in vivo applications.

5.1 Introduction

Luminescence nanothermometry, a noninvasive technique, allows for local temperature measurement with high spatial resolution, high thermal sensitivity, and minimal physical contact with the object.(Brites *et al.*, 2019; Jaque *et al.*, 2012; Zhou *et al.*, 2020d) Benefiting from these advantages, luminescence nanothermometry is highly desired for thermal sensing in both fundamental studies and preclinical research.(Castioni *et al.*, 2025; del Rosal *et al.*, 2018; Wang *et al.*, 2024b) For instance, luminescence nanothermometry has made it possible to diagnose early-stage cancer as well as conduct thermal therapies.(Li *et al.*, 2024b; Wang *et al.*, 2024b; Wu *et al.*, 2024) Rare-earth doped nanoparticles are of particular interest among various luminescent nanothermometers. Their significance arises from the ability to convert the NIR excitation light into higher-energy emissions spanning the UV-visible and NIR regions via a multiphoton process known as upconversion.(Chen *et al.*, 2014b; Liu *et al.*, 2018a; Shi *et al.*, 2014) Meanwhile, under the same NIR laser excitation, RENPs can also emit a lower-energy photon in the NIR region, a process called downshifting (DS). (Liu *et al.*, 2024a; Zhong *et al.*, 2017b)The typical UC emission for nanothermometry is from Er^{3+} doped RENPs in which the $^{2}H_{11/2}$ and $^{4}S_{3/2}$ excited states are in Boltzmann equilibrium such that changes in the surrounding temperature will affect their populations and also the luminescence intensity ratio. (Liu *et al.*, 2024d; Vetrone *et al.*, 2010) Different from the thermally coupled energy states of UC emission, temperature-dependent DS emission mostly necessitates phonon-assisted energy transfer processes (e.g. Yb^{3+}/Nd^{3+}, Er^{3+}/Ho^{3+}). (Kolesnikov *et al.*, 2022; Skripka *et al.*, 2017) Stark sublevels that follow Boltzmann equilibrium could also be employed in DS nanothermometry, although a special host material with high crystal field strength (e.g., $LiYbF_4$, $LiLuF_4$) is indispensable. (Liu *et al.*, 2024d) With the widespread development of RENPs from structural design to optimization in optical performance, both UC and DS emissions of RENPs have successfully demonstrated their leading role as temperature probes in biomedicine, including cell apoptosis, brain activity, immune reaction, and metabolic rate. (Brites *et al.*, 2019; Rodríguez-Sevilla *et al.*, 2022; Ximendes *et al.*, 2016b)

Nevertheless, luminescence properties are affected by certain factors and thus the accuracy of RENP nanothermometry has been traditionally underestimated. (Bednarkiewicz *et al.*, 2020) The emission of the luminescent ions is susceptible to alteration by experimental and external factors such as excitation power density and the attenuation coefficient of the surrounding media.(Bednarkiewicz *et al.*, 2020; Marciniak *et al.*, 2016) To minimize potential errors in temperature detection, maintaining identical *in vitro* and *in vivo* experimental conditions is ideal.

However, this is not always possible, making it essential to analyze and describe the influence of external factors to ensure more reliable temperature readouts. One key external factor is the surrounding medium, water (H_2O), as it is the major constituent of the human body. (Labrador-Páez *et al.*, 2023)It has been reported that DS emission of Er^{3+} in aqueous solution can be severely quenched compared with that in cyclohexane.(Huang *et al.*, 2024; Jia *et al.*, 2020a; Zhong *et al.*, 2017b) In fact, H_2O molecules close to the surface of RENPs will quench specific excited states of luminescent ions, regardless of whether RENPs are dispersed in aqueous solutions or exposed to air as a powder. This quenching happens to both UC and DS emissions as if the dipole-dipole coupling of the electronic state transitions of the luminescent ions interacts with the stretching vibration (3000-3600 cm^{-1}) of the −OH group in the water.(Arppe *et al.*, 2015; Feng *et al.*, 2021; Wang *et al.*, 2019) As a result, the penetration depth in tissues is limited, and temperature readouts can become inaccurate, thereby hampering broader biomedical applications of RENP nanothermometry. While great effort has been made toward enhancing the emission intensity or tuning the emission wavelength to the biological windows where the absorption coefficient of water is relatively low, the influence of H_2O on the accuracy of RENP nanothermometry has not been explored in detail. To raise awareness about the importance of this matter, examining the reliability of RENP nanothermometry by evaluating how UC and DS emissions are affected in the physiological range (20-45 °C) by the H_2O cannot be overlooked.

In this work, we present Er^{3+} doped $LiLuF_4$ RENPs operating in aqueous medium as nanothermometers. The developed structure takes advantage of both visible and NIR emissions by UC and DS luminescence processes under the same excitation source. The effect of water on UC and DS nanothermometry is systematically studied within the physiological temperature range. The possible reasons for the different H_2O-induced temperature readouts are discussed in detail. Herein, we shed light on the fundamental aspects governing the optical response of RENPs to temperature change in aqueous environments, advancing the reliability of nanothermometry in biomedical contexts.

5.2 Results and discussion

5.2.1 Crystallinity and morphology

$LiLuF_4$:18%Yb^{3+}, 2%Er^{3+}, 1%Ce^{3+}@$LiLuF_4$ (Lu:Er@Lu) core-shell RENPs were prepared *via* a thermal decomposition method.(Cheng *et al.*, 2018c) Briefly, the core $LiLuF_4$:18%Yb^{3+}, 2%Er^{3+}, 1%Ce^{3+} (Lu:Er) RENPs were stabilized from the first nuclei nanoparticles, followed by the

epitaxial growth of the inert shell layer to form the desired core-shell architecture. As shown in Figure 5.1a, both Lu:Er and Lu:Er@Lu RENPs crystalized in the tetragonal phase. The peaks in the XRD pattern of Lu:Er@Lu are quite sharp, implying the desirable crystallinity of Lu:Er@Lu nanocrystals. TEM images (Figure 5.1b, c) present the monodispersed RENPs with uniform size and bipyramidal shape. The exact size was then estimated from 200 nanoparticles in the TEM images. As shown in Figure 5.1e, the size of Lu:Er falls within a narrow range of 10-13 nm, whereas Lu:Er@Lu is larger at 20–26 nm due to the addition of the shell layer. The corresponding shell thickness was calculated to be 5-7.5 nm. The high-resolution TEM image further confirmed the crystal structure, as the measured lattice fringes of 0.46 nm matched the (101) plane spacing of tetragonal $LiLuF_4$ Moreover, the magnified image clearly presents the bipyramidal morphology.

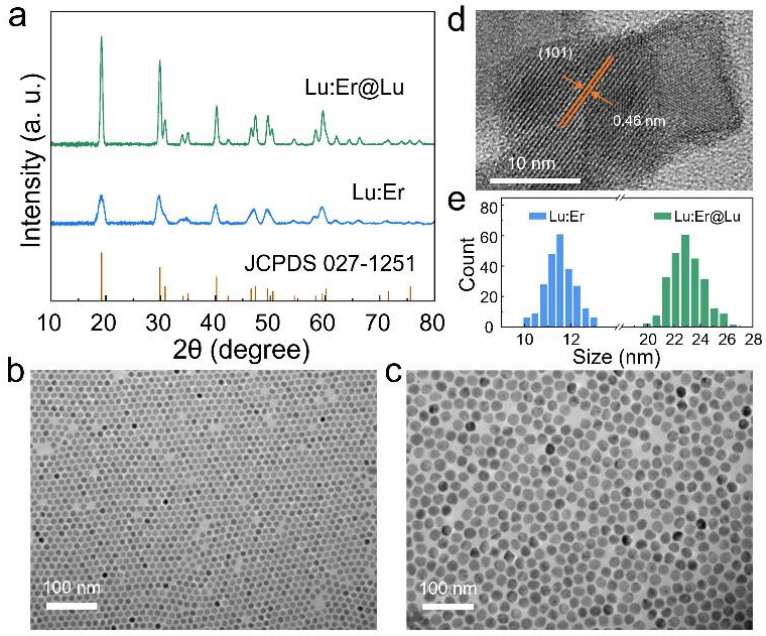

Figure 5.1 Crystallinity and morphology of Lu:Er and Lu:Er@Lu RENPs.

(a) XRD patterns of Lu:Er core and Lu:Er@Lu core-shell RENPs. The reference pattern corresponds to β-$LiLuF_4$ (JCPDS 027-1251). (b, c) TEM images of Lu:Er and Lu:Er@Lu RENPs. (d) High-resolution TEM image of Lu:Er@Lu RENPs. (e) Size distribution of Lu:Er and Lu:Er@Lu RENPs.

5.2.2 UC and DS optical properties

Under 980 nm excitation, the UC spectrum (Figure 5.2a) of Lu:Er and Lu:Er@Lu RENPs spans in the visible region with the major emission peaks located at around 407 nm, 523 nm, 552 nm, and 669 nm, which correspond to the radiative transitions of $^2H_{9/2} \rightarrow {}^4I_{15/2}$, $^2H_{11/2} \rightarrow {}^4I_{15/2}$, $^4S_{3/2} \rightarrow$

$^4I_{15/2}$, $^4F_{9/2} \rightarrow ^4I_{15/2}$, respectively. With the protection of the inert layer, the integrated UC emission intensity of Lu:Er@Lu increased by about eightfold compared with the core-only Lu:Er RENPs. With the same excitation wavelength, the DS emission could also be observed in Figure 5.2b. The emission at around 1535 nm is attributed to the $^4I_{13/2} \rightarrow ^4I_{15/2}$ transition of Er^{3+}. Multiple emission peaks originate from the split Stark sublevels in the $LiLuF_4$ host, which exerts high crystal field strength on the dopant ions. Similar to the UC emission enhancement, the DS emission intensity was also increased by about sixfold due to the inert shell which successfully prevented quenching at the nanoparticle surface. The luminescence mechanism is illustrated in Figure 5.2c. The Yb^{3+} ions, acting as the sensitizer, absorb the 980 nm excitation energy and transfer it to the adjacent Er^{3+} ions (the activator). The $^4I_{11/2}$ state of Er^{3+} is then populated by the ground-state absorption process. Subsequent energy transfer from Yb^{3+} to Er^{3+} ions induces a population of the $^4F_{7/2}$ state. After nonradiative relaxation from the $^4F_{7/2}$ to the lower $^2H_{11/2}$ and $^4S_{3/2}$ states, green emission occurs at 523/552 nm via the $^2H_{11/2}/^4S_{3/2} \rightarrow ^4I_{15/2}$ radiative transition. The $^4I_{11/2}$ state can also be deactivated by the nonradiative transition to the $^4I_{13/2}$ state, followed by the DS emission from $^4I_{13/2} \rightarrow ^4I_{15/2}$ or UC process from $^4I_{13/2}$ to $^4F_{9/2}$ by excited state absorption. Electrons in the $^4F_{9/2}$ level can either be excited to the higher $^2H_{9/2}$ state (leading to the blue emission at 407 nm) or radiatively decay to the $^4I_{15/2}$ ground state, resulting in red emission at around 669 nm.

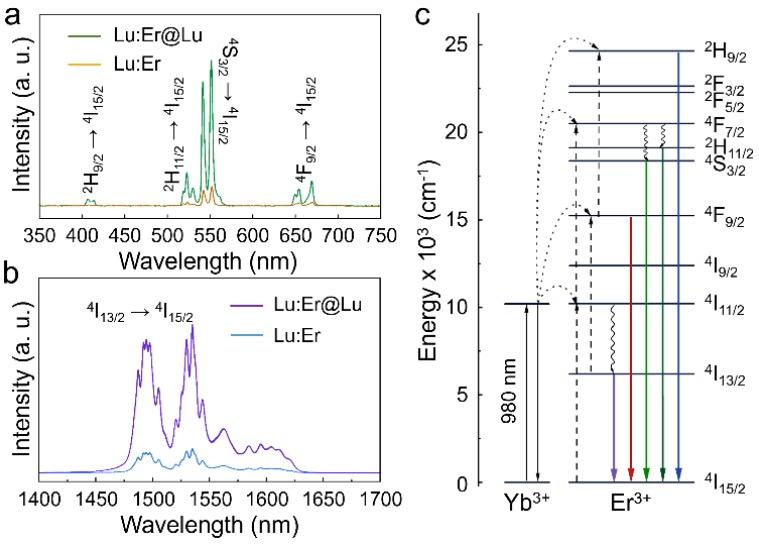

Figure 5.2 Optical properties of Lu:Er and Lu:Er@Lu RENPs.

(a, b) Upconversion and downshifting emission spectra of Lu:Er and Lu:Er@Lu RENPs excited by a 980 nm laser. (c) Energy level diagram of the Yb^{3+}, Er^{3+} co-doped system.

5.2.3 H_2O effect on the UC and DS nanothemometry

The temperature dependent UC emission characteristics of Lu:Er@Lu RENPs were then evaluated as the green emission of Er^{3+} is classically used for temperature sensing. The collected spectra were normalized to the highest peak, 552 nm. In Figure 5.3a empirical evidence indicates that the intensity profile near 523 nm exhibits an increment as the temperature increases from 20 °C to 45 °C This temperature-dependent UC emission was expected since the population of thermally coupled $^2H_{11/2}/^4S_{3/2}$ states follows the Boltzmann distribution, a phenomenon that is well established.(Brites *et al.*, 2019) The higher emission intensity at elevated temperatures was attributed to the enhanced population transfer from the $^4S_{3/2}$ level to the $^2H_{11/2}$ level. The UC luminescence intensity ratio (Δ_{UC}) between $^2H_{11/2} \rightarrow {}^4I_{15/2}$ (514−535 nm) and $^4S_{3/2} \rightarrow {}^4I_{15/2}$ (535−565 nm) transition was then calculated to indicate the temperature. To investigate the correlation between the H_2O content and the UC nanothermometry, the same measurement was conducted in the mixed solutions of H_2O and D_2O. The volume content of H_2O was changed from 0% to 45%. Dependencies of the measured $\Delta_{UC}(^2H_{11/2}/^4S_{3/2})$ on temperature were plotted in Figure 5.3b. A linear rise of the Δ_{UC} was observed in all mixed solutions; moreover, the slope of each curve appears to be consistent. According to the definition (Equation S3), the slope of the intensity-ratio curve reflects the absolute sensitivity (S_a) of the nanothermometers. As shown in Figure 5.3c, the derived S_a of Lu:Er@Lu RENPs in different mixed solutions remained nearly the same although subtle variations could still be discerned. Considering the slight difference (4.3%) between the lowest S_a value (0.162% $°C^{-1}$) and the highest S_a value (0.169% $°C^{-1}$), this minor discrepancy may be attributed to measurement or fitting errors. The preliminary result is that the absolute sensitivity appeared unaffected by H_2O content consistent with the principle that the thermometric nanothermometer characteristic depends on the intrinsic properties of nanothermometers. However, the relative sensitivity (S_r) showed a decreasing trend. To explore the reason for this decline in S_r, the calculation formula was revisited. Due to the nearly constant value of S_a, the change of S_r at different H_2O content mainly came from the altered Δ_{UC}, despite the same measurement temperature. Setting the Δ_{UC} at 0% H_2O as a standard, the linear deviation caused by H_2O content was plotted in Figure 5.3d. Although Δ_{UC} at 45% H_2O deviated by about 10%, this is a relatively large variation, given that the total change in the measured temperature range was only 20.8%. Therefore, this 10% deviation cannot be overlooked. In Figure 5.2a, UC luminescence intensity of Lu:Er@Lu RENPs was gradually decreased in mixed solutions with higher H_2O content. Interestingly, the quenching effect on the two emission bands was not equal; as shown in Figure S5.2b, 535−565 nm band was quenched more than the 514−535 nm

band. In addition, the UC red emission was also quenched in the presence of more H_2O (Figure S5.3). To better understand these observations, the absorption coefficients of H_2O and D_2O were examined at both the emission bands of RENPs and the excitation wavelength. In the emission range (Figure S5.3a), the absorption coefficients of H_2O and D_2O were relatively flat; however, at 980 nm, H_2O (0.473 cm^{-1}) had an absorption coefficient about 333 times higher than that of D_2O (0.0142 cm^{-1}). (Sullivan, 1963) This strong absorption of H_2O at 980 nm severely reduces the excitation power density, thereby affecting both the luminescence process and the resulting intensity. (Huang *et al.*, 2018a; Huang *et al.*, 2018b) Similar result of laser power density-induced variation on Δ_{UC} has already been observed before.(Jia *et al.*, 2024; Rühl *et al.*, 2021; Wang *et al.*, 2017) In mixed solutions with varying H_2O contents, the absorption at 980 nm differed, leading to non-identical excitation densities on the RENPs and hence shifts in Δ_{UC}. By converting Δ_{UC} to temperature, the readout temperature at various H_2O contents is presented in Figure S5.4, with more detailed values in Table S5.1. Note that the measured temperature difference between the mixed solution containing 45% and 0% H_2O can exceed 10 °C when Δ_{UC} deviates by 10%. Such a large difference in the readout temperature caused by the H_2O content emphasizes the importance of *in situ* calibration of nanothermometers. Moreover, the reliability of using the same nanothermometer in various biological media (e.g., cells with different hydration levels) should be carefully verified.

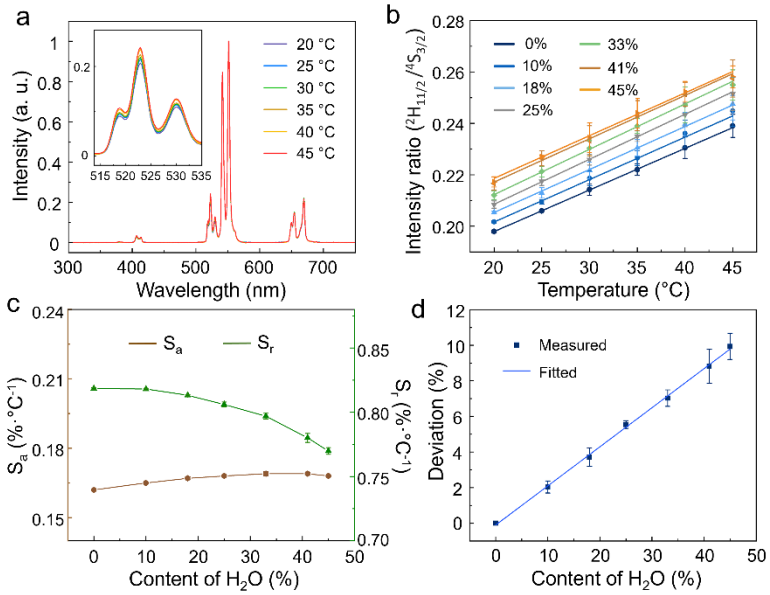

Figure 5.3 H_2O effect on the UC nanothermometry characteristics of Lu:Er@Lu RENPs.

(a) Temperature dependent UC emission spectrum of Lu:Er@Lu RENPs measured in pure D_2O solution. (b) UC emission intensity ratio of $^2H_{11/2}/^4S_{3/2}$ from 20 °C to 45 °C in the mixed solution of D_2O and H_2O, with H_2O content ranging from 0% to 45%. (c) Absolute sensitivity (S_a) and relative sensitivity (S_r) at 20 °C of Lu:Er@Lu RENPs. (d) Deviation of UC intensity ratio in the mixed solution with varying H_2O content.

In addition to the UC nanothermometry, the influence of H_2O content on the DS nanothermometry was also examined. The DS luminescence spectrum and the corresponding energy level diagram are shown in Figure 5.4. Owing to the high crystal field strength of the Lu-based host material, the $^4I_{13/2}$ and $^4I_{15/2}$ manifolds of Er^{3+} split into seven (Y_i, i = 1−7) and eight (X_j, j = 1−8) Stark sublevels, respectively. (Couto dos Santos *et al.*, 1998; Karayianis, 1971) Based on the energy gap, these Stark sublevels are divided into four groups: X_{1-4}, X_{5-8}, Y_{1-3}, and Y_{4-7}. The radiative transitions among these four groups are following: $Y_{4-7}\rightarrow X_{1-4}$, $Y_{1-3}\rightarrow X_{1-4}$, $Y_{4-7}\rightarrow X_{5-8}$, $Y_{1-3}\rightarrow X_{5-8}$, which correspond to emissions at 1494, 1534, 1562, and 1595 nm, respectively. Notably, the energy gap between Y_{1-3}, and Y_{4-7} is less than 200 cm^{-1}, meaning the higher Stark sublevel (Y_{4-7}) is easily thermally populated from the lower one (Y_{1-3}). As a result, the DS intensity ratio Y_{4-7}/Y_{1-3} (Δ_{DS}) increases with temperature. Emission from Y_{1-3} state includes bands 2 and 4, while emission from Y_{4-7} contains band 1 and 3 (Figure 5.4b).(Liu *et al.*, 2023; Zhao *et al.*, 2024) To determine which emission bands are most suitable for nanothermometry, DS luminescence spectra were recorded in mixed solutions with H_2O content varying from 0% to 33% (Figure 5.5a). After normalization at 1534 nm, the integrated intensity of each emission band was plotted (Figure S5.6). Emission band 1 showed a marked decline with higher H_2O content in the mixed solution, likely due to the high absorption coefficient of H_2O at this wavelength/range (Figure S5.7). The energy gap between $^4I_{13/2}$ and $^4I_{15/2}$ is about 6700 cm^{-1},(Couto dos Santos *et al.*, 1998) −roughly twice the stretch vibration frequency of -OH (3100-3700 cm^{-1}).(Hazra *et al.*, 2020a) As a result, the $^4I_{13/2}$ state can be deactivated by two-phonon vibrations of the −OH group, attenuating the overall DS emission. Moreover, the first overtone of water's stretching vibrations reaches its absorption maximum in the 1400-1500 nm range, overlapping with the band 1.(Labrador-Páez *et al.*, 2023; Renati *et al.*, 2019) Thus, band 1 is not ideal for temperature detection. Although the long-wavelength side of the DS emission was also attenuated, the quenching was much weaker than at band 1. Therefore, DS emission bands 3 and 4 (corresponding to $Y_{4-7}\rightarrow X_{5-8}$, and $Y_{1-3}\rightarrow X_{5-8}$ transitions) were used for temperature monitoring (Figure 5.5b). In contrast, D_2O exhibits no evident absorption across the entire DS luminescence spectrum, making it an ideal reference for evaluating the impact of H_2O on the DS nanothermometry.

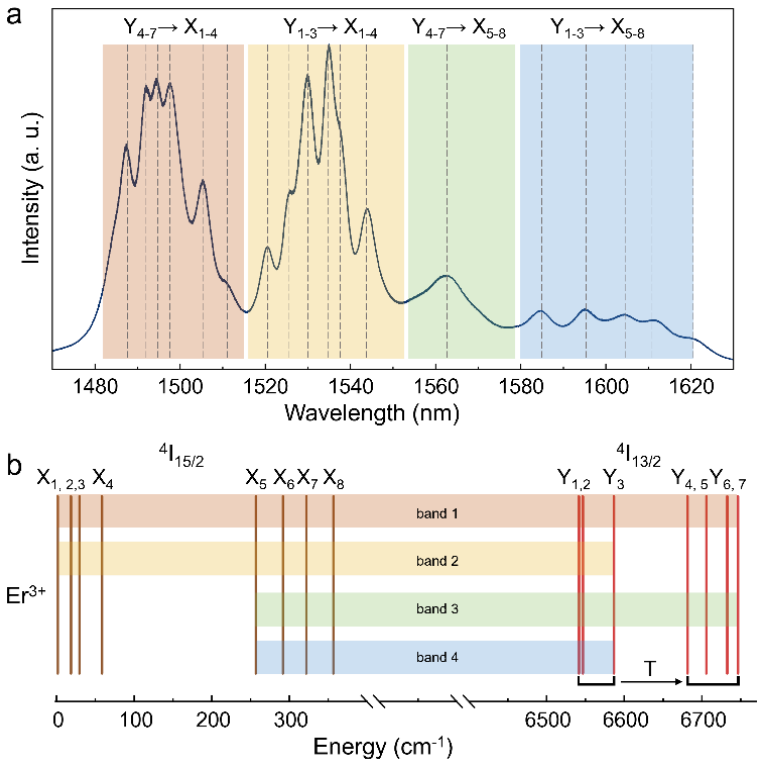

Figure 5.4 DS photoluminescence spectrum of Lu:Er@Lu RENPs and energy level diagram.

(a) DS emission spectrum of Lu:Er@Lu RENPs under 980 nm laser excitation. The dashed lines denote transitions from the Y_{1-7} Stark sublevels to the X_{1-8} sublevels. (b) Energy levels of the $^4I_{15/2}$ and $^4I_{13/2}$ multiplets of Er^{3+} in $LiLuF_4$ RENPs, showing four grouped transitions observed in (a).

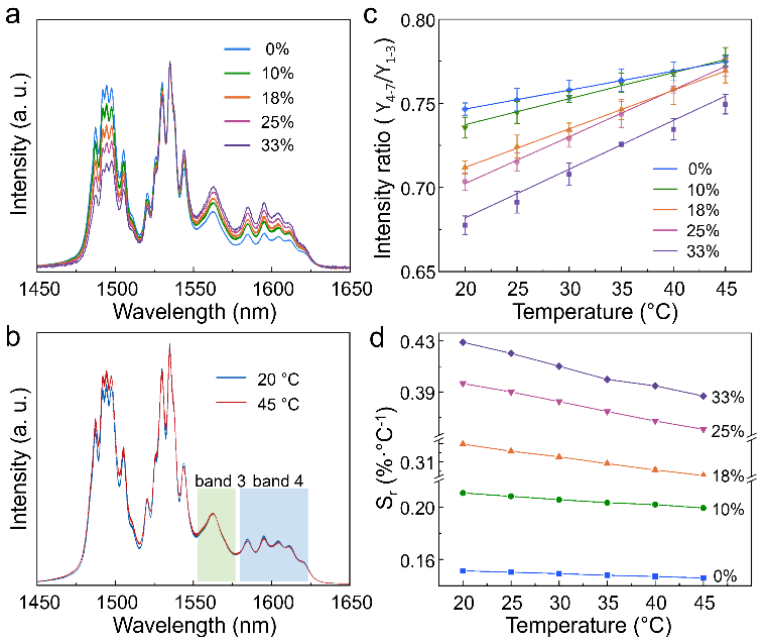

Figure 5.5 H_2O effect on the DS nanothermometry characteristics of Lu:Er@Lu RENPs.

(a) Normalized DS emission spectra of Lu:Er@Lu RENPs in mixed solutions with various H_2O contents at room temperature. (b) Temperature-dependent DS emission spectra of Lu:Er@Lu RENPs in pure D_2O solution. (c) DS intensity ratio of Y_{4-7} /Y_{1-3} from 20 °C to 45 °C in mixed solutions with H_2O content ranging from 0% to 45%. (d) Relative sensitivity of Lu:Er@Lu RENPs in mixed solutions with different H_2O contents.

Because H_2O quenching at the longer-wavelength side of the studied range, luminescence intensity from the Y_{4-7} state decreased more than that from the Y_{1-3} state. Consequently, Δ_{DS} for Y_{4-7}/Y_{1-3} at 20 °C dropped greatly in Figure 5.5c as more H_2O was added to the mixed solution. At elevated temperatures, the higher Δ_{DS} arises from thermally enhanced population in the Y_{4-7} state. Although all the curves could be fitted linearly regardless of the solution, their slopes were not identical. This difference indicates that thermally induced enhancement of Δ_{DS} varies in mixed solutions with different H_2O contents. The relative sensitivity also behaves differently (Figure 5.5d), reflecting the fact that emissions from the thermally coupled Y_{4-7}/Y_{1-3} states are sensitive to H_2O content. In pure D_2O solution, the relative sensitivity exhibited only a minor change because of the low thermal enhancement in DS intensity ratio $\left(\frac{\partial \Delta_{DS}}{\partial T}\right)$ and the high ratio values (Δ_{DS}) compared with the counterpart in solutions mixed with H_2O. Meanwhile, the substantial improvement of absolute sensitivity when more H_2O was added suggests that the contribution from H_2O outweighs the effect of temperature change. The change in Δ_{DS} prompted by H_2O during temperature measurement should be attributed to two aspects. First, H_2O-induced quenching affects the $\Delta_{DS,}$ since the absorption coefficient of H_2O at emission bands 3 and 4 are relatively high and differ from each other. The detected emission intensity undergoes attenuation as it propagates through the surrounding medium, which follows the Beer–Lambert law. According to this law, the detected intensity I_λ decreases exponentially, as described by the following equation:(Muñoz-Ortiz *et al.*, 2022)

$$I_\lambda \sim I_0 e^{-h*\alpha_{ext}} \tag{5.1}$$

Where I_0 is the originally emitted intensity from the Lu:Er@Lu RENPs, λ is the emitted wavelength, α is the extinction coefficient, *h* is the travel depth of the emitted photons to the detector, and $h*$ is the average distance travelled by the emitted photons, depending on *h* and the number of internal reflections in the cuvette wall before reaching the detector. The extinction of the emitted light is primarily attributed to the absorption and scattering, as follows:

$$\alpha(\lambda) = \alpha_a(\lambda) + \alpha_s(\lambda) \tag{5.2}$$

Where $\alpha_a(\lambda)$ and $\alpha_s(\lambda)$ are the absorption and scattering coefficients, respectively. The effect of scattering can be neglected because the size of the scattering centers (circa 23 nm) is much smaller than the analyzed wavelengths (>1560 nm). Equation (1) can thus be written as:

$$I_\lambda \sim I_0 e^{-h*\alpha_a(\lambda)} \quad (5.3)$$

Since the measurement conditions remained unchanged, we assume that *h** is constant for all the DS wavelengths studied. I_0 here was derived from the integrated intensity of each band recorded in pure D_2O. To demonstrate the impact of different water absorption coefficients at bands 3 and 4 (which form the ratio used in temperature measurement), a rough estimate was made using the midpoint absorption coefficients: 9.48 cm^{-1} at 1562 nm in band 3 and 6.99 cm^{-1} at 1600 nm in band 4.(Wieliczka *et al.*, 1989) According to Equation (3), after passing through the cuvette in pure water, the detected emission intensity ratio I_{band3}/I_{band4} can diverge from the initial emission intensity ratio ($I_{0\ band3}/I_{0\ band4}$) by as much as 0.29-fold (see SI, 71% decrement). Crucially, this significant discrepancy stems solely from the distinct absorption coefficients of H_2O at different wavelengths within the considered ranges, and the effect becomes more pronounced as the optical path length increases.

Temperature-dependent Δ_{DS} in pure D_2O solution changed from 0.747 at 20 °C to 0.775 at 45 °C, increasing by 1.04-fold (4% increment). In contrast, H_2O-induced variation in the intensity ratio is much greater than that caused by temperature change, overshadowing the temperature effect and thereby reducing the thermometers' accuracy. Moreover, the absorption coefficient spectrum of H_2O also depends on temperature. Essentially, a blue shift of the absorption spectrum has been observed at increased temperatures.(Czarnik-Matusewicz *et al.*, 2005) Thus, the Δ_{DS} will also be modified at various temperatures. To provide a direct impression of H_2O-induced temperature-sensing errors, a comparison of readout temperatures at different water contents was shown in Table S5.2. Using the temperature in pure D_2O solution as the standard, the reading error could exceed 20 °C. Such a large deviation again emphasizes the potential artifacts in real temperature sensing by utilizing the NIR emission of RENPs.

Given the importance of H_2O–induced temperature-reading errors, the next question is how to mitigate them to obtain reliable measurements. A complete characterization of the hydration level in the target region should be conducted. Meanwhile, other major absorption sources should be considered as well before performing *in vivo* experiments. A more convincing result could be provided by measuring the temperature in the same medium found in the tissues or organs under study, rather than using H_2O or another generic solution. *In situ* calibration is a promising solution although, it can sometimes be challenging to implement.

5.3 Conclusion

In summary, we explored a typical Lu:Er@Lu RENPs nanothermometer featuring both upconversion and downshifting emission under 980 nm excitation. The developed RENPs were successfully applied for temperature sensing within the physiological range of 20 to 45 °C. H_2O-induced attenuation of the luminescence intensity was observed in both UC and DS emissions. Further characterization revealed that differences in attenuation at each emission band affected the luminescence intensity ratio and, consequently, the temperature measurement result. In UC nanothermometry, the strong absorption of H_2O at 980 nm reduced the excitation power density, altering the $^2H_{11/2}/^4S_{3/2}$ intensity ratio and leading to deviations in the detected temperature. Meanwhile, in DS nanothermometry, the stretch vibration of OH in H_2O molecules interacted with the $^4I_{13/2} \rightarrow {}^4I_{15/2}$ transition substantially modifying the Stark sublevel intensity ratio (Y_{4-7}/Y_{1-3}) with the change in water content. The resulting deviations in temperature readout were analyzed in mixed solutions with varying H_2O content, using D_2O as a standard. These findings highlight the necessity of further standardization to ensure reliable RENP nanothermometry in biomedical applications.

Conflicts of interest

There are no conflicts to declare.

Data availability

The data supporting this article have been included as part of the ESI.† The corresponding author is available to provide further data upon request.

Acknowledgments

This work was supported in part by Natural Sciences and Engineering Research Council of Canada (RGPIN-2024-05551, I2IPJ 592655-24), Canada Research Chair Programs (CRC-2022-00119), INRS Chair in Nano-biophotonics, Canadian Cancer Society (707056); New Frontier in Research Fund (NFRFE-2020-00267); Fonds de Recherche du Québec–Nature et Technologies (203345–Centre d'Optique, Photonique, et Lasers); Fonds de Recherche du Québec–Santé (267406,280229).

5.4 References

Arppe R, Hyppänen I, Perälä N, Peltomaa R, Kaiser M, Würth C, Christ S, Resch-Genger U, Schäferling M, Soukka T (2015) Quenching of the upconversion luminescence of NaYF4:Yb3+,Er3+ and NaYF4:Yb3+,Tm3+ nanophosphors by water: the role of the sensitizer Yb3+ in non-radiative relaxation. *Nanoscale* 7(27):11746-11757.

Bednarkiewicz A, Marciniak L, Carlos LD, Jaque D (2020) Standardizing Luminescence Nanothermometry for Biomedical Applications. *Nanoscale* 12(27):14405-14421.

Brites CDS, Balabhadra S, Carlos LD (2019) Lanthanide-Based Thermometers: At the Cutting-Edge of Luminescence Thermometry. *Adv. Opt. Mat.* 7(5):1801239.

Castioni F, Auad Y, Blazit J-D, Li X, Woo SY, Watanabe K, Taniguchi T, Ho C-H, Stéphan O, Kociak M, Tizei LHG (2025) Nanosecond Nanothermometry in an Electron Microscope. *Nano Letters* 10.1021/acs.nanolett.4c05692.

Chen G, Qiu H, Prasad PN, Chen X (2014b) Upconversion Nanoparticles: Design, Nanochemistry, and Applications in Theranostics. *Chem. Rev.* 114(10):5161-5214.

Cheng T, Marin R, Skripka A, Vetrone F (2018c) Small and Bright Lithium-Based Upconverting Nanoparticles. *J. Am. Chem. Soc.* 140(40):12890-12899.

Couto dos Santos MA, Antic-Fidancev E, Gesland JY, Krupa JC, Lemaître-Blaise M, Porcher P (1998) Absorption and fluorescence of Er3+-doped LiYF4: measurements and simulation. *J. Alloys Comp.* 275-277:435-441.

Czarnik-Matusewicz B, Pilorz S, Hawranek JP (2005) Temperature-dependent water structural transitions examined by near-IR and mid-IR spectra analyzed by multivariate curve resolution and two-dimensional correlation spectroscopy. *Anal. Chim. Acta* 544(1):15-25.

del Rosal B, Ruiz D, Chaves-Coira I, Juárez BH, Monge L, Hong G, Fernández N, Jaque D (2018) In Vivo Contactless Brain Nanothermometry. *Adv. Funct. Mater.* 28(52):1806088.

Feng Y, Li Z, Li Q, Yuan J, Tu L, Ning L, Zhang H (2021) Internal OH− induced cascade quenching of upconversion luminescence in NaYF4:Yb/Er nanocrystals. *Light Sci. Appl* 10(1):105.

Hazra C, Skripka A, Ribeiro SJL, Vetrone F (2020a) Erbium Single-Band Nanothermometry in the Third Biological Imaging Window: Potential and Limitations. *Adv. Opt. Mater.* 8(23):2001178.

Huang B, Bergstrand J, Duan S, Zhan Q, Widengren J, Ågren H, Liu H (2018a) Overtone Vibrational Transition-Induced Lanthanide Excited-State Quenching in Yb3+/Er3+-Doped Upconversion Nanocrystals. *ACS Nano* 12(11):10572-10575.

Huang K, Liu H, Kraft M, Shikha S, Zheng X, Ågren H, Würth C, Resch-Genger U, Zhang Y (2018b) A protected excitation-energy reservoir for efficient upconversion luminescence. *Nanoscale* 10(1):250-259.

Huang Y, Hu J, Guo Y, Wang Z, Lin F, Zhu H (2024) Effect of –OH on the thermal enhancement properties of NIR-II lanthanide-doped nanoparticles in water. *Inorg. Chem. Front.* 11(10):3063-3072.

Jaque D, Vetrone F (2012) Luminescence nanothermometry. *Nanoscale* 4(15):4301-4326.

Jia M, Fu Z, Liu G, Sun Z, Li P, Zhang A, Lin F, Hou B, Chen G (2020a) NIR-II/III Luminescence Ratiometric Nanothermometry with Phonon-Tuned Sensitivity. *Adv. Opt. Mater.* 8(6):1901173.

Jia M, Li M, Li D, Zhang X, Chen G (2024) Excitation-Power Dependence of Lanthanide-Based Ratiometric Luminescent Nanothermometry. *Nano Lett.* 24(48):15450-15456.

Karayianis N (1971) Theoretical energy levels and g values for the 4I terms of Nd3+ and Er3+ in LiYF4. *Phys. Chem. Solids* 32(10):2385-2391.

Kolesnikov IE, Afanaseva EV, Kurochkin MA, Vaishlia EI, Kolesnikov EY, Lähderanta E (2022) Dual-center co-doped and mixed ratiometric LuVO4:Nd3+/Yb3+ nanothermometers. *Nanotechnology* 33(16):165504.

Labrador-Páez L, Kostiv U, Widengren J, Liu H (2023) Water: An Influential Agent for Lanthanide-Doped Luminescent Nanoparticles in Nanomedicine. *Adv. Opt. Mater.* 11(11):2200513.

Li D, Jia M, Jia T, Chen G (2024b) Ultrasensitive NIR-II Ratiometric Nanothermometers for 3D In Vivo Thermal Imaging. *Adv. Mater.* 36(11):2309452.

Liu M, Lai Y, Marquez M, Vetrone F, Liang J (2024a) Short-wave Infrared Photoluminescence Lifetime Mapping of Rare-Earth Doped Nanoparticles Using All-Optical Streak Imaging. *Adv. Sci.* 11(11):2305284.

Liu M, Liang J, Vetrone F (2024d) Toward Accurate Photoluminescence Nanothermometry Using Rare-Earth Doped Nanoparticles for Biomedical Applications. *Acc. Chem. Res.* 57(18):2653-2664.

Liu M, Shi Z, Wang X, Zhang Y, Mo X, Jiang R, Liu Z, Fan L, Ma C-g, Shi F (2018a) Simultaneous enhancement of red upconversion luminescence and CT contrast of NaGdF4:Yb,Er nanoparticles via Lu3+ doping. *Nanoscale* 10(43):20279-20288.

Liu S, An Z, Huang J, Zhou B (2023) Enabling efficient NIR-II luminescence in lithium-sublattice core—shell nanocrystals towards Stark sublevel based nanothermometry. *Nano Res.* 16(1):1626-1633.

Marciniak L, Waszniewska K, Bednarkiewicz A, Hreniak D, Strek W (2016) Sensitivity of a Nanocrystalline Luminescent Thermometer in High and Low Excitation Density Regimes. *J. Phys. Chem. C* 120(16):8877-8882.

Muñoz-Ortiz T, Abiven L, Marin R, Hu J, Ortgies DH, Benayas A, Gazeau F, Castaing V, Viana B, Chanéac C, Jaque D, Maturi FE, Carlos LD, Martín Rodríguez E, García Solé J (2022) Temperature Dependence of Water Absorption in the Biological Windows and Its Impact on the Performance of Ag2S Luminescent Nanothermometers. *Part. Part. Syst. Charact.* 39(11):2200100.

Renati P, Kovacs Z, De Ninno A, Tsenkova R (2019) Temperature dependence analysis of the NIR spectra of liquid water confirms the existence of two phases, one of which is in a coherent state. *J. Mol. Liq.* 292:111449.

Rodríguez-Sevilla P, Marin R, Ximendes E, del Rosal B, Benayas A, Jaque D (2022) Luminescence Thermometry for Brain Activity Monitoring: A Perspective. *Frontiers in Chemistry* 10.

Rühl P, Wang D, Garwe F, Müller R, Haase M, Krämer KW, Paa W, Heintzmann R, Heinemann SH, Stafast H (2021) Notes on thermometric artefacts by Er3+ luminescence band interference. *J. Lumin.* 232:117860.

Shi F, Zhao Y (2014) Sub-10 nm and monodisperse β-NaYF4:Yb,Tm,Gd nanocrystals with intense ultraviolet upconversion luminescence. *J. Mater. Chem. C* 2(12):2198-2203.

Skripka A, Benayas A, Marin R, Canton P, Hemmer E, Vetrone F (2017) Double rare-earth nanothermometer in aqueous media: opening the third optical transparency window to temperature sensing. *Nanoscale* 9(9):3079-3085.

Sullivan SA (1963) Experimental Study of the Absorption in Distilled Water, Artificial Sea Water, and Heavy Water in the Visible Region of the Spectrum*. *Journal of the Optical Society of America* 53(8):962-968.

Vetrone F, Naccache R, Zamarrón A, Juarranz de la Fuente A, Sanz-Rodríguez F, Martinez Maestro L, Martín Rodriguez E, Jaque D, García Solé J, Capobianco JA (2010) Temperature Sensing Using Fluorescent Nanothermometers. *ACS Nano* 4(6):3254-3258.

Wang M, Skripka A, Zhang Y, Cheng T, Ng M, Wong SY, Zhao Y, Sun X, Li X, Bhakoo KK, Chang AY, Rosei F, Vetrone F (2024b) Theranostic Nanocapsules: Heating, Imaging, and Luminescence Nanothermometry. *Chem. Mater.* 36(7):3285-3295.

Wang X, Wang Y, Bu Y, Yan X, Wang J, Cai P, Vu T, Seo HJ (2017) Influence of Doping and Excitation Powers on Optical Thermometry in Yb3+-Er3+ doped CaWO4. *Sci. Rep.* 7(1):43383.

Wang Z, Christiansen J, Wezendonk D, Xie X, van Huis MA, Meijerink A (2019) Thermal enhancement and quenching of upconversion emission in nanocrystals. *Nanoscale* 11(25):12188-12197.

Wieliczka DM, Weng S, Querry MR (1989) Wedge shaped cell for highly absorbent liquids: infrared optical constants of water. *Appl. Opt.* 28(9):1714-1719.

Wu Y, Li F, Wu Y, Wang H, Gu L, Zhang J, Qi Y, Meng L, Kong N, Chai Y, Hu Q, Xing Z, Ren W, Li F, Zhu X (2024) Lanthanide luminescence nanothermometer with working wavelength beyond 1500 nm for cerebrovascular temperature imaging in vivo. *Nat. Commun.* 15(1):2341.

Ximendes EC, Santos WQ, Rocha U, Kagola UK, Sanz-Rodríguez F, Fernández N, Gouveia-Neto AdS, Bravo D, Domingo AM, del Rosal B, Brites CDS, Carlos LD, Jaque D, Jacinto C (2016b) Unveiling in Vivo Subcutaneous Thermal Dynamics by Infrared Luminescent Nanothermometers. *Nano Lett.* 16(3):1695-1703.

Zhao Z, Dai M, Li K, Liang G, Wei Y, Fu Z (2024) Towards ultra-sensitive multimodal luminescent thermometers enabled by high crystal field strength of Lu2CaMg2Ge3O12:Yb3+,Nd3+,Er3+ phosphors. *Inorg. Chem. Front.* 11(22):7955-7965.

Zhong Y, Ma Z, Zhu S, Yue J, Zhang M, Antaris AL, Yuan J, Cui R, Wan H, Zhou Y, Wang W, Huang NF, Luo J, Hu Z, Dai H (2017b) Boosting the down-shifting luminescence of rare-earth nanocrystals for biological imaging beyond 1500 nm. *Nat. Commun.* 8(1):737.

Zhou J, Del Rosal B, Jaque D, Uchiyama S, Jin D (2020d) Advances and Challenges for Fluorescence Nanothermometry. *Nat. Methods* 17(10):967-980.

Supporting information

ELECTRONIC SUPPLEMENTARY INFORMATION (ESI)

Effect of H_2O on the upconversion and downshifting luminescence nanothermometry

Miao Liu[a], Paulina Rajchel-Mieldzioć[b], Piotr Fita[b], Jinyang Liang[a], Fiorenzo Vetrone*[a]*

[a] Centre Énergie, Matériaux et Télécommunications, Institut National de la Recherche Scientifique, Université du Québec, 1650 boulevard Lionel-Boulet, Varennes, Québec J3X 1P7, CANADA

*E-mail: jinyang.liang@inrs.ca, fiorenzo.vetrone@inrs.ca

[b] Institute of Experimental Physics, Faculty of Physics, University of Warsaw, Pasteura 5, 02-093 Warsaw, Poland.

Materials

Lu_2O_3 (REacton, 99.999%),Yb_2O_3 (REacton, 99.998%), Er_2O_3 (REacton, 99.99%), $Ce_2(CO_3)_3{\cdot}xH_2O$ (REacton, 99.9%), 1-octadecene (ODE, 90%), and oleic acid (OA, 90%) were obtained from Alfa Aesar (USA); lithium trifluoroacetate (98%), oleylamine (OM, 70%), trifluoroacetic acid (TFA, 99%), were purchased from Sigma-Aldrich. Water (H_2O, Distilled and filtered), and heavy water (D_2O, 99.9%) were purchased from MilliporeSigma. All chemicals were used as received.

Preparation of RENPs

Stoichiometric amounts of RE_2O_3 (RE = Lu, Yb, Er) and $Ce_2(CO_3)_3$ were selectively mixed with 5 mL trifluoroacetic acid and 5 mL distilled water in a 50 mL three-neck round bottom flask. The mixture was kept at 80 °C under vigorous stirring until the solution became clear. The temperature was then reduced to 60 °C to evaporate the residual trifluoroacetic acid and water and the precursor in powder was obtained.

Synthesis of $LiLuF_4$:18 mol% Yb^{3+}, 2 mol% Er^{3+}, 1 mol% Ce^{3+}. Core RENPs were prepared via thermal decomposition method from the first nuclei. A mixture (Solution A1) of 7 mL of OA, 7 mL

of oleylamine (OM), and 14 mL ODE was degassed at 110 °C for 15 min and then heated to 330 °C under an argon atmosphere. Meanwhile, 2.5 mmol CF_3COOLi and $(CF_3COO)_3RE$ (RE = Lu, Yb, Er, Ce) were mixed with 3 mL OA and 6 mL ODE (Solution B1) and then degassed at 125 °C for 30 min. Next, OM (3 mL) was added to Solution B1 and left to degas for 5 min. Once the temperature of Solution A1 was stable, Solution B1 was injected into Solution A1 at a rate of 1.5 mL min^{-1}. After a 1 h reaction at 330 °C, the preparation of the first nuclei was finished. Core RENPs were formed by stabilizing first nuclei with an excess OA. Specifically, 1.25 mmol first nuclei were mixed with 16 mL of OA and 16 mL of ODE in a 100 mL three-neck round bottom flask. The solution was degassed at 110 °C for 30 min and backfilled with argon gas. The temperature was raised to 315 °C, after which the reaction was continued for 1 h.

Synthesis of $LiLuF_4$:18 mol% Yb^{3+}, 2 mol% Er^{3+}, 1 mol% Ce^{3+}@$LiLuF_4$. The core-shell structure was prepared by epitaxial growth of the shell on the prepared cores. 0.5 mmol of $LiLuF_4$ core RENPs were mixed with 10 mL of OA and 10 mL of ODE (Solution A2). 2 mmol shell precursors $(CF_3COO)_3Lu$ together with CF_3COOLi were mixed with 10 mL of OA and 10 mL of ODE (Solution B2). Solution A1 and B1 were both degassed at 110 °C for 30 min. After degassing, Solution A1 was heated to 315 °C. Solution B1 was injected into Solution A1 at a 1.5 mL min^{-1} rate once the temperature of Solution A1 was stable. After cooling down to room temperature, the core-shell RENPs were washed with a hexane/ethanol (1:3) mixture three times and re-dispersed in hexane.

Surface modification: The OA ligand on the surface of RENPs was stripped with the assistance of nitrosyl tetrafluoroborate ($NOBF_4$). A total of 25 mg RENPs dispersed in 5 mL hexane was mixed with 5 mL dichloromethane solution of $NOBF_4$ (0.01 mol/L). The mixed solution was then shaken for 5 min until the precipitation of RENPs was clearly observed. The supernatant was removed after centrifugation. The precipitated RENPs were washed with a toluene and hexane mixture (1:1 by volume) once, followed by one wash in water. The final RENPs were redispersed in H_2O or D_2O for spectral measurements.

Characterization

Structural characterization: The crystallinity and phase of the Lu:Er core and Lu:Er@Lu core-shell RENPs were determined via X-ray powder diffraction (XRD) analysis on a Bruker D8 Advance Diffractometer using Cu Kα radiation (□□= 1.5418 Å). The morphology and size distribution of both core and core-shell were further investigated by TEM (Philips Tecnai 12).

The particle size was determined from TEM images using ImageJ software with a minimal set size of 200 particles.

Optical characterization: Upconversion (UC) and downshifting (DS) spectra of RENPs were recorded at room temperature under excitation from a 980 nm laser diode (MDL-SN-980-10W, CNI, China). The Laser excitation power density was approximately 30 W/cm^2 (based on power measurement and focal point size). All spectra were recorded in mixed solutions of D_2O and various volume ratios of H_2O at RENPs concentration of 4 mg/mL. The UC emission was recorded/collected using an Avaspec-ULS2048L spectrometer (Avantes, The Netherlands). Stray light from the excitation source was removed with an 830 nm short-pass filter (Newport Corp., USA). The DS spectra were collected using a Shamrock 500i monochromator (Andor, Ireland) equipped with an iDus InGaAs 1.7 NIR detector (Andor, Ireland). A 980 nm long-pass filter was used to remove any stray light from the excitation source.

Thermosensitivity characterization: The thermal response of Lu:Er@Lu RENPs was measured from 20 to 45 ºC in 5 ºC increments. The temperature was changed using a peltier-based cuvette holder (qpod 2e by Quantum Northwest, Washington, USA). To ensure thermal equilibrium at the set temperature, 8 min intervals were maintained between measurements.

The nanothermometric properties of the Lu:Er@Lu core-shell RENPs were determined from three consecutive heating–cooling cycles. Characteristic nanothermometry parameters were calculated following the guidelines set by C. D. S. Brites et al.(Brites *et al.*, 2019) The thermometric parameter, Δ (referring to the luminescence intensity ratio) was determined from the intensity ratio of the two separate regions of the UC and DS emissions of RENPs. Specifically, $\Delta_{UC} = I(^2H_{11/2})/I(^4S_{3/2})$ for upconversion emission and $\Delta_{DS} = I(Y_{4-7})/I(Y_{1-3})$ for downshifting. The Luminescence intensity ratio (between I_n and I_m) between thermally coupled electronic levels follows the Boltzmann distribution:

$$\Delta = \frac{I_n}{I_m} = B\exp\left(-\frac{\Delta E}{k_B T}\right), \tag{S5.1}$$

where ΔE is the energy gap between the thermally coupled electronic levels, k_B Boltzmann's constant, T is the absolute temperature and B is defined by:

$$B = \frac{c_n(\nu)A_n g_n h\nu_n}{c_m(\nu)A_m g_m h\nu_m} \tag{S5.2}$$

Where A_i (i = n, m) represents the spontaneous emission rates of the thermally coupled states (Einstein coefficients); g_i denotes these degeneracies, $c_i(\nu)$ is the spectral response of the experimental setup at the emission frequency ν_i, and h is Planck's constant.

Relative sensitivity, S_r, of the RENPs is given by:

$$S_r = \frac{1}{\Delta}\left|\frac{\partial \Delta}{\partial T}\right|, \tag{S5.3}$$

where $\left|\frac{\partial \Delta}{\partial T}\right|$ is the absolute sensitivity, S_a.

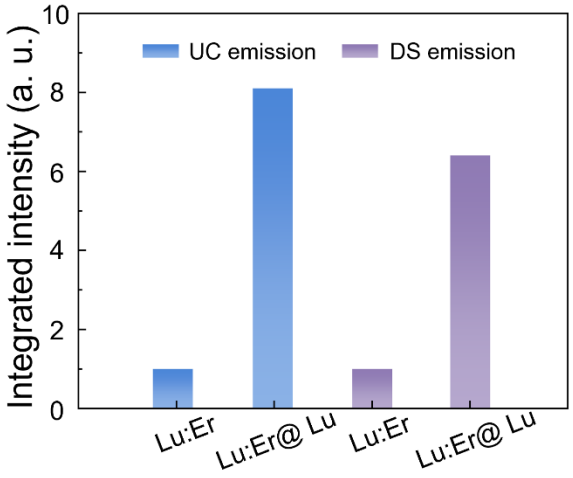

Figure S5.1 **Integrated UC and DS emission intensities of the whole spectrum of Lu:Er core and Lu:Er@Lu core-shell RENPs.**

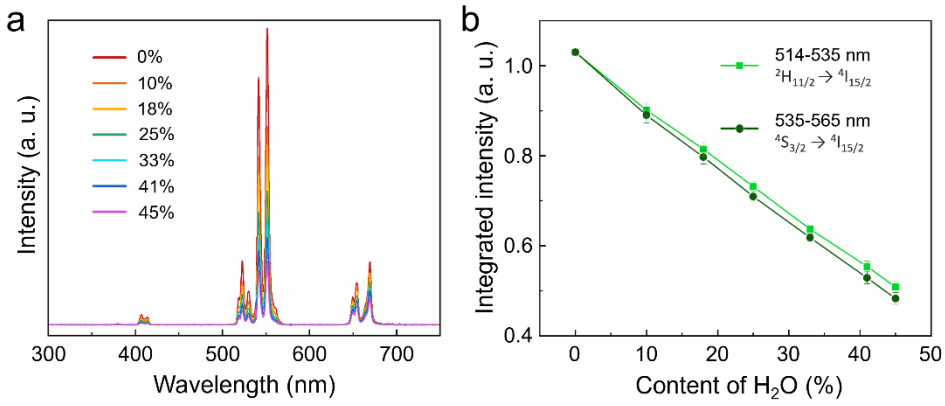

Figure S5.2 **H_2O effect on the UC photoluminescence spectrum of Lu:Er@Lu RENPs.**

(a) UC luminescence spectrum of Lu:Er@Lu RENPs recorded under 980 nm excitation in mixed solutions of D_2O with varying volume ratios of H_2O ranging from 0% to 45%. (b) Integrated intensities of emissions at 514−535 nm ($^2H_{11/2} \rightarrow {}^4I_{15/2}$) and 535−565 nm ($^4S_{3/2} \rightarrow {}^4I_{15/2}$) in (a) as a function of H_2O content.

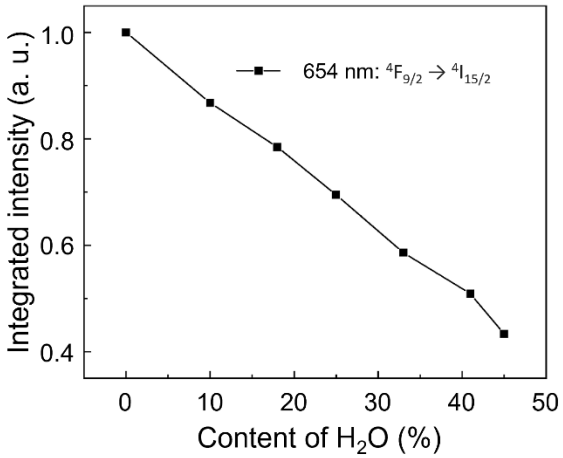

Figure S5.3 **The integrated intensity of emissions from 640 to 685 nm corresponding to the $^4F_{9/2} \rightarrow {}^4I_{15/2}$ transition with different contents of H_2O in the mixed solution.**

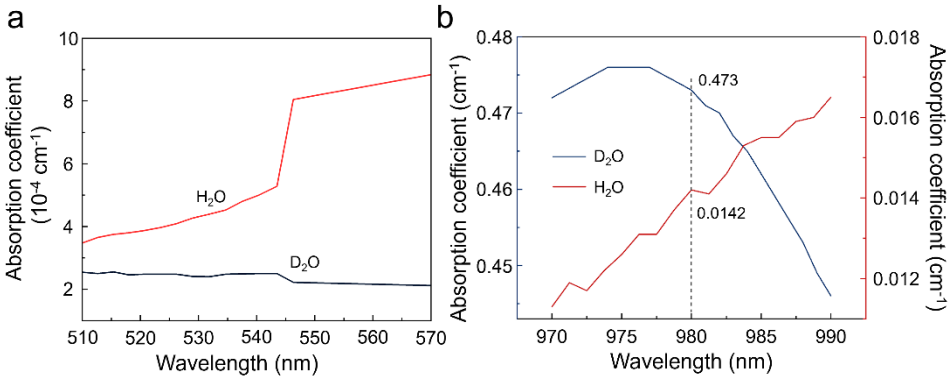

Figure S5.4 **The absorption coefficient of H_2O and D_2O in the studied UC emission range (510-570 nm) and at the excitation wavelength (980 nm).**

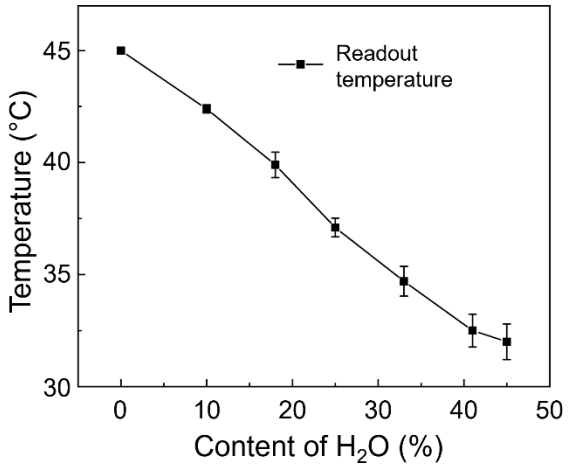

Figure S5.5 **Temperature readout based on the UC intensity ratio of $^2H_{11/2}/^4S_{3/2}$ in mixed solutions with varying H_2O content. The temperature in pure D_2O solution was set to be the standard.**

Content of H_2O (%)	Readout temperature (°C)		
0	45	40	35
10	42.4	37.2	32.4
18	39.9	34.3	30.0
25	37.1	32.4	27.6
33	34.7	29.9	25.4
41	32.5	27.9	22.8
45	32.0	26.8	22.2

Table S5.1 **Detailed temperature readouts based on the UC intensity ratio of $^2H_{11/2}/^4S_{3/2}$ in mixed solutions with varying H_2O content.**

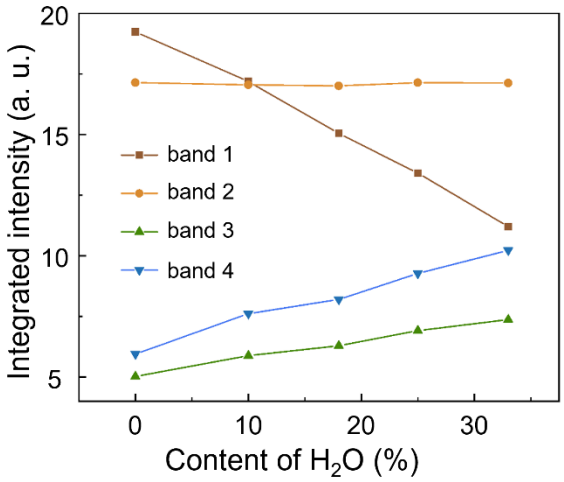

Figure S5.6 **Integrated intensities of the four emission bands (1−4) from the DS spectrum in mixed solutions with varying H_2O content.**

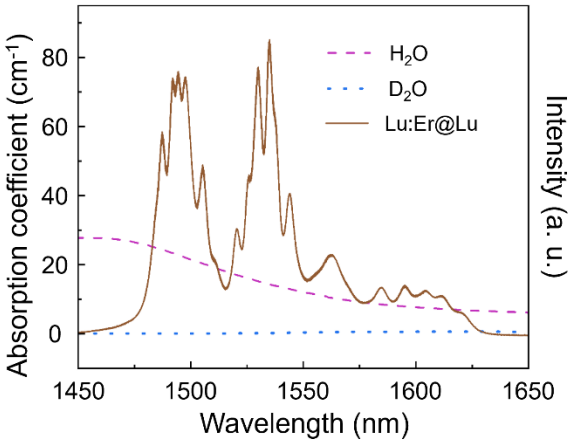

Figure S5.7 **DS luminescence spectrum of Lu:Er@Lu core-shell RENPs and the absorption coefficients of H_2O and D_2O in the studied emission range (1450-1650 nm).**

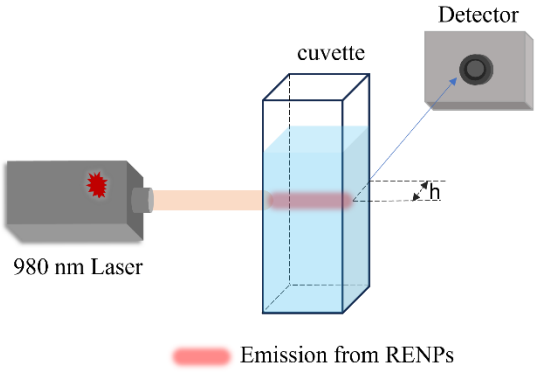

Figure S5.8 **Schematic of the experimental setup used to record luminescence spectra of Lu:Er core and Lu:Er@Lu core-shell RENPs..**

$$\frac{I_3}{I_4} == \frac{I_{03}}{I_{04}}\left(e^{(-9.48+6.99)}\right)^{0.5} = \frac{I_{03}}{I_{04}} \cdot 0.29 \qquad (S5.4)$$

I_{03} and I_{04} represent the originally emitted DS intensities of bands 3 and 4 from Lu:Er@Lu RENPs. These values are obtained by integrating the intensities of bands 3 and 4, as recorded in pure heavy water (D_2O).

Content of H_2O (%)	Readout temperature (°C)
0	20.0
10	25.8
18	35.1
25	35.9
33	42.3

Table S5.2 **Detailed temperature readouts based on the DS intensity ratio of $Y_{4\text{-}7}$ /$Y_{1\text{-}3}$ in mixed solutions with varying H_2O content. The temperature in pure D_2O solution was set to be the standard.**

6 CONCLUSIONS AND FUTURE PERSPECTIVES

Photoluminescence nanothermometry has addressed several challenges associated with conventional thermometers and presents potential in biomedicine in both fundamental studies as well as preclinical research. Advanced photoluminescence nanothermometry will provide even more opportunities for early cancer diagnosis. Such great potential has driven higher requirements for the development of photoluminescence nanothermometry. The two essential components: nanothermometers and instruments, both play a key role in determining the temperature. Research in photoluminescence nanothermometry must adopt an interdisciplinary approach that encompasses materials design and optical engineering.

Rare-earth doped nanoparticle is a promising candidate that can be flexibly engineered to match the growing demands of safe, deep-tissue temperature monitoring with high accuracy, and further therapy. PLIR and lifetime-based nanothermometry are the two common methodologies using RENPs as the probe. PLIR has been the mainstream method owing to the readily available spectrometers for photoluminescence acquisition. However, this technique is restricted by undesirable fluctuation in photoluminescence intensity ascribed to factors such as probe concentration, excitation power density, and bio-chemical surroundings. Lifetime-based nanothermometry is less susceptible to various experimental factors but is still breaking ground due to relatively expensive and complex instrumentation, and long data acquisition.

This thesis hinges on i) prompting lifetime-based nanothermometry from the instrument perspective as a staple system in photoluminescence mapping and temperature sensing; ii) rational design of RENPs: tuning and exploring the dopant concentration, core-shell architecture, and the growth dynamics. Improved optical performance is the basis for their successful applications; iii) inspecting the influential factors of temperature readouts. The centerpiece of this thesis is still NIR emission for nanothermometry. Given that the extinction coefficient of tissue is strongly wavelength-dependent, the emission of RENPs lies in the biological windows thus offering considerable advantages for accurate temperature reading. In that vein, Er^{3+} ion is deployed as the main activator for its emission in the NIR-IIb (1500-1700 nm) region. Structural design, optical properties optimization, and thermometry characteristics analysis are conducted in detail from chapter 3 to chapter 5.

In chapter 3, SWIR-PLIMASC—an efficient photoluminescence lifetime mapping platform specialized for RENPs in the SWIR spectral range is developed. SWIR-PLIMASC synergistically combines scanning optics with a SWIR camera for high-sensitivity ultrahigh-speed one-

dimensional imaging at ~140 kHz. This operation scheme allows the entire RENP's photoluminescence intensity decay to be collected in one acquisition, which enables efficient SWIR photoluminescence lifetime quantification. The high throughput nullifies the need for the large number of repeated excitations, which hence circumvents long dwelling time, particularly for the long SWIR photoluminescence lifetimes in RENPs. To the best of our knowledge, this is the first SWIR high-sensitivity streak camera, marking remarkable progress in SWIR ultrahigh-speed imaging instrumentation. Through the use of different Er^{3+}-doped RENPs, this technique reveals its capability of characterizing RENPs with various lifetimes ranging from microseconds to milliseconds. Combined with Ho^{3+}-doped RENPs as the nanothermometers, SWIR-PLIMASC is implemented in 2D lifetime-based nanothermometry, confirming that it can accurately sense temperature in a biological phantom and affirming its superior detection ability compared to conventional thermal imaging.

In chapter 4, we have developed a novel architecture, $LiLuF_4$@$LiLuF_4$:Ce^{3+}, Yb^{3+}, Er^{3+}@$LiLuF_4$ inert core-active shell-inert shell RENP. Er^{3+} dopant concentration in the structure can reach 5%, yielding 12-fold enhanced NIR downshifting emission intensity at around 1550 nm compared to conventional active core-inert shell architecture. The high dopant concentration is allowed in the extended shell layer where the concentration of Er^{3+} is diluted and thus the distance among Er^{3+} ions is lengthened without severe CR. The extended shell layer is attributed to two sides: the ultra-small inert core (5 nm) and the double interfaces. The ultra-small inert core is in low crystallinity, prone to lose its integrity, and thus enables easy intermixing with the shell layer. Meanwhile, the double homogeneous interfaces in $LiLuF_4$@$LiLuF_4$:Ce^{3+}, Yb^{3+}, Er^{3+}@$LiLuF_4$ core-shell-shell architecture provided more chances for Er^{3+} dopant diffusion. This method suggests a general way to suppress concentration quenching to further increase not only NIR downshifting emission intensity but also visible emissions. The highly boosted NIR intensity provides a high SNR image through opaque obstacles, offering the potential in deep tissue applications.

In chapter 5, temperature-dependent UC and DS emission intensity of $LiLuF_4$:Ce^{3+}, Yb^{3+}, Er^{3+}@$LiLuF_4$ are inspected in a mixed solution of H_2O and D_2O. The strong absorption of H_2O at 980 nm reduced the excitation power density, altering the $^2H_{11/2}$/$^4S_{3/2}$ intensity ratio in UC nanothermometry and leading to deviations in the detected temperature. Water-induced deviation in temperature sensing also occurs in DS nanothermometry since the excitation and emission light of RENPs are both attenuated by water. In DS nanothermometry, the stretch vibration of OH in H_2O molecules interacted with the $^4I_{13/2} \rightarrow {}^4I_{15/2}$ transition, substantially

modifying the Stark sublevel intensity ratio (Y_{4-7}/Y_{1-3}) with the change in water content. These findings point out the influence of the surrounding medium on the temperature readout and emphasize the necessity of further standardization to ensure reliable RENP nanothermometry in biomedical applications.

Based on the current result, the future work will be carried out in the following aspects:

First, we plan to further upgrade SWIR-PLIMASC to develop a lifetime-resolved photoluminescence spectrometer. A grating will be integrated into the system to provide spectrum information. Using this new optical system, we will be able to collect the spectrum and lifetime results at the same time. Combining the PLIR nanothermometry and lifetime-based nanothermometry, we could get a more powerful and accurate temperature detection methodology. This advanced instrument may provide us with more possibilities for developing new methods for photoluminescence nanothermometry.

Second, we will apply the newly designed inert core-active shell-inert shell architecture for *ex vivo* temperature measurement. To avoid other possible error sources, the same medium found in the tissues or organs under study will be used to inspect the characteristics of PLIR nanothermometers rather than using H_2O or another generic solution. A calibration will also be conducted to get more reliable temperature readouts. Meanwhile, the temperature-dependent photoluminescence lifetime of these nanoparticles will also be studied. RENPs with high-temperature sensing sensitivity will be

Finally, combining the optimized new architecture and the advanced instrument, we will apply RENP nanothermometry for *in vivo* temperature monitoring.

7 SUMMAIRE

Vers une nanothermométrie précise par photoluminescence utilisant des nanoparticules dopées aux terres rares pour des applications biomédicales

7.1 L'introduction

L'un des biomarqueurs les plus importants en biologie, la température, affecte directement d'innombrables processus dans le corps. La surveillance de ce paramètre pourrait donc être un moyen simple et efficace d'étudier les fonctions biologiques de base. De l'invention du thermoscope par Galileo (Anonyme, 2001) à ce jour, les sondes de température ont évolué de l'ancienne génération de thermomètres micrométriques à contact invasifs (ex: le thermocouple) vers des nouveaux thermomètres à distance, peu invasifs, à échelle inférieure au micron (ex : nanothermomètres à photoluminescence). La nanothermométrie à photoluminescence repose sur la performance optique de la sonde, qui est affectée par la température de son environnement, établissant une corrélation entre ses propriétés de photoluminescence et la température. Parmi les différentes sondes photoluminescentes étudiées, les nanoparticules dopées au terres rares (RENP) sont au premier plan en raison de leur photostabilité élevée, faible toxicité et facilité relative de modification de surface (Gai *et al.*, 2014; Matulionyte *et al.*, 2023). Surtout, les RENP ont des propriétés optiques uniques telles que des bandes de transition *4f-4f* étroites, des longues durées de vie, une bonne résistance aux interférences provenant de leurs environnements, et multiples émissions dans l'UV, le visible et le proche infrarouge (Dong *et al.*, 2015; Gai *et al.*, 2014; Matulionyte *et al.*, 2023). Plus particulièrement, leur capacité à être excités et à émettre dans la région NIR les rend particulièrement bien adaptés à l'imagerie des tissus profonds et à la nanothermométrie. Ces propriétés mettent en évidence la versatilité des RENP et les distinguent de leurs homologues.

Les RENP comprennent généralement un hôte inorganique dopé d'ions de terres rares, servant de sensibilisateurs et activateurs (figure 1.1). Les matériaux hôtes idéaux doivent être chimiquement et thermiquement stables, transparent dans la gamme spectrale d'intérêt et avoir un seuil de dommage optique élevé. Avant tout, les hôtes ayant une faible énergie de phonon sont préférables pour minimiser les relaxations non radiatives. Le sensibilisateur absorbe efficacement l'énergie d'excitation et la transfère ensuite aux ions luminescents adjacents, l'activateur. Pour permettre une photoluminescence efficace, le sensibilisateur incorporé présente normalement une section efficace d'absorption élevée à la longueur d'onde

d'excitation et un diagramme d'énergie simple pour éviter l'auto-émission. Un transfert d'énergie efficace entre le sensibilisateur et l'activateur est également nécessaire. La plupart des ions de terres rares possèdent de nombreux niveaux d'énergie (figure 1.2) qui peuvent servir d'activateurs. Les multiples niveaux d'énergie des ions libres sont divisés en raison de l'interaction coulombienne, de l'interaction spin-orbite et du champ cristallin (figure 1.3). Bénéficiant de la disposition en échelle des états d'énergie, certains ions de terres rares sont capables d'absorber deux photons ou plus de manière séquentielle pour les «pomper» vers des niveaux d'énergie élevés. Basé sur les différentes positions des bandes d'excitation et d'émission, les matériaux photoluminescents peuvent être classés comme matériaux luminescents de type Stokes ou Anti-stokes. La conversion ascendante de photons (UC) est une émission Anti-stokes typique qui convertit deux ou plusieurs photons de faible énergie en un photon de haute énergie. Le mécanisme exploré jusqu'à présent dans les nanoparticules à conversion ascendante (UCNP) est principalement divisé en quatre classes de base (figure 1.4-1.7): l'absorption à l'état excité (ESA), le transfert d'énergie par conversion ascendante (ETU), la relaxation croisée (CR) et l'avalanche de photons (PA). L'émission de type Stokes provient de deux différents processus : la conversion descendante et le décalage descendant. Dans la conversion descendante, deux photons ou plus de faible énergie sont émis après l'absorption d'un photon de haute énergie. En revanche, un seul photon de faible énergie est émis dans le processus de décalage descendant lorsqu'il est excité par un photon de haute énergie. Les processus d'émission UC et DS typiques dans le système codopé Yb^{3+} / Er^{3+} sont illustrés dans la figure 1.8.

Différentes méthodes peuvent être utilisées pour obtenir une intensité de photoluminescence plus élevée. Premièrement, il y a la réduction de l'atténuation de la surface. La synthèse de RENP de grande taille est un moyen efficace de réduire le rapport surface/volume et donc d'améliorer l'intensité de la photoluminescence. Cependant, la taille maximale des RENP est limitée dans certaines applications. La construction d'une architecture cœur-coquille est également un moyen de protéger les activateurs des atténuateurs de surface. Après le dépôt d'une coquille, les activateurs atténués à la surface du cœur peuvent être réactivés. D'autre part, la distance entre l'activateur dans le cœur et les atténuateurs à la surface est plus grande, ce qui permet de minimiser efficacement la relaxation non radiative. Normalement, la couche coquille est inerte avec la même structure que le cœur et son épaisseur doit être suffisante pour assurer la protection totale des activateurs internes. Des coquilles hétérogènes peuvent également être employées pour améliorer l'intensité de la photoluminescence, et l'exigence est d'avoir une faible inadéquation du réseau avec celui des nanoparticules du cœur.

Deuxièmement, il y a l'élimination des CR nuisibles. Les ions de terres rares avec des niveaux d'énergie abondants sont susceptibles d'avoir des processus de CR destructeurs avec les ions situés à proximité. Lorsque différents ions de terres rares sont codopés dans la même région, la faible distance entre les ions voisins favorise les processus de transfert d'énergie non radiative néfastes. L'augmentation de la distance entre les ions de terres rares est donc une solution potentielle. Troisièmement, il y a l'adaptation de la symétrie locale du centre photoluminescent. C'est la modification de la symétrie locale des ions de terres rares qui permet aux transitions *4f-4f* interdites par parité d'être partiellement autorisées lorsqu'ils sont intégrés dans la matrice hôte. L'adaptation de la symétrie locale des activateurs devrait faciliter la transition radiative et donc améliorer l'intensité de la photoluminescence. Le dopage est l'un des moyens les plus simples de modifier la symétrie locale dans le réseau cristallin. Pour la sélection des ions dopants, les ions optiquement inertes avec des rayons ioniques différents des ions de terres rares sont une bonne option, par exemple les ions Li^{+}, Bi^{3+}, Mo^{3+}, et Sr^{2+}. (Chen *et al.*, 2008; Jiang *et al.*, 2012; Yin *et al.*, 2014; Zhao *et al.*, 2013). D'autres méthodes, telles que la résonance des plasmons de surface localisés (LSPR) et la sensibilisation par ajout de colorants, ont également été signalées pour améliorer l'intensité de la photoluminescence des RENP. Après la synthèse des RENP, l'ingénierie de surface est obligatoire pour les applications biomédicales. L'application des RENP à la nanothermométrie par photoluminescence est présentée au point 1.6. Normalement, le principe de fonctionnement de la nanothermométrie par photoluminescence inclut des changements dans l'anisotropie de polarisation des sondes, l'intensité de la photoluminescence, la position des pics, la largeur de bande, la forme de bande et la durée de vie.(Brites *et al.*, 2018a). Dans le cas des RENP, la PLIR entre deux pics ou deux transitions est progressivement devenue la méthode établie dans la nanothermométrie par photoluminescence. La nanothermométrie basée sur la durée de vie des RENP en est encore à ses débuts, bien qu'elle ait été reconnue comme une technique potentielle pour la détection précise de la température avec une erreur systématique moindre. (Liu *et al.*, 2021b; Tan *et al.*, 2020a). En fonction des différents types de centres photoluminescents dopés (activateurs), la nanothermométrie PLIR est divisée en deux catégories : centre unique (singulièrement dopé) et centre double (codopé).

Dans un nanothermomètre à centre unique, la PLIR est déterminée par les transitions radiatives de deux niveaux d'énergie thermiquement couplés du même activateur vers son état fondamental (figure 1.9). Le potentiel de la nanothermométrie PLIR à centre unique a été largement étudié dans la photoluminescence UC et DS (par exemple, les RENP dopés à Er^{3+}, Eu^{3+}, Ho^{3+}, Nd^{3+} ou Pr^{3+}). Dans le cas des nanothermomètres à double centre, la PLIR est

définie par deux bandes d'émission distinctes provenant d'activateurs différents. La dépendance en température de leur PLIR est affectée par des processus basés sur les phonons, y compris la relaxation multiphonon non radiative et le transfert d'énergie non résonant assisté par les phonons. Des exemples de nanothermomètres à double centre ont également été rapportés dans le domaine visible : Eu^{3+}/Tb^{3+}, Pr^{3+}/Tb^{3+} et Ho^{3+}/Tm^{3+}, et dans le proche infrarouge : systèmes codopés Yb^{3+}/Nd^{3+}, Ho^{3+}/Nd^{3+} et Er^{3+}/Nd^{3+}. La durée de vie de photoluminescence τ d'un état excité est déterminée par les taux de décroissance radiatifs W_r et les taux de décroissance non radiatifs W_{nr} qui dépendent fortement de l'existence de la relaxation multiphonon, du transfert d'énergie non résonant assisté par les phonons et d'autres processus non radiatifs. Par conséquent, la durée de vie totale (τ) de l'état excité est influencée par la température. Notamment, la durée de vie de photoluminescence est une propriété intrinsèque qui est moins vulnérable aux variations dues à la profondeur de pénétration de la lumière, à la présence d'autres fluorophores/chromophores (par exemple dans un milieu biologique), aux solvants dans lequel la sonde est dispersée, etc. La nanothermométrie basée sur la durée de vie est considérée comme une technique robuste qui présente un potentiel crucial pour surmonter certaines des limitations associées à la nanothermométrie PLIR. La performance de la nanothermométrie par photoluminescence peut être caractérisée par la sensibilité absolue (S_a), la sensibilité relative (S_r) et l'incertitude de température (δT).

Les limitations possibles de la nanothermométrie par photoluminescence PLIR peuvent provenir du laser d'excitation, des tissus biologiques, de la performance optique des nanothermomètres photoluminescents et du processus d'étalonnage (figure 1.10).

Tout d'abord, une source d'excitation possède deux caractéristiques principales : la densité de puissance et la longueur d'onde. Il est impératif de maintenir les conditions d'excitation identiques pendant les mesures de température et le processus d'étalonnage. De plus, l'effet de chauffage du laser d'excitation doit également être pris en compte. La deuxième source d'erreur potentielle est le tissu biologique en raison de son coefficient d'atténuation élevé. Les nanothermomètres, en particulier les RENP, dont les émissions se situent dans les fenêtres biologiques (NIR-I : 700-900 nm, NIR-IIa:1300-1400 nm, NIR-IIb:1500-1700 nm) offrent donc des avantages considérables en raison de la faible absorption de ces longueurs d'onde par les tissus. Pour mitiger les différentes distorsions induites par les tissus, une étude compréhensive des propriétés optiques thermodépendantes des tissus pourrait être une approche. Troisièmement, le rapport signal / bruit (SNR) est également un problème grave qui entrave la poursuite de l'application des RENP en nanothermométrie, où l'incertitude de la température

des nanothermomètres RENP présente une relation fortement non linéaire avec le SNR. (van Swieten *et al.*, 2022). La conception et la synthèse de RENP avec un rendement quantique élevé est donc un sujet urgent qui demeure un défi. De l'autre côté, si les RENP ont un faible rendement quantique, leur mérite réel est le SNR, qui est comparativement élevé puisqu'elles sont excitées dans la région NIR et que certaines d'entre elles émettent également dans la région NIR. Par conséquent, même lorsque le signal RENP est faible, le SNR est élevé car l'autofluorescence de fond est également très faible. Quatrièmement, le processus d'étalonnage des nanothermomètres secondaires peut également entraîner une erreur de détection de la température. Les nanothermomètres primaires où δE et B peuvent être déterminés en connaissance des lois thermodynamiques ne nécessitent pas d'étalonnage et devraient donc être davantage développés.

La détermination de la température thermodynamique est une procédure complexe qui fait appel à des instruments de précision et à des nanothermomètres. Pour la nanothermométrie PLIR : cette technique est limitée par les performances optiques des nanothermomètres en raison de l'intensité relativement faible et de la fluctuation indésirable attribuée à des facteurs tels que la densité de puissance d'excitation et l'environnement biochimique. Les efforts concertés se poursuivent pour fabriquer des nanothermomètres PLIR avec de meilleures performances optiques adaptées à la biomédecine. Entre-temps, l'influence des facteurs environnants sur la précision de la nanothermométrie doit être examinée avec soin, car le principal constituant du corps, l'eau, a une forte absorption pour certaines des émissions des RENP. En revanche, la durée de vie de la photoluminescence des RENP est moins sensible que l'intensité à la variation de l'intensité de l'excitation, à l'atténuation inhomogène du signal et à l'environnement. De ce fait, la nanothermométrie basée sur la durée de vie des RENP est reconnue comme une technique potentielle pour la détection précise de la température avec moins d'erreur systématique. Cependant, la nanothermométrie basée sur la durée de vie est encore en début de développement en raison du coût relativement élevé et de la complexité de l'instrumentation. La technique la plus courante, la TCSPC, n'est pas idéale pour mesurer efficacement la durée de vie des RENP en raison de ses excitations répétitives, de sa capacité de traitement des photons limitée à chacune des excitations et du temps d'acquisition prolongé pour chacun des pixels. Le balayage ponctuel de la durée de vie pour la cartographie sur à champ large prend également beaucoup de temps et, par conséquent, le TCSPS sera limité dans le suivi des activités dynamiques biologiques utilisant la durée de vie comme indicateur. Plus de recherche du côté de l'instrumentation est nécessaire pour rendre la nanothermométrie

basée sur la durée de vie plus facile d'utilisation, chose qui pourrait la rapprocher des applications translationnelles. Des efforts multidisciplinaires en matière d'ingénierie optique et de matériaux chimiques ont été déployés dans le cadre de cette thèse en vue d'une détection précise de la température.

7.2 Méthodes

Méthodes : Les précurseurs RE_3^+-trifluoroacétate $(CF_3COO)_3RE$ ont été préparés à partir de RE_2O_3 et $RE_2(CO_3)_3$. Les matériaux de départ visés ont été sélectivement mélangés avec de l'acide trifluoroacétique et de l'eau distillée et maintenus à 80 °C sous forte agitation jusqu'à ce que la solution devienne claire. L'acide trifluoroacétique résiduel et l'eau ont ensuite été évaporés et les précurseurs $(CF_3COO)_3RE$ en poudre ont été obtenus.

La décomposition thermique des précurseurs $(CF_3COO)_3RE$ a été employée pour préparer toutes les RENP de cette thèse. Les RENP à base de Na ont été synthétisées par thermolyse en une étape et les RENP à base de Li ont été synthétisées par stabilisation des premiers noyaux (FN). Plus de détails sont donnés dans les chapitres 3 à 5.

Dans la thermolyse typique en une étape, les précurseurs $(CF_3COO)_3RE$ et CF_3COONa ont d'abord été dissous dans un mélange (solution A) d'OA et d'ODE sous vide à 125 °C pendant 30 minutes sous forte agitation. La solution B était le mélange d'OA et d'ODE. La température a ensuite été augmentée à 315 °C. Une fois la température de la solution B stable, la solution A a été injectée dans la solution B. La solution finale a été maintenue à 315 °C sous atmosphère d'argon pendant une heure pour obtenir les cœurs de RENP.

Synthèse des FN : les précurseurs $(CF_3COO)_3RE$ et CF_3COOLi ont été mélangés avec l'OA et l'ODE (solution A), puis dégazés à 125 °C pendant 30 minutes. Lorsque les précurseurs ont été dissous, l'OM a été ajouté à la solution A et a été laissé à dégazer. Pendant ce temps, un mélange (solution B) d'OA, d'OM et d'ODE a été dégazé à 110 °C pendant 15 minutes, puis chauffé à 330 °C sous atmosphère d'argon. La solution A a été injectée dans la solution B et la solution finale a été maintenue à 330 °C sous atmosphère d'argon pendant 1 heure.

Stabilisation des FN : Les FN ont été mélangés avec l'OA et l'ODE et dégazés à 110 °C pendant 30 minutes. La température a été augmenté jusqu'à 315 °C, puis la réaction s'est poursuivie pendant une heure.

Les RENP cœur-coquille ont été préparées par croissance épitaxiale de la coquille sur le coeur. Dans la solution A, les précurseurs de la coquille ont été mélangés avec du

CF_3COONa/CF_3COOLi, l'OA et l'ODE. La solution A a été dégazée à 110 °C pendant 30 minutes. La solution B est mélangée avec les RENP du cœur, l'OA et l'ODE. Après dégazage, la température de la solution B a été portée à 315 °C sous argon. La solution A a ensuite été injectée dans la solution B et la solution mélangée a réagi à 315 °C pendant 1 heure. Après refroidissement à température ambiante, le produit final a été lavé trois fois avec de l'hexane/éthanol (1:3) et redispersé dans de l'hexane.

Le ligand OA à la surface des RENPs a été décapé à l'aide de tétrafluoroborate de nitrosyle ($NOBF_4$).

La cristallinité et la phase de toutes les RENP ont été déterminées par une analyse de diffraction des rayons X sur poudre (XRD). La morphologie des RENP a été étudiée par microscopie électronique à transmission (TEM ; Philips Tecnai 12, USA). Des images TEM à haute résolution, des images de microscopie électronique à transmission à champ sombre annulaire à angle élevé (HAADF-STEM) et des balayages linéaires de spectrométrie X à dispersion d'énergie (EDS) ont été pris sur le Jeol JEM-2100F TEM (JEOL). Les spectres UC et DS des RENP ont été obtenus sous excitation par diode laser à 980 nm. L'émission UC a été enregistrée avec un spectromètre Avaspec-ULS2048L (Avantes, Pays-Bas). Le spectre DS a été collecté avec un monochromateur Shamrock 500i (Andor, Irlande) équipé d'un détecteur NIR iDus InGaAs 1.7 (Andor, Irlande). Le profil d'intensité d'émission NIR résolu dans le temps a été mesuré par un microscope d'imagerie à durée de vie de photoluminescence NIR fait maison, utilisant une caméra à stries tout-optique (SWIR-PLIMASC développé dans le chapitre 3). La réponse thermique des RENP a été mesurée à l'aide d'un porte-cuvette à température contrôlée (qpod 2e de Quantum Northwest, Washington, USA).

7.3 Résultats

7.3.1 Cartographie de la durée de vie de la photoluminescence dans l'infrarouge à ondes courtes des nanoparticules dopées aux terres rares à l'aide d'une imagerie par caméra à balayage totalement optique

Malgré des progrès fulgurants dans la conception et la synthèse de RENP aux propriétés optiques attrayantes, les systèmes optiques existants pour l'imagerie à durée de vie par photoluminescence infrarouge à courtes ondes (SWIR) sont encore considérablement limités par une détection inefficace des photons, une vitesse d'imagerie limitée et une faible sensibilité. Pour surmonter ces difficultés, nous avons mis au point une microscopie d'imagerie à durée de vie par photoluminescence SWIR à l'aide d'une caméra à balayage tout-optique (PLIMASC).

SWIR-PLIMASC présente plusieurs avantages intéressants pour la caractérisation de la durée de vie de photoluminescence des RENP. Tout d'abord, le système répond à une large gamme spectrale de 900 nm à 1700 nm et la photoluminescence à différentes longueurs d'onde et/ou bandes spectrales peut donc être détectée en changeant le filtre passe-bande. À notre connaissance, SWIR-PLIMASC est le premier système d'imagerie SWIR à haute sensibilité et à très haute vitesse. Deuxièmement, le système offre une grande adaptabilité de la vitesse d'imagerie 1D de 10,3 kHz à 138,9 kHz. Grâce à cette capacité, les durées de vie de la photoluminescence SWIR allant de la microseconde à la milliseconde peuvent être directement capturées à l'aide du même système. De plus, l'opération de cisaillement attribue les informations temporelles de la photoluminescence à différentes positions spatiales, de sorte que l'ensemble du processus de décroissance de l'intensité de la photoluminescence 1D peut être enregistré en une capture. En contournant le temps mort dans le traitement des photons, SWIR-PLIMASC a un débit de lumière plus élevé que les techniques TCSPC et SPAD. Pour démontrer la puissance de la SWIR-PLIMASC, une série de RENP dopés à l'Er^{3+} avec des durées de vie de photoluminescence SWIR distinctes a été synthétisée. La SWIR-PLIMASC révèle une topologie complexe des marqueurs basés sur la durée de vie de photoluminescence, ce qui démontre un grand potentiel comme agent anti-contrefaçon à haute sécurité. En utilisant des RENP dopés à l'Ho^{3+} comme indicateurs de température, la SWIR-PLIMASC est appliquée à la détection précise de la température dans un fantôme biologique, démontrant sa capacité de détection supérieure à celle de l'imagerie thermique conventionnelle.

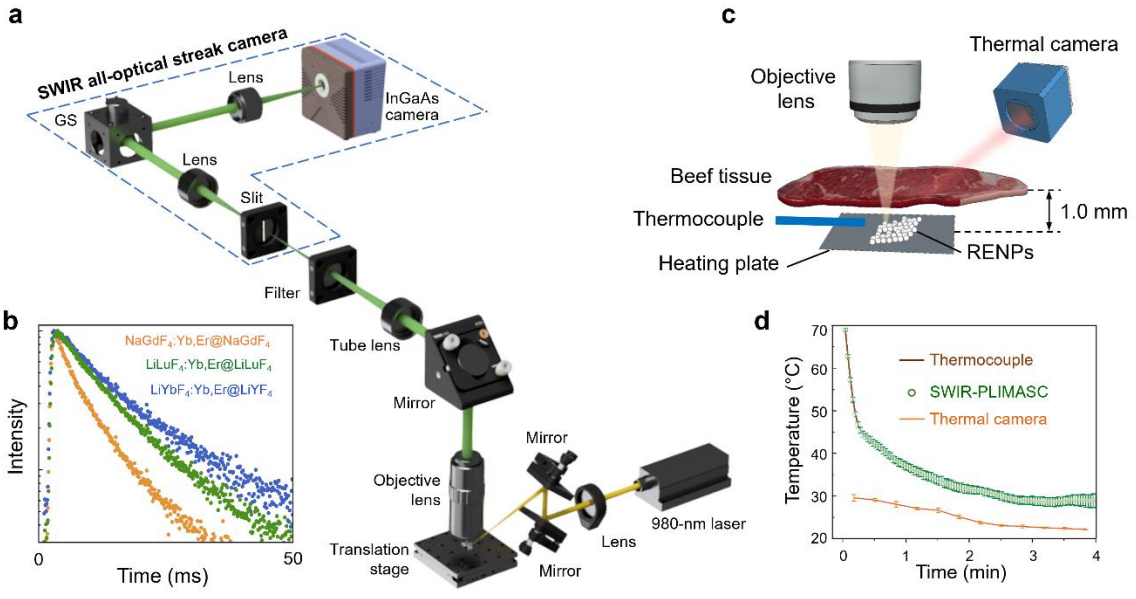

Figure 7.1 **SWIR-PLIMASC pour la mesure de la durée de vie de photoluminescence et la nanothermométrie basée sur la durée de vie.**

(a) Schéma du SWIR-PLIMASC. (b) Courbes de décroissance de l'intensité moyenne normalisée de la photoluminescence, tracées à partir des images. (c) Installation expérimentale pour la détection de la température. (d) Comparaison de la capacité de détection de la température du SWIR-PLIMASC avec celle de la caméra thermique.

7.3.2 Augmentation de l'intensité de la luminescence de décalage vers le rouge grâce à une couche active étendue

Pour améliorer la luminosité et enrichir les fonctionnalités de la luminescence du décalage descendant des RENP, de nombreuses études ont exploité des coquilles inertes pour protéger les dopants de terres rares des extincteurs de surface. Cependant, l'extinction liée la concentration interne reste une problématique à résoudre lorsqu'on utilise des concentrations plus élevées de dopants de terres rares pour tenter d'obtenir une émission plus importante. À la suite d'une pléthore de recherches sur les structures cœur-coquille, l'interface s'est révélée contrôlable, allant d'une limite abrupte et bien définie à une limite obscure où les cations se mélangent. En utilisant pour la première fois cette propriété de cœur-coquille intermélangés, nous créons une nouvelle architecture d'interface cœur-coquille homogène à double couche afin d'étendre la couche active, ce qui permet d'augmenter le nombre de centres luminescents sans effet important d'extinction liée à la concentration. Basée sur une structure cœur inerte-coquille active-coquille inerte, spécifiquement $LiLuF_4$@$LiLuF_4$:Ce^{3+}, Yb^{3+}, Er^{3+}@$LiLuF_4$, dans laquelle la concentration du dopant Er^{3+} peut être augmentée jusqu'à 5%, on produit une intensité d'émission provenant du décalade descendant dans le NIR à environ 1550 nm qui est 12 fois supérieure à celle de l'architecture cœur-coquille conventionnelle. Le mécanisme d'amélioration a été étudié plus en détail en ajustant la taille / cristallinité du cœur inerte (5 nm et 10 nm) ainsi que la dynamique de croissance de la coquille. Le cœur inerte instable de très petite taille a permis un mélange plus facile avec les couches de la coquille. Par ailleurs, les interfaces doubles dans l'architecture cœur-coquille $LiLuF_4$@$LiLuF_4$:Ce^{3+}, Yb^{3+}, Er^{3+}@$LiLuF_4$ ont fourni une couche étendue pour le dopage Er^{3+} afin de surmonter l'effet d'extinction liée à la concentration qui se produit normalement dans la structure cœur-coquille conventionnelle. Notre méthode permet de mieux comprendre les avantages potentiels de la structure cœur-coquille intermélangée, suggérant un moyen de supprimer l'effet d'atténuation liée à la concentration pour améliorer considérablement les performances optiques dans le NIR. La structure optimisée IC_{5nm}-AS_{5Er}-IS a été déployée avec succès pour transmettre des signaux NIR à travers des obstacles tels que des boîtes en plastique et en papier, démontrant ainsi leur capacité exceptionnelle à surmonter les obstacles pour la détection des signaux.

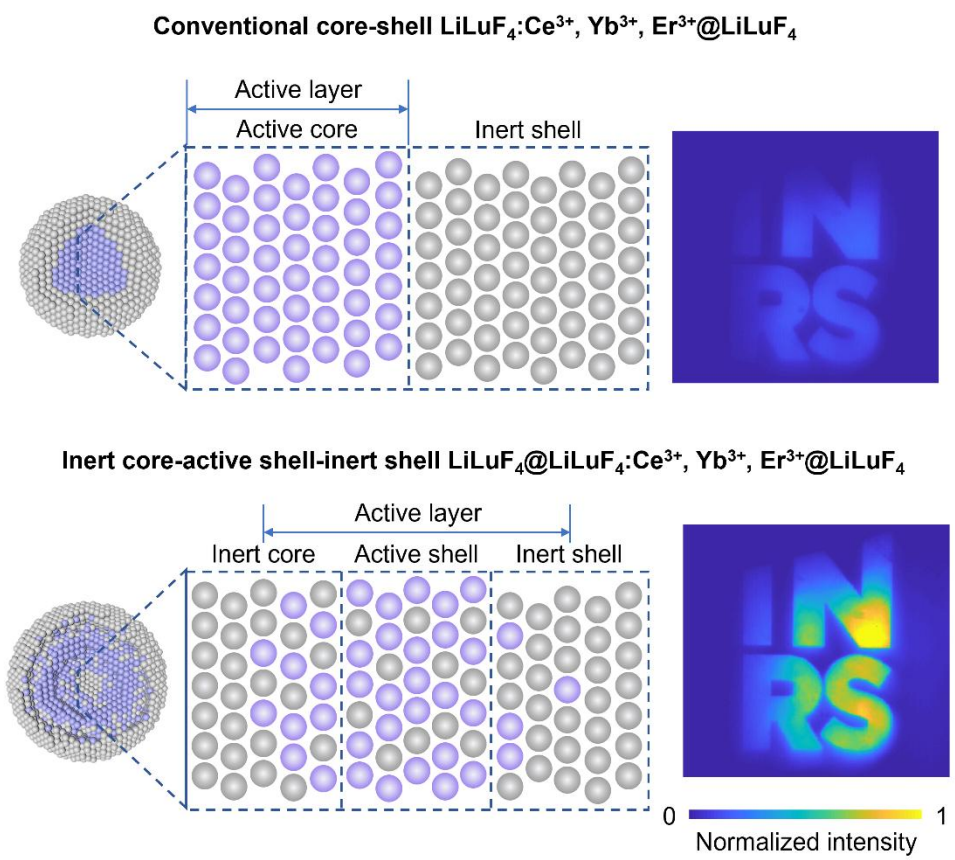

Figure 7.2 **Schéma d'une structure cœur-coquille conventionnelle et d'une architecture cœur inerte-coquille active-coquille inerte avec une couche active étendue.**

7.3.3 Effet de l'H2O sur la nanothermométrie par luminescence de conversion ascendante (UC) et de décalage vers le rouge (DS)

Les propriétés de luminescence des RENP sont affectées par divers facteurs tels que la densité de puissance d'excitation et le milieu environnant, ce qui peut compromettre la fiabilité de la température mesurée et limiter les applications ultérieures. Pour mieux comprendre l'effet de l'eau (H_2O) sur les propriétés de luminescence, le spectre des RENP en fonction de la température a été mesuré dans une solution mixte d'oxyde de deutérium (D_2O) et de H_2O à différents rapports volumétriques. Plus précisément, les RENP Lu:Er@Lu, qui présentent à la fois des émissions UC et DS sous une excitation de 980 nm, ont été développées et appliquées pour la détection de la température dans la gamme physiologique de 20 à 45 °C. Une atténuation de l'intensité de la luminescence induite par le H_2O a été observée dans les émissions UC et DS. Une caractérisation plus poussée a révélé que les différences d'atténuation dans chaque bande d'émission affectaient le rapport d'intensité de la luminescence et, par conséquent, le résultat de la mesure de la température. Dans la

nanothermométrie UC, la forte absorption provenant de l'H_2O à 980 nm a réduit la densité de puissance d'excitation, modifiant le rapport d'intensité $^2H_{11/2}/^4S_{3/2}$ et entraînant des écarts dans la température détectée. Parallèlement, dans la nanothermométrie DS, la vibration d'étirement de OH dans les molécules de H_2O a interagi avec la transition $^4I_{13/2} \rightarrow {}^4I_{15/2}$, modifiant considérablement le rapport d'intensité du sous-niveau Stark (Y_{4-7}/Y_{1-3}) avec le changement de la teneur en eau. Les écarts résultants dans la lecture de la température ont été analysés dans des solutions mixtes à teneur variable en H_2O, en utilisant le D_2O comme standard. Ces résultats donnent une image réaliste de l'effet du H_2O sur la nanothermométrie UC et DS et soulignent la nécessité d'une normalisation plus poussée pour garantir la fiabilité de la nanothermométrie RENP dans les applications biomédicales.

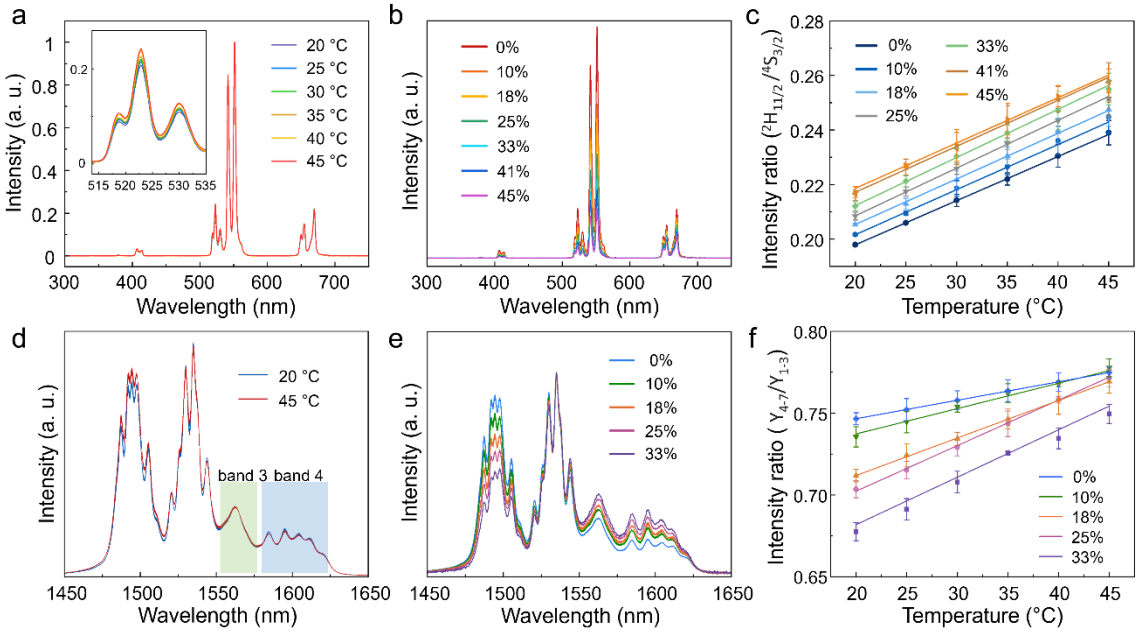

Figure 7.3 Effet de l'eau sur la nanothermométrie UC et DS.

Spectre d'émission en fonction de la température : (a) UC et (b) DS des RENPs Lu:Er@Lu mesurés dans une solution pure de D2O. (c) Spectre d'émission UC et (d) spectre d'émission DS de 20 °C à 45 °C dans une solution mixte de D2O avec différentes concentrations de H2O. Rapport d'intensité de (e) $^2H_{11/2}/^4S_{3/2}$ et (f) Y_{4-7}/Y_{1-3} de 20 °C à 45 °C dans des solutions mixtes avec différentes concentrations de H2O.

7.4 Références

Anonyme (2001) Temperature Scales and Classification of Thermometers. *Temperature Measurement*. p 1-18.

Brites CDS, Balabhadra S, Carlos LD (2018a) Lanthanide-Based Thermometers: At the Cutting-Edge of Luminescence Thermometry. *Adv. Optical Mater.* 7(5):1801239-1801268.

Chen G, Liu H, Liang H, Somesfalean G, Zhang Z (2008) Upconversion Emission Enhancement in Yb3+/Er3+-Codoped Y2O3 Nanocrystals by Tridoping with Li+ Ions. *Journal of Physical Chemistry C* 112:12030-12036.

Dong H, Du SR, Zheng XY, Lyu GM, Sun LD, Li LD, Zhang PZ, Zhang C, Yan CH (2015) Lanthanide Nanoparticles: From Design toward Bioimaging and Therapy. *Chem. Rev.* 115(19):10725-10815.

Gai S, Li C, Yang P, Lin J (2014) Recent Progress in Rare Earth Micro/Nanocrystals: Soft Chemical Synthesis, Luminescent Properties, and Biomedical Applications. *Chem. Rev.* 114(4):2343-2389.

Jiang L, Xiao S, Yang X, Ding J, Dong K (2012) Enhancement of up-conversion luminescence in Zn2SiO4:Yb3+, Er3+ by co-doping with Li+ or Bi3+. *Applied Physics B* 107(2):477-481.

Liu X, Skripka A, Lai Y, Jiang C, Liu J, Vetrone F, Liang J (2021b) Fast Wide-Field Upconversion Luminescence Lifetime Thermometry Enabled by Single-Shot Compressed Ultrahigh-Speed Imaging. *Nat. Commun.* 12(1):6401-6409.

Matulionyte M, Skripka A, Ramos-Guerra A, Benayas A, Vetrone F (2023) The Coming of Age of Neodymium: Redefining Its Role in Rare Earth Doped Nanoparticles. *Chem. Rev.* 123(1):515-554.

Tan M, Li F, Cao N, Li H, Wang X, Zhang C, Jaque D, Chen G (2020a) Accurate In Vivo Nanothermometry Through NIR-II Lanthanide Luminescence Lifetime. *Small* 16(48):2004118-2004127.

van Swieten TP, Meijerink A, Rabouw FT (2022) Impact of Noise and Background on Measurement Uncertainties in Luminescence Thermometry. *ACS Photonics* 9(4):1366-1374.

Yin D, Wang C, Ouyang J, Song K, Liu B, Cao X, Zhang L, Han Y, Long X, Wu M (2014) Enhancing upconversion luminescence of NaYF4:Yb/Er nanocrystals by Mo3+ doping and their application in bioimaging. *Dalton Transactions* 43(31):12037-12043.

Zhao Q, Shao B, Lü W, Jia Y, Lv W, Jiao M, You H (2013) Doping alkaline-earth: a strategy of stabilizing hexagonal GdF3 at room temperature. *Dalton Transactions* 42(43):15482-15488.